

C. Schröder

Experimental investigations on drift waves in linear magnetized plasmas

IPP 15/5
Februar 2004

C. Schröder

Experimental investigations on drift waves in linear magnetized plasmas

IPP 15/5
Februar 2004

Experimental investigations on drift waves in linear magnetized plasmas

INAUGURALDISSERTATION

zur

Erlangung des akademischen Grades

doctor rerum naturalium (Dr. rer. nat.)

an der Mathematisch-Naturwissenschaftlichen Fakultät

der

Ernst-Moritz-Arndt-Universität Greifswald

vorgelegt von
Christiane Schröder
geboren am 24.08.1974
in Rostock

Greifswald, 1.12.2003

Dekan: Prof. Dr. Jan-Peter Hildebrandt

1. Gutachter: Prof. Dr. Thomas Klinger

2. Gutachter: Prof. Dr. Mark E. Koepke

Tag der Promotion: 6.2.2004

Contents

General Introduction	3
1 Introduction	3
2 Theoretical background	7
2.1 Drift wave mechanism	7
2.2 Derivation of the drift wave dispersion relation	9
2.3 Experimentally observable features of drift waves	18
2.4 Nonlinear drift wave models	18
2.5 Other plasma instabilities localized in the gradient regions	19
3 Methods of data analysis	23
3.1 The probability density function	23
3.2 Spectral analysis	24
3.3 Cross correlation function	25
I Resistive drift waves in the VINETA device	27
4 The VINETA device: setup and diagnostics	29
4.1 The VINETA device	29
4.1.1 Vacuum system	30
4.1.2 Magnetic field	31
4.1.3 The plasma source	32
4.1.4 Operation and Plasma Parameters	34
4.2 Diagnostics	37
4.2.1 Langmuir Probes	37
4.2.2 Diagnostic setup	45

5	Plasma parameters in VINETA	51
5.1	Axial variation	51
5.2	Variation with the magnetic field	53
5.3	Variation with the neutral gas pressure	55
5.4	Discussion	56
6	Low-frequency instability in VINETA	63
6.1	Time evolution	64
6.2	Localization of fluctuations	66
6.3	Phase between density and potential fluctuations	69
6.4	Poloidal Mode structure	71
6.5	Parallel Wavelength	74
6.6	Dependency on magnetic field	75
6.7	Dependency on neutral gas pressure	80
6.8	Discussion	84
7	Numerical solution of the drift wave dispersion relation	89
7.1	The numerical model	90
7.2	Comparison with previous results	92
7.3	Results for VINETA parameters	95
7.4	Discussion	100
8	Summary and Conclusions	103
II	Synchronization of drift waves	107
9	Introduction	109
9.1	What is synchronization?	111
10	Experimental setup for the synchronization of drift waves	113
10.1	The MIRABELLE device	113
10.2	Diagnostics	115
10.3	The octupole exciter	116
11	Synchronization of drift waves: experimental results	119
11.1	Temporal versus spatiotemporal drive	119
11.2	Spatiotemporal synchronization	121

11.3 Final remarks	124
12 Synchronization of drift waves: simulation results	125
12.1 The theoretical model	125
12.2 Simulation results	126
13 Summary and Conclusions	129
A Derivation of the drift wave dispersion relation	131
A.1 Preparative remarks	131
A.2 Normalization	132
A.3 Cartesian coordinates (Local slab model)	134
A.4 Cylindrical coordinates	136
B Collisions	141
B.1 Coulomb-Collisions	142
B.2 Electron-neutral collisions	143
B.3 Ion-neutral collisions	144
C List of Symbols	147
Bibliography	151
Danksagung	

General Introduction

Chapter 1

Introduction

Bounded plasmas are never in a global thermodynamical equilibrium state. Sources of free energy exist, manifesting in, e.g., electric fields, particle drifts, and parameter gradients [1]. This free energy can drive a number of different plasma instabilities mostly propagating as waves [2]. A sub-class are gradient-driven instabilities in magnetized plasmas [3,4]. Owing to the strong drive, often, instead of single waves, fluctuations with continuous signal power spectra are observed, i.e., turbulence. Turbulent fluctuations induce particle transport perpendicular to the magnetic field [5], which is believed to be the origin of the so-called anomalous transport in magnetized plasmas, where the particle transport is much higher than expected from classical and neoclassical theories [6]. On the way towards a working, affordable fusion reactor, the anomalous transport is a major challenge and has thus been a subject of intense theoretical and experimental research during the last decades [5–7].

The drift instability is probably the most promising candidate for causing anomalous transport at the plasma edge [8]. It is driven by plasma pressure gradients perpendicular to the ambient magnetic field and leads to perturbations, called drift waves. They propagate in the direction perpendicular to the pressure gradient and the magnetic field with a velocity close to the electron diamagnetic drift velocity, and much slower along the magnetic field. Fluctuations caused by drift waves affect plasma density and potential, and occur in the low-frequency regime well below the ion cyclotron frequency. The maximum fluctuation amplitude is localized in the region of the steepest pressure gradient. The dynamics perpendicular to the magnetic field are tightly coupled to the electron dynamics along the magnetic field, the latter also determining the actual instability mechanism [9,10].

The first experimental observation of drift waves is attributed to D'ANGELO et al. in the early 1960s [11–13]. Since then, drift waves became a topic of various experiments [9,14–17]. First theoretical work was done by MOISEEV and SAGDEEV [18], and JUKES [19]. Very soon after, CHEN [20–24] and LASHINSKY [25] identified the role of the microscopic physical processes for the instability and its universal character. Here, linearized local models ('local slab' models) were used [14,21,22,26] where the cylindrical geometry of the laboratory plasma was replaced by local cartesian coordinates. Only a few years later, the first non-local cylindrical models, assuming Gaussian density profiles, were used to improve the theory [27,28]. ELLIS, MARDEN-MARSHALL and coworkers showed that non-

local cylindrical models are mandatory for quantitative agreement between experiment and theory [9,29]. It is also important to take into consideration the static radial electric field and the resulting $E \times B$ rotation of the plasma column [15].

Drift waves also occur in the edge of high-temperature fusion plasmas where the experimental access is sometimes limited [5,8]. Low-temperature plasmas with cylindrical geometry allow to investigate drift waves without effects due to curved and inhomogeneous magnetic fields present in toroidal geometry. The drift instability has been studied in many different plasma parameter regimes accessible in linear devices, comprising collisionless [30] as well as collisional plasmas [10,14], weakly ionized [10] as well as fully ionized plasmas [14]. Most of the experimental work on drift waves in laboratory plasmas has been done in plasmas with β (the ratio of plasma pressure to magnetic-field pressure) well below the electron-ion mass ratio m_e/M . In this low- β regime, drift waves are electrostatic [3], whereas for higher β electromagnetic effects become important, i.e. the parallel electron response becomes Alfvénic. Electromagnetic drift waves were first observed by NISHIDA, TANG, LUHMANN and coworkers in an arcjet plasma [31–33].

Helicon sources are efficient plasma sources [34]. Relatively high beta plasmas with $\beta > m_e/M$ can easily be sustained with only a few kW of RF power. Helicon plasma sources allow for plasmas with peak densities of $n = 10^{18} - 10^{20} \text{ m}^{-3}$ at electron temperatures of a few eV [34] and are nowadays widely established in research laboratories all over the world. This plasma source was invented about 20 years ago, but the discharge mechanism itself is still under intense scientific debate [35–40]. Radial density profiles of helicon produced plasmas typically exhibit steep gradients that can drive instabilities. However, helicon discharges have often been claimed to be quiescent [41,42]. Although numerous papers have been published on helicon discharges, little was reported about the observation of low-frequency instabilities. DEGELING and coworkers observed relaxation oscillations in the kHz-range, which were identified as global oscillations between different discharge modes, though [43,44]. LIGHT and coworkers found a low-frequency, electrostatic instability above a critical magnetic field that might be responsible for saturation or decrease of plasma density with increasing magnetic field [42,45]. The instability was identified as a hybrid of resistive drift waves and Kelvin-Helmholtz instability. Recently, TYNAN and coworkers presented first observations of drift waves in the new CSDX device [46].

Within the course of the present thesis, a new experimental helicon device – VINETA¹ – has been developed, constructed and put into operation. Soon after first operation of VINETA, in the helicon wave sustained discharge mode, low-frequency fluctuations were observed. Because of their localization in the density gradient region at the plasma edge, drift-type instabilities were candidates from the beginning. In part I of the thesis, this instability is investigated in some detail by characterization of its temporal and spatial features. Our main objectives are the identification of the instability and of its chief destabilization mechanisms. Proper control parameters provide the possibility to change the dynamical state of the instability. The experiments are closely accompanied by a numerical study of the drift wave dispersion. In particular, we compare theoretically predicted frequencies to experimental observations and study the influence of plasma parameters on mode frequencies and growth rates. Mode structures of coherent modes in a plane perpendicular to the ambient magnetic field are investigated in the numerical

¹Versatile Instrument for studies on Nonlinearity, Electromagnetism, Turbulence, and Applications

model as well as in experiment.

Drift waves often occur not as a single mode but exhibit turbulent dynamics which means that many modes interact nonlinearly. Drift wave turbulence is of considerable interest because of its role in anomalous transport. It seems reasonable to assume that controlling the drift wave dynamics also controls fluctuation-induced transport. Thus, active control of the turbulent dynamics of drift waves is of great interest for improving the plasma confinement in magnetic fusion devices. Already since the late 1960s, attempts to control drift wave dynamics and the associated transport have been made where feedback techniques were used to suppress single drift modes [47–49]. Usually, fluctuations were recorded, phase-shifted, amplified and fed back into the plasma via electrodes. Alternatively, modulated microwaves at low power were used to suppress drift waves [50]. The confinement could be improved by suppression of fluctuations, but each drift mode requires separate feedback parameters for suppression. Consequently, it was not possible to achieve suppression of broadband fluctuations. Promising results in fusion devices were obtained with biasing techniques which suppress turbulence by sheared flow [51].

A different approach to change the drift wave dynamics is based on chaos control techniques [52]. Here, the goal is the stabilization of preselected regular dynamical states, not the total suppression. For drift wave chaos, successful control was recently demonstrated [53]. However, drift wave chaos is rather an exception and exists only in a narrow regime on the route to developed turbulence [54].

Drift wave dynamics are of spatiotemporal nature. Therefore, it can barely be expected that a purely temporal or spatial control technique proves to be efficient and robust. The full spatial component of the dynamics, however, was often ignored in the feedback methods used. Part II of the thesis reports on experiments and computer simulations of mode-selective synchronization of drift waves, using an open-loop control scheme acting in space and time [55]. The aim is to suppress drift wave turbulence by driving preselected drift modes at the expense of the broadband spectrum.

The thesis is organized as follows: The theoretical background of the drift instability is briefly discussed in chapter 2. The data analysis methods that were used are described in chapter 3. The results of the present work are presented in two parts. Part I reports about investigations of the drift instability in a helicon plasma. The experimental device VINETA and the plasma diagnostic tools are reviewed in chapter 4. The experimental results are presented in chapters 5 and 6, and numerical results on the drift wave dispersion relation are presented in chapter 7. In chapter 8 conclusions on part I are drawn. Part II reports about mode-selective synchronization of drift waves. Chapter 9 gives a brief introduction into the concept of synchronization. The experimental arrangement is described in chapter 10. Experimental results on the synchronization of drift waves are presented in chapter 11 and compared to numerical results in chapter 12. Conclusions on part II are drawn in chapter 13.

Chapter 2

Theoretical background

This chapter gives a brief introduction into the physics of drift waves in cylindrical homogeneous magnetic field geometry. Linear drift wave models in the fluid picture are described and typical observable features are summarized. The goal of part I of the present thesis is the identification of observed low-frequency instabilities in the VINETA device. Candidates for instabilities causing fluctuations are resistive drift waves as well as related plasma instabilities like the Kelvin-Helmholtz instability and the Rayleigh-Taylor instability [2]. This variety of instabilities is briefly introduced and criteria for their distinction are given.

Drift waves have been investigated since the mid-1960s. In early theoretical work on drift waves, cylindrical geometry, typical for many laboratory plasmas, was replaced by a simpler cartesian geometry, at the local position of the fluctuations (so-called local slab models) [14,22]. These models were useful for understanding the physical mechanisms. However, it became clear that improved models are needed for a more quantitative comparison between theory and experiment, taking into account the cylindrical geometry [29]. ELLIS, MARDEN-MARSHALL and co-workers developed a global, cylindrical, linear model which includes a variety of physical mechanisms, e.g., parallel electron current and collisions with neutrals [9,10,15]. Numerical results from this model have been in good agreement with experimental results in linear magnetized devices [9,56].

The experimental parts of the present work are discussed along with numerical calculations, based on models and codes developed by NAULIN¹. Subsequently, the drift wave equations are derived as a basis for the numerical models introduced in chapters 7 and 12.

2.1 Drift wave mechanism

In this section, a ‘pictorial’ description of the drift wave mechanism is given. The mathematical framework follows in the subsequent section.

Drift waves are low-frequency waves in magnetized plasmas, driven by a pressure gradient. Temperature fluctuations and temperature gradients are neglected here, so that only

¹Volker Naulin, Risø National Laboratory, Roskilde, Denmark

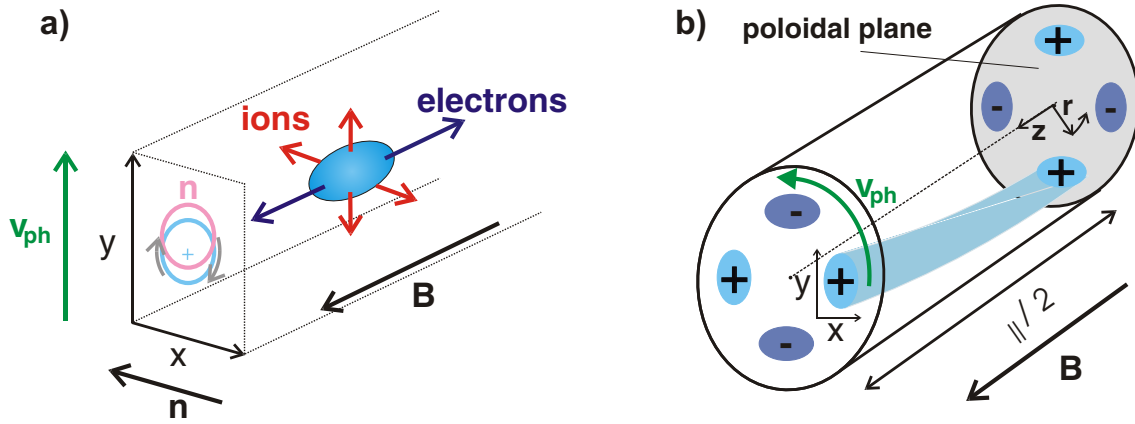


Figure 2.1: The drift wave mechanism: a) sketch of the basic process [57]. ∇n is the direction of the density gradient. \tilde{n} and $\tilde{\phi}$ denote the density and potential perturbation, respectively. v_{ph} denotes the net drift of the entire structure. b) sketch of the global situation in a cylinder for an $m = 2$ mode, characterized by two maxima (+) and minima (-) of the perturbations on one circumference. λ_{\parallel} is the parallel wavelength. The local cartesian coordinate system of a) is also indicated.

density gradients provide the free energy which drives the instability. Key features of the drift instability are the tight coupling of the dynamics parallel and perpendicular to the ambient magnetic field, as well as the coupling between the ion and the electron dynamics.

Figure 2.1a) shows a schematic drawing of the basic drift wave mechanism in a local slab (cartesian) coordinate system. Consider a plasma with a homogenous magnetic field $\mathbf{B} = -B\mathbf{e}_z$ and a density gradient perpendicular to the ambient magnetic field in the $-x$ -direction. Assume a small density perturbation \tilde{n} which is electrically neutral in the beginning. Due to their small mass, the electrons are much more mobile than the ions and move almost instantly along the magnetic field \mathbf{B} whereas the ions remain at their position. This gives rise to a surplus of charge which causes a local increase of the plasma potential $\tilde{\phi}$ and thereby form an electric field distribution $\tilde{\mathbf{E}}$. The temporally increasing electric field leads to polarization drift of the ions, which ensures quasineutrality $\nabla \cdot \mathbf{J} = 0$. Furthermore, the electric field perturbation $\tilde{\mathbf{E}}$ together with the ambient magnetic field \mathbf{B} gives rise to a local $\mathbf{E} \times \mathbf{B}$ drift around the density perturbation. Due to the density gradient, the $\mathbf{E} \times \mathbf{B}$ drift convects more plasma in the $+y$ -direction than in the opposite ($-y$) direction. Hence, the perturbation propagates in the y -direction which is identical to the direction of the diamagnetic electron drift $\mathbf{v}_{D,e} = k_B T_e \nabla n \times \mathbf{B} / neB^2$, perpendicular to the density gradient and to the ambient magnetic field.

A stability analysis reveals that the situation is stable (that is no instability occurs) if the density fluctuations \tilde{n} and the potential fluctuations $\tilde{\phi}$ are exactly in phase [22]. This is

the case for adiabatic electrons, i.e., if the (linearized) Boltzmann relation

$$\tilde{n} = n_0 \exp\left(\frac{\tilde{\phi}}{T_{[eV]}}\right) \approx n_0 \frac{\tilde{\phi}}{T_{[eV]}} \quad (2.1)$$

holds². For instability, there must be a (small) phase shift $\angle(\tilde{n}, \tilde{\phi}) > 0$ while the density fluctuations must develop ahead of the potential fluctuations in the drift direction [57]. This is already indicated in figure 2.1a). If the electron flow along \mathbf{B} is impeded by some extra mechanism (e.g. Landau damping [58], collisions [14] or inductance [33]), the Boltzmann relation is violated which leads to a non-zero phase shift and a destabilization of drift waves.

Figure 2.1b) depicts a drift wave in cylindrical geometry. The local cartesian coordinate system of figure 2.1a) is also indicated. The transformation between cartesian and cylindrical coordinate system is done by $r \rightarrow x$ and $\theta r \rightarrow y$. The plane perpendicular to the magnetic field is referred to as the poloidal plane. The direction around the plasma center, that is perpendicular to the ambient magnetic field as well as perpendicular to the radial density gradient, is referred to as the poloidal direction. Parallel (\parallel) and perpendicular (\perp) are always used in relation to the ambient magnetic field.

In cylindrical geometry, the density and potential perturbations propagate in the poloidal direction. Due to the non-adiabatic electron response, the structure also evolves in the direction parallel to the magnetic field, giving rise to a finite axial wavelength. The parallel wavelength is much larger than the perpendicular wavelength. Note that the actual fluid does not propagate but only the plasma perturbation. It is a typical wave phenomenon, characterized by the angular frequency ω and the wave vector $\mathbf{k} = \mathbf{k}_\perp + \mathbf{k}_\parallel$. The periodic boundary conditions in the poloidal direction restrict the possible poloidal wave number k_θ values for drift modes. The number of maxima (or minima) on one circumference is referred to as the (poloidal) mode number m and is connected by the relation $m = rk_\theta$ to k_θ (see figure 2.1b).

2.2 Derivation of the drift wave dispersion relation

There are three approaches to describe collective phenomena in magnetized plasmas [1]. The kinetic theory gives the most comprehensive description of a plasma. Here, the probability distribution of particle velocities is fully taken into account. In the fluid approximation, the plasma is considered to be composed of two or more interpenetrating and interacting fluids, one for each particle species. Plasma parameters such as density, velocity and temperature of each species enter the fluid equations which are the statistical moments of the kinetic equations. The most simplifying picture is magnetohydrodynamics where the plasma is treated as a single fluid. Drift waves must be described in the two-fluid picture of a plasma because electron and ion dynamics have to be treated separately.

² $T_{[eV]}$ is the electron temperature in eV. $T_{[eV]} = k_B T_e / e$ with the electron temperature T_e in K.

Basic fluid equations

The basic two-fluid equations for the description of drift waves are:

- the electron continuity equation

$$\partial_t n_e + \nabla \cdot (n_e \mathbf{v}_e) = 0 \quad (2.2)$$

- the ion continuity equation

$$\partial_t n_i + \nabla \cdot (n_i \mathbf{v}_i) = 0 \quad (2.3)$$

- the electron momentum transfer equation

$$nm_e d_t \mathbf{v} = -\nabla p - ne(\mathbf{E} + \mathbf{v} \times \mathbf{B}) + n\nu_{ei}m_e(\mathbf{u} - \mathbf{v}) - n\nu_{en}m_e\mathbf{v} \quad (2.4)$$

- the ion momentum transfer equation

$$nM d_t \mathbf{u} = -\nabla p + ne(\mathbf{E} + \mathbf{u} \times \mathbf{B}) - n\nu_{in}M\mathbf{u} \quad (2.5)$$

where $n_{i,e}$ are the densities of ions (i) and electrons (e), \mathbf{v} is the electron velocity, \mathbf{u} is the ion velocity, m_e is the electron mass, M is the ion mass, \mathbf{E} is the electric field, \mathbf{B} is the magnetic field, and p is the plasma pressure. $\nu_{\alpha\beta}$ are the collision frequencies between species α and β (where the involved species are electrons e , ions i and neutrals n). For the convective derivative the following notation is used

$$d_t = \partial_t + \mathbf{v}_E \cdot \nabla_{\perp} \quad , \quad (2.6)$$

where \mathbf{v}_E is the $\mathbf{E} \times \mathbf{B}$ drift velocity (see below).

From the continuity equations for both species (2.2) and (2.3), an equation for the current divergency in a quasi-neutral plasma with $n := n_e = n_i$ is obtained:

$$\nabla \cdot \mathbf{J} = 0 \quad . \quad (2.7)$$

Splitting (2.7) into the components parallel and perpendicular to the ambient magnetic field yields

$$\nabla_{\perp} \cdot \mathbf{J}_{\perp} = -\nabla_{\parallel} \cdot \mathbf{J}_{\parallel} \quad . \quad (2.8)$$

This equation governs the tight coupling between the parallel and the perpendicular drift wave dynamics.

Electromagnetic effects

Electromagnetic effects can play a significant role in drift wave physics. The electrons can easily flow along the magnetic field lines giving rise to a net parallel current. These fluctuation currents induce magnetic fields perpendicular to the ambient magnetic field.

From the parallel component of the electron momentum equation (2.4), it can be estimated under which conditions magnetic field fluctuations become important:

$$\underbrace{-\frac{m_e}{e} d_t \mathbf{J}_{\parallel}}_{(1)} = -\nabla_{\parallel} p + ne \nabla_{\parallel} \phi + \underbrace{ne \partial_t \psi}_{(2)} - \underbrace{\frac{m_e \nu_e}{e} \mathbf{J}_{\parallel}}_{(3)} \quad (2.9)$$

where $E_{\parallel} = -\nabla_{\parallel} \phi - \partial_t \psi$, $\mathbf{J} = -en\mathbf{v}$, $d_t \mathbf{J} \approx -en d_t \mathbf{v}$, $\nu_e = \nu_{ei} + \nu_{en}$, $\psi = \mathbf{A}_{\parallel}$ and \mathbf{A} is the vector potential of the magnetic field $\mathbf{B} = \nabla \times \mathbf{A}$. If magnetic field fluctuations are important, the magnetic induction term (2) is greater than the two terms (1) and (3) which include the parallel current. Since for drift waves perpendicular scale lengths are typically much smaller than parallel scale lengths, Ampere's law can be used in the form $\mathbf{J}_{\parallel} = (\nabla_{\perp}^2 + \nabla_{\parallel}^2) \psi / \mu_0 \approx \nabla_{\perp}^2 \psi / \mu_0$. Replacing the derivatives with typical time and length scales, the comparison of terms (1) and (2) leads to

$$ne \partial_t \psi > \frac{m_e}{e} d_t \nabla_{\perp}^2 \psi \implies ne \omega \psi > \frac{m_e}{e} \omega k_{\perp}^2 \psi \implies \frac{M}{2m_e} \underbrace{\frac{e^2 B^2}{k_B T_e M}}_{1/\rho_s^2} \underbrace{\frac{2nk_B T_e \mu_0}{B^2}}_{\beta} > k_{\perp}^2 \quad ,$$

where the drift scale ρ_s and the plasma- β have been introduced. β is the ratio between particle pressure and magnetic field pressure in the plasma while ρ_s is the ion gyro radius taken at electron temperature. Since $k_{\perp}^2 \rho_s^2$ is typically of the order of unity for drift waves, the condition

$$\beta > 2k_{\perp} \rho_s \frac{m_e}{M} \approx \frac{m_e}{M} \quad (2.10)$$

is obtained for non-negligible magnetic field fluctuations. In the literature this condition is usually quoted for electrostatic fluctuations [4,33]. However, comparison of the induction term (2) with the friction term (3) yields

$$ne \partial_{\theta} \psi > \frac{m_e \nu_e}{e \mu_0} \nabla_{\perp}^2 \psi \implies ne \omega \psi > \frac{m_e \nu_e}{e \mu_0} k_{\perp}^2 \psi \implies \frac{M}{2} \underbrace{\frac{e^2 B^2}{k_B T_e M}}_{1/\rho_s^2} \underbrace{\frac{2nk_B T_e \mu_0}{B^2}}_{\beta} \omega > m_e \nu_e k_{\perp}^2 \quad .$$

This gives the condition

$$\beta > 2k_{\perp}^2 \rho_s^2 \frac{m_e}{M} \frac{\nu_e}{\omega} \approx \frac{m_e}{M} \frac{\nu_e}{\omega} \quad (2.11)$$

for non-negligible magnetic field fluctuations compared to damping caused by the electron friction. With $k_{\perp}^2 \rho_s^2$ being of the order of unity and using a typical collision frequency for the argon plasma of the VINETA device (see chapter 5) this condition reads to be $\beta \gtrsim 10^{-5} \cdot 1000 = 10^{-2}$, while the plasma β in the VINETA device is usually below 10^{-3} . This means that, due to the relatively high collisionality, the magnetic field fluctuations are negligible in the VINETA device where the experiments of part I of this thesis are conducted. In the MIRABELLE device (see part II of the present thesis), $\beta \ll m_e/M$ always holds. Thus, magnetic field fluctuations can be neglected for all experimental conditions investigated in the present work and only electrostatic fluctuations must be taken into account.

singly charged positive ions	$A \longrightarrow A^+ + e^-$	
homogeneous magnetic field	$\mathbf{B} = B\mathbf{e}_z$	
constant electron temperature	$T_e = \text{const}$	$\nabla p = k_B T_e \nabla n$
cold ions and neutrals	$T_i \approx 0$	$T_n \approx 0$
constant parallel electron velocity	$V = \text{const}$	
no parallel ion and neutral velocities	$U \approx 0$	$W \approx 0$
electrostatic fluctuations	$\mathbf{E} = -\nabla\phi$	
small frequencies	$\omega \ll \Omega_{ci}$	
propagation mainly perpendicular to \mathbf{B}	$k_{\parallel}/k_{\perp} \ll 1$	
collision frequencies radially dependent	$\nu_{ei} = \nu_{ei}(r)$	$\nu_{en} = \nu_{en}(r), \nu_{in} = \nu_{in}(r)$

Table 2.1: Summary of assumptions used for the electrostatic drift wave model.

Assumptions for the model

Starting with equations (2.2–2.8), a model describing drift waves is derived with the assumptions given in table 2.1. Fluctuating plasma parameters are split into a time-averaged value denoted by the index 0 and a fluctuating part denoted by a tilde $\tilde{}$, for instance $\phi = \phi_0 + \tilde{\phi}$. The so-called drift ordering is assumed:

$$\frac{\omega}{\Omega_{ci}} \sim \frac{k_{\parallel}}{k_{\perp}} \sim \frac{\tilde{\phi}}{T_{[eV]}} \sim \frac{\tilde{n}}{n_0} \sim \frac{\rho_s}{L_{\perp}} \sim \epsilon \ll 1 \quad (2.12)$$

where $\Omega_{ci} = eB/M$ is the ion cyclotron frequency, ϕ denotes the potential and L_{\perp} is a typical scale length of the density gradient. The particle drifts perpendicular to \mathbf{B} of both species are taken from the perpendicular part of the momentum transfer equations (2.4) and (2.5). Under these assumptions, the model can be reduced to three equations: the electron continuity equation (2.2), the parallel component of the electron momentum equation (2.4) and the quasineutrality equation (2.8). These equations are normalized, linearized and harmonic oscillations of a proper wave form are assumed.

Perpendicular drifts

The particle drifts perpendicular to the magnetic field are obtained by crossing the momentum equations with \mathbf{B} . For the electrons the collision terms are neglected and one obtains

$$\begin{aligned} \mathbf{v}_{\perp} &= \underbrace{\frac{\mathbf{E} \times \mathbf{B}}{B^2}}_{\mathbf{v}_E} + \underbrace{\frac{k_B T_e}{neB^2} \nabla n \times \mathbf{B}}_{\mathbf{v}_{D,e}} - \underbrace{\frac{m_e}{eB^2} d_t \mathbf{E}}_{\mathbf{v}_{p,e}} \\ &\approx \mathbf{v}_E + \mathbf{v}_{D,e} \quad . \end{aligned} \quad (2.13)$$

where the following drifts are introduced:

$$\text{E}\times\text{B drift: } \mathbf{v}_E = \frac{\mathbf{E} \times \mathbf{B}}{B^2} \quad (2.14)$$

$$\text{electron diamagnetic drift: } \mathbf{v}_{D,e} = \frac{k_B T_e}{neB^2} \nabla n \times \mathbf{B} \quad (2.15)$$

$$\text{electron polarization drift: } \mathbf{v}_{p,e} = -\frac{m_e}{eB^2} d_t \mathbf{E} \quad (2.16)$$

The electron polarization drift is a higher order electron inertia effect and is much smaller than both the E×B drift and the diamagnetic drift. It is neglected in the following.

The collision terms for the ions must be taken into account. One obtains

$$\begin{aligned} \mathbf{u}_\perp &= \underbrace{\frac{\mathbf{E} \times \mathbf{B}}{B^2}}_{\mathbf{u}_E} - \underbrace{\frac{k_B T_i}{enB^2} \nabla n \times \mathbf{B}}_{\mathbf{u}_{D,i}} + \underbrace{\frac{M}{eB^2} d_t \mathbf{E}}_{\mathbf{u}_{p,i}} - \underbrace{\frac{\nu_{in} M}{eB^2} \nabla_\perp \phi}_{\mathbf{u}_{Ped}} \\ &\approx \mathbf{u}_E + \mathbf{u}_{p,i} + \mathbf{u}_{Ped} \quad . \end{aligned} \quad (2.17)$$

Besides the E×B drift \mathbf{u}_E , the ion polarization drift $\mathbf{u}_{p,i}$ and the ion diamagnetic drift $\mathbf{u}_{D,i}$, an extra term is found: \mathbf{u}_{Ped} is a velocity corresponding to the so-called Pedersen current [59] due to the ion-neutral collisions. The assumption of cold ions allows neglection of the diamagnetic drift of the ions. The ion polarization drift is kept since it is the only perpendicular drift with a non-vanishing divergence and therefore the only perpendicular contribution to equation (2.8).

Normalization

The drift wave equations are made dimensionless by scaling the physical quantities with length scales and frequencies typical for drift wave dynamics (table 2.2). Normalized quantities and derivatives are indicated by a hat $\hat{\cdot}$ which is later omitted for simplicity. $N = \ln n$ is introduced, with $n = n_0(1 + \tilde{n})$ where $n(t)$ is the total density and n_0 is the time-averaged density³. For the derivative with respect to ξ follows

$$d_\xi N = \frac{1}{n} d_\xi n \quad . \quad (2.18)$$

With the assumption $\tilde{n} \ll 1$ one obtains

$$d_\xi \ln n = d_\xi \ln [n_0(1 + \tilde{n})] \approx d_\xi \ln n_0 + d_\xi \tilde{n} \quad . \quad (2.19)$$

With the introduced normalization and the above assumptions, a set of normalized equations can be derived (see appendix A). Defining $V := \mathbf{v}_\parallel$ for the parallel electron velocity and introducing the vorticity $\Omega := \nabla^2 \phi$, the normalized equations are

- electron momentum equation, from the parallel component of (2.4):

$$\hat{d}_t \hat{V} = \frac{M}{m_e} \left(\hat{\nabla}_\parallel \hat{\phi} - \hat{\nabla}_\parallel N \right) - (\hat{\nu}_{ei} + \hat{\nu}_{en}) \hat{V} \quad (2.20)$$

³For the plasma density, two notations are used in the present work: in relation to measured quantities, the notation $n = n_0 + \tilde{n}$ is used and in the theoretical model derived here $n = n_0(1 + \tilde{n})$ is used. The ratio \tilde{n}/n_0 is always related to the notation $n = n_0 + \tilde{n}$.

quantity	normalization factor	norm. quantity	norm. derivative
length	drift scale $\rho_s = \sqrt{\frac{k_B T_e M}{e^2 B^2}}$	$\hat{l} = \frac{l}{\rho_s}$	$\hat{\partial}_l = \rho_s \partial_l$
wave vector		$\hat{k} = \rho_s k$	
time	ion cyclotron frequency $\Omega_{ci} = \frac{eB}{M}$	$\hat{t} = \Omega_{ci} t$	$\hat{\partial}_t = \frac{1}{\Omega_{ci}} \partial_t$
frequency		$\hat{\nu}_{\alpha\beta} = \frac{\nu_{\alpha\beta}}{\Omega_{ci}}$	
velocity	ion sound speed $c_s = \sqrt{\frac{k_B T_e}{M}}$	$\hat{v} = v/c_s$	
potential	electron temperature $T_{[eV]} = \frac{k_B T_e}{e}$	$\hat{\phi} = \frac{e}{k_B T_e} \phi$	

Table 2.2: Normalization of physical quantities in our model.

- electron continuity equation, from (2.2):

$$\hat{d}_t N = -\hat{V} \hat{\nabla}_{\parallel} N - \hat{\nabla}_{\parallel} \hat{V} \quad (2.21)$$

- quasineutrality condition, from (2.8):

$$\hat{d}_t \hat{\Omega} = \hat{\nabla} N \cdot (-\nu_{in} \hat{\nabla}_{\perp} \hat{\phi} - \hat{d}_t \hat{\nabla}_{\perp} \hat{\phi}) - \nu_{in} \hat{\Omega} - \hat{\nabla}_{\parallel} \hat{V} - \hat{V} \hat{\nabla}_{\parallel} N \quad . \quad (2.22)$$

It is found that the normalized equations can be completely written in terms of the logarithm of the density reflecting the fact that density cannot become negative.

Subsequently, the notation $\hat{\cdot}$ for normalized quantities is dropped for convenience.

Linear Properties of a local slab model

The previous equations are independent of the coordinate system used. For further evaluation of the model equations, a coordinate system needs to be specified. Following the historical development, a local slab model in cartesian coordinates is at first introduced. The transformation between cartesian and cylindrical coordinate system is done by

$$r \rightarrow x \quad \text{and} \quad \theta r \rightarrow y \quad . \quad (2.23)$$

For the local slab model, the $E \times B$ background drift of the plasma column is neglected ($\phi_0 = \text{const}$, $\mathbf{\Omega}_0 = 0$). The equilibrium density gradient is in the x direction $n_0 = n_0(x)$ and is assumed to be constant. The background parallel electron drift is assumed to be

electron diamagnetic drift frequency: $\omega^* := -\frac{k_y}{L_n} = -k_y \partial_x \ln n_0$	effective electron collision frequency: $\nu_e := \nu_{ei} + \nu_{en}$
normalized collision frequency: $\tau := \frac{M}{m_e \nu_e}$	electron parallel drift frequency: $\omega_1 := V_0 k_{\parallel}$
$\tau_e := \frac{M}{m \nu_e} k_{\parallel}^2$	$b := k_y^2$

Table 2.3: Abbreviations used for the local slab model.

radially and axially constant $V_0 = \text{const}$, corresponding to a constant electron current through the discharge. Harmonic oscillations of the form

$$V, \Omega, \phi, n \propto \exp(-i\omega t + ik_y y + ik_{\parallel} z) \quad (2.24)$$

are assumed. This yields the derivatives: $\partial_t = -i\omega$, $\partial_y = ik_y$ and $\partial_z = ik_{\parallel}$. All components of the wave vector \mathbf{k} are assumed to be real, but the frequency $\omega = \omega_R + i\omega_I$ is a complex quantity. This allows for temporal growing or damping of the wave whereas spatial growing and damping is excluded. Table 2.3 compiles abbreviations used for the local slab model.

Linearization of equations (2.20–2.22) finally yields the dispersion relation for collisional drift waves in the local slab model:

$$0 = b\omega^2 + (i\tau_e(1+b) + ib\nu_i - b\omega_1)\omega - \tau_e(b\nu_i + i\omega^*) + \omega_1(\omega^* - ib\nu_i) \quad (2.25)$$

(see appendix A.3 for more details). This is equation (9) of reference [9]. For the limiting case $\omega, \omega_1, \omega^* \ll \tau_e$, the solution can be approximated as:

$$\omega_R = \frac{\omega^*}{1+b} \quad , \quad (2.26)$$

$$\omega_I = \frac{\omega^*}{\tau_e(1+b)} \left(\frac{b\omega^*}{(1+b)^2} + \omega_1 \right) - \frac{b}{1+b} \nu_{in} \quad . \quad (2.27)$$

Equation (2.26) shows that the frequency of the fluctuations ω_R depends only on ω^* and b . In physical units we have $b = \rho_s^2 k_y^2$, being a measure of finite ion inertia effects perpendicular to the magnetic field. It is also a measure for finite Larmor radius effects and it is found that these reduce the wave frequency [10].

Equation (2.27) gives some insight into the physical mechanisms which lead to stabilization and destabilization of drift waves. For a growth rate $\omega_I > 0$ drift waves are destabilized while for $\omega_I < 0$ they are stabilized, i.e. any perturbations are damped. It is found:

- For instability, a background density gradient is required such that $\omega^* > 0$. The density gradient provides the free energy for the growth of the fluctuations.
- The instability vanishes if τ_e goes to infinity since $\omega_I < 0$. This means that drift waves are stable for an adiabatic electron response.
- The parallel electron drift increases the growth rate since it affects the phase shift between density and potential fluctuations (see equation (A.7)).
- Ion collisions lead to stabilization of drift waves.
- The dependency on $b = k_\perp^2 \rho_s^2 \propto 1/B$ (in physical units) is more complex and yields no monotonic increase or decrease of the growth rate. A careful analysis shows that drift waves are destabilized only above a certain critical magnetic field [9].

For comparison between theory and the experimentally observed frequency ω , the mode frequency ω_R must be corrected to account for the Doppler shift due to the radial electric field:

$$\omega \approx \frac{m}{1+b} \omega^* \pm \omega_E \quad (2.28)$$

where $\omega_E = v_E/r$ is the frequency related to the $\mathbf{E} \times \mathbf{B}$ drift. The sign depends on the directions of electron diamagnetic drift and $\mathbf{E} \times \mathbf{B}$ drift.

Linear cylindrical model

For a model in cylindrical coordinates, again equations (2.20–2.22) are used. Different from the local slab model, the background plasma potential $\phi_0 = \phi_0(r)$ and the background plasma density $n_0 = n_0(r)$ are explicitly considered. Harmonic oscillations of the form

$$n, \phi, \Omega, V \propto \exp(-i\omega t + ik_\parallel z + im\theta) \quad (2.29)$$

are assumed where an arbitrary radial dependency of the fluctuation amplitude is allowed. Derivatives read $\partial_t = -i\omega$, $\partial_z = ik_\parallel$ and $\partial_\theta = im$, where m is the integer poloidal mode number. The frequency $\omega = \omega_R + i\omega_I$ is again a complex number to allow for temporal growing/damping. Table 2.4 summarizes the abbreviations used for the cylindrical model. Note that, different from the model of ELLIS, MARDEN-MARSHALL and coworkers [9,10,15], here the radial dependency of the collision frequencies $\nu(r)$ is taken into account. Additionally, electron inertia is not fully neglected (i.e. $d_t \mathbf{v} \neq 0$) here, i.e. the poloidal $\mathbf{E} \times \mathbf{B}$ drift of the electrons is taken into account in the convective derivative (2.6).

Evaluation of the linearized equations (2.20–2.22) with the given assumptions yields a second-order differential equation:

$$\partial_{rr}\phi + \left(\frac{1}{r} - \kappa(r) + RD(r) \right) \partial_r \phi + \left(Q(r) - \frac{m^2}{r^2} \right) \phi = 0 \quad , \quad (2.30)$$

where Q is defined as

$$Q(r) := \frac{1}{\tilde{\omega} + i\nu_{in}} \left[\omega^* + \frac{m}{r} S_p - \tilde{\omega} \frac{\omega^* + iP}{\tilde{\omega} - \omega_1 + iP} \right] \quad (2.31)$$

and the rotational drag term RD as

$$RD(r) := i \frac{1}{\tilde{\omega} + i\nu_{in}} \left(\frac{\omega^* + iP}{\tilde{\omega} - \omega_1 + iP} \right) \nu_{in} r V_p \quad . \quad (2.32)$$

(see appendix A for more details). A direct comparison to the dispersion relation obtained in references [10,15] is not a straightforward procedure. In any case, the dispersion relations differ due to different approximations used (e.g. $d_t \mathbf{v} = 0$ was assumed there). If the $\mathbf{E} \times \mathbf{B}$ rotation of the plasma column is neglected ($V_p = S_p = 0$), the dispersion relation (2.30) for drift waves reduces to equation (12) of reference [9]. Model equations (2.30-2.32) are used in the present work for the numerical solution of the drift wave dispersion relation (see chapter 7).

The relation between density fluctuation n and potential fluctuations ϕ is given by

$$n = \frac{\omega^* + iP}{\tilde{\omega} - \omega_1 + iP} \phi \quad . \quad (2.33)$$

This equation describes the phase shift between density and potential fluctuations. It depends on several physical parameters (for instance the parallel wave vector, the electron collisions, the mode number and mode frequency and the parallel electron velocity). Destabilization of drift waves due to a non-zero phase shift between density and potential fluctuations can thus be established by different physical mechanisms.

effective electron collision frequency: $\nu_e(r) := \nu_{en}(r) + \nu_{ei}(r)$	electron parallel drift frequency: $\omega_1 := V_0 k_{\parallel}$
inverse density gradient scale length $\kappa(r) := -\partial_r \ln n_0$	electron diamagnetic drift frequency $\omega^* := \frac{m}{r} \kappa(r)$
$\mathbf{E} \times \mathbf{B}$ velocity: $V_p(r) := \frac{1}{r} \partial_r \phi_0(r)$	curvature of flow profile: $S_p(r) := \partial_r \Omega_0(r) = \partial_r \left(\frac{1}{r} \partial_r + \partial_{rr} \right) \phi_0(r)$
$\tilde{\omega}(r) := \omega(r) - mV_p(r)$	$P(r) := \frac{M}{m_e} \frac{k_{\parallel}^2}{\nu_e + imV_p}$

Table 2.4: Abbreviations used for the cylindrical model. ω^* denotes the frequency corresponding to the diamagnetic electron drift velocity. The collision frequencies ν_{ei}, ν_{en} and ν_{in} , the wave vector $\mathbf{k} = \mathbf{k}_{\perp} + \mathbf{k}_{\parallel}$, ω_1 , κ and ω^* are real, whereas the wave frequency ω is a complex quantity.

2.3 Experimentally observable features of drift waves

The dispersion relation of drift waves is complex and depends on a number of physical quantities. Therefore, a direct quantitative comparison between theory and experiment is usually difficult to do. However, there exist several characteristic features for drift waves which allow for the identification of an observed instability as the drift instability. Experimentally observable drift wave features are [14,60]:

1. \tilde{n}/n_0 amplitude peaks at the maximum radial density gradient,
2. the magnitude of plasma density and potential fluctuations is similar, $\tilde{n}/n_0 \approx \tilde{\phi}/T_{[eV]}$,
3. the phase velocity (corrected for the Doppler shift due to $\mathbf{E} \times \mathbf{B}$ rotation of the entire plasma column) points in the direction of the electron diamagnetic drift $\mathbf{v}_{D,e}$,
4. the phase velocity cannot be higher than the electron diamagnetic drift velocity and for optimum growth rate $v_{ph} \approx 0.5 v_{D,e}$ is estimated,
5. the parallel wavelength is finite, i.e. $k_{\parallel} > 0$, and typically of the order of the machine length,
6. density fluctuations are ahead of the potential fluctuations with $0 < \angle(\tilde{n}, \tilde{\phi}) < 45^\circ$.

In chapter 6, criteria 1–6 are verified in the experimental observation.

2.4 Nonlinear drift wave models

Linear theory gives already some insight into the physical mechanisms of drift waves. It can, however, not explain phenomena such as the saturation of linearly unstable modes, the interaction between different modes or drift wave turbulence. With increasing computer power, numerical simulations have become a useful tool to explore drift wave dynamics recently [8,57]. Simulations must be separated into two-dimensional (2D) and three-dimensional (3D) geometry. A particular nonlinear, 2D model is the HASEGAWA-MIMA model [61,62] which describes electrostatic drift wave turbulence with only one variable, namely the electrostatic potential ϕ . It is based on the assumption of adiabatic electrons and no instability mechanism is included in the model. Nevertheless, the model has been extensively investigated because it allows one to study basic nonlinear mechanisms [8]. In order to introduce instability, so-called $i\delta$ -models have been developed which include a non-adiabatic electron response by introducing a relation in \mathbf{k} -space of the form $\tilde{n}_{\mathbf{k}} = (1 - i\delta_{\mathbf{k}}\tilde{\phi}_{\mathbf{k}})$ [8]. The TERRY-HORTON model is such a nonlinear 2D model, retaining the single field description [63]. Generally, in 2D turbulence models the energy is inversely cascaded from short wavelengths to long wavelengths and large-scale fluctuation structures play an important role [17]. In 3D models, large-scale structures are less important and a strict inverse energy cascade is generally not observed [58,64].

The HASEGAWA-WAKATANI model is a well established nonlinear two-field model which is derived from the fluid equations [65]. It is a set of two coupled equations for the

normalized potential fluctuations $\phi = \tilde{\phi}/T_{[eV]}$ and the normalized density fluctuations $n = \tilde{n}/n_0$ that can be written in the form with retained parallel current as

$$\frac{\partial}{\partial t} \nabla_{\perp}^2 \phi + \mathbf{v}_E \cdot \nabla \nabla_{\perp}^2 \phi = \nabla_{\parallel} J_{\parallel} + \mu_w \nabla_{\perp}^4 \phi \quad (2.34)$$

$$\frac{\partial}{\partial t} n + \mathbf{v}_E \cdot \nabla (n_0 + n) = \nabla_{\parallel} J_{\parallel} + \mu_n \nabla_{\perp}^2 n \quad (2.35)$$

where $J_{\parallel} = -\sigma \nabla_{\parallel} (\phi - n)$ is the current parallel to the ambient magnetic field, and $\sigma = \rho_s T_e / m_e c_s \nu_{ei}$ is the normalized parallel conductivity. The viscous terms $\mu_w \nabla_{\perp}^4$ and $\mu_n \nabla_{\perp}^2$ have been artificially introduced to assure regularity of density and potential. Often, this 3D model is reduced to a 2D model by introducing an effective wave length $\nabla_{\parallel}^2 \rightarrow k_{\parallel}^2$ [8]. This is motivated by the scale separation between parallel and perpendicular length and reduces the computational efforts significantly. A 2D HASEGAWA-WAKATANI model is used for numerical simulation of synchronization of drift waves (see chapter 12).

2.5 Other plasma instabilities localized in the gradient regions

Two further instabilities are briefly discussed, namely the Rayleigh-Taylor instability and the Kelvin-Helmholtz instability [1]. As is the case with drift waves, for both instabilities $k_{\perp} \gg k_{\parallel}$ and, furthermore, density as well as potential fluctuations occur that are radially located in the strong gradient region. Both instabilities are known from neutral fluids. In part I of the present thesis, an instability observed in the VINETA device is to be identified. It is thus important to have experimentally observable criteria to distinguish the instabilities from each other. This is sometimes not straightforward to do. For instance, LIGHT and coworkers identified an instability occurring in the gradient region of a helicon plasma as a complex combination of the resistive drift instability and the Kelvin-Helmholtz instability [42,45].

The Kelvin-Helmholtz instability

The Kelvin-Helmholtz instability is well known from hydrodynamic systems and plays a role, e.g., in meteorology [67]. The instability is driven by sheared flows. For two fluids on either side of an interface and moving with different velocities, a ‘wrinkling’ effect occurs at the interface [68]. A daily example of this phenomenon is the rippled surface of water when wind blows on it. Figure 2.2 shows an example of two fluids streaming with different velocities. In plasma physics, the Kelvin-Helmholtz instability has first been investigated in Q-machines where a shear in the $E \times B$ rotation of the plasma column is located in the edge regions [69].

The experimentally observable features of the Kelvin-Helmholtz instability in a plasma are [60,70]:

1. the instability is driven by poloidal velocity shear (i.e. shear in \mathbf{v}_E),

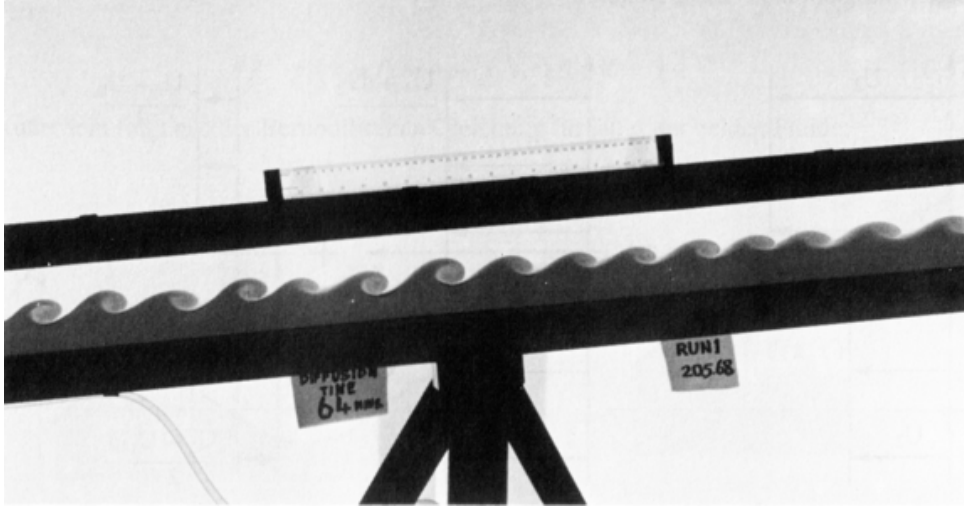


Figure 2.2: Boundary layer instability between two fluids. The vessel contains two immiscible fluids and is tilted from its originally horizontal position. The fluids tend to reestablish a horizontal interface which leads to a sheared flow. The resulting Kelvin-Helmholtz instability leads to a curling which is well visible. From reference [66].

2. maxima of \tilde{n}/n_0 and $\tilde{\phi}/T_{[eV]}$ are located in the velocity shear region,
3. the magnitude of potential fluctuations is much bigger than that of density fluctuations: $\tilde{\phi}/T_{[eV]} \gg \tilde{n}/n_0$,
4. the parallel wavelength is infinite, i.e. $k_{\parallel} \approx 0$,
5. the wave frequency is in the range of $\omega \approx (0.2 - 0.6) \max(v_E/r)$,
6. the local radial phase shift is $\angle(\tilde{n}, \tilde{\phi}) \approx 90^\circ - 180^\circ$.

Rayleigh-Taylor instability

In neutral fluids, an instability occurs when a dense fluid is stratified on top of a less dense fluid in a gravitational field. This instability is called Rayleigh-Taylor instability or gravitational instability and was discovered at the end of the 19th century [68,71]. The physical mechanism of this instability in a magnetized plasma is depicted in figure 2.3. Imagine a more dense plasma on top of a less dense plasma in a gravitation field $\mathbf{F}_g = -mg\mathbf{e}_y$ where m is the particle mass and g is the gravitational acceleration. An external magnetic field is applied in the z -direction. The gravitational drift for the ions reads

$$\mathbf{v}_{gr,i} = \frac{M\mathbf{g} \times \mathbf{B}}{eB^2} \quad (2.36)$$

and is directed in the negative x -direction (i.e. to the left). Since the electrons are much lighter than the ions, their gravitational drift can be neglected. If a small wave-like perturbation develops at the interface between a dense and a less dense plasma, the ion gravitational drift leads to a separation of charges as shown in figure 2.3. As a

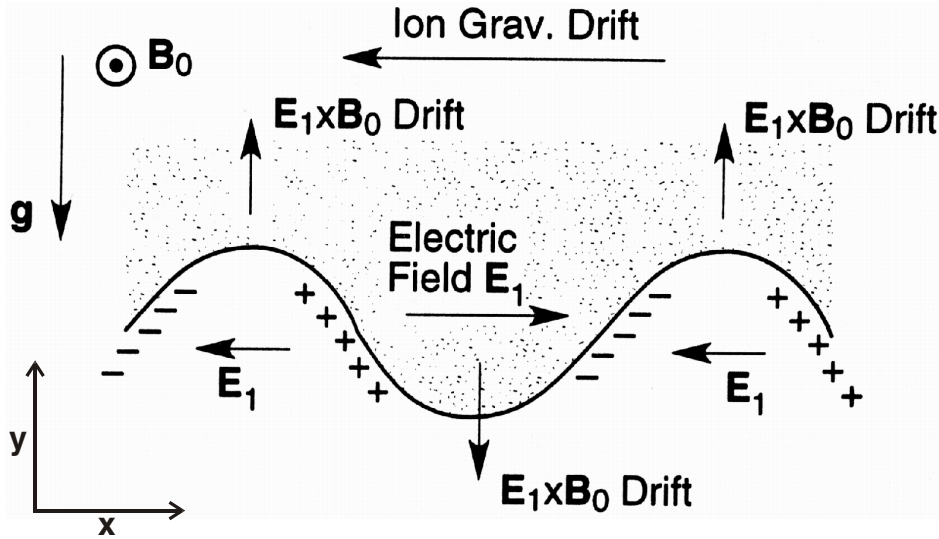


Figure 2.3: Physical mechanism of the Rayleigh-Taylor instability. Taken from reference [71].

consequence, an electric field E_1 develops which causes an $E \times B$ drift. This drift amplifies the initial perturbation since it is directed upwards in regions where the interface has already moved upwards and vice versa.

In a plasma, the effect of gravitational forces is generally negligible but other forces can take the role of the gravitational force. In plasmas with a nonuniform magnetic field, the ∇B drift and the curvature drift lead to a related instability which is called interchange instability. The Rayleigh-Taylor instability is also called flute instability or centrifugal instability if the centrifugal force of a rotating plasma replaces the gravitational force. The reason for the name flute instability is that in a cylindrical plasma the waves travel in the poloidal direction only, and the surfaces of constant density resemble Greek columns.

Typical experimentally observable features are [60]:

1. the parallel wavelength is infinite, i.e. $k_{\parallel} = 0$,
2. maxima of \tilde{n}/n_0 and $\tilde{\phi}/T_{[eV]}$ are localized at $\max(|1/n d_r n|)$,
3. the magnitude of potential fluctuations is much bigger than that of density fluctuations: $\tilde{\phi}/T_{[eV]} \gg \tilde{n}/n_0$,
4. the local radial phase shift is $\angle(\tilde{n}, \tilde{\phi}) \approx 45^\circ - 90^\circ$.

Chapter 3

Methods of data analysis

The present work deals with instabilities in magnetized plasmas which are observable by fluctuations of plasma parameters such as density and potential. Time series of the fluctuations can be recorded using oscilloscopes or transient recorders. It is important to know the spatial distribution of the fluctuations. This can be done using several probes simultaneously or by performing subsequent measurements with a single probe. For the time series analysis, statistical methods are used. This chapter provides a brief overview of the analysis techniques used [72,73].

3.1 The probability density function

The amplitude distribution of a time series is characterized by the probability density function (PDF). The probability p to find a continuous random variable X in an interval $[x, x + dx]$ is

$$p[x < X \leq x + dx] = \int_x^{x+dx} P(X) dX \quad , \quad (3.1)$$

where $P(X)$ is the probability density function. Two basic properties of the PDF are

$$P(X) \geq 0, \quad \forall X \quad \text{and} \quad \int_{-\infty}^{\infty} P(X) dX = 1 \quad . \quad (3.2)$$

For discrete experimental data X_n , the PDF becomes a discrete function P_n and in all equations the integral is replaced by a sum. The PDF is then estimated by binning the points of a time series into equipartition intervals i and counting the number of events found within an amplitude interval. When N is the total number of events and N_i is the number of events found in an interval i , the probability to find a value X_i in the interval i is

$$p(X_i) = \frac{N_i}{N} \quad . \quad (3.3)$$

The probability density function P is found by normalization to the interval width.

The central moments μ_j ($j \in \mathbb{N}$) of a PDF are defined by

$$\mu_j := \sum_n (X_n - \langle X \rangle)^j P_n = \langle (X - \langle X \rangle)^j \rangle \quad \text{with} \quad \langle X \rangle := \sum_n X_n P_n \quad (3.4)$$

and can be used to characterize its features. The first two moments are the most important ones, but, for a complete description of the PDF, higher moments must be considered as well. The first moment is the mean value

$$\mu = \langle X \rangle := \sum_n X_n P_n \quad , \quad (3.5)$$

and the second moment is the variance

$$\sigma^2 := \sum_n (X_n - \mu)^2 P_n = \langle X^2 \rangle - \langle X \rangle^2 \quad . \quad (3.6)$$

The square root of the variance is the standard deviation σ which describes the ‘spread’ of the distribution around the mean value, i.e., the mean deviation of X_n from μ .

For purely random processes the PDF is often given by a Gaussian distribution

$$P(X) = \frac{1}{\sqrt{2\pi}\sigma} \exp\left(-\frac{(X - \mu)^2}{2\sigma^2}\right) \quad (3.7)$$

which is fully determined by the mean value and the variance.

For a purely sinusoidal signal $f(t) = A \sin(\omega t)$, the PDF peaks at the amplitude values $\pm A$ and is rather flat and small between the peaks. If the signal is not fully coherent, but noisy, the amplitude A can not easily be determined from the time series. The standard deviation can always be estimated from a time series and is therefore used in this work as a quantitative measure of the amplitude distribution of the fluctuations. For pure sinusoidal signals the amplitude of the signal and the standard deviation are related as $A = \sqrt{2} \sigma$.

3.2 Spectral analysis

Fourier methods are a standard tool for the description of the average temporal behavior of time series of fluctuating quantities. The Fourier transform $F(\omega)$ of a time series and the inverse Fourier transform $f(t)$ are defined by

$$F(\omega) = \frac{1}{\sqrt{2\pi}} \int_{-\infty}^{\infty} f(t) \exp(-i\omega t) dt \quad (3.8)$$

$$f(t) = \frac{1}{\sqrt{2\pi}} \int_{-\infty}^{\infty} F(\omega) \exp(i\omega t) d\omega \quad . \quad (3.9)$$

In an analog way the Fourier transform can be defined for multi-dimensional data, e.g., spatiotemporal data. The spectral power density of a fluctuating quantity is given by

$$S(k, \omega) = \langle F^*(k, \omega) F(k, \omega) \rangle \quad (3.10)$$

where $\langle \rangle$ defines the ensemble average over statistically independent realizations und F^* denotes the complex-conjugate of F . For two fluctuating quantities $f(t)$ and $g(t)$ one can define the cross power spectral density by

$$S_{f,g}(k, \omega) = \langle F^*(k, \omega) G(k, \omega) \rangle \quad (3.11)$$

where $S_{f,g}$ is a complex function. The magnitude $|S_{f,g}(\omega)|$ is a measure for the ‘similarity’ of both signals at each frequency. The phase shift between the two signals for each frequency ω is given by the angle $\angle(f, g) = \angle(S_{f,g})$.

For numerical computation of the Fourier transform of discrete time series, the Fast Fourier Transform Algorithm (FFT) is used [72] which reduces the numerical effort dramatically.

3.3 Cross correlation function

The phase coherence of two time signals recorded at different spatial positions can be quantified by the cross correlation function

$$r_{f,g}(d, \tau) = \langle f(x, t)g(x + d, t + \tau) \rangle \quad (3.12)$$

where $r_{f,g}$ is a function of the time lag τ and the spatial separation d only. The auto-correlation function of a function f is defined as $r_{f,f}(d, \tau)$.

The quantities f and g can have very different amplitudes. For quantitative comparisons of different cross correlations an appropriate normalization is useful. Usually, the cross correlation is normalized to the geometrical mean of the respective auto-correlation functions

$$R_{f,g}(d, \tau) = \frac{r_{f,g}(d, \tau)}{\sqrt{r_{f,f}(0, 0)r_{g,g}(0, 0)}} \quad (3.13)$$

Using this normalization the correlation function is bounded to the interval $[-1 \leq R \leq 1]$.

By definition, the cross-correlation of identical time series is equivalent to an auto-correlation of one of the time series and has a maximum $R = 1$ at $\tau = 0$. If both time series are shifted against each other by t_s the maximum $R = 1$ is found at $\tau = t_s$. A negative correlation $R(\tau = 0) = -1$ is found if both signals behave contrary $f(t) = -g(t)$. The cross correlation function becomes zero for completely independent time series.

The numerical computation of the cross-correlation function according to equation (3.12) is time consuming. A much more efficient way is to use the Wiener-Kintchine theorem [72] which states that the cross-correlation function $R_{f,g}$ is the inverse Fourier transform of the cross-power spectral density $S_{f,g}$:

$$r_{f,g}(\tau) = \int_{-\infty}^{\infty} S_{f,g}(\omega) \exp(i\omega\tau) d\omega \quad . \quad (3.14)$$

This can be computed fast using the FFT algorithm.

Part I

Resistive drift waves in the VINETA device

Chapter 4

The VINETA device: setup and diagnostics

In this chapter, the VINETA device and the experimental techniques are described. In particular, the experimental arrangement used for the investigation of drift waves is discussed. Possibilities to change the plasma parameters are also briefly reviewed.

4.1 The VINETA device

The conception of the VINETA device aims at a flexible and versatile linear, magnetized plasma device that allows for various experiments on the dynamics of plasma waves and instabilities. The device is built in a modular way. It is comparatively easy to shorten or lengthen the whole device by one or even more modules. At present, four modules are installed. A schematic view of the device is given in figure 4.1 and a photograph of the device is shown in figure 4.2.

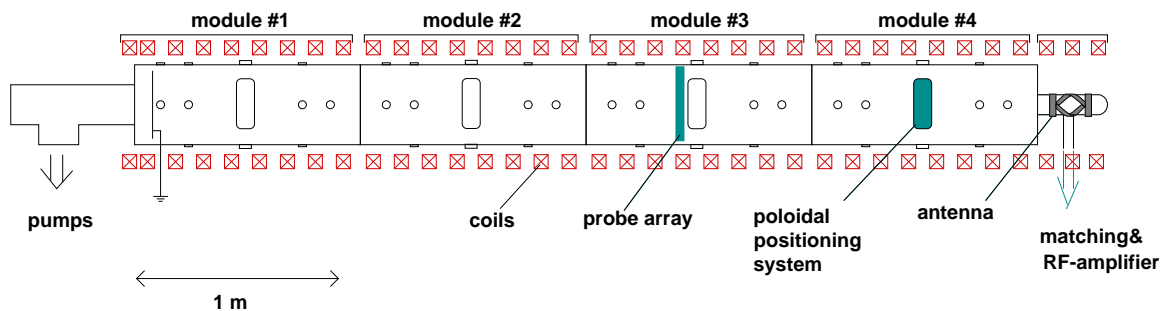


Figure 4.1: Schematic of the linear, magnetized plasma experiment VINETA in the configuration used for this work. Shown are the four modules of the vacuum chamber, the equidistantly spaced magnetic field coils (red) and the glass tube extensions with the surrounding RF antenna on the right hand side. Each module has its own separate power supply for the coils. The vacuum pumps are located on the left hand side of the sketch.

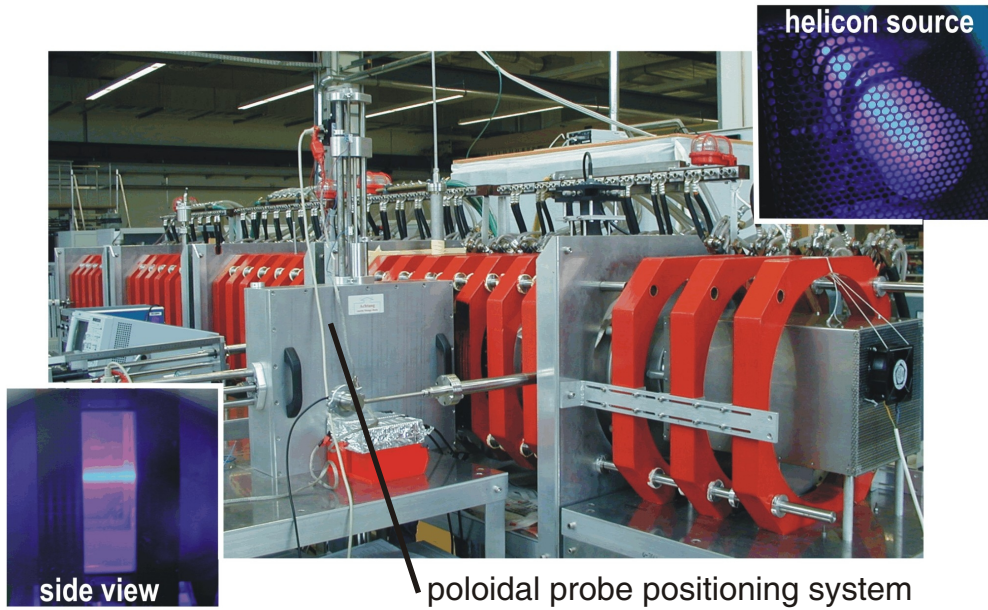


Figure 4.2: *Picture of the VINETA device. The plasma source is on the right hand side of the image, hidden from view by the metal RF shielding which surrounds it. The poloidal positioning system is installed at module #4. The insets show an argon plasma in the helicon discharge mode with its typical blue core.*

4.1.1 Vacuum system

The vacuum chamber consists of four identical cylindrical stainless steel modules, each 1128 mm in length and 400 mm in diameter. A chamber module has two CF-63, 13 CF-40 flanges and two rectangular windows of 100 mm in width and 260 mm in height. The rectangular flanges reach some centimeters into the chamber, such that the inner vessel surface is not fully cylindrical. The modules are connected via ISO-K 400 flanges and are placed on trolleys. This allows for easy handling of the chamber. A variety of different diagnostics can be installed at different positions of the device.

As shown in figure 4.1, the pumping system is installed at one end of the device. The system is pumped using a turbo pump in conjunction with a rotary pump. A base pressure of approximately $5 \cdot 10^{-5}$ Pa is reached without baking. A steel shield has been placed around the pump for protection against stray magnetic fields. Between both pumps, a valve is installed which closes automatically when the pumps are switched off. This ensures that no oil from the rotary pump is sucked into the turbo pump and into the vacuum chamber itself. Two different pressure gauges are used: a full range gauge and a baratron. Both are installed in module #1 close to the pumps. The gas inlet is also located in module #1. In principle, the VINETA can be operated with different gases. Throughout this work, only argon has been used as a filling gas.

4.1.2 Magnetic field

The magnetic field is created by a set of 36 coils (see figure 4.1). Each chamber module is immersed in a set of eight coils. One extra coil is installed at the pump side of the device to extend the region of the homogeneous magnetic field. The helicon plasma source is immersed in three additional coils. All coils are identical and have 45 windings of water-cooled copper wire. The coil size is optimized for the dimension of the vacuum chamber: the inner diameter of the coils of 520 mm is only slightly bigger than the chamber diameter (extended by the rectangular windows). The maximum electric current through the coils is 260 A. This allows for a homogeneous magnetic field of up to 100 mT.

The coils are installed on four stainless steel rods such that they can be moved in the axial

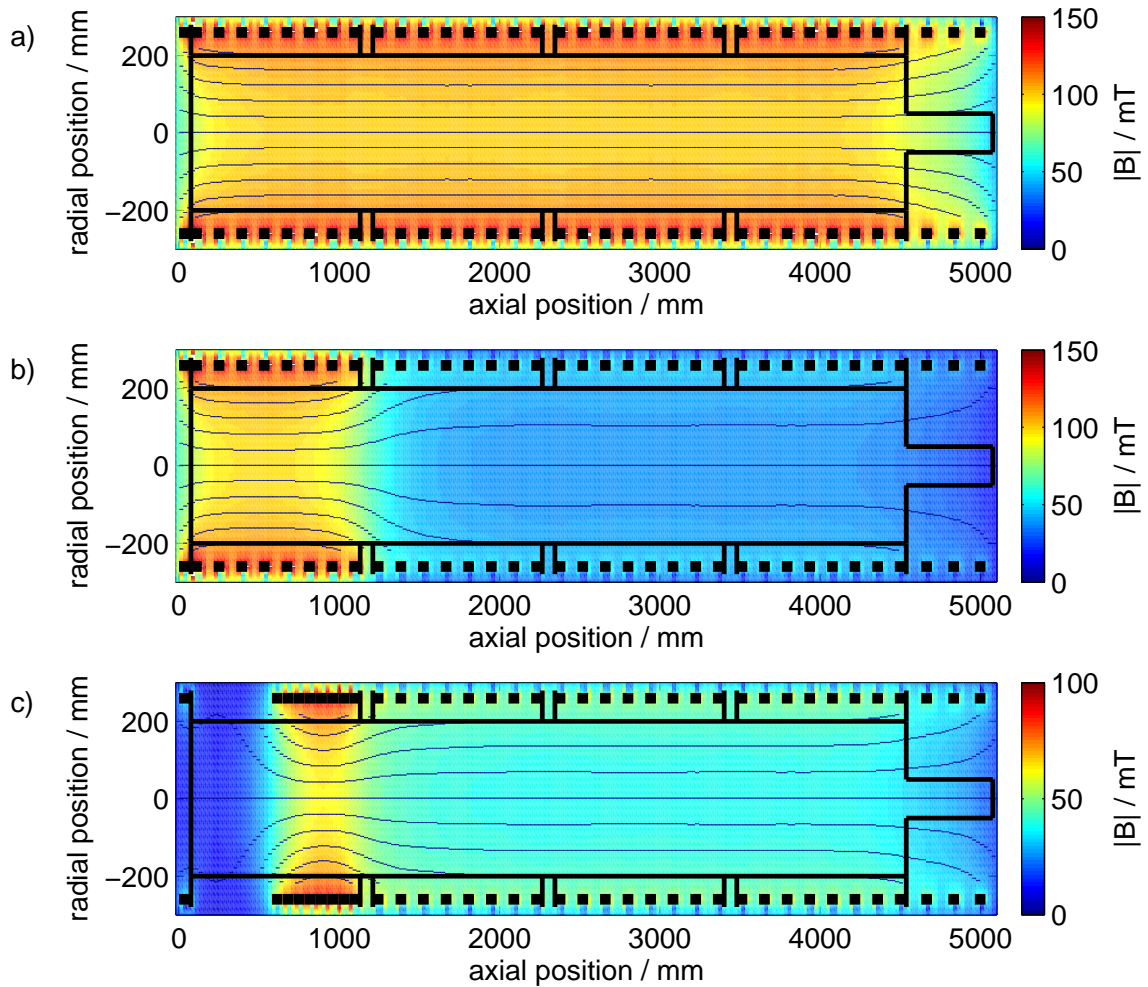


Figure 4.3: Three examples of magnetic field configurations of the VINETA device: The magnetic field $|\mathbf{B}|$ is shown color coded for a) homogenous magnetic field ($I=260$ A for all coils), b) magnetic field gradient created by different currents through the coils of the different modules ($I = 260$ A for coils of module #1, $I = 100$ A for all other coils), c) magnetic field gradient created by repositioning the coils of module #1 ($I = 100$ A for all coils). Black lines indicate the position of the vacuum vessel including the glass tube extension. Black squares indicate the positions of the coils. Magnetic field lines are shown as solid blue lines.

direction. Thus, the axial coil positions can be arbitrarily chosen within each module. The coils of each module are powered by a separate 50 kW DC power supply. An additional power supply is used for the three coils in the helicon source region. The magnetic field of the VINETA device can be easily changed by changing the spacing between the coils and/or by altering the coil currents per module. This allows the creation of very different configurations of the magnetic field. Figure 4.3 shows calculated magnetic fields for three exemplary configurations. Figure 4.3a) shows the magnetic field for equidistant coil positions at modules #1 to #4 with the maximum possible current of 260 A applied to all coils. In this configuration, the axial component of the magnetic field is nearly constant throughout the device, with an axial magnetic field ripple of less than 3%. Due to the slightly larger distances between the coils in the plasma source region, the magnitude of the magnetic field in this region drops to approximately 70 % of the value in modules #1 to #4. Figures 4.3c,d) show two configurations which lead to a localized magnetic field gradient in the plasma: In figure 4.3c) the coils are positioned as in figure 4.3a) but a current of 260 A is applied to module #1 while all other modules are maintained at 100 A. In figure 4.3d) the current through all coils is 100 A, but all coils of module #1 have been repositioned to be as close as possible to module #2. In this work, only the homogeneous configuration (i.e. the same current applied to all coils) has been used in order to exclude effects of the magnetic field geometry.

4.1.3 The plasma source

According to the conception of a highly flexible experimental device, the modular setup of the VINETA provides the possibility of operation with different plasma sources such as radio-frequency (RF) and direct current (DC) sources. In this section, only the helicon source (which is a specialized RF source) is presented in more detail since only this source was used for the present work. The helicon source is located opposite to the pump, see figures 4.1 and 4.2.

Helicon source basics

Helicon waves are bounded plasma whistler waves in the frequency range well below the electron cyclotron frequency ω_{ce} , but well above the ion cyclotron frequency Ω_{ci} [74]. Whistler waves are right-hand circular polarized electromagnetic waves in free space [1]. Their dispersion relation is given by

$$\frac{c^2 k^2}{\omega^2} = 1 - \frac{\omega_{pe}^2}{\omega(\omega - \omega_{ce} \cos \theta)} \quad (4.1)$$

where ω is the angular frequency and k the wave number, $\omega_{p,e}$ is the plasma frequency, $\omega_{c,e}$ is the electron cyclotron frequency in the uniform background magnetic field \mathbf{B} , and θ is the angle of \mathbf{k} relative to \mathbf{B} [75]. If whistler waves are confined to a cylinder, the boundary conditions impose an eigenmode structure on the whistler wave. Their propagation and polarization properties are also changed. In particular, left hand propagation becomes possible. The eigenmodes are characterized by a poloidal mode number m , whereas positive (negative) mode numbers correspond to global right (left) hand rotation of the

wave pattern with respect to \mathbf{B} [76]. In a bounded cylinder the dispersion relation can be written as

$$\frac{n_0}{B} = \alpha \frac{k_{\parallel}}{\omega} \quad , \quad (4.2)$$

where α is a constant given by the boundary conditions [77]. In practice, the frequency ω of the excited helicon mode is constant and determined by the RF source. Assuming that the parallel wavelength $\lambda_{\parallel} = 2\pi/k_{\parallel}$ is determined by the antenna geometry, the plasma density is proportional to the applied background magnetic field \mathbf{B} . This is also seen in the experiment [78]. Thus, from the dispersion relation equation (4.2) it is concluded that the plasma density can be controlled by the externally applied magnetic field.

Helicon waves have been investigated since the 1960s in solid state plasmas [79,80] as well as in gaseous plasmas [81]. In the mid-1980s, BOSWELL found that helicon waves can be used to produce plasmas with a very high efficiency [34] and plasma densities up to 10^{20} m^{-3} can be reached with only a few kW of RF power. Nowadays, helicon sources are widely used in research as well as in industrial plasma engineering [82,83]. Overviews of helicon sources can be found in references [41,74,84].

Typically, a helicon source consists of an RF antenna which surrounds a cylindrical glass tube, immersed into a magnetic field \mathbf{B} . Generally, \mathbf{B} is in the range 10–100 mT but also at low magnetic fields $< 10 \text{ mT}$ plasma generation can be achieved [85]. Different antenna designs have been studied which lead to primary excitation of different helicon wave eigenmodes [76,86]. In general, the right hand polarized waves (especially the $m = +1$ mode) are found to be preferentially excited [76]. Helical antennas usually show a distinct directivity, such that one-sided plasmas are produced [87]. Despite all the efforts of the permanently growing scientific community dealing with helicon sources, the mechanism of the power absorption is still not well understood and it is a topic of intense research. The Coulomb collision frequencies were found to be too small to explain the strong coupling of the helicon waves to the plasma [34]. Three often discussed explanations for the power transfer from the helicon wave to the plasma are the following:

1. A second wave – the so-called Trivelpiece-Gould (TG) mode – is excited at the plasma boundary by the helicon wave. This secondary wave is efficiently absorbed by the plasma [35,36].
2. The wave energy is transferred to electrons travelling with a velocity slightly lower than the phase velocity of the helicon wave. These electrons are accelerated by the wave due to LANDAU damping, which is a collisionless kinetic effect. In earlier experiments, evidence for high energy electrons was indeed found [37], but more recent experiments with more appropriate diagnostics techniques could not confirm this [38].
3. Although already BOSWELL's original paper [34] suggests that a resonance at the lower hybrid frequency might be responsible for the efficiency of the plasma production, this idea was neglected for a long time and has regained attention only recently [39,40].

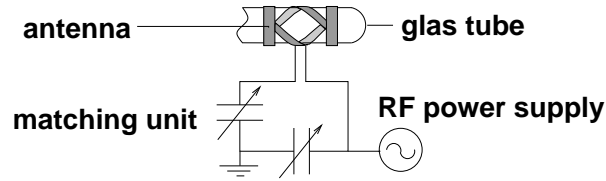


Figure 4.4: Schematic of the helicon source: The glass tube is surrounded by a helical antenna. RF is fed to the antenna via a matching unit.

The helicon source of the VINETA device

The technical equipment of the helicon source consists of a radio frequency transmitter, an amplifier, a matching network and the helicon antenna itself.

The transmitter was manufactured by ELMER/MAGNAVOX and was originally designed for military use. The frequency that can be selected ranges from 2 MHz to 30 MHz and a preamplifier generates an output power of up to 400 W. An arbitrary wave form generator is used to create the RF signal and only the preamplifier of the transmitter is used. The RF signal is amplified by a HENRY 8K ULTRA amplifier. The frequency range of this device is 1.8-30 MHz and the maximum output power is 2.5 kW in steady state operation or 6 kW in pulsed operation.

Opposite to the pumping system, the vacuum vessel is extended by a glass tube with a diameter of 10 cm and a length of 40 cm. A helically twisted RF antenna of the so-called ‘Nagoya type’ [76] surrounds the glass tube (see figure 4.4). The antenna has a length of 31 cm, RF is fed to the antenna legs. A matching network consisting of two capacitors is placed between the RF source and the antenna itself, to account for the mismatch between the amplifier’s output impedance of $50\ \Omega$ and the low antenna impedance (see figure 4.4). For RF powers $\gtrsim 1\ \text{kW}$, the antenna is overheated and the glass tube tends to melt. Thus, the antenna is water-cooled and the source is usually operated in pulsed mode. Pulse lengths of up to several seconds are possible without damage, if the duty cycle is chosen accordingly. In this work, pulse lengths of typically 300 – 600 ms are used.

With such an antenna setup, three different discharge modes can be established in the VINETA device. For increasing RF power, the plasma heating changes from capacitively to inductively to helicon wave sustained operation. At the same time, the density increases by several orders of magnitude. The transition between these modes in the VINETA device is described in reference [88]. For this work, the source was always operated in the helicon mode.

4.1.4 Operation and Plasma Parameters

Typical operation and plasma parameters for an argon plasma produced with the helicon source are given in table 4.1. A generic feature of helicon sources is that they produce a rather dense plasma with electron temperatures of only a few eV. In the present configuration of the VINETA device, the helicon discharge mode cannot be maintained below a neutral gas pressure of about 0.1 Pa. In principle, helicon discharges at neutral gas pressures $\gtrsim 1\ \text{Pa}$ can be maintained but have not been used here. The ion temperature

parameter	typical	range
base pressure	$1 \cdot 10^{-4}$ Pa	$5 \cdot 10^{-5} - 2 \cdot 10^{-4}$ Pa
neutral gas pressure (argon)	0.3 Pa	0.1 – 1 Pa
magnetic field	75 mT	10 – 100 mT
RF power	2.5 kW	1-5 kW
peak electron density	$5 \cdot 10^{18} \text{ m}^{-3}$	$10^{18} - 10^{20} \text{ m}^{-3}$
electron temperature	2 eV	1 – 5 eV
ion temperature	0.25 eV	0.2 – 0.5 eV

Table 4.1: *Typical operation and plasma parameters for the VINETA device operated in the helicon discharge mode.*

in argon plasmas has been measured by Laser Induced Fluorescence (LIF) as described in reference [78]. Values in the range 0.05 – 0.5 eV have been found [89].

Table 4.2 gives an overview of plasma parameters for typical experimental conditions. Besides typical frequencies, lengths and velocities, the plasma β is also given. This is the ratio between the particle pressure and the magnetic field pressure [1]. β_μ is the ratio between the plasma β and the mass ratio m_e/M . More details on the plasma parameters are given in chapter 5 where experimental results on time-averaged parameter profiles are presented.

parameter	formula	typical value	range
electr. plasma frequency [rad/s]	$\omega_{p,e} = \sqrt{\frac{ne^2}{\epsilon_0 m_e}}$	$1.3 \cdot 10^{11}$	$(5 - 50) \cdot 10^{10}$
ion plasma frequency [rad/s]	$\omega_{p,i} = \sqrt{\frac{Z^2 ne^2}{\epsilon_0 M}}$	$4.5 \cdot 10^8$	$(2 - 20) \cdot 10^8$
electron gyrofrequency [rad/s]	$\omega_{c,e} = \frac{eB}{m_e}$	$1.2 \cdot 10^{10}$	$(0.9 - 1.8) \cdot 10^{10}$
ion gyrofrequency [rad/s]	$\Omega_{ci} = \frac{eB}{M}$	$1.7 \cdot 10^5$	$(1.2 - 2.4) \cdot 10^5$
electron gyro radius [mm]	$r_{c,e} = \frac{v_{th,e}}{\omega_{c,e}}$	0.05	0.02 - 0.1
ion gyro radius [mm]	$r_{c,i} = \frac{v_{th,i}}{\omega_{c,i}}$	4.5	3 - 9
effective gyro radius [mm]	$\rho_s = \sqrt{\frac{k_B T_e M}{e^2 B^2}}$	13	6 - 29
Debye length [mm]	$\lambda_D = \sqrt{\frac{\epsilon_0 k_B T_e}{ne^2}}$	0.005	0.0007 - 0.017
thermal electron velocity [m/s]	$v_{th,e} = \sqrt{\frac{k_B T_e}{m_e}}$	590 000	420 000 - 940 000
thermal ion velocity [m/s]	$v_{th,i} = \sqrt{\frac{k_B T_i}{M}}$	770	700 - 1000
ion sound velocity [m/s]	$c_s = \sqrt{\frac{k_B T_e}{M}}$	2600	2000 - 3600
diamagn. el. drift velocity [m/s]	$v_{D,e} = -\frac{k_B T_e}{eB} \frac{\partial_r n}{n}$	1500	< 3000
plasma β	$\beta = \frac{2\mu_0 n k_B T_e}{B^2}$	$8 \cdot 10^{-4}$	$4 \cdot 10^{-5} - 8 \cdot 10^{-2}$
β_μ	$\beta_\mu = \frac{\beta}{m_e/M}$	60	3 - 6000

Table 4.2: Plasma parameters for an argon helicon discharge in the VINETA device. Typical parameters are calculated for $T_e = 2$ eV, $T_i = 0.25$ eV, $n = 5 \cdot 10^{18} \text{ m}^{-3}$, $B = 70$ mT. Parameter ranges are calculated for $T_e = 1 - 5$ eV, $T_i = 0.2 - 0.5$ eV, $n = 10^{18} - 10^{20} \text{ m}^{-3}$, $B = 50 - 100$ mT.

4.2 Diagnostics

Adequate diagnostics tools are essential for the characterization of the time-averaged plasma as well as of any waves and instabilities occurring in the VINETA plasma. Measurements of propagation and dispersion properties call for diagnostics with appropriate spatial as well as temporal resolution. Electrostatic (or LANGMUIR) probes are an established technique to accomplish this [90,91] and are the chief diagnostic tool of the present work. The technique itself, as well as special setups, are described in detail in sections 4.2.1 and 4.2.2. Electrostatic probes are intrusive diagnostics and therefore always impose a certain disturbance to the plasma. Non-intrusive techniques would be preferable but their spatial resolution is often not good enough.

Other diagnostics techniques have been established as well at the VINETA device and shall be briefly mentioned here. Laser Induced Fluorescence (LIF) is used for the measurement of ion distribution functions [78] and allows the determination of the ion temperature if the distribution is a Maxwellian. For line integrated density measurements, it is planned to use a microwave interferometer in near future [78]. Magnetic fluctuations at frequencies ≥ 100 kHz have been measured with so-called \dot{B} -probes [92]. For lower frequencies, Hall detectors shall be used for which operation up to 100 kHz was recently reported [93].

4.2.1 Langmuir Probes

A Langmuir probe is basically a conducting electrode inserted into the plasma. In the mid 1920s, MOTT-SMITH and LANGMUIR described electrostatic probes for the first time [94]. They are easy to build and to operate. To obtain plasma parameters like density, electron temperature or plasma potential, the probe is biased with respect to ground (i.e. the vacuum vessel) and the current-voltage characteristic is measured in an external electrical circuit. For successful operation of Langmuir probes two requirements must be fulfilled: On the one hand, the probe must be able to withstand the heat load caused by the plasma. (For low-temperature plasmas this is usually not a problem.) On the other hand, the probe must be small enough in relation to typical plasma scale lengths such that it does not perturb the plasma too much.

The biggest advantage of Langmuir probes is that they allow for a high spatial and temporal resolution, much better than that of many other diagnostics methods used in plasma physics. The spatial resolution of the probe is limited by the thickness of sheath and presheath which form around the probe and which can extend to several Debye lengths (see table 4.2). The accuracy of absolute values measured with Langmuir probes is usually not very good and calibration with other measurement methods is required for better results. However, relative measurements are often sufficient.

Figure 4.5a) shows a schematic of a simple cylindrical Langmuir probe. The probe tips are made of tungsten and are typically 0.1–0.3 mm in diameter and 2–5 mm in length. They are connected via a copper wire to the external measurement circuit. In order to insulate the copper supply wire from the plasma, the wire is immersed into a ceramic tube and connected to the probe tip. The ceramic tubes are kept as small as possible. In figure 4.5c), a typical circuit for the measurement of a probe characteristic is shown. The probe is biased by a DC power supply which is controlled by a PC. The current is

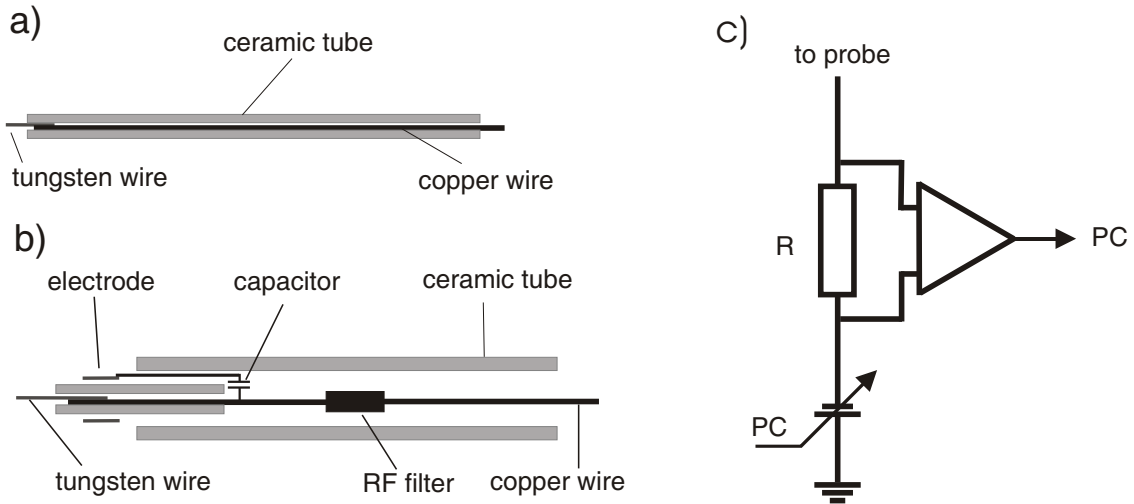


Figure 4.5: Schematic picture of a) cylindrical Langmuir probe, b) RF compensated Langmuir probe. c) Circuit for measurement of probe characteristic.

measured as the voltage drop over a shunt resistor and the amplified signal is fed back into the PC.

It has been known for decades that a plasma oscillating in the RF range distorts the probe characteristic and additionally complicates its interpretation [90]. The time-varying plasma potential leads to an averaging over the probe characteristic. Since the characteristic is strongly nonlinear, this averaging changes the characteristic and leads, for instance, to a systematic overestimation of the electron temperature. The influence of RF oscillations can be compensated by special probe designs. Here, a technique proposed by SUDIT and CHEN is used [95,96] which is schematically shown in figure 4.5b). Close to the probe tip, a floating electrode is exposed to the plasma in order to sample the local plasma potential fluctuations. The electrode is coupled to the probe tip through a capacitor such that the probe tip follows the local potential fluctuations. Additionally, RF chokes are connected close to the probe tip which present a large impedance to RF signals but not to low-frequency signals. Indeed, in the VINETA device, operated in the helicon discharge mode, such compensated probes were found to give different results from uncompensated ones. Thus, for measurements of the background (time-averaged) plasma profiles, compensated probes have been used. On the other hand, it is quite challenging to choose proper filters and coupling capacitors such that low-frequency signals can be detected correctly using the same setup [95]. Therefore, uncompensated probes have been used for fluctuation measurements.

Unfortunately, the analysis of the probe characteristics is often much more complicated than the probe operation. For different experimental conditions, different probe theories are needed [97]. The operation and the interpretation of probe characteristics is still a field of intense research [98–100]. In the VINETA device, besides the necessary RF compensation one deals with further difficulties:

1. The magnetic field introduces anisotropy in the plasma which complicates the theoretical description of probes [97].

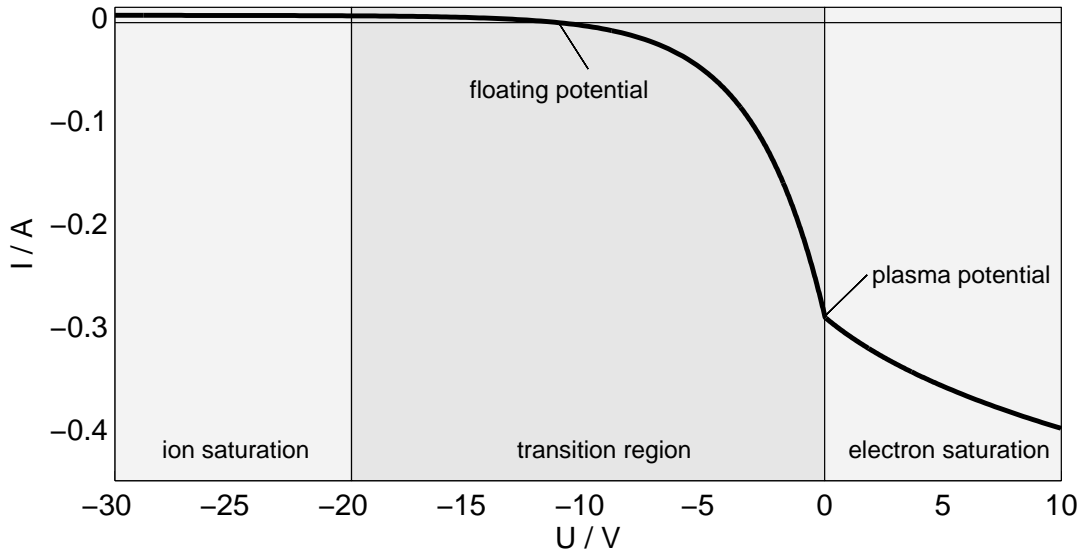


Figure 4.6: *Idealized Langmuir probe characteristics.*

2. Helicon sources produce plasmas with a comparably high plasma density, but with electron temperatures of only a few eV. For these conditions, the collisionality of the plasma is not negligible. Thus, methods to interpret LANGMUIR probe characteristics in collisionless plasmas are no longer valid [101].

Subsequently, a basic, simplified theory for collisionless, unmagnetized plasmas, and an advanced kinetic theory developed for weakly ionized, magnetized plasmas, are briefly discussed and the resulting plasma parameters are compared.

Langmuir theory for an unmagnetized, collisionless plasma

The theory is simplified and strictly holds only for unmagnetized, collisionless plasmas. An idealized I-U characteristic of a cylindrical Langmuir probe is shown in figure 4.6. Three different regions are distinguished [90,91]:

Ion saturation current regime: If the probe is negatively biased with respect to the plasma potential ($U < (5 \dots 10) k_B T_e / e$), even the fastest electrons are repelled by the probe and the probe collects only positively charged ions. The ion saturation current is determined by the Bohm-criterion [98] and is given by

$$I_{i,sat} = 0.61 n e A \sqrt{\frac{k_B T_e}{M}} \quad (4.3)$$

where A is the effective probe surface and the factor 0.61 is a geometry factor [90,91]. Apparently, the ion saturation current of a given probe depends only on the plasma density n and the electron temperature T_e .

Electron saturation current regime: At a probe bias above the plasma potential, the ions are repelled and only electrons reach the probe. The electron saturation

current at the plasma potential is given by

$$I_{e,sat} = -neA\sqrt{\frac{k_B T_e}{2\pi m_e}}. \quad (4.4)$$

This depends (for a given probe geometry) only on the density n and the electron temperature T_e . In contrast to the ion saturation regime, the electron saturation current depends on the shape of the probe. A real saturation is observed only for an ideal planar probe, whereas, for real planar probes, as well as for cylindrical and spherical probes, the electron saturation current increases monotonically with the bias voltage due to expansion of the sheath [91].

Transition region: In between the two saturation regimes, increasingly more electrons can reach the probe for increasing probe bias. For a Maxwellian electron velocity distribution, the electron current in this regime depends exponentially on the applied probe voltage U

$$I_e = I_{e,sat} \exp\left(-\frac{e(U - \phi_p)}{k_B T_e}\right). \quad (4.5)$$

The voltage at which the net current is zero is called the floating potential ϕ_f . The electron temperature can be obtained using equation (4.5). To get the pure electron current, the

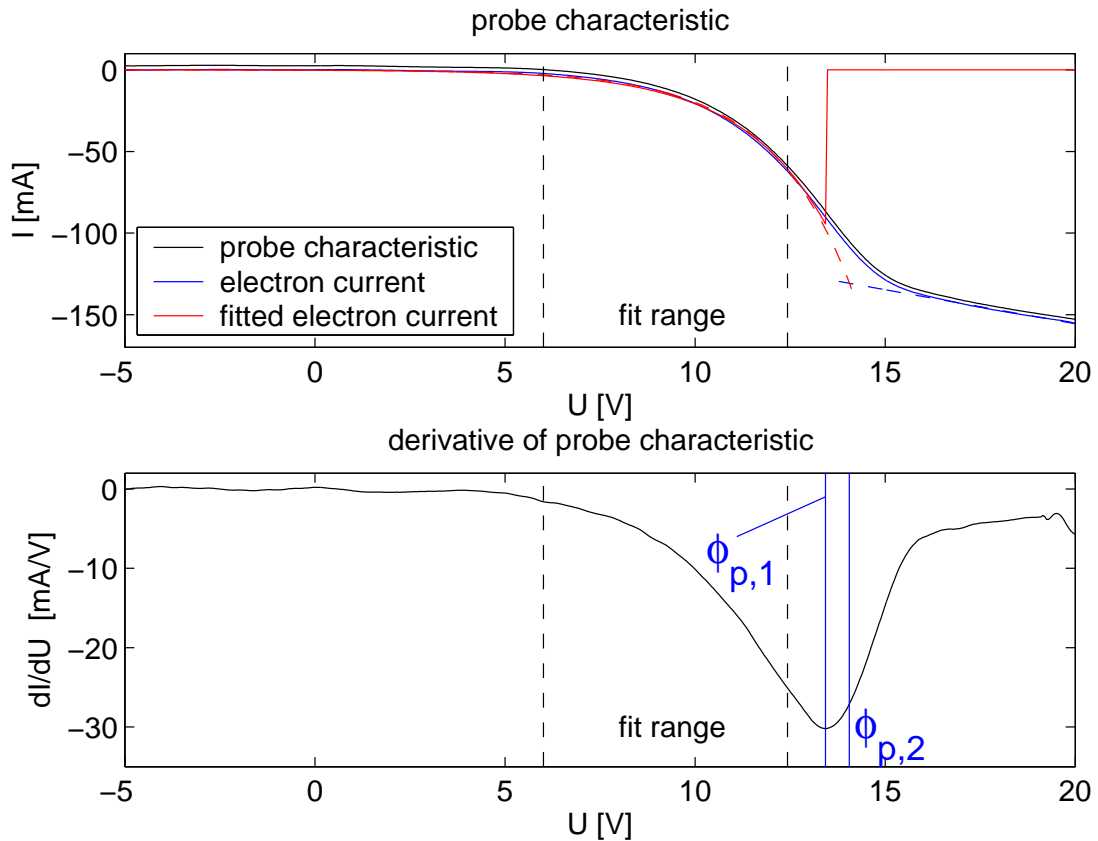


Figure 4.7: Exponential Langmuir fit for a measured I - U characteristic. Evaluation gives $\phi_{p,1} = 13.4$ V, $\phi_{p,2} = 14.1$ V, $\phi_f = 6.0$ V, $n = 8.1 \cdot 10^{17} \text{ m}^{-3}$, $T_e = 2.3$ eV.

measured total current is corrected by the extrapolated ion current $I_e = I - I_{i,sat}$. In case of a Maxwellian distribution, the electron current upon probe voltage is a straight line in the transition region when plotted semi-logarithmically. The temperature can be obtained directly from the slope of this curve.

The plasma density can be extracted from the saturation current if the electron temperature and the probe size are known. The plasma potential ϕ_p is usually obtained from the knee of the probe characteristic. In practice there are two methods: The first one takes the point where I_e starts to deviate from exponential growth. That is the case when dI_e/dU is minimal or d^2I_e/dU^2 is zero. The second method takes the intersection of an exponential fitting the transition region and a straight line fitting the electron saturation current [102]. Floating potential and plasma potential are related by $\phi_p = \phi_f + \alpha T_e$ where α is a constant that depends, among other things, on the gas used and the geometry of the probe (for argon $\alpha \approx 5.4$).

In figure 4.7, an experimentally obtained probe characteristic is shown together with its first derivative and the fitted curve in the exponential region. In this case, the difference between the plasma potential values obtained with the two methods is $\Delta\phi_p = 0.7\text{V}$. Generally, a systematic error $< 1\text{V}$ can be assumed. Subsequently, the plasma potential is taken as the minimum of the first derivative of the probe characteristic when the I-U characteristic is analyzed according to the LANGMUIR theory.

Kinetic theory for a strongly magnetized, weakly ionized plasma

In magnetized plasmas, the anisotropy between the directions parallel and perpendicular to the the magnetic field further complicates the theoretical description of probes. If the probe collects electrons, the flux tube is ‘emptied’ and has to be refilled by cross-field transport. Thus, the electron current is usually smaller than that in an unmagnetized plasma. The energy distribution function of the electrons is anisotropic which makes the modelling of the sheath surrounding the probe very complicated.

A comparatively simple analysis scheme for strongly magnetized plasmas was recently given by DEMIDOV and coworkers [97,103]. It is based on a kinetic theory by ARSLANBEKOV [104]. In this theory the Boltzmann equation [1] is solved for probes in the nonlocal regime $\lambda_\epsilon \gg d + h \gg \lambda_e$ where λ_ϵ is the energy relaxation length, λ_e is the mean free path of the electrons, d is the characteristic probe dimension and h is the sheath thickness. In that theory, the electron distribution function is directly connected to the first derivative of the electron current density. For a cylindrical probe oriented perpendicular to the magnetic field the relation

$$\frac{dj_e}{dV} = -\frac{8\pi e^3 r_{c,e} V}{3m_e^2 R \ln \frac{\pi L}{4R}} f(W) \quad (4.6)$$

is derived where j_e is the electron current density, V is the voltage with respect to the plasma potential, $r_{c,e}(V)$ is the electron Larmor radius and W is the electron energy (in eV). R and L denote the probe radius and length, respectively. Assuming a Maxwellian distribution [103]

$$f(W) = n \left(\frac{m_e}{2\pi T_{[eV]}} \right)^{3/2} \exp\left(\frac{-W}{T_{[eV]}} \right) \quad (4.7)$$

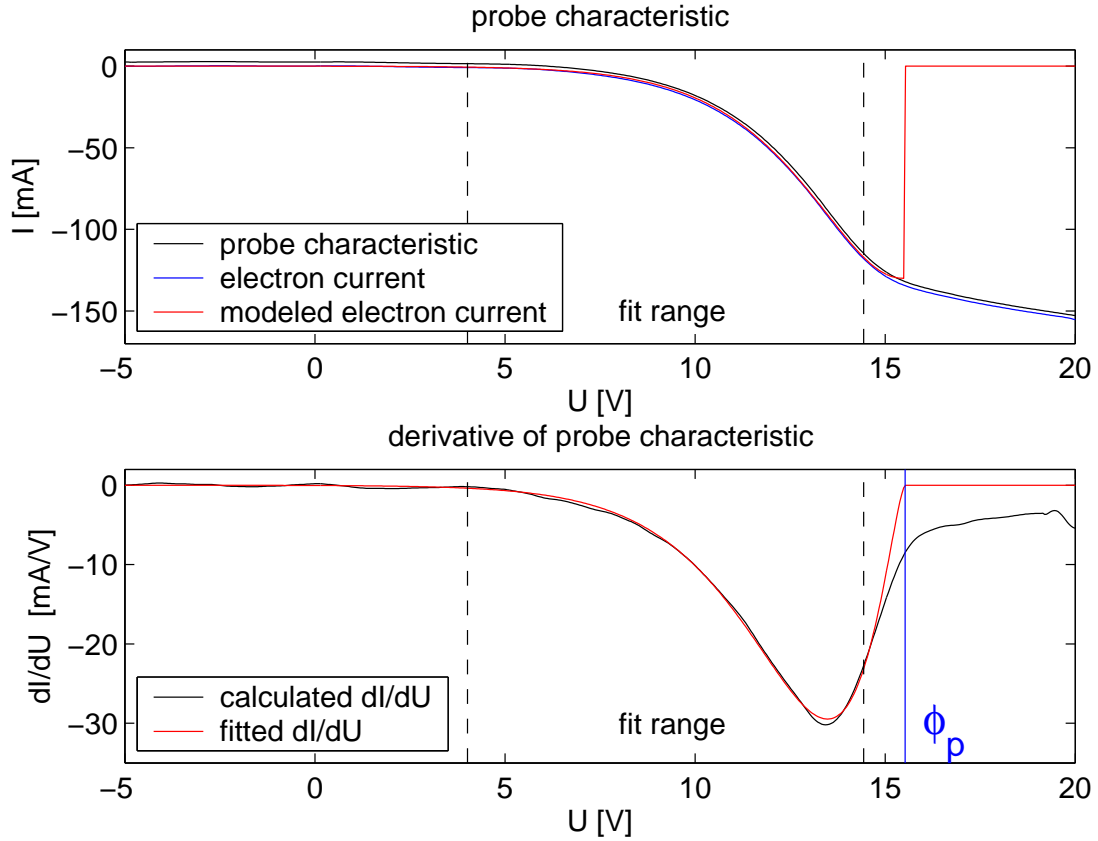


Figure 4.8: Kinetic fit for the same probe characteristic as in figure 4.7. Evaluation gives $\phi_p = 15.5$ V, $\phi_f = 6.0$ V, $n = 4.7 \cdot 10^{18} \text{ m}^{-3}$, $T_e = 1.4$ eV.

equation (4.6) can be fitted to the derivative of the measured j_e by varying the parameters $T_{[eV]}$, n and ϕ_p . The plasma potential ϕ_p is a fitting parameter because $V = U - \phi_p$ is the probe voltage with respect to the plasma potential. In this kinetic theory it is found that the plasma potential is not located at the minimum of the first derivative of the electron current, but where the fitted theoretical curve crosses zero [97]. This implies that application of this theory to a given probe characteristic always yields a higher plasma potential than analyzing the same probe characteristic using the LANGMUIR theory [97]. In figure 4.8 the same probe characteristic as in figure 4.7 is shown, this time analyzed according to this kinetic theory. Here, for the plasma potential $\phi_p = 15.5$ V is obtained and thus the difference between the plasma potential values obtained by applying the three methods of its determination is $\Delta\phi_p = 2.1$ V (and thereby $\Delta\phi_p/\phi_p \approx 15\%$). Generally, the minimum of the first derivative yields the lowest value for ϕ_p and the kinetic theory yields the highest value. Also, from the kinetic theory it is found that the electron current grows more slowly with V than exponential, in particular close to the plasma potential. Thus, although $\ln I_e(V)$ behaves like a straight line for high negative potentials, the slope of the curve is smaller than in the Langmuir case. For this reason, an overestimation of the electron temperature of up to 30% is possible when the Langmuir theory is applied instead [97].

Regime	Condition
Collisionless	$\lambda_e \gg d + h$
Nonlocal	$\lambda_e \gg d + h \gg \lambda_e$
Hydrodynamic (local)	$d + h \gg \lambda_e$

Table 4.3: *The main regimes for electrons in a weakly ionized unmagnetized plasma according to reference [97]. λ_e is the energy relaxation length, λ_e is the mean free path of the electrons, d is the characteristic probe dimension and h is the sheath thickness. For a magnetized plasma, parallel and perpendicular parameters should be compared, respectively.*

Applicability of the probe theories

Table 4.3 shows the three main operation parameter regimes in a weakly ionized plasma according to reference [97]. LANGMUIR's simple probe theory is strictly valid only in collisionless, unmagnetized plasmas. The kinetic theory of DEMIDOV was developed for magnetized plasmas in the nonlocal regime which requires that electron neutral collisions dominate over electron-electron collisions. This condition is not fulfilled in the plasma center of the VINETA device. Strictly speaking, a theory for the hydrodynamic regime must be applied instead. However, to the best of our knowledge, no applicable theory for this regime in a magnetized plasma exists. For the plasma edge, the conditions for application of the kinetic theory are fulfilled. Appealing advantages of the kinetic theory are that the magnetic field is appropriately accounted for, and it is relatively simple to apply.

Figure 4.9 shows the result of a radial scan of probe characteristics, analyzed with both methods discussed above. It is found that, in this example, the maximum density is very similar for both evaluation methods (figure 4.9a). The profile obtained using DEMIDOV's kinetic theory is slightly smoother as well as broader compared with the LANGMUIR theory. The electron temperature obtained with the kinetic theory is systematically smaller than that using the LANGMUIR theory (figure 4.9b). That is an inherent feature of DEMIDOV's theory, as discussed above. However, the shape of both curves is similar. The kinetic theory yields higher plasma potentials than the LANGMUIR theory, if both theories are applied to the same probe characteristic. This is indeed confirmed in figure 4.9c). Again, the shape of the radial profiles is similar, although the kinetic theory gives higher gradients. For the investigation of drift waves, knowledge about the radial electric field is of importance in order to determine the poloidal $E \times B$ velocity. Radial electric field profiles obtained from the spline fitted plasma potential profiles of figure 4.9c) are shown in figure 4.10. It is found that the maximum electric field is about 30% higher if the probe characteristic is evaluated according to DEMIDOV's kinetic theory. In addition, the position of the maximum electric field is found at higher radial positions if the kinetic theory is used. Figure 4.9d) shows the floating potential which is by definition independent of the probe theory applied.

In conclusion, it is found that the differences between the two evaluation methods are acceptable. The shapes of the curves are similar for all parameters shown in figure 4.9. In the VINETA device, the conditions for the kinetic theory are better satisfied than for

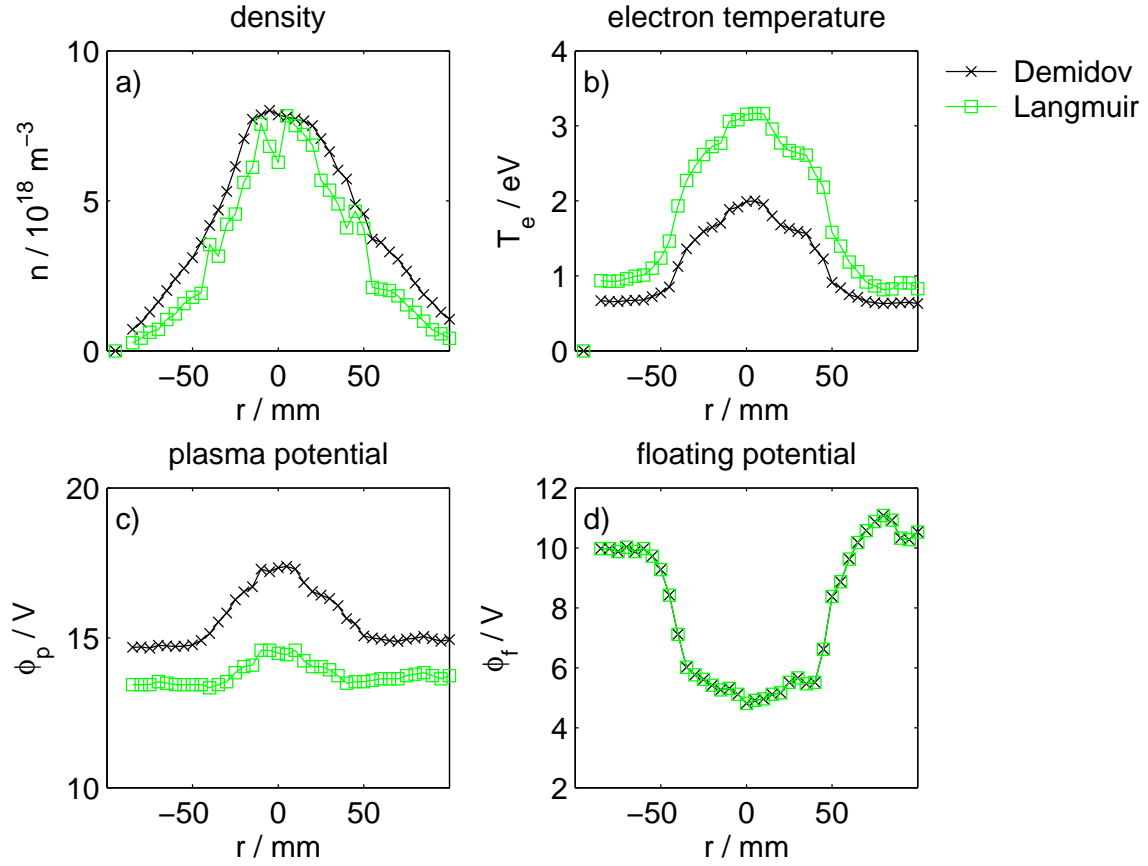


Figure 4.9: Comparison of the evaluation of a radial scan of probe characteristics analyzed with Langmuir theory and Demidov kinetic theory.

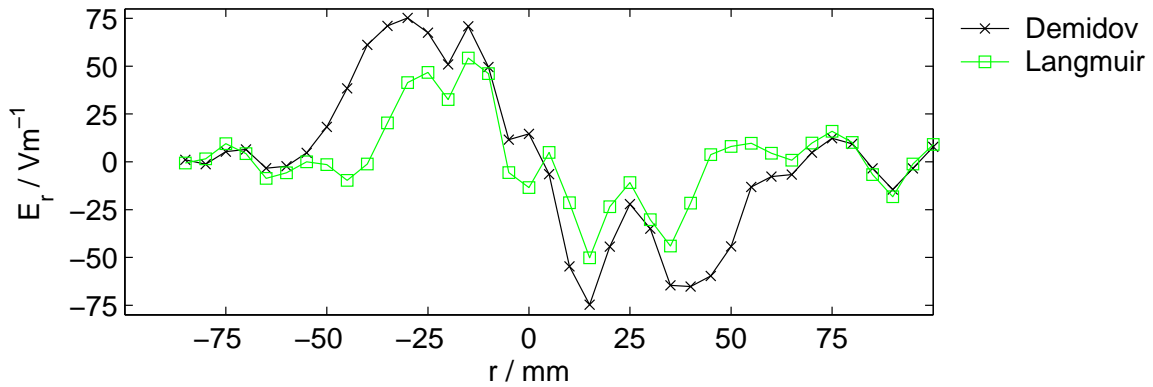


Figure 4.10: Comparison of resulting radial electric field profiles for plasma potential profiles of figure 4.9c).

the simple LANGMUIR theory because the measurements are conducted in a magnetized collisional plasma and it is desirable to take at least the magnetic field into account. Therefore, the kinetic theory is used to obtain plasma parameters for measurements in the helicon mode of the VINETA device.

Fluctuation measurements

For fluctuation measurements, recordings of the entire probe characteristic are usually avoided, since the time needed for the acquisition of the complete characteristic has to be shorter than the time scale of the fluctuations. This is technically quite challenging and investigated elsewhere [105]. Two operation modes are very common in cases where temperature fluctuations are negligible:

1. As described above, the ion saturation current is proportional to $n\sqrt{T_e}$. With the assumption of small temperature fluctuations ($\tilde{T}_e/\bar{T}_e \ll \tilde{n}/n_0 \ll 1$), the fluctuations of plasma density can be approximated by the fluctuations of the ion saturation current:

$$\begin{aligned}
 I_{i,sat} &= \underbrace{0.61eA\sqrt{\frac{k_B}{M}}}_{\gamma} (n_0 + \tilde{n}) \sqrt{\bar{T}_e + \tilde{T}_e} \approx \gamma n_0 \sqrt{\bar{T}_e} + \gamma n_0 \sqrt{\bar{T}_e} \left(\frac{\tilde{n}}{n_0} + \frac{1}{2} \frac{\tilde{T}_e}{\bar{T}_e} \right) \\
 &\approx \underbrace{\gamma n_0 \sqrt{\bar{T}_e}}_{\bar{I}_{i,sat}} + \underbrace{\gamma \sqrt{\bar{T}_e} \tilde{n}}_{\tilde{I}_{i,sat}}
 \end{aligned}$$

and thereby $\tilde{I}_{i,sat} \propto \tilde{n}$.

2. With the same assumption of small temperature fluctuations the floating potential fluctuations are proportional to plasma potential fluctuations:

$$\tilde{\phi}_p = \tilde{\phi}_f + \alpha \tilde{T}_e \approx \tilde{\phi}_f \quad .$$

4.2.2 Diagnostic setup

Drift wave dynamics is a spatiotemporal phenomenon with important dynamics occurring in the poloidal plane perpendicular to the magnetic field. Ideally, one would be able to measure dynamical evolution with both high spatial as well as high temporal resolution. In reality, this is impossible, of course. There are two possibilities to do measurements with a good spatial resolution. Firstly, it is possible to move a limited number of probes with probe positioning systems and measure fluctuations at a discrete number of points in space. Statistical methods can be used to reconstruct the dynamics in the whole plane. Secondly, a large number of probes can be installed in a fixed configuration. This gives the possibility to do simultaneous measurements at a discrete number of points in space.

The poloidal probe array COURONNE

Figure 4.11 shows a schematic of the probe array COURONNE, used for spatiotemporal measurements in the poloidal direction. Similar probe arrays have been used before in the experimental devices KIWI and MIRABELLE¹ [106]. The probe array consists of a circular arrangement of 64 equally spaced cylindrical Langmuir probes. The probes are

¹More information on these devices is given in chapters 5 and 10.

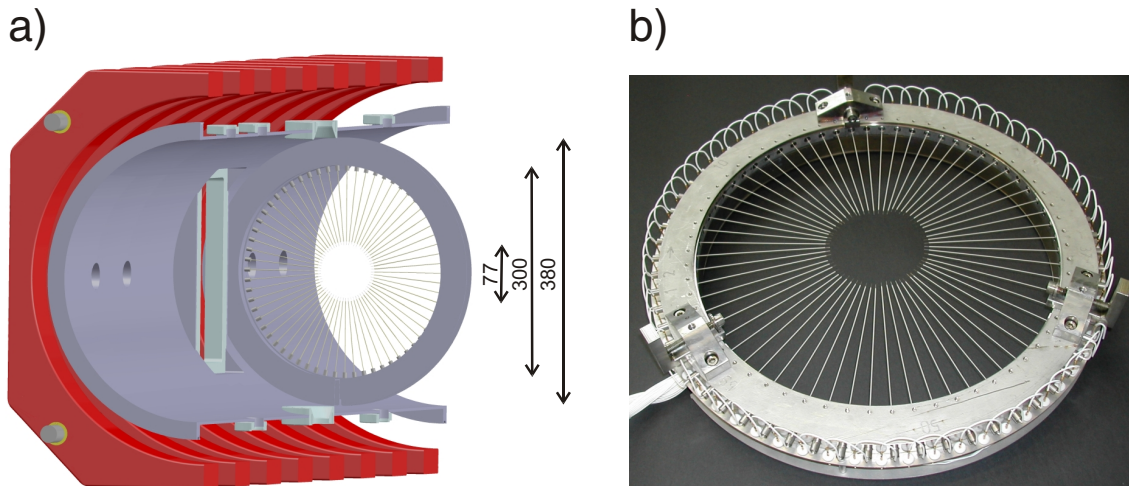


Figure 4.11: a) CAD-drawing of the 64 probe array COURONNE installed inside the vacuum vessel of the VINETA device. b) Picture of the probe array.

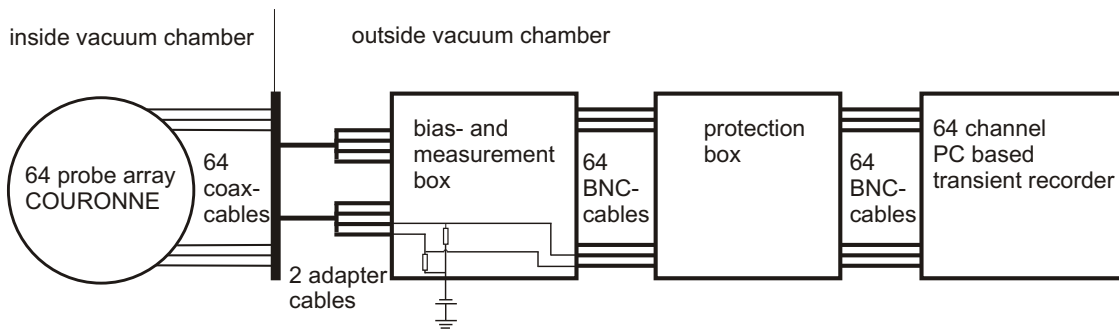


Figure 4.12: Block diagram of the data acquisition setup of the poloidal probe array COURONNE.

mounted on an aluminum ring with an inner diameter of 30 cm. The radial position of the probes is chosen in such a way that the probe tips are in the region of high fluctuations (i.e. in the gradient region of the plasma). Great care was taken to allow for exchange of probe tips. It turned out that probe tips of tungsten wire of 0.1 mm diameter were not able to withstand the permanent heat load in the argon helicon plasma in the VINETA device. Therefore, the probe tips are made of tungsten wire of 0.2 mm diameter and 4 mm length, separated by 4 mm poloidally. The tungsten wire is insulated from the plasma by ceramic tubes with an outer diameter of 0.6 mm. The electrical connection between the 64 probes and the outer electronic controls is achieved by use of 64 small coaxial cables (teflon insulation) that lead to two 50pin vacuum feedthrough SUB-D connectors (whereas only 32 pins are used per connector) installed in one rectangular flange. Two purpose-built adapter cables are used for the connection between the vacuum feedthroughs and the eight 9pin SUB-D inputs of the data acquisition system.

The data acquisition system consists of three devices as shown in figure 4.12. It is possible to measure (electron or ion) saturation current fluctuations or floating potential fluctuations with the probe array. At present, only an interface for measuring saturation

currents has been built which allows to bias all 64 probes to the same voltage (typically $-100 \dots -50$ V for ion saturation). The saturation current is measured as the voltage drop over a 100Ω shunt resistor. A good resolution of the fluctuating part of the saturation current is achieved by coupling the signal out of the interface box via an 1 nF capacitor, such that the DC part of the time series is filtered out.

A second interface has been installed between the measurement interface and the transient recorder in order to protect the transient recorder from too high (and therefore possibly damaging) input voltages. In this protection interface, the input signals are amplified by a factor of 2 and output signals are limited to ± 15 V.

The data is stored with a PC based 12 bit transient recorder, designed by the company JET-Systemtechnik GmbH. It consists of eight T112-8 boards, each with 8 channels. Measurement ranges are between ± 200 mV and ± 5 V. The incoming signals are DC coupled. The maximum input voltage is 50 V. The sampling frequency can be chosen up to 1.25 MHz corresponding to a Nyquist frequency of more than 500 kHz. Time series of up to 512 kS per channel can be stored, but typically only 8 kS are used. All 64 channels are operated in a way that time series are recorded simultaneously, triggered by an external trigger signal.

Positioning systems

Consistent with the concept of having a very flexible experimental device, several probe positioning systems have been built for the VINETA device. Probes can be moved with computer controlled servo motors. The accuracy of the positioning is better than 1 mm.

Poloidal (2D) positioning system: A poloidal probe positioning system is mountable to any one of the large rectangular windows of the vacuum chamber. It allows for measurements with high spatial resolution in a plane perpendicular to the ambient magnetic field (independent motion 200 mm in vertical and 260 mm in horizontal direction). The system itself is mounted outside the vacuum chamber and only the probe is immersed into the plasma. For the measurements presented in the present work, this poloidal positioning system has always been installed at module #4, close to the helicon antenna.

Radial (1D) positioning system: A radial positioning system can be mounted to any of the horizontal CF-40 flanges. The probe can be moved horizontally throughout the whole vacuum chamber. As for the poloidal system, only the probe itself is placed into the cylindrical vacuum chamber.

Horizontal (2D) probe positioning system: Different from the two probe positioning systems described above, this system is installed completely inside the vacuum chamber, with only the two servo motors installed outside the vacuum and connected via rotational vacuum feedthroughs to the positioning system. The probes can be positioned in a horizontal plane parallel to the ambient magnetic field (200 mm in radial and about 3 m in axial direction). The carriage, on which probes can be mounted, is only 70 mm in height and is therefore quite far away from the plasma core.

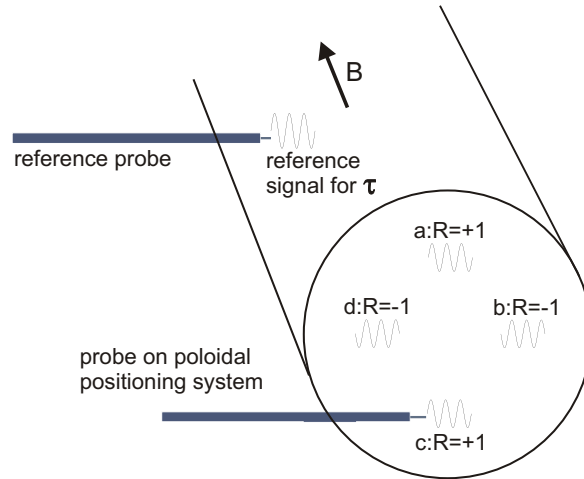


Figure 4.13: Experimental arrangement for cross correlation measurements for reconstruction of the poloidal mode structures. The reference probe is maintained at a fixed position. The other probe measures time series subsequently at a discrete number of points on a poloidal grid. The observed signals for an ideal sinusoidal $m = 2$ mode at different positions in the poloidal plane are shown. R is the value of the cross correlation function $R(d, \tau)$ for the signals at these positions.

The horizontal positioning system has been used only for measurements of the time-averaged plasma (see chapter 5) because it was found to have an unexpected high and undesired influence on the observed low-frequency fluctuations. For fluctuation measurements both the poloidal and the radial positioning systems have been used.

Measurement of poloidal mode structures

As mentioned earlier, statistical methods provide a reconstruction of fluctuation dynamics in space and time, even if not observed simultaneously for all positions. For the case of coherent modes with only one dominating frequency, the cross correlation (see chapter 3) between signals of a movable probe and a reference probe can be used. Figure 4.13 shows the experimental setup for this measurement. A fixed reference probe is placed in the region of highest fluctuations, axially 0.5–1.5 m apart from the poloidal probe positioning system. Here, another probe is installed and moved to a number of points on a grid in a poloidal plane. At each point, time series of the signals of both probes are recorded simultaneously.

The cross correlation is a measure of the ‘similarity’ of two signals at a certain time lag τ . Imagine an ideal $m = 2$ mode with two maxima and minima in the poloidal plane. Figure 4.13 indicates the principle of such a measurement. For a fixed time lag there are two positions in the plane separated by 180° (positions ‘a’ and ‘c’ in the figure), where the time series measured with the movable probe are in phase with the shifted reference signal and therefore have their maxima at the same time. For these positions the cross correlation function is $R(d, \tau) = 1$. For positions 90° separated from here (‘b’ and ‘d’ in the figure), the time signal will be 180° phase-shifted and therefore we have $R(d, \tau) = -1$. In between the two positions, one finds a smooth transition from $R = 1$ to $R = -1$.

For a different time lag, the positions of the maxima will be different. If the time lag is changed step by step from $\tau = 0$ to one period of the signal $\tau = T$ one finds that the obtained pattern of the cross correlation function makes one full rotation in the plane which reflects the rotation of the mode structure itself. Results obtained by using the correlation method are presented in section 6.4.

Measurement of parallel wavelength

For wavelength measurements one usually measures phase differences between the signals at two or more different positions. In the poloidal direction the 64 probe array is used to measure the poloidal wavelength (or the mode number). However, in the axial direction (parallel to the magnetic field) a measurement of the wavelength is quite challenging, because for gradient-driven instabilities the wavelength is typically quite long, of the order of several meter. Therefore, the probes need to be arranged at a certain distance from each other, but must be aligned properly since a small misalignment in radial or poloidal direction can cause large systematic errors in the estimation of the wavelength due to the small poloidal wavelength. In the VINETA device this has been achieved in the following way: One emissive probe and one LANGMUIR probe are used without plasma. The emissive probe is placed in the region where maximal ion saturation current fluctuations are observed in plasma operation. It is heated such that the glowing probe emits electrons. The other probe is mounted on the poloidal probe positioning system and both probes are roughly aligned by eye. This is possible with an accuracy of 1-2 cm in each direction. With a Keithley source meter, the current between this movable probe on the poloidal probe positioning system and ground is measured with magnetic field, but without plasma. If the two probes are on one magnetic field line, a (small) current

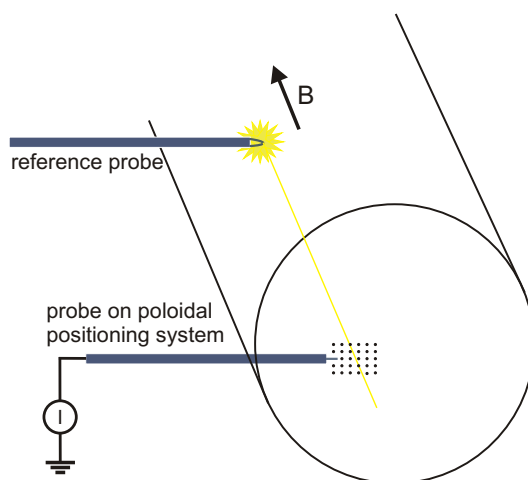


Figure 4.14: *Experimental setup for the alignment of two axially separated probes. One emissive probe is placed in the region of the highest fluctuations. A second probe on the poloidal positioning system is roughly aligned by eye. Without plasma, the current between this probe and ground is measured. In a magnetic field a very localized regions shows an increase of the measured current of several orders of magnitude.*

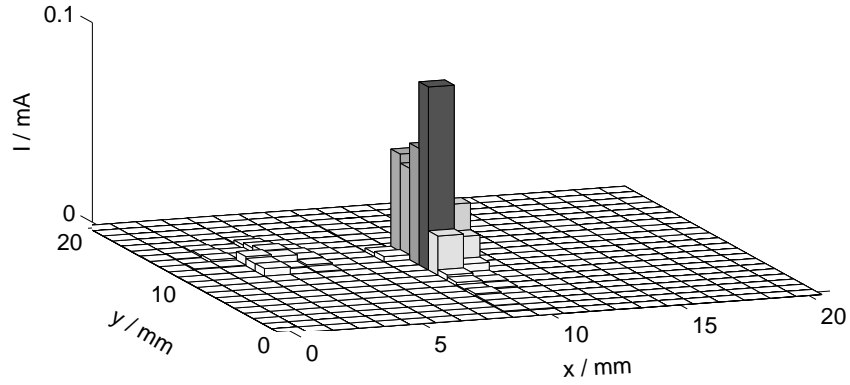


Figure 4.15: *The result of the alignment of two axially separated probes: In a very small region the observed current is by two orders of magnitude higher than at neighboring positions. The size of this region agrees quite well with the size of the emissive probe.*

is expected to flow. This measurement is repeated for every point on a two-dimensional poloidal grid (2cm x 2cm) with only 1 mm between the measurement points. Indeed, in a very small region, the detected current rises into the 10^{-4} A-range, in contrast, outside this position, the current is below 10^{-6} A. This is shown in figure 4.15.

For the measurement of the parallel wavelength of pressure gradient driven waves, a coherent state is usually established. Time series of both probes are recorded and the phase φ between both time series is determined by using either cross-correlation or cross-power spectrum analysis (see chapter 3). Practically, the cross-power spectrum is preferred because it also allows the determination of the phase for different frequencies. The axial wavelength is then determined from $\lambda_z = 2\pi\Delta z/\varphi$, where Δz is the axial distance of the probes.

Chapter 5

Plasma parameters in VINETA

The VINETA device is a new experimental device with a unique setup that was built in the course of the present thesis. Soon after first operation in the helicon discharge mode, an instability with frequencies well below the ion cyclotron frequency was observed, showing characteristic features of drift instabilities. A detailed characterization of the instability is given in the next chapter. For a clear identification of this instability, background plasma parameters are of crucial importance. Experimental results on time-averaged plasma parameters are presented and subsequently discussed¹.

The following issues are of importance for drift wave dynamics:

- Gradient-driven instabilities show the highest fluctuation level in the region of the steepest gradients. This demands for detailed knowledge of gradients of plasma density, electron temperature and plasma potential in both the direction parallel and perpendicular to the ambient magnetic field.
- Density and potential profiles determine the electron diamagnetic drift as well as the $E \times B$ drift which are of importance for a quantitative comparison with drift wave dispersion.
- Operation parameters like magnetic field and neutral gas pressure influence plasma parameters and parameter profiles.

5.1 Axial variation

Figure 5.1 shows radial profiles of plasma density, electron temperature, plasma potential and floating potential for four axial positions in the range $z \sim 1.5 - 2.5$ m where z denotes the distance from the helicon antenna.

The density profiles in figure 5.1a) are peaked with maximum densities of about $7 \cdot 10^{18} \text{ m}^{-3}$ for all four z -positions. The bulk plasma is radially restricted to less than the antenna region, suggesting that the helicon discharge mechanism deposits its power mainly in the center of the antenna. At the edge region, the density is still in the range of

¹Here, *time-averaged* stands for an averaging over a time much longer than the time scales of the low-frequency instability. The typical averaging time is between several 10 ms and several 100 ms.

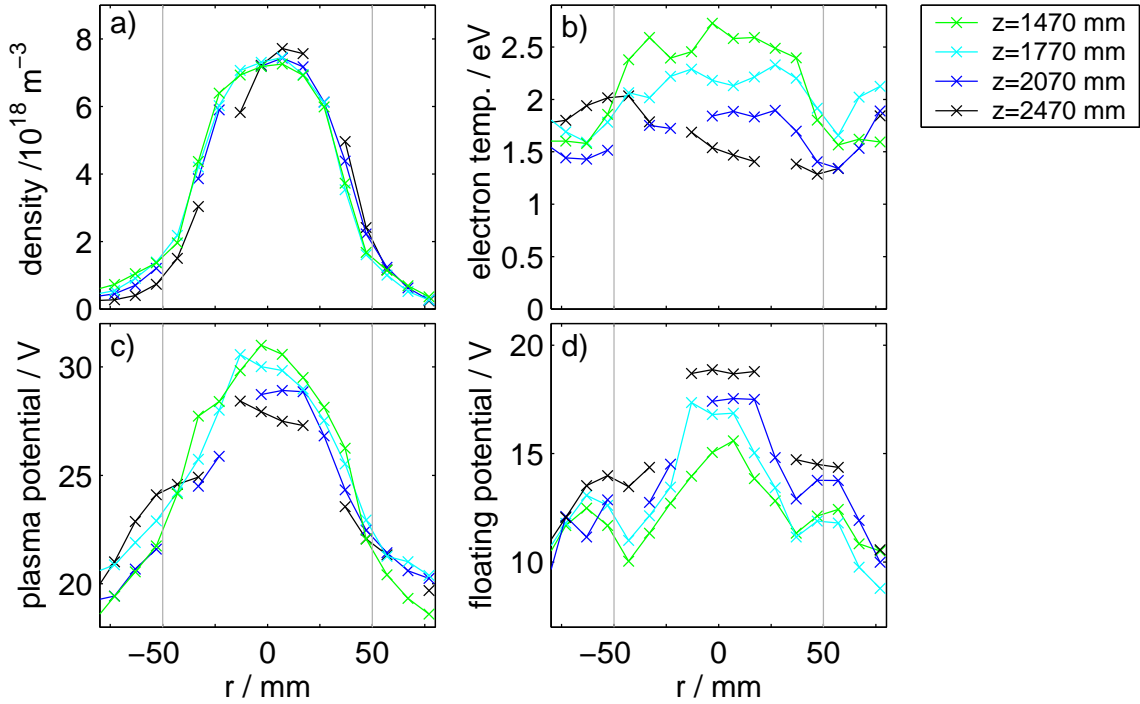


Figure 5.1: Radial plasma parameter profiles at different axial positions for $B = 71 \text{ mT}$, $p_{Ar} = 0.3 \text{ Pa}$ and $P_{RF} = 2.5 \text{ kW}$. z is the distance from the antenna edge. The gray lines indicate the radial position of the antenna. a) plasma density, b) electron temperature, c) plasma potential, d) floating potential. A compensated probe on the horizontal probe positioning system was used for the measurement.

$10^{16} \dots 10^{17} \text{ m}^{-3}$. For some discharge conditions, density profiles are found to be close to Gaussian, but often profiles are broader. Figure 5.1a) shows that the density profiles remain very similar over an axial distance of 1 m.

Figure 5.1b) shows the corresponding electron temperature profiles. Different from the density profiles, there is a clear dependence of the electron temperature on the axial position. In the center of the plasma column the electron temperature decreases with increasing distance from the plasma source. For the curves in the range $z = 1470 - 2070 \text{ mm}$, the profiles have a plateau in the center and drop towards the edge. The curve for $z = 2470 \text{ mm}$ has a different shape: the electron temperature in the plasma center is lower than at the edge. Extrapolating the linear decrease of the temperature to the antenna position (figure 5.2), one obtains an electron temperature of $4 - 4.5 \text{ eV}$.

Plasma potential profiles are shown in figure 5.1c). The maximum is always in the center of the plasma column. The profiles decrease monotonically towards the edge. As is the case for the electron temperature, the plasma potential was also observed to depend on the distance from the antenna. The plasma potential is found to be smaller for greater distances from the antenna ($\Delta\phi_p \approx 3 \text{ V}$ for $\Delta z = 1 \text{ m}$). The potential profile gradients in the edge region are slightly steeper for positions closer to the antenna.

The floating potential profiles in figure 5.1d) also have a maximum in the center of the plasma column and decrease towards the plasma edge. The floating potential in the

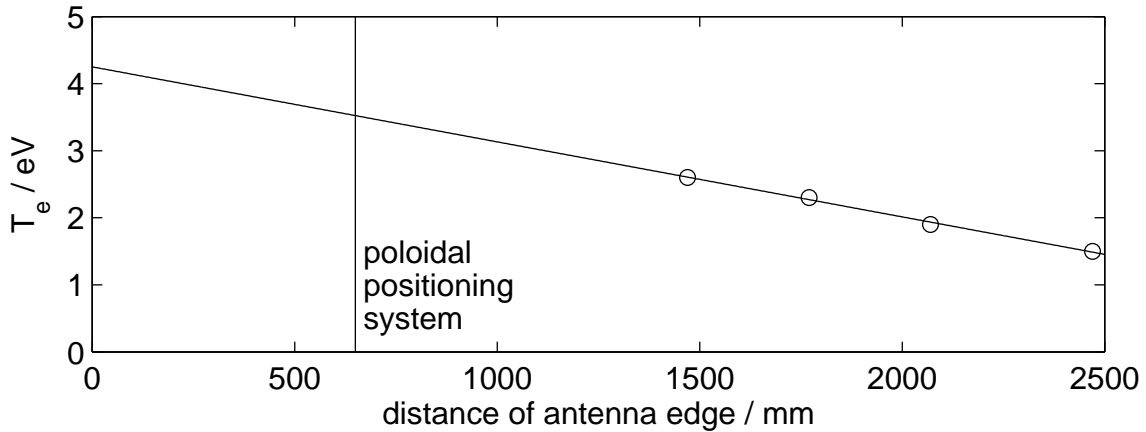


Figure 5.2: Extrapolation of the peak electron temperature of figure 5.1b) towards the antenna. The dotted points indicate the four measurement points. The antenna edge is at $z = 0$. The poloidal positioning system is at 650 mm as indicated by the vertical line.

plasma center becomes higher with increased distance from the helicon source.

5.2 Variation with the magnetic field

An important external control parameter of the VINETA is the magnetic field which influences a number of physical quantities. Radial lengths (drift scale ρ_s , the ion gyro radius) as well as the perpendicular drift velocities depend explicitly on the magnetic field. From the dispersion relation of helicon waves it is expected that the plasma density increases with increasing magnetic field (see equation (4.2)). Also, diffusion lengths both parallel and perpendicular to the ambient magnetic field depend on the magnetic field strength, which also influences the density gradients in the plasma.

As already introduced in chapter 2, the radial density and plasma potential profiles determine the electron diamagnetic drift $\mathbf{v}_{D,e}$ and the $\mathbf{E} \times \mathbf{B}$ drift, respectively. In cylindrical geometry one obtains

$$\mathbf{v}_{D,e} = -\frac{k_B T_e}{eB} \frac{1}{n} \frac{\partial n}{\partial r} \mathbf{e}_\theta \quad \text{and} \quad \mathbf{v}_E = \frac{1}{B} \frac{\partial \phi}{\partial r} \mathbf{e}_\theta \quad . \quad (5.1)$$

The corresponding frequencies are

$$f_{D,e} = v_{D,e}/2\pi r \quad \text{and} \quad f_E = v_E/2\pi r \quad . \quad (5.2)$$

For a Gaussian density profile the diamagnetic drift increases linearly with radius, which corresponds to a frequency independent of the radial position. The frequency related to the $\mathbf{E} \times \mathbf{B}$ drift is independent of radial position for potential profiles of the functional form $\phi(r) = ar^2 + b$. Under this condition, the plasma column rotates as a rigid body. In the VINETA device both conditions are usually not fulfilled, thus velocity and frequency profiles are found to depend on the radial position (also called ‘velocity shear’).

In figure 5.3, radial density and potential profiles are shown together with the derived velocities and frequencies. The measurement points are indicated by circles, the lines

are fitted curves of the form $f(r) = a \exp(-|r/b|^c) + d$. Velocities and frequencies are calculated from the fitted curves. From the shape of the density and potential profiles it is found that electron diamagnetic drift and $E \times B$ drift are in opposite directions.

Figure 5.3a) shows that the plasma density increases with increasing magnetic field, as expected for a helicon discharge. At 78 mT, the peak is close to or even below the density at 71 mT, i.e. a saturation of the density is observed. The highest density gradient is found at radial positions $r = 30 - 35$ mm for all three cases shown. Unlike the density profiles, the electron diamagnetic drift velocity (figure 5.3b) is fairly independent on the magnetic field for $|r| \leq 40$ mm. $v_{D,e}$ radially increases monotonically up to values in the

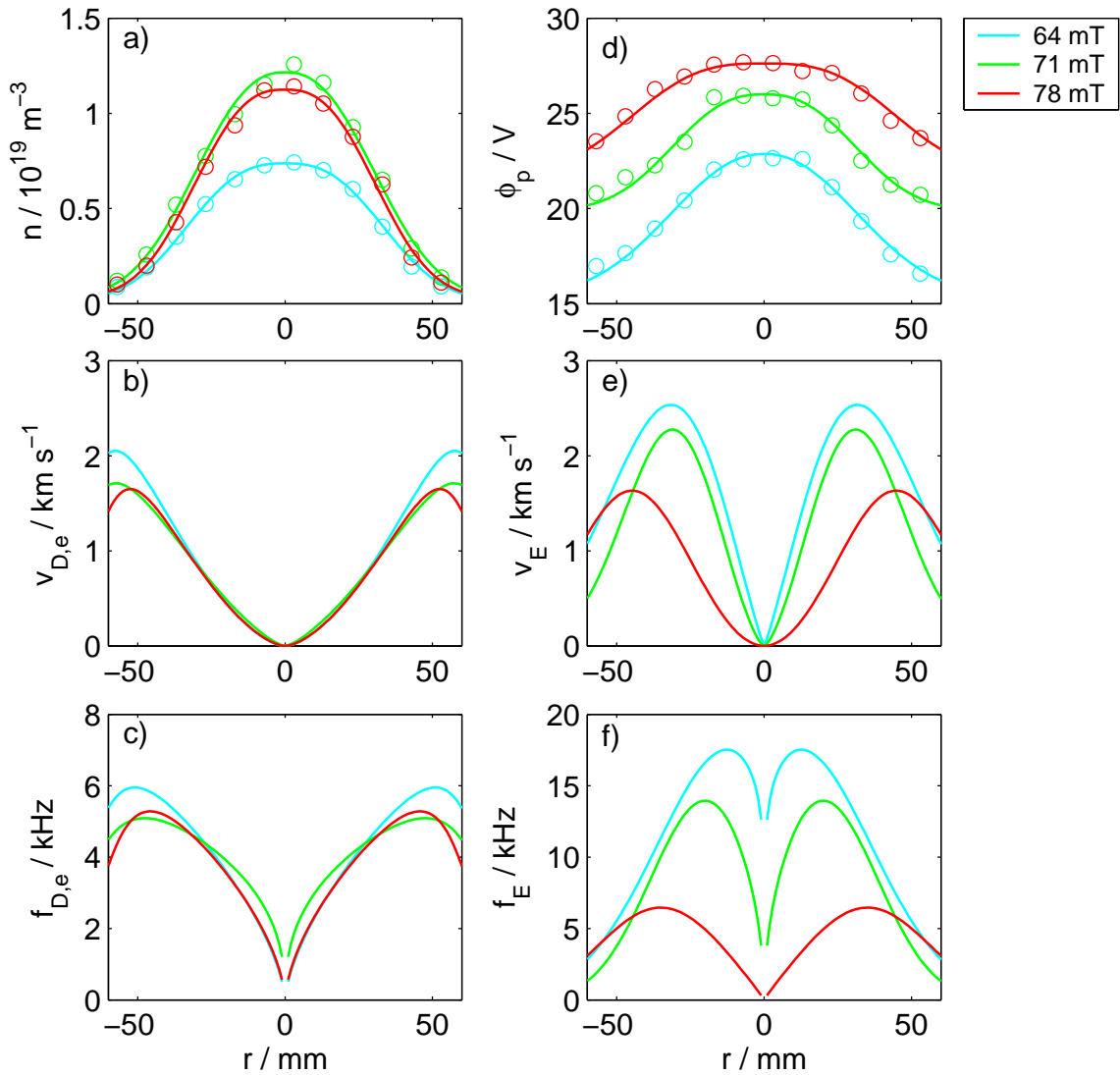


Figure 5.3: Radial plasma parameter profiles at different magnetic fields (\circ measured points, $-$ fitted / derived curve): a) plasma density, b) electron diamagnetic drift, c) frequency corresponding to the electron diamagnetic drift, d) plasma potential, e) $E \times B$ drift, f) frequency corresponding to the $E \times B$ drift. A compensated probe on the horizontal probe positioning system at $z = 2470$ mm was used. The signs of the velocities (indicating the direction) are omitted. The discharge parameters are $p_{Ar} = 0.3$ Pa, $P_{RF} = 2.5$ kW, $T_e \approx 1.4$ eV for all magnetic fields.

range of $1700 - 2000 \text{ ms}^{-1}$ at the plasma edge. The electron diamagnetic drift velocity is radially sheared such that the corresponding frequency (figure 5.3c) depends on r as well. It increases towards the plasma edge and in the relevant gradient region, $f_{D,e} \approx 3 - 4 \text{ kHz}$. Figure 5.3d) shows radial plasma potential profiles. It is found that the plasma potential rises monotonically with increasing magnetic field. For higher magnetic field, the plateau in the center is broader than for lower magnetic fields. The steepest gradients are found at radii $r = 30 - 35 \text{ mm}$ for $B = 64 \text{ mT}$ and $B = 71 \text{ mT}$ and at $r \approx 45 \text{ mm}$ for 78 mT . The derived $\mathbf{E} \times \mathbf{B}$ drift velocity is shown in figure 5.3e). Its magnitude is comparable to that of the electron diamagnetic drift velocity. The highest $\mathbf{E} \times \mathbf{B}$ velocities are in the range of $1500 - 2600 \text{ ms}^{-1}$ and are found at radial positions $r = 30 - 45 \text{ mm}$. Here, the position depends on the magnetic field, corresponding to the different widths of the potential profiles. The corresponding frequencies in figure 5.3f) have maxima in the range of $5 - 18 \text{ kHz}$, whereas the radial position of the maximum again depends on the magnetic field. In any case, the maxima are found at lower radii than for the electron diamagnetic drift frequency. Whereas the latter is nearly independent of the ambient magnetic field, the $\mathbf{E} \times \mathbf{B}$ drift frequency shows a decrease with increasing magnetic field.

5.3 Variation with the neutral gas pressure

The neutral gas pressure is a different external control parameter of the experiment. Collision frequencies and thereby classical diffusion are determined by the neutral gas pressure.

Figure 5.4 shows the dependencies of radial density and potential profiles and, using these, the derived velocities and corresponding frequencies on the neutral gas pressure (see also figure 5.3). The density profiles are insensitive to neutral gas pressure changes (figure 5.4a). The steepest density gradients are always at $r \approx 30 \text{ mm}$. However, small deviations in the far edge region lead to a slightly different shape of the sheared electron diamagnetic velocity profiles in figure 5.4b). The peak values are around 3000 ms^{-1} at the plasma edge. The corresponding frequencies also depend on the radial position and values in the range $8 - 10 \text{ kHz}$ are found in the region of the steepest density gradients (figure 5.4c).

The potential profiles for the two different neutral gas pressure values are shown in figure 5.4d). For higher neutral gas pressure, the plasma potential is found to be higher. We note that the measurements are more scattered and seem to form a hollow profile. Nevertheless, for sake of simplicity and owing to relatively high uncertainties, a flat-top profile is fitted to the measured points. The derived $\mathbf{E} \times \mathbf{B}$ velocities are shown in figure 5.4e). The velocity is strongly sheared and increases towards the plasma edge to peak values of $2000 - 2500 \text{ ms}^{-1}$. In the relevant density gradient region, the $\mathbf{E} \times \mathbf{B}$ drift frequencies are in the range $4 - 7 \text{ kHz}$ (figure 5.4f).

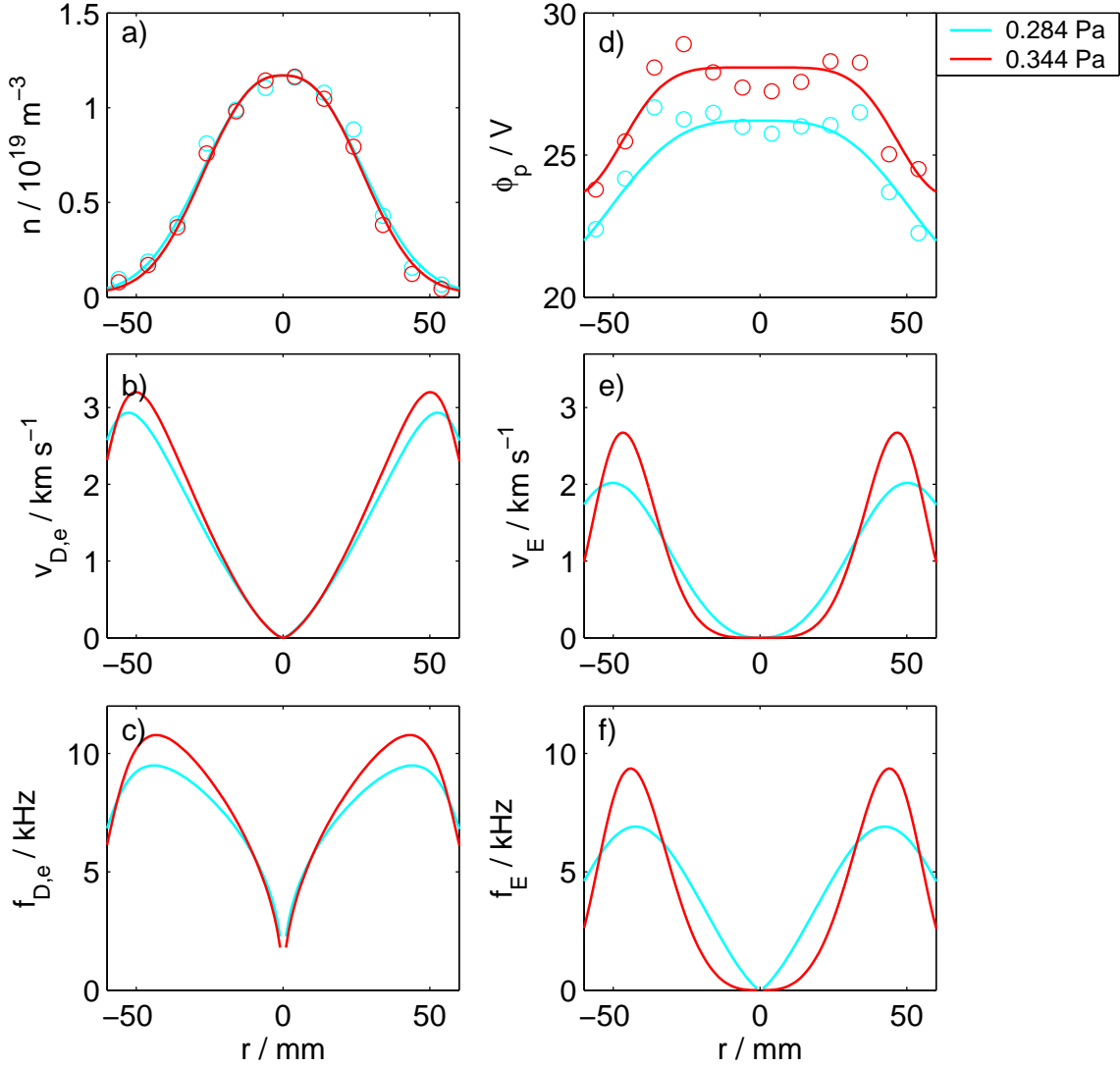


Figure 5.4: Radial parameter profile at different neutral gas pressure: a) plasma density (\circ measured points, – fitted curve), b) electron diamagnetic drift, c) frequency corresponding to the electron diamagnetic drift, d) plasma potential (\circ measured points, – fitted curve), e) $E \times B$ drift, f) frequency corresponding to the $E \times B$ drift. A compensated probe on the horizontal probe positioning system at $z = 1770$ mm was used for the measurement. Discharge parameters: $B = 67$ mT, $P_{RF} = 2.2$ kW, $T_e \approx 2$ eV for both pressures.

5.4 Discussion

Prior to the discussion, we give a brief summary of the most important findings:

- The plasma density is peaked in the plasma center with maximum densities in the range of $10^{18} \dots 10^{20} \text{ m}^{-3}$. The radial density gradient is located at $r = 10 - 40$ mm. The electron temperature profiles are relatively flat and radial temperature gradients can be neglected to first order. The plasma potential has a similar shape as the density but it is flat in the center. The location of strong potential gradients depends more on discharge parameters such as the ambient magnetic field and the neutral

gas pressure. The density gradient region often coincides with the potential gradient region and a clear distinction between both regions is in general not possible.

- The radial density profiles remain axially unchanged over a distance of 1 m. The electron temperature decreases linearly with increasing distance from the plasma source. $T_e = 2 \text{ eV}$ is observed approximately 2 m away from the antenna and is taken as a mean value. The plasma potential and the radial electric field also decrease with increasing distance from the antenna.
- Both the electron diamagnetic drift and the $E \times B$ drift are sheared and have peak values in the range $1500 - 3000 \text{ ms}^{-1}$. Both drifts are in opposite directions. The corresponding frequencies have peak values in the range $5 - 15 \text{ kHz}$.
- The plasma density increases with increasing magnetic field and saturates for higher magnetic field. The electron temperature is nearly independent of the magnetic field and neutral gas pressure. The plasma potential increases with increasing magnetic field as well as with increasing pressure. The radial electric field and thereby the $E \times B$ drift frequency decrease with increasing magnetic field. The electron diamagnetic drift frequency is nearly independent of the magnetic field and the neutral gas pressure.

Ionization degree

The ionization degree $n_i/(n_i + n_n)$ is an important quantity referred to in the following discussion of collision processes. To date, no measurements of neutral densities have been performed for the VINETA device. The gas temperature and neutral density profiles can be estimated as follows:

Assuming that the neutral gas is at room temperature, it is determined from the equation for an ideal gas $p = nk_B T$, that the neutral density is connected to the neutral gas pressure by $n_g = 2.5 \cdot 10^{20} p [\text{Pa}] \text{ m}^{-3}$. At a pressure of 0.1 Pa the neutral gas density is $2.5 \cdot 10^{19} \text{ m}^{-3}$ which is close to the observed peak plasma densities. In other helicon devices, heating of the neutral gas up to 1000 K has been observed [107], as well as a depletion of neutral gas in the plasma center due to neutral pumping [34,107]. Both lead to a further reduction of the neutral gas density and suggest ionization degrees close to 100% in the plasma center, especially at low neutral gas pressures. This is supported by the observed breakdown of the helicon discharge for neutral gas pressures below 0.1 Pa. The helicon wave dispersion relates the plasma density with the ambient magnetic field and the axial wavelength of the helicon wave (see equation (4.2)). If the neutral gas density n_g is less than the corresponding plasma density, the helicon discharge cannot be sustained.

On the other hand, a big reservoir of neutral gas is present around the plasma core. This should provide refilling with neutral gas from the surrounding reservoir and the neutral gas density would remain essentially constant, leading to ionization degrees of several 10% in the plasma center. Such a *gas plenum* was proposed to further increase the densities achievable with helicon discharges [108]. The breakdown of the helicon mode for pressures below 0.1 Pa suggest that this does not happen effectively enough in the VINETA device. This might be due to the position of the gas feed (opposite to the plasma source). In any case, the ionization degree in the center is much higher than 1%, of the order of several

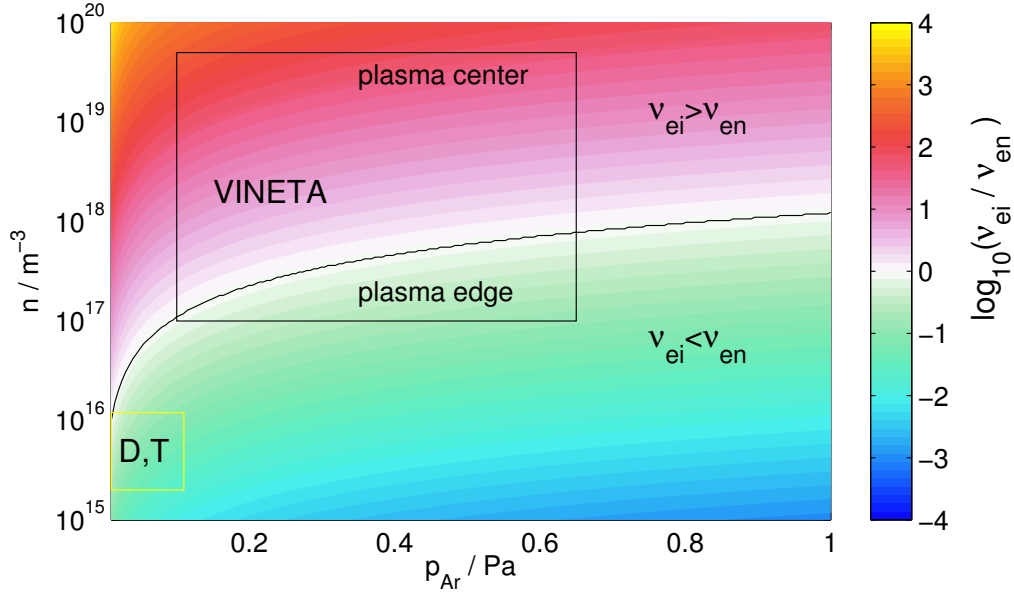


Figure 5.5: Color coded ratio between Coulomb collision frequency ν_{ei} and frequency ν_{en} for collisions between electrons and neutrals. Argon pressure and plasma density are the parameters. T_e is kept fixed at 2 eV and the neutral gas temperature is kept fixed at $T_g = 300 \text{ K} = 0.025 \text{ eV}$. Note the logarithmic scale. The black line indicates $\nu_{ei} = \nu_{en}$. The operation regime of the VINETA device is indicated by the black rectangle. The yellow rectangle indicates the operation regime of the DLPD device and triple-plasma devices KIWI and MIRABELLE (see below).

10% up to 100% in the plasma center. Under these conditions, not only electron collisions with neutrals, but also Coulomb collisions must be accounted for.

Collision frequencies

Collision frequencies are not easily determined and the values depend to a large extent on the atomic data used, especially for collisions with neutrals. The formulas used in this thesis to estimate collision frequencies are provided in appendix B.

For Coulomb collisions between electrons and ions, the collision frequency varies between $\nu_{ei} = 10^6 \text{ s}^{-1}$ at edge densities of 10^{17} m^{-3} and $\nu_{ei} = 10^8 \text{ s}^{-1}$ at core densities of 10^{19} m^{-3} (assuming $T_e = 2 \text{ eV}$). The combination of high plasma density at low electron temperature is responsible for these high collision frequencies. The collision frequency for electron-neutral collisions is in the range $\nu_{en} = 10^6 \text{ s}^{-1}$ for a neutral gas pressure of 0.1 Pa and $\nu_{en} = 10^7 \text{ s}^{-1}$ for 0.8 Pa.

Figure 5.5 shows the ratio between Coulomb collision frequency ν_{ei} and electron-neutral collision frequency ν_{en} as a function of the neutral gas pressure and the plasma density. Electron temperature T_e and neutral gas temperature T_g are kept fixed at $T_e = 2 \text{ eV}$ and $T_g = 0.025 \text{ eV}$. The plot is color coded with logarithmic scale. The gas pressure is chosen to be between 0.1 Pa and 0.65 Pa. The plasma density is $10^{18} - 10^{20} \text{ m}^{-3}$ in the plasma center and $10^{16} - 10^{17} \text{ m}^{-3}$ at the edge. The parameter regime determined by these density and neutral gas pressure ranges is indicated by the black square. In the plasma

center, Coulomb collisions clearly dominate for all pressures, however, at the plasma edge, collisions with neutrals play a significant role. For higher neutral gas temperatures, Coulomb collisions are even more dominant.

The yellow rectangle indicates a parameter regime which is achieved in three other devices where drift waves have been studied in argon plasmas. These devices are the Dartmouth Linear Plasma Device (DLPD) [9,10], KIWI and MIRABELLE [109,110], and in these, collisions with neutrals clearly dominate.

The discharge equilibrium

The discharge equilibrium² is determined by plasma sources and sinks, and also by transport processes parallel and perpendicular to the ambient magnetic field. A comprehensive discussion of the discharge equilibrium is beyond the scope of the present thesis and only a few remarks are given subsequently. The helicon source produces a radially peaked plasma profile, localized within the antenna region. This is typical for helicon sources with helical antenna coupling and indicates that in the helicon discharge mode the plasma production occurs detached from the antenna [76,111]. This is in contrast to capacitive coupling where the highest densities are found close to the antenna [78]. Electrons and ions are lost by diffusion to the walls. Electron and ion motion parallel to the magnetic field is not affected by the Lorentz force, but is slowed down by collisions. Across the magnetic field, collisions lead to diffusion and the perpendicular diffusion is thus dependent on the collision frequencies [1]. Diffusion processes also determine the density profiles. The plasma density remains axially constant in the considered region, but a decay of the plasma density further downstream is likely due to perpendicular diffusion and possibly volume recombination. If the total particle fluxes of electrons and ions would differ significantly, a serious charge imbalance would soon arise [1]. Thus, diffusion rates of electrons and ions must adjust themselves by creation of self-consistent electric fields (and thereby potential profiles). Furthermore, a sheath forming in front of the grounded endplate determines the plasma potential [98]. The electron temperature is found to decrease monotonically with distance from the antenna. In references [112,113], the axial profile of the electron temperature in a helicon discharge is quantitatively explained by classical heat conduction. It was found that the electrons are heated only in a region within a helicon wavelength of the antenna. The T_e decay length is determined by heat conduction and electron cooling by inelastic collisions (such as excitation and ionization collisions with neutrals).

Parallel electron drift

A parallel electron drift is one of the destabilizing factors for the drift instability (see equation (2.27)) [114]. The drift velocity V can be roughly estimated from the parallel component of equation (2.4):

$$0 = -\nabla_{\parallel} k_B T_e n - neE_{\parallel} - n\nu_e m_e V \quad . \quad (5.3)$$

²In this context, the term *equilibrium* does not mean a thermodynamical equilibrium which is nearly never reached in laboratory plasmas. Instead, the equilibrium between plasma production and plasma loss is meant which leads to nearly constant conditions within a short time (\ll pulse length).

From figure 5.1 it is found that $n(z) \approx \text{const.}$, $\nabla_{\parallel} T_e \approx -1 \text{ eV/m}$ and $E_{\parallel} = -\nabla_{\parallel} \phi_p \approx 3 \text{ V/m}$. With the electron collision frequency $\nu_e \approx 10^8 \text{ s}^{-1}$ (see above) this leads to

$$V = \frac{1}{n\nu_e m_e} (-ne\nabla_{\parallel} T_e - neE_{\parallel}) \approx \frac{e}{\nu_e m_e} 2V/m = 3500 \text{ m/s} \quad . \quad (5.4)$$

This value for the parallel electron velocity V is close to the ion sound speed c_s , differing by only 35% from the typical value $c_s \approx 2600 \text{ m/s}$ which was given in chapter 4. In comparison to the electron thermal velocity, $V \approx 0.006 v_{th,e}$. Thus, as expected for a helicon discharge [113], a relatively small axial flow of electrons occurs. Assuming for simplicity a radially constant axial electron drift and a radially constant plasma density of $5 \cdot 10^{18} \text{ m}^{-3}$ up to a radius of 30 mm, the current density $J_{\parallel} = enV$ is then estimated to be $J_{\parallel} = 2800 \text{ A/m}^2$. With the same assumptions, the electron current is estimated to be $I = J_{\parallel} A \approx 8 \text{ A}$. Due to the high plasma density, this value is much higher than in other discharges, where the parallel electron drift velocity is much higher but the plasma densities are lower by orders of magnitudes [9,115].

Comparison to other drift wave experiments

Drift waves have been investigated in different plasmas since the 1960s. In table 5.1, plasma parameters of the VINETA device are compared to the parameters of three other linear magnetized plasma devices in which experiments on drift waves have been conducted. The MIRABELLE device [109,116] and the KIWI device [110] are triple-plasma devices. The DLPD is a single-sided device used by ELLIS, MARDEN-MARSHALL and coworkers [9,10]. In all devices, argon is used as filling gas.

In all four devices, the values for the ion cyclotron frequency Ω_{ci} , the drift scale ρ_s and the ion sound velocity c_s are quite similar. In the VINETA device Coulomb collisions dominate. In the other three devices electron-neutral collisions dominate due to the much lower degree of ionization. The effective electron collision frequency $\nu_e = \nu_{ei} + \nu_{en}$ is two orders of magnitude higher in the VINETA device than in the other devices. Also the ion collision frequency is one order of magnitude higher in the our device if neutral depletion effects are neglected. This means that the VINETA plasma has a much higher collisionality than the plasma in other devices used for drift wave studies.

The plasma β is 750 times larger in the VINETA device than in MIRABELLE and KIWI, and 4000 times larger than in the DLPD. Consequently, β exceeds the mass ratio m_e/M by a factor of 60, whereas in the other devices β is well below the mass ratio. In low- β plasmas (i.e. $\beta_{\mu} < 1$), electromagnetic effects can generally be neglected. Although in our device $\beta_{\mu} > 1$, the high collisionality leads to negligible magnetic field fluctuations (see chapter 2).

We note a further difference: the parallel electron velocity V . As estimated above, V is an order of magnitude lower in the VINETA device than in the other devices where the parallel electron drift is considered as an important destabilizing effect. On the other hand, in the VINETA device, the destabilization due to the parallel electron drift is a less important factor while the destabilizing role of electron collisions is significant. Consequences on the drift wave physics will be discussed in more detail in chapter 7.

parameter	VINETA	MIRABELLE	KIWI	DLPD
peak plasma density [m^{-3}]	$1 \cdot 10^{19}$	$2 \cdot 10^{15}$	$1 \cdot 10^{16}$	$1 \cdot 10^{16}$
electron temperature [eV]	2	2	1.5	2
gas pressure [Pa]	0.3	0.01	0.1	0.1
magnetic field [mT]	70 mT	40 mT	70 mT	200 mT
ionization degree [%]	10-100	0.1	0.1	0.3
Ω_{ci} [rad/s]	$1.7 \cdot 10^5$	$1.0 \cdot 10^5$	$1.8 \cdot 10^5$	$4.8 \cdot 10^5$
ρ_s [mm]	13	23	11	5
c_s [m/s]	2600	2500	1900	2500
ν_{en} [1/s]	$5 \cdot 10^6$	$2.5 \cdot 10^5$	$1 \cdot 10^6$	$2 \cdot 10^6$
ν_{en}/Ω_{ci}	30	2.5	5.5	4
ν_{ei} [1/s]	$1 \cdot 10^8$	$3 \cdot 10^4$	$2 \cdot 10^5$	$1 \cdot 10^5$
ν_{ei}/Ω_{ci}	600	0.3	1.1	0.2
ν_{in} [1/s]	$6 \cdot 10^4$	$9 \cdot 10^2$	$6 \cdot 10^3$	$6 \cdot 10^3$
ν_{in}/Ω_{ci}	0.3	0.01	0.03	0.01
plasma β	$8 \cdot 10^{-4}$	$1 \cdot 10^{-6}$	$1 \cdot 10^{-6}$	$2 \cdot 10^{-7}$
$\beta_\mu = \beta/(m_e/M)$	60	0.07	0.09	0.01
V/c_s	1	$-^1$	40	50

Table 5.1: Comparison between different experimental devices in which experimental investigations on drift waves have been conducted. In all devices, argon is used and the neutrals are assumed to be at room temperature. Values for the MIRABELLE device from reference [116], for the KIWI device from reference [115] and for the DLPD from references [9,10].

¹ No data available. Due to the similarity between KIWI and MIRABELLE, V is expected to be of similar magnitude in both devices.

Chapter 6

Low-frequency instability in VINETA

A low-frequency instability with frequencies well below the ion cyclotron frequency is observed in the helicon plasma of the VINETA device. Because of its edge-localization it was suggested to be a drift-type instability right from the beginning. The main goal is thus the identification and systematic control of this instability. Main features of drift waves for non-ambiguous identification are the following:

- highest fluctuation levels are in the density gradient regions.
- normalized density and potential fluctuations are similar in magnitude:
 $\tilde{n}/n \approx \tilde{\phi}_p/T_{[eV]}$.
- phase angle between \tilde{n} and $\tilde{\phi}$ is non-zero with \tilde{n} leading $\tilde{\phi}$.
- phase velocity is in the electron diamagnetic drift direction.
- parallel wavelength $\lambda_{\parallel} = 2\pi/k_{\parallel}$ is non-zero and $k_{\parallel} \sim (\text{machine length})^{-1} \ll k_{\perp}$.
- frequencies and wavelengths are compatible with drift wave theory.

Different dynamical states of the instability can be observed in the VINETA device. It is sometimes of advantage to consider single saturated modes which are characterized by poloidal mode number and frequency. Subsequently, also the poloidal mode structure of saturated modes is discussed. Nonlinear interaction of different modes and turbulence have also been observed and some examples are shown.

Typical length scales for the drift wave dynamics, such as the ion gyro radius and drift scale ρ_s , depend on the ambient magnetic field B . Neutral collision frequencies depend on the neutral gas pressure p_g . The $E \times B$ drift was found to depend on both, the ambient magnetic field and the neutral gas pressure. It is thus reasonable to expect that the discharge parameters determine the drift wave dynamics. This allows one to control the drift wave dynamics. The variation of the drift wave dynamics also gives some insight into important physical mechanisms, especially the dominating destabilization effects.

For drift waves, plasma density and plasma potential fluctuate interdependently. To gain good spatial and temporal resolution of both quantities, ion saturation current fluctuations $\tilde{I}_{i,sat}$ are taken to be proportional to density fluctuations \tilde{n} and floating potential fluctuations $\tilde{\phi}_f$ are taken to be proportional to plasma potential fluctuations $\tilde{\phi}_p$. As outlined in section 4.2.1, these assumptions are valid for negligible temperature fluctuations \tilde{T}_e , which may be assumed in the VINETA device.

6.1 Time evolution

The helicon discharge was operated in pulsed mode with typical pulse length 300–500 ms. For ensemble averaging, a sequence of pulses at the same operation parameters is recorded. It is thus essential to consider the evolution of the fluctuation dynamics during a pulse as well as the reproducibility for subsequent plasma pulses.

Figure 6.1a) shows a typical time series of the ion saturation current for a 500 ms pulse. After triggering the plasma, the ion saturation current raises within ~ 4 ms up to a certain level where fluctuations are already visible. About 15 ms after the plasma is switched on, the ion saturation current increases again and within ~ 25 ms reaches a mean level where it remains rather constant for the rest of the pulse, as seen in the moving average curve. The exact shape of the start-up phase is very different for different discharge parameters. While the mean density is constant over several 100 ms, during the whole pulse the ion saturation current shows strong fluctuations discussed below. When the RF power is switched off at 500 ms, the plasma decays within a few ms.

By inspecting the pulse in figure 6.1a) one gets the impression that the fluctuation dynamics change at least twice after the start-up phase. The time instants where fluctuation changes occur are indicated by arrows. At 105 ms, the fluctuation degree suddenly increases, at 335 ms the same happens again. Figures 6.1b-j) give more insight into the fluctuation dynamics for the three indicated time intervals. For each, a 5 ms sample interval of the time series is shown in figures 6.1b-d). Frequency power spectra and PDF's for each indicated 40 ms interval are shown in figures 6.1e-j).

In interval I, the time series has a certain periodicity but the amplitude is rather irregular (figure 6.1b). This is seen in the power spectrum where a peak at 4.4 kHz is embedded into a broad background with a number of smaller peaks. The PDF is double humped and nearly symmetric, as expected for sinusoidal signals. For interval II, the minima of the fluctuations remain at nearly the same level while the maxima are systematically higher and show more irregularity if compared to I (figure 6.1c). This is clearly seen in the corresponding PDF in figure 6.1i), showing a peak for amplitudes below the mean. The PDF for amplitudes above the mean is flat and broadened. The power spectrum in figure 6.1f) is similar to the one in figure 6.1e). Figure 6.1d) shows that in interval III the fluctuation amplitude increases again. The PDF is broader and again asymmetric with a peak for amplitudes below the mean value (figure 6.1j). The power spectrum still shows a pronounced peak, but at a different frequency, 3.6 kHz. This corresponds to one of the smaller peaks in figures 6.1e,f), which means that a different mode took over.

Figure 6.1 reveals that even within one pulse the fluctuation dynamics can change significantly with respect to amplitude and spectrum. It has been found that the fluctuation

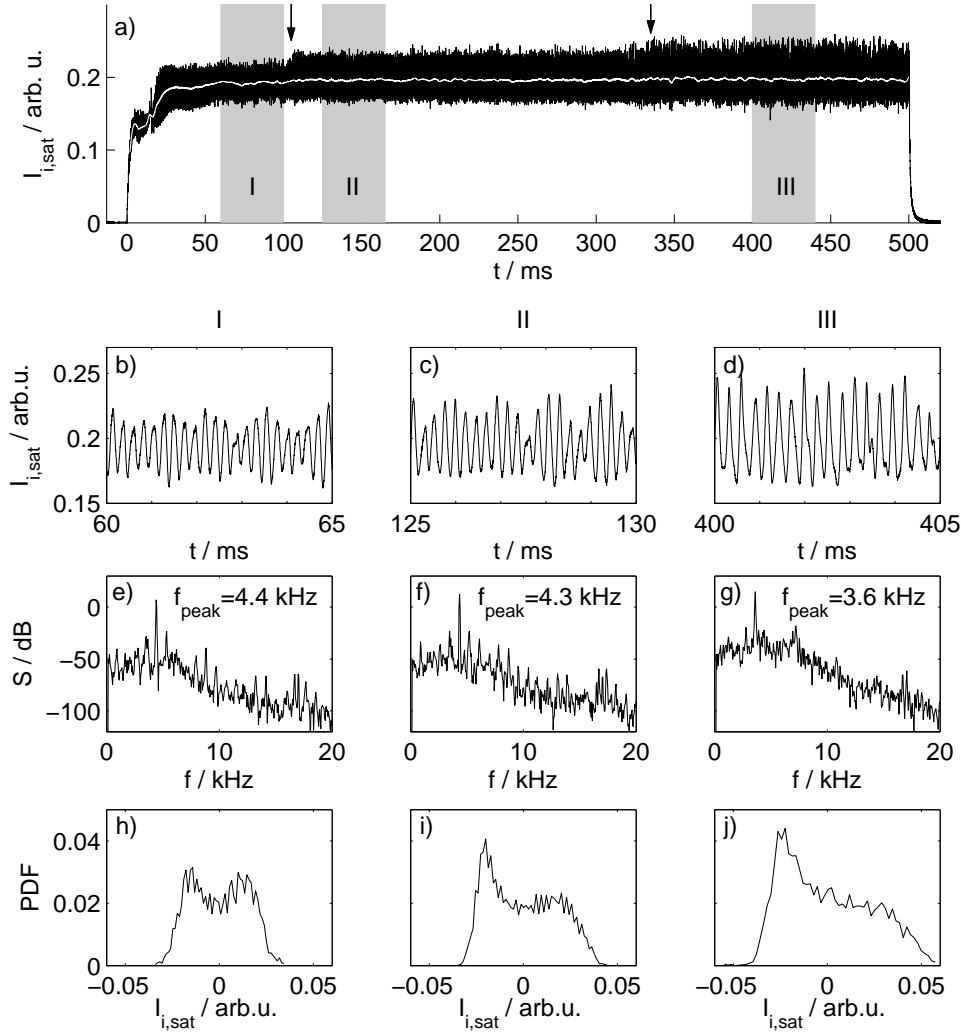


Figure 6.1: Time series for a 500 ms plasma pulse. a) time series of the entire pulse. The white line shows the moving average of the time series. The arrows indicate the points where the fluctuation dynamics obviously change while the gray boxes indicate the time windows for which the fluctuation dynamics are shown in more detail in the subplots b-j): b-d): 5 ms sample time series from the three indicated time windows. e-g): Power spectra for the three indicated time windows. h-j): PDF for the three indicated time windows. Discharge parameters: $B = 82$ mT, $p_{Ar} = 0.25$ Pa, $P_{RF} = 3.1$ kW.

dynamics within subsequent pulses are very similar (the same frequencies and mode numbers are observed) and sudden changes of the dynamics are found at nearly the same time instants. The cause of these sudden but reproducible changes of the fluctuation dynamics can only be speculated. The slow neutrals might play a role here. Consequently, for ensemble averaging, a certain time window out of the entire pulse is chosen where the fluctuation dynamics remain stationary. Usually, these time windows are chosen to be at least several tens of ms after the start of the pulse. For measurements with the probe array (where usually only time series of several 10 ms are recorded), care has been taken to choose a proper delay time for triggering. From simultaneous measurements with probes located at different axial and radial positions it has been found that the fluctua-

tion dynamics are global, which means that throughout the machine the features of the fluctuations are similar.

6.2 Localization of fluctuations

One of the most obvious characteristics of gradient driven instabilities is that the fluctuation degree peaks in the region of maximum gradient. For drift waves, a localization in the region of highest density gradients is expected. These are at radial positions $r = 25 - 35$ mm in the VINETA device.

In figure 6.2a) a radial profile of the mean ion saturation current is shown¹. Assuming $I_{i,sat} \propto n$ one finds that within 50 mm from the plasma center the density decreases to less

¹The mean values of ion saturation current as well as the fluctuating part of the ion saturation current are normalized to the peak value of the mean ion saturation current.

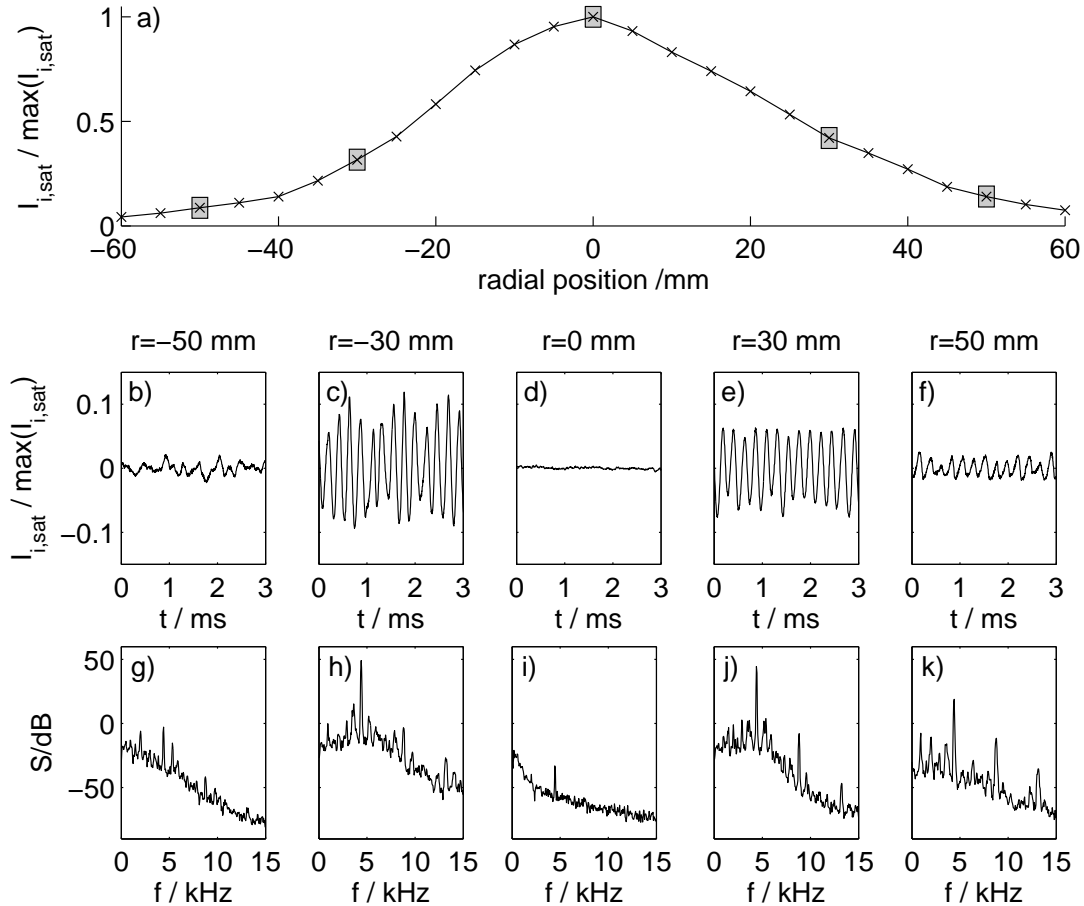


Figure 6.2: Radial localization of ion saturation current fluctuations. a) shows a time-averaged profile of the ion saturation current. For five marked radial positions, time series starting 200 ms after the start of the pulse (b-f), and power spectra (g-k) are given. The ion saturation current is normalized to the peak value in the center of the plasma column. Discharge parameters: $B = 82$ mT, $p_{Ar} = 0.25$ Pa, $P_{RF} = 3.1$ kW.

than 10% of the peak value. The profile is not completely symmetric and looks a little flatter for positive r . For five marked radial positions, time series and power spectra are shown in figures 6.2b-k). The positions are symmetric around the plasma center.

At the plasma far edge, at $r = \pm 50$ mm (figure 6.2b,f,g and k), the plasma is relatively quiet. Small fluctuations are observed with amplitudes of up to 3% of the peak density. At $r = +50$ mm, they have slightly higher amplitude than at $r = -50$ mm. Small peaks are found in the power spectrum, whereas the most pronounced peak is at 4.4 kHz, accompanied by higher harmonics of this frequency. In the gradient region $r = \pm 30$ mm, the observed fluctuations become large with amplitudes up to 10% of the peak density (figure 6.2c,e) which corresponds to 30% of the local plasma density. The corresponding power spectra in figure 6.2h,j) show a single pronounced, narrow peak at 4.4 kHz and higher harmonics. Besides the 4.4 kHz peak a number of smaller peaks are found, some of these are sidebands of the main peak. In the center of the plasma, no fluctuations are observed (figure 6.2d,i). The spectral power is much smaller, although a small peak at 4.4 kHz remains.

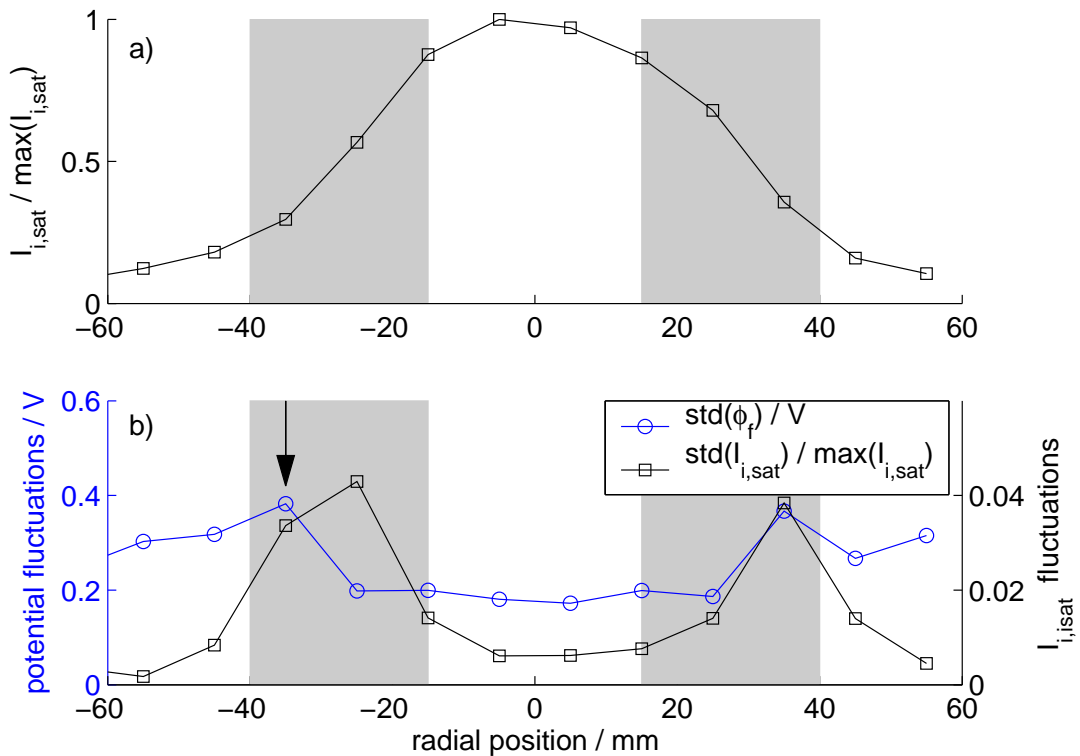


Figure 6.3: Localization of the observed fluctuations. a) Radial ion saturation profile normalized to its peak value. b) Radial profiles of the standard deviation (std) of ion saturation current fluctuations and floating potential fluctuations. Floating potential is measured in V, while ion saturation current fluctuations are normalized to the peak value of the background profile. The arrow indicates the position where the phase shift between ion saturation current fluctuations and floating potential fluctuations is measured (see section 6.3). Discharge parameters: $B = 78$ mT, $p_{Ar} = 0.25$ Pa, $P_{RF} = 3.1$ kW.

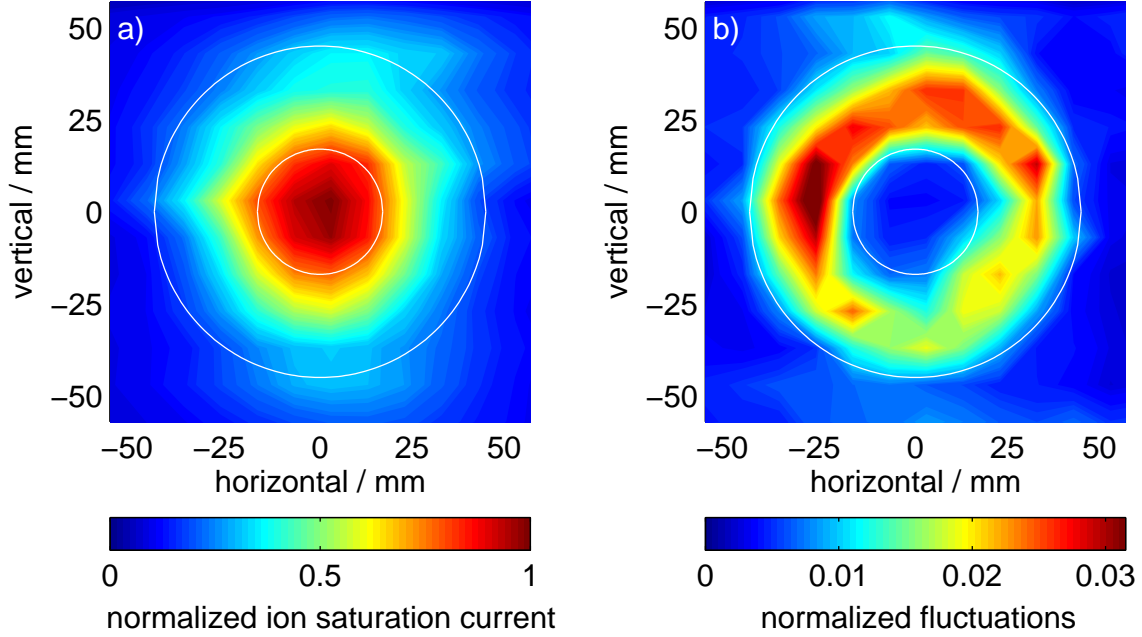


Figure 6.4: Localization of ion saturation current fluctuations in the poloidal plane: a) ion saturation current normalized to its peak value, b) standard deviation of ion saturation current normalized to the peak value of the time-averaged profile. The circles indicate the region where fluctuations are significant. Discharge parameters: $B = 67$ mT, $p_{Ar} = 0.45$ Pa, $P_{RF} = 2.5$ kW.

Figure 6.3b) shows radial profiles of standard deviations² of ion saturation current fluctuations and floating potential fluctuations for a coherent mode with a frequency of 3.5 kHz. For comparison, a profile of the mean ion saturation is given in figure 6.3a). Both density and potential fluctuations are found to have a maximum in a region between $r = 15$ mm and $r = 40$ mm, the region of steepest density gradients. In the center of the plasma column the fluctuations are much smaller. The potential fluctuations do not become much smaller at the edge of the plasma, density fluctuations decrease significantly towards the edge.

For the position indicated by the arrow one finds a density fluctuation level of $\tilde{n}/n \approx 0.13$. The electron temperature is estimated to be 2.5 eV (see figure 5.2)³ which leads to a potential fluctuation level of $\tilde{\phi}/T_{[eV]} \approx 0.15$. Thus, both fluctuation levels are equal. At $r = -25$ mm, where density fluctuations are highest but floating potential fluctuations are smaller, it is found that $\tilde{\phi}/T_{[eV]} \approx 1.8 \tilde{n}/n$. In conclusion, the relative fluctuation levels of density (\tilde{n}/n) and potential ($\tilde{\phi}/T_{[eV]}$) are of similar magnitude in the strong gradient regions.

Figure 6.4 shows color coded poloidal profiles of the mean ion saturation current and the standard deviation of ion saturation current fluctuations. They are measured by a single movable probe and averaged over a series of plasma pulses. The ion saturation current is normalized to its peak value. Time series were recorded with a spatial resolution

²Note that this differs from the amplitude of the fluctuations, e.g. for a purely sinusoidal signal the amplitude is by a factor of $\sqrt{2} \approx 1.4$ higher than the standard deviation.

³The measurement was conducted close to $z = 1500$ mm.

of 10 mm. This picture confirms that the fluctuations are localized within the density gradient region of the plasma. The white circles indicate the ring around the plasma center where the fluctuation degree is above $\sim 30\%$ of the maximum fluctuation degree. While the plasma density profile looks rather symmetric, the fluctuation profile is found to be slightly asymmetric. This is, however, mainly a measurement artefact. The probe is moved inwards from the left side of the diagram and extends far into the plasma for measurements at the right hand side of the picture which might disturb the plasma dynamics. Nevertheless, this does not explain the up-down asymmetry which has been observed during other measurements as well⁴. A possible explanation is that the plasma source does not produce a fully symmetric plasma. In reference [78], such asymmetries were reported for magnetic fluctuations.

6.3 Phase between density and potential fluctuations

For the observed instability, the spectral features of density and potential fluctuations are generally similar. From drift wave theory a small phase shift between density and potential fluctuations is expected. The density fluctuations should be ahead of the potential fluctuations (see chapter 2).

The average phase shift between ion saturation current fluctuations and floating potential fluctuations at one position is measured for a coherent mode. A pair of axially separated uncompensated Langmuir probes is used, which are arranged as shown in figure 4.13. Both probes are located at fixed positions in the region of strongest fluctuations. Probe #1 serves as a reference probe and records time series of the ion saturation current. With probe #2, located at $r = -35$ mm (see figure 6.3), time series of ion saturation current and floating potential are recorded successively. Time series of reference signal 1 and the floating potential were recorded simultaneously. Afterwards, simultaneous time series of reference signal 2 and of ion saturation current were recorded. The two reference signals are time shifted such that they have zero phase shift (see figure 6.5a). The time series of ion saturation current and of floating potential are accordingly time shifted. The result is depicted in figure 6.5b). We note here that the ion saturation current fluctuations are much more regular than the floating potential fluctuations. In figure 6.5b) it is clearly observed that a small average phase shift between fluctuations of the ion saturation current and the floating potential exists. The ion saturation fluctuations are ahead of the floating potential fluctuations. From the cross power spectrum figure 6.5c), a value of about $10^\circ = \pi/18$ is found for the phase shift. Repeated measurements for different plasma parameters yielded phase shifts of up to $35^\circ \approx \pi/5$ in the region of the strongest fluctuations. The phase shift dependency on the radial position was not investigated here.

⁴This asymmetry is also found independent of whether or not the horizontal probe positioning is installed inside the vacuum chamber.

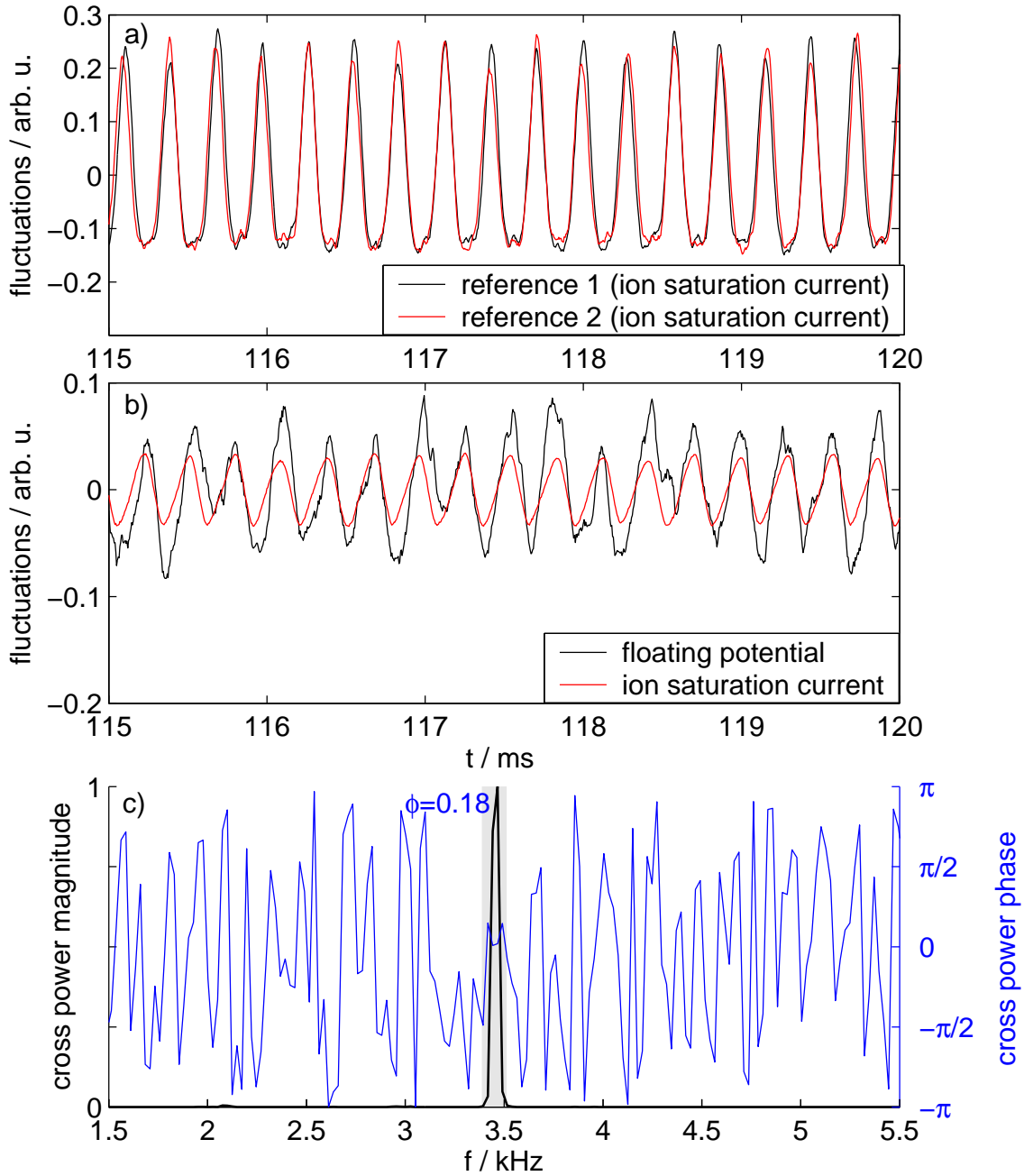


Figure 6.5: For an estimation of the phase shift between density and potential fluctuations, time series for ion saturation current fluctuations and floating potential fluctuations have been measured successively. a) Adjusted time series of the reference probe. b) Time series of ion saturation and potential fluctuations. The floating potential was measured simultaneously with reference signal 1, ion saturation with reference signal 2. Time series of reference signal 2 and ion saturation current are shifted in time in order to get zero phase shift between reference signals. c) Magnitude and phase of the cross power spectrum between the two adjusted time series. Discharge parameters: $B = 78$ mT, $p_{Ar} = 0.25$ Pa, $P_{RF} = 3.1$ kW.

6.4 Poloidal Mode structure

Drift waves propagate mainly in poloidal direction. The observation of the dynamics in the poloidal plane allows one to analyze mode numbers, propagation velocities, and also the mode structure itself. Two methods are used for measurements in the poloidal plane (see also chapter 4). With the poloidal 64 probe array, time series on one circle in the poloidal plane can be measured simultaneously which gives immediate access to mode numbers and phase velocities. A poloidal probe positioning system allows for subsequent measurements of time series in the entire poloidal plane. Statistical methods are used to reconstruct poloidal mode structures.

Figure 6.6 shows the results of measurements with the poloidal probe array COURONNE for three different dynamical states, obtained for different discharge conditions. In figure 6.6a), the space-time diagram for a single saturated $m = 6$ mode is plotted. Minima (blue) and maxima (red) of the ion saturation current form a regular stripe pattern. The probe signals are normalized to their standard deviation. A pronounced peak is found in the corresponding frequency-mode-number spectrum (figure 6.6b). The ‘sidebands’ are due to the limited number of points in the spatial direction (spectral leakage [117]). Figures 6.6c,d) show a state with a number of interacting modes. There is still a regularity in the stripe pattern but it is modulated and sometimes broken. The slope of the striations differs for different positions in space and time, indicating non-constant

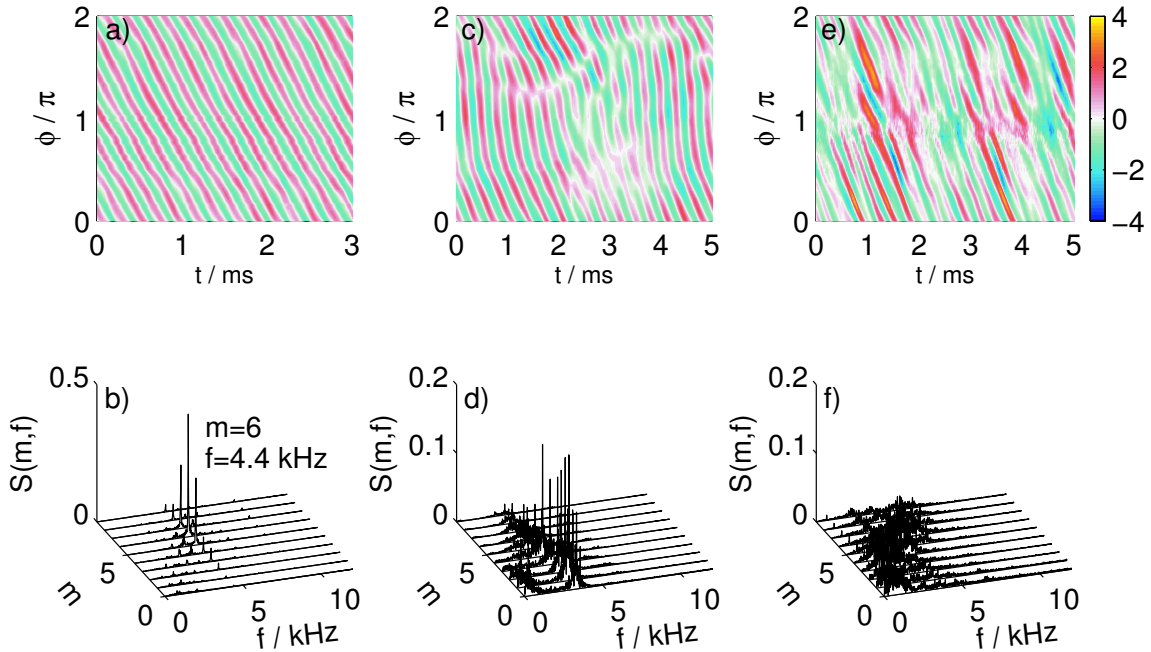


Figure 6.6: Spatiotemporal dynamics measured with the probe array COURONNE for three exemplary dynamical states. First row: color coded space-time diagrams. Second row: frequency-mode-number spectra (linear scale). a,b) saturated $m = 6$ mode. (Discharge parameters: $B = 82$ mT, $p_{Ar} = 0.25$ Pa, $P_{RF} = 3.1$ kW) c,d) state with interacting modes. (Discharge parameters: $B = 46$ mT, $p_{Ar} = 0.18$ Pa, $P_{RF} = 3.6$ kW) e,f) weakly turbulent state. (Discharge parameters: $B = 69$ mT, $p_{Ar} = 0.30$ Pa, $P_{RF} = 2.6$ kW)

poloidal propagation. Similar dynamics have been observed in other linear devices and were explained in terms of modulated monochromatic travelling waves [118]. The associated frequency-mode-number spectrum shows a number of broadened peaks for at least two different frequency ranges, around 4 kHz and below 1 kHz. In the third column (figures 6.6e,f), a weakly developed turbulent state is shown. The spatiotemporal plot reveals structures that are irregular and non-periodic in time. This means that large scale fluctuation structures dominate, propagating in the same direction as coherent modes, but with a certain velocity spread. Similar dynamics have been observed in other experiments [17,119]. In the frequency-mode-number spectrum, no pronounced peaks are found. Instead, the spectral power is scattered over a broad region in frequency and mode numbers.

From the space-time diagram the phase velocity of the wave can be estimated. For the $m = 6$ mode in figure 6.6a), a phase velocity of 180 m/s $\approx 0.1 v_{D,e}$ is found (see figures 5.3, 5.4 and 6.14). The propagation direction of the wave can also be easily deduced from these diagrams. It is always found that the observed instability propagates in the electron diamagnetic drift direction.

In figure 6.7, poloidal mode structures are shown. Cross correlations between time series of a fixed reference probe and a probe on the poloidal positioning system are shown in a color coded diagram for nine different time lags (see also section 4.2.2). For maximum cross-correlation (yellow regions), the time series of both probes are shifted against each other by the respective time lag. This means that here time series have coinciding maxima and minima. Accordingly, for positions with minimum cross correlation (blue regions), time series have coinciding maxima and minima as well. Note that in the cross correlation analysis only phase information is retained.

The two circles around the plasma center indicate the region of highest fluctuation levels (see figure 6.4). We note that also small fluctuations outside this region show a high correlation, especially in the left half of the plots. On both circles, a black bullet follows a maximum of the correlation function. There are five spiral arms on one circumference, indicating an $m = 5$ mode structure. This is confirmed by measurements with the poloidal probe array. There is a distortion at the right hand side of the plots which is probably an effect of the intrusive probe extending far into the plasma.

Striking is the spiral structure observed. The ‘arms’ of maximum and minimum cross correlation do not extend just radially outward, as one might naively expect. Instead, they are strongly bent clockwise. The same holds true for other modes with different mode numbers. In the following, these structures are referred to as sheared structures. In chapter 7 it is shown that also in the numerical solution of the linear dispersion relation similar sheared structures are found.

The comparison of the entire sequence of plots yields that for increasing time lag the structure rotates anti-clockwise until for a time lag of 320 ms the maxima and minima of the structure are found to be at the same positions as for zero time lag. This time corresponds well to the frequency peak at 3.1 kHz obtained from the time series. Since the bullets on both circles are rotated by 9° between each two subsequent plots, it is concluded that the sheared structure rotates rigidly. After 320 ms the arm of the structure has rotated by 72° which is $1/5$ of one full rotation, consistent with mode number $m = 5$.

Figure 6.7 contains no information about the amplitude of the fluctuations. A more real-

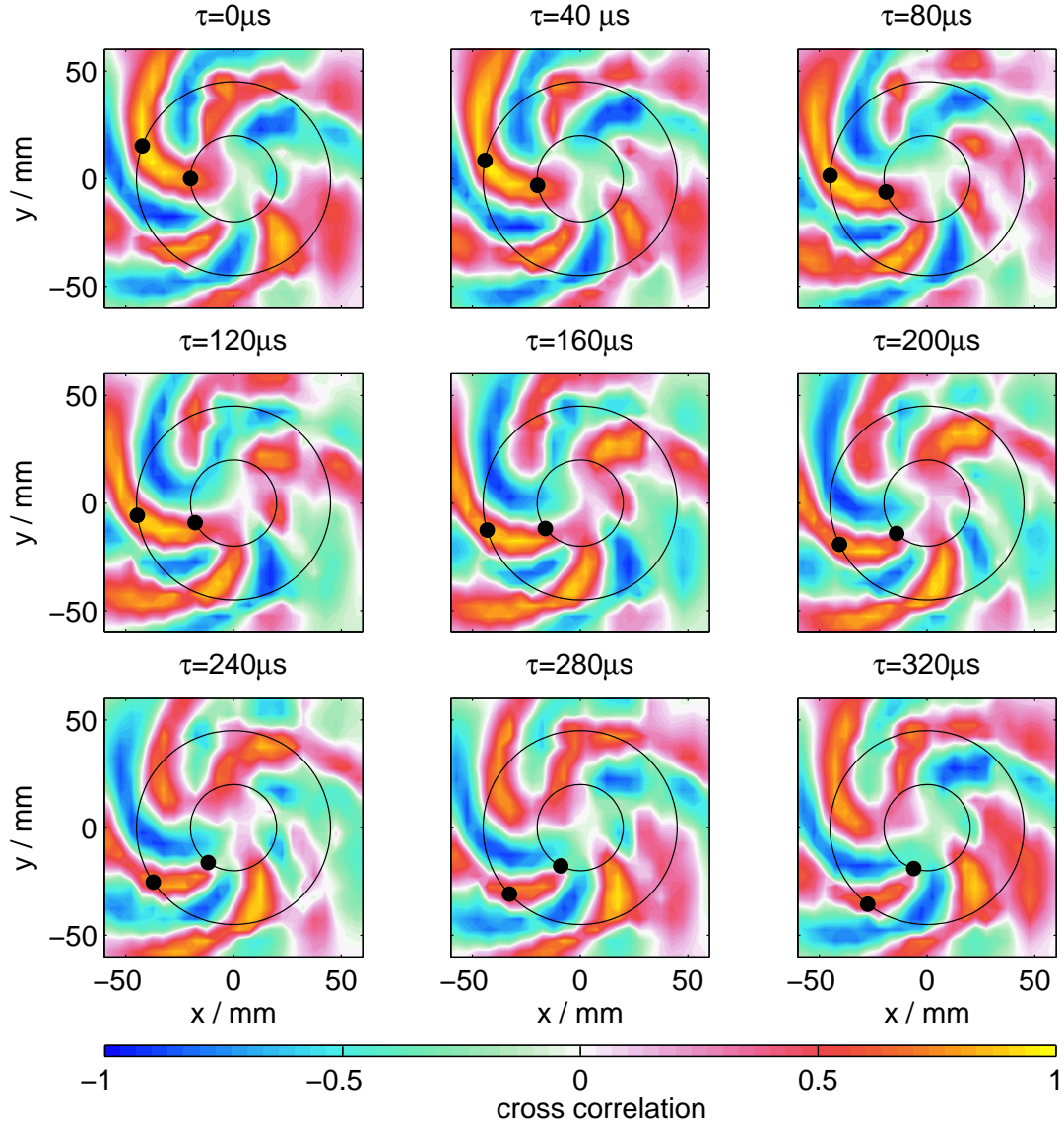


Figure 6.7: Poloidal mode structure reconstructed from the cross-correlation between two probes and different time lags. Time series were recorded with a spatial resolution of 5 mm. The two circles indicate the region where fluctuations are strongest as in figure 6.4. The black dots on both circles indicate one maximum of the correlation structure and are rotated by 9° between subsequent plots. Discharge parameters: $B = 65 \text{ mT}$, $p_{Ar} = 0.36 \text{ Pa}$, $P_{RF} = 2.8 \text{ kW}$.

istic picture of the actual poloidal mode structure can be obtained if the cross correlation is pointwise multiplied with the poloidal fluctuation profile. A fluctuation profile similar to the one in figure 6.4b) was measured. However, the asymmetry of the observed fluctuation profiles makes it difficult to distinguish between amplitude and phase information in the resulting profile. Therefore, only a radial fluctuation profile was considered and rotated in the poloidal plane to obtain a rotationally symmetric fluctuation profile. The result is shown in figure 6.8. The shear of the mode structure is still there but the arms do not extend anymore into the far plasma edge due to the small fluctuation amplitudes there. In the plasma center the mode structure vanishes for the same reason.

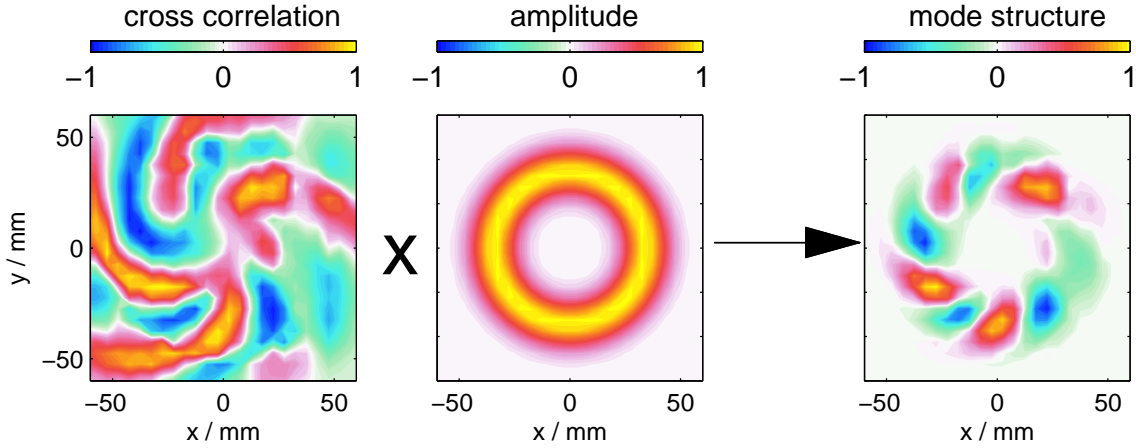


Figure 6.8: Poloidal mode amplitudes reconstructed from cross-correlation between two probes (see figure 6.7) and from a poloidally symmetric fluctuation profile (see figure 6.4).

6.5 Parallel Wavelength

Drift waves have a long but finite parallel wave length. This provides a non-ambiguous distinction to flute-like modes which have infinite parallel wavelength. The measurement of the parallel wavelength is thus important for the identification of drift waves. In the VINETA device the parallel wavelength of the observed instability has been measured as described in section 4.2.2. Two probes are axially aligned along the magnetic field and time series of both probes are measured simultaneously. Figure 6.9 shows a cross power spectrum between the signals of both probes for an $m = 6$ mode. The magnitude of the cross power is peaked at 4.4 kHz. The cross power phase spuriously fluctuates within the full $\pm\pi$ range at most frequencies, but the phase is constant around the frequency 4.4 kHz. From this, the phase shift between the two signals is found to be $23^\circ \pm 3^\circ = (0.064 \pm 0.008) \times 2\pi$. The distance between the two probes was (30 ± 0.5) cm. This yields an value of (4.7 ± 0.7) m for the parallel wavelength, which agrees very well with the device length (about 5 m between the grounded endplate and the end of the glass tube). For other measurements, the axial distance between the two probes was changed to (85 ± 2) cm. Similar results were obtained for both probe distances.

A number of measurements were carried out for modes with mode numbers $m = 4 - 6$. The obtained wavelengths are plotted in figure 6.10 with error bars. The wavelength values are not arbitrarily scattered but fall into two groups indicated by the gray bars: five measurements gave wavelengths between 4.3 m and 6.1 m, two were close to 11 m. In one single case, an unusually long wavelength of (30 ± 10) m was measured. From these measurements no clear relationship between the different wavelengths and the mode numbers and frequencies could be established. For the two cases where $\lambda_z \approx 11$ m was obtained, the frequencies were slightly lower (with a deviation of less than 15%) than for other modes with $\lambda_z \approx 5$ m, having the same mode number at similar experimental conditions. Given by the axial boundary conditions, one can expect that the parallel wavelength is determined by the machine length. Either one wavelength or half the wavelength fit well the device length. To conclude, the observed instability clearly has a

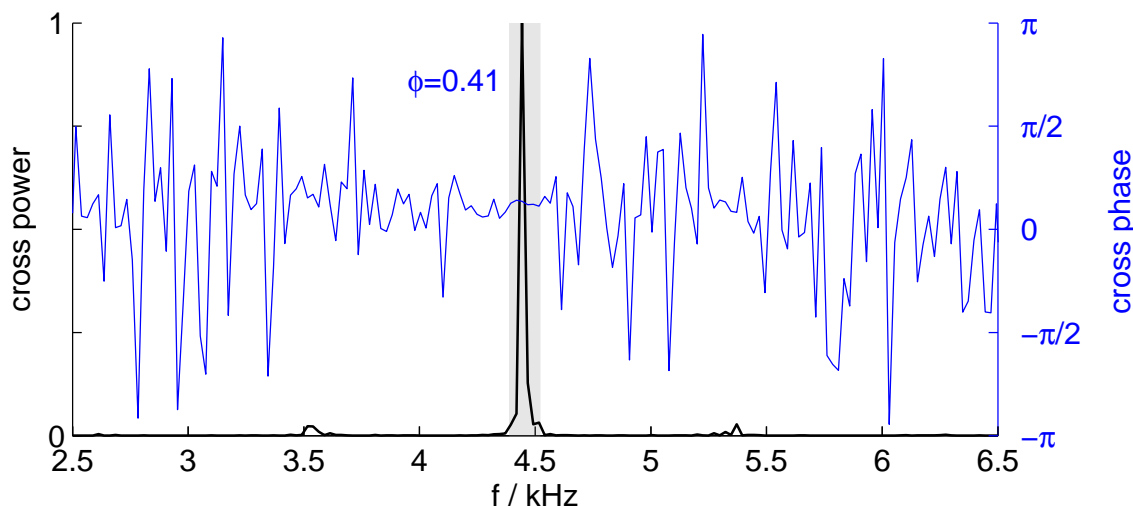


Figure 6.9: Cross power and cross phase of signals of two by 30 cm axially separated probes used for the measurements of the parallel wavelength. Discharge parameters: $B = 82 \text{ mT}$, $p_{Ar} = 0.25 \text{ Pa}$, $P_{RF} = 3.0 \text{ kW}$.

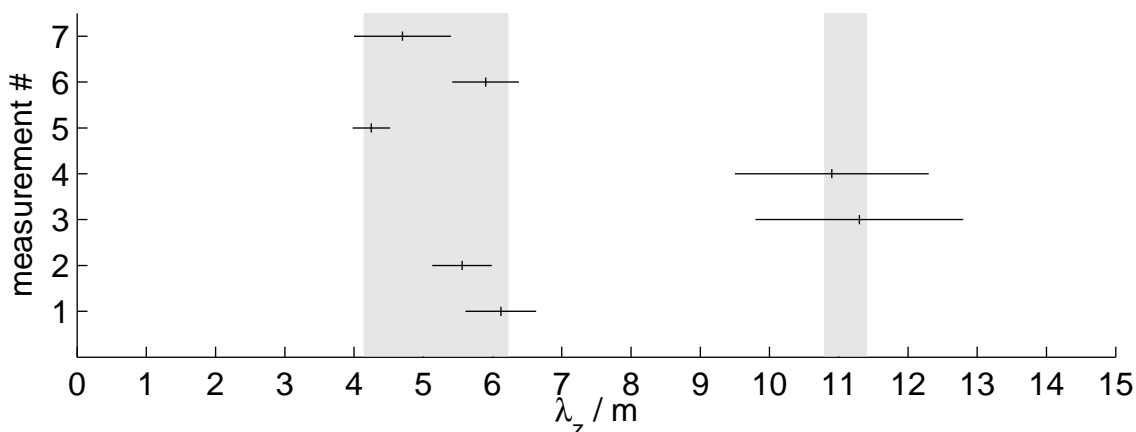


Figure 6.10: Result of the measurements of the parallel wavelength. The measured wavelength are plotted with error bars. The boxes indicate the grouping of the measured values.

finite parallel wavelength.

6.6 Dependency on magnetic field

There are two reasons for interest in the dependency of fluctuation dynamics on discharge parameters. On the one hand, it is useful to identify control parameters which allow for changing the fluctuation dynamics within certain limits. On the other hand, it gives some insight into mechanisms that influence the fluctuation dynamics.

Figures 6.11 and 6.12 show the change of the fluctuation dynamics due to variation of the ambient magnetic field. The probe array was used for measurement of the fluctuation

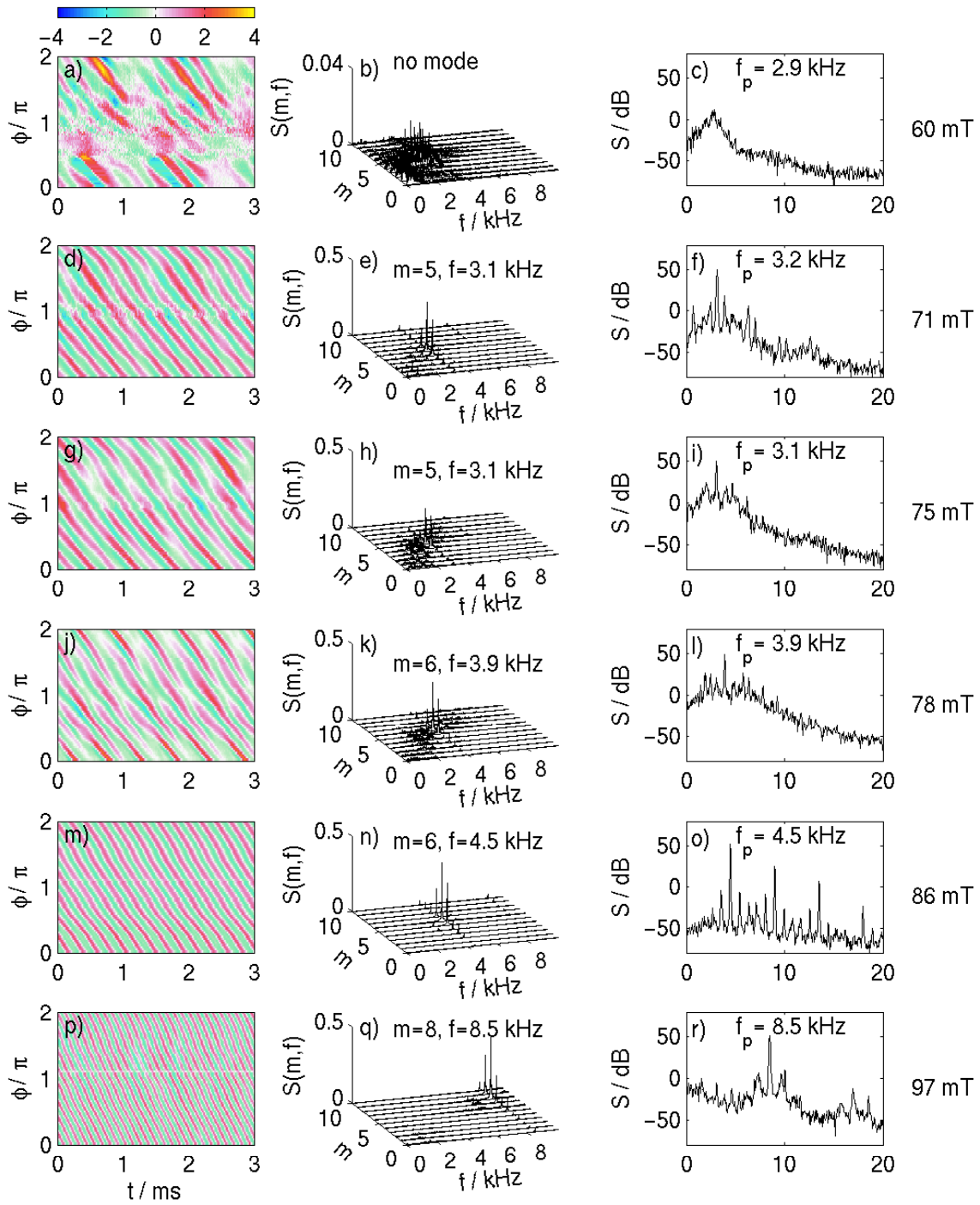


Figure 6.11: Dependency on magnetic field: Dynamics for six different values of the background magnetic field. The first column shows color coded space-time diagrams measured with the probe array. The second column shows frequency-mode-number spectra in linear scale while the third row shows a logarithmical power spectrum obtained from a time series of one probe of the probe array. Discharge parameters: $p_{Ar} = 0.35 \text{ Pa}$, $P_{RF} = 2.2 \text{ kW}$.

dynamics. For magnetic fields below ~ 50 mT the plasma is generally very quiescent. Figures 6.11a-c) show fluctuation dynamics for an ambient magnetic field of 60 mT. Fluctuations are noise-like at low fluctuation levels. The frequency-mode-number spectrum shows that the spectral power is scattered over a wide range of frequencies and mode numbers. Also, the (logarithmically plotted) frequency power spectrum of one single probe shows a broadband spectrum with significant power only in the low-frequency range up to 5 kHz.

For ambient magnetic field 71 mT, a totally different situation is found (figures 6.11d-f). The space-time diagram shows a regular stripe pattern, slightly bent and indicating an $m = 5$ mode. The frequency-mode-number spectrum confirms a dominant $m = 5$ mode at a frequency of 3.1 kHz. Beside this, a small peak is observed at $m = 1$ and $f \approx 0.7$ kHz, consistent with a small amplitude and phase modulation observed in figure 6.11d. This peak is also seen in the frequency spectrum and leads to modulation sidebands of the 3.2 kHz peak.

If the magnetic field is further increased to 75 mT, the fluctuations become more irregular as shown in figure 6.11g-i). The $m = 5$ mode is still present, but the phase fronts break occasionally. As above, also a spatiotemporal modulation is observed. The frequency-mode-number spectrum (figure 6.11h) still shows a peak at $m = 5$ with a corresponding frequency of 3.1 kHz but there is a broadband background, also seen in the frequency power spectrum 6.11i).

For a magnetic field of 78 mT, the situation has again changed, shown in figures 6.11j-l). It is similar to the case for 75 mT, except that now an $m = 6$ mode at 3.9 kHz is found to be the strongest mode, still embedded within a broad noise-like spectrum. A remaining small peak of the $m = 5$ mode is also observed.

If the magnetic field is further increased, the $m = 6$ mode becomes more and more dominant. In figures 6.11m-o), at $B = 86$ mT, one finds very regular fluctuation dynamics while the noisy background in the power spectra has nearly completely vanished. Besides the $m = 6$ mode at 4.5 kHz, there is also a smaller peak at $m = 5$ and frequency 3.5 kHz. The nonlinear interaction of these two modes leads to a picket fence of peaks in the frequency power spectrum figure 6.11o). Also the higher harmonics of the $m = 6$ mode are pronounced.

The last case, figures 6.11p-r), shows the fluctuation dynamics at 97 mT, close to the highest possible magnetic field in the VINETA device. Another mode has taken over, with mode number $m = 8$ and frequency 8.5 kHz. The fluctuations are very regular and the noise level is rather low. There are fewer sideband peaks than for 86 mT. The $m = 8$ mode is the mode with the highest mode number observed.

Figure 6.12 summarizes the evolution of the power spectrum with variation of the ambient magnetic field. The bars on top of the diagram indicate the dominating mode. The black bullets mark the peak values of the spectral power. It is found that the frequencies of the observed $m = 5$ and $m = 6$ modes increase with increasing magnetic field. Only at 75 mT, the frequency of the $m = 5$ mode decreases slightly which might be an effect of strong nonlinear interaction with other modes. After onset of the first mode, i.e. for $B \gtrsim 64$ mT, the fluctuation level remains relatively constant (the highest peaks in the power spectra are close to 50 dB).

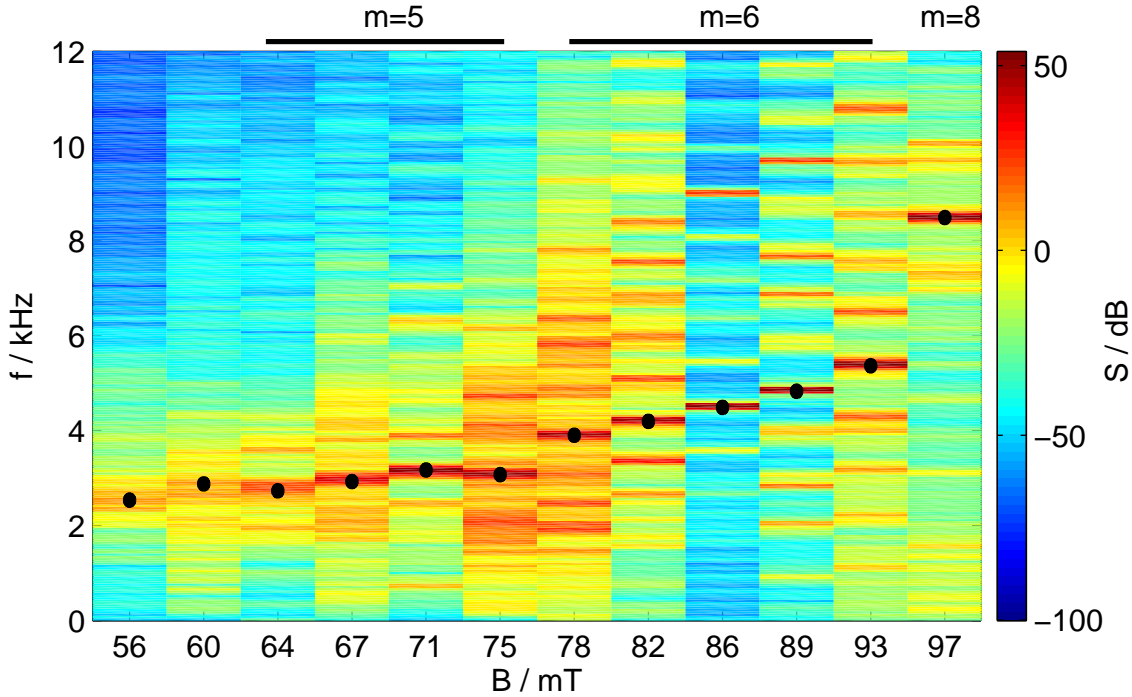


Figure 6.12: *Dependency on magnetic field: Color-coded power spectra for different magnetic fields. The bars atop the diagram indicate the dominating mode while the black dots indicate the maximum of each spectrum. The discharge parameters are identical to those of figure 6.11.*

Variation of the ambient magnetic field does not only change the fluctuation dynamics but also the mean plasma profiles. Figure 6.13 shows radial profiles of plasma density, ion saturation current, plasma potential and electron temperature for increasing magnetic field. The probe characteristics for a magnetic field above 60 mT could not be fully evaluated for the gradient regions of the plasma. Here, only ion saturation current profiles are shown.

From figure 6.13a,c) one finds that the plasma density increases with increasing magnetic field (see also figure 5.3). At the same time, the profiles become steeper. The plasma potential increases with increasing magnetic field. The electron temperature increases slightly with increasing magnetic field, but remains almost constant for magnetic fields above 56 mT.

For the three magnetic field values at which fluctuations are observed, drift velocities and frequencies are calculated and shown in figure 6.14. The measured ion saturation current profiles were fitted numerically to a Gaussian of the form $f(r) = a \cdot \exp(-r^2/b^2) + c$ (figure 6.14a). The potential profiles were fitted to $f(r) = a \cdot \exp(-|(r/b)^3|) + c$, shown in figure 6.14b). In the case of potential profiles, only those at 56 mT and 75 mT have been analyzed since for 93 mT too few points could be measured.

The results obtained are similar to previous ones shown in figure 5.3. The electron diamagnetic drift raises nearly linearly up to a radius of about 40 mm and then decreases (figure 6.14c). The curves for the three magnetic fields are relatively close to each other, having their maxima in the range $2200 \dots 2500 \text{ ms}^{-1}$. The $E \times B$ drift (figure 6.14d) has

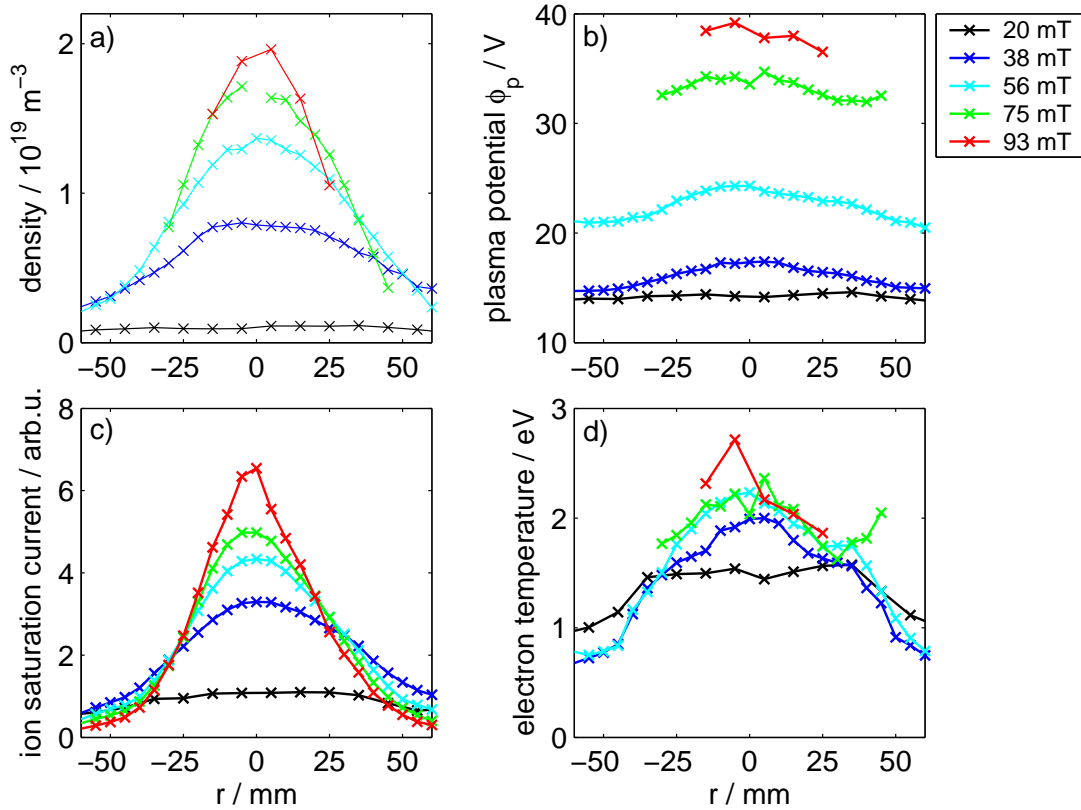


Figure 6.13: Dependency of time-averaged profiles on the magnetic field: a) plasma density, b) plasma potential c) ion saturation current, d) electron temperature. The discharge parameters are identical to those of figure 6.11.

a Maxwellian shape with maximum between $r = 25$ mm and $r = 30$ mm. At 56 mT the maximum velocity is about 2300 ms^{-1} , close to the value found for the electron diamagnetic drift. These two curves confirm the previous finding that the $E \times B$ drift decreases with increasing magnetic field (see figure 5.3d).

The frequency related to the electron diamagnetic drift velocity is shown in figure 6.14e). The three curves nearly coincide and frequencies in the range of 11 – 12 kHz are found in all three cases for radial positions $\lesssim 40$ mm. The profiles in figure 5.3 show a more sheared electron diamagnetic drift, which is either due to the electron temperature influence on the ion saturation current or due to uncertainties in the fit. It is concluded that the diamagnetic drift is nearly insensitive to changes of the magnetic field.

The $E \times B$ drift frequency is non-constant over the whole radius, with a maximum around $r = 20$ mm. The maximum frequency is again close to the electron diamagnetic drift frequency. The $E \times B$ drift frequency decreases with increasing magnetic field.

Considering the values for the electron diamagnetic drift frequency and the $E \times B$ drift frequency at ambient magnetic field 75 mT, it is found that the local slab model (2.28) yields mode frequencies several times higher than the observed frequencies. A local slab model is thus inconsistent with observation. For a better agreement, a cylindrical model has been applied (see chapter 7).

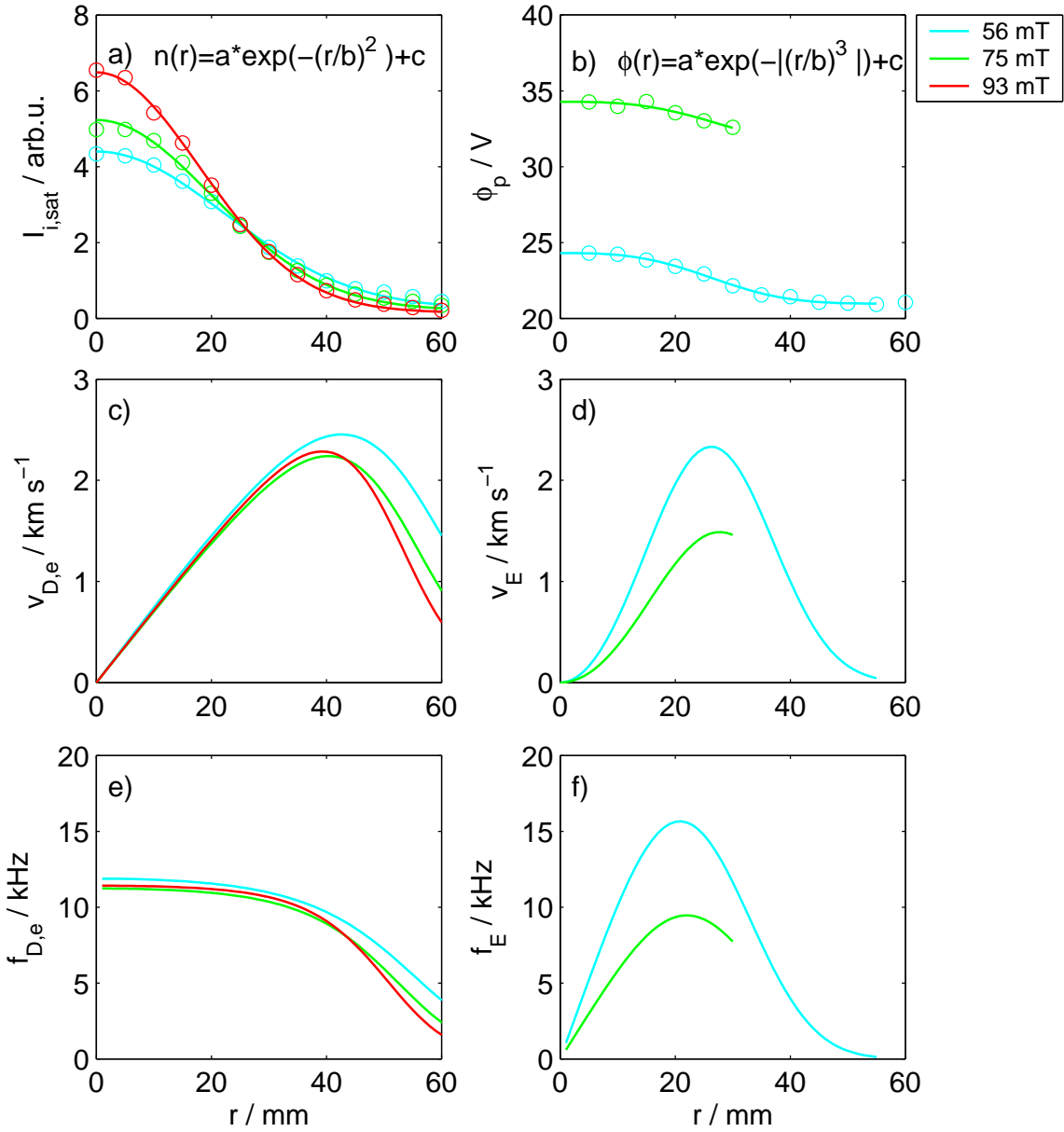


Figure 6.14: Dependency on the ambient magnetic field: From the ion saturation profile and the potential profile, absolute values of the poloidal drifts and corresponding frequencies are calculated. Note that electron diamagnetic drift and $E \times B$ drift are in opposite direction. a) ion saturation current profile, b) plasma potential profile, c) electron diamagnetic drift velocity, d) $E \times B$ drift velocity e) frequency connected with the electron diamagnetic drift for an $m = 1$ mode, f) frequency connected with the $E \times B$ drift. The discharge parameters are identical to those of figure 6.11.

6.7 Dependency on neutral gas pressure

A parameter scan for the neutral gas pressure was conducted. It is limited to pressures between 0.15 Pa and 0.7 Pa. For pressures lower than 0.15 Pa, no stable helicon mode could be established. For pressures above 0.7 Pa the fluctuations become too small. The

magnetic field was maintained at 67 mT and the RF power was 2.8 kW in pulsed operation. An uncompensated probe is used for measurement of the fluctuation dynamics and of radial ion saturation current profiles.

Figures 6.15 and 6.16 show the fluctuation dynamics for six different neutral gas pressures p , ranging between 0.16 Pa and 0.66 Pa. Both figures are organized in the same manner as figures 6.11 and 6.12, respectively.

At $p = 0.16$ Pa (figure 6.15a-c), irregular behavior is observed. The space-time diagram is dominated by mode-type patterns, which are, however, modulated in space and time and frequently interrupted by phase defects. The average phase velocity is higher than in the cases of increased pressure. In the frequency-mode number spectrum, one broadened peak around $m = 2$ and 4.1 kHz is found, embedded in a rather broadband background. The frequency power spectrum figure 6.15c) also reveals the broadened peak around 4.1 kHz. This frequency is remarkably high for an $m = 2$ mode, consistent with the observed high phase velocity. Consequently, due to the extended frequency range, the power in the broadband spectrum drops more slowly than in previous cases.

At $p = 0.21$ Pa the dominant feature is an $m = 4$ mode with a frequency of 1.8 kHz as shown in figure 6.15d-f). The spatiotemporal diagram shows a fairly regular stripe pattern with significant transient changes in frequency and mode number as well as amplitude variations. This is also seen in the power spectra which shows a sharp peak at 1.9 kHz, corresponding to a mode number $m = 4$, embedded within a broadband background in which other, smaller spectral peaks are also found. For instance, the smaller peak at $f = 2.4$ kHz in figure 6.15f) belongs to a different mode number $m = 5$.

If the pressure is increased to $p = 0.31$ Pa, weakly developed turbulence establishes with relatively irregular dynamics (figure 6.15g-i). Mode-type stripe patterns are still seen in figure 6.15g) but only within small intervals. In the spectra, figure 6.15h,i), two broadened peaks are at frequencies 2.1 kHz and 3 kHz, associated with mode numbers $m = 4$ and $m = 5$, respectively. The broadband fluctuation power is still very high.

The dynamical behavior changes completely at pressure $p = 0.41$ Pa, as shown in figure 6.15j-l). An $m = 5$ mode clearly dominates the fluctuation dynamics. The space-time pattern in figure 6.15j) is strictly periodic, although some modulation is still present. Both spectra show a sharp peak at $f = 2.8$ kHz with a small broadband background.

A further increase of the pressure to $p = 0.51$ Pa leads again to a change of the fluctuation dynamics. The space-time diagram is rather irregular without much periodicity between the striations. Two broadened peaks arise in the spectra, corresponding to an $m = 4$ mode at $f=1.6$ kHz and $m = 5$ at $f=2.5$ kHz. The broadband power level is much higher than above.

At $p = 0.61$ Pa, the $m = 5$ mode has again taken over and is now found at 2.2 kHz as shown in figure 6.15p-r). Again, there is a number of other, smaller peaks, especially one at 1.3 kHz corresponding to $m = 4$. The amplitude of the fluctuations is so small that some probes of the probe array hardly detect any fluctuations.

An overview of the fluctuation dynamics is given in figure 6.16, showing color-coded power spectra at pressures between 0.16 Pa and 0.66 Pa in steps of 0.05 Pa. The black bars on top of the diagram indicate the dominating mode number, and the black bullets mark the highest peak of each spectrum. The decrease of the frequency of the $m = 5$ mode

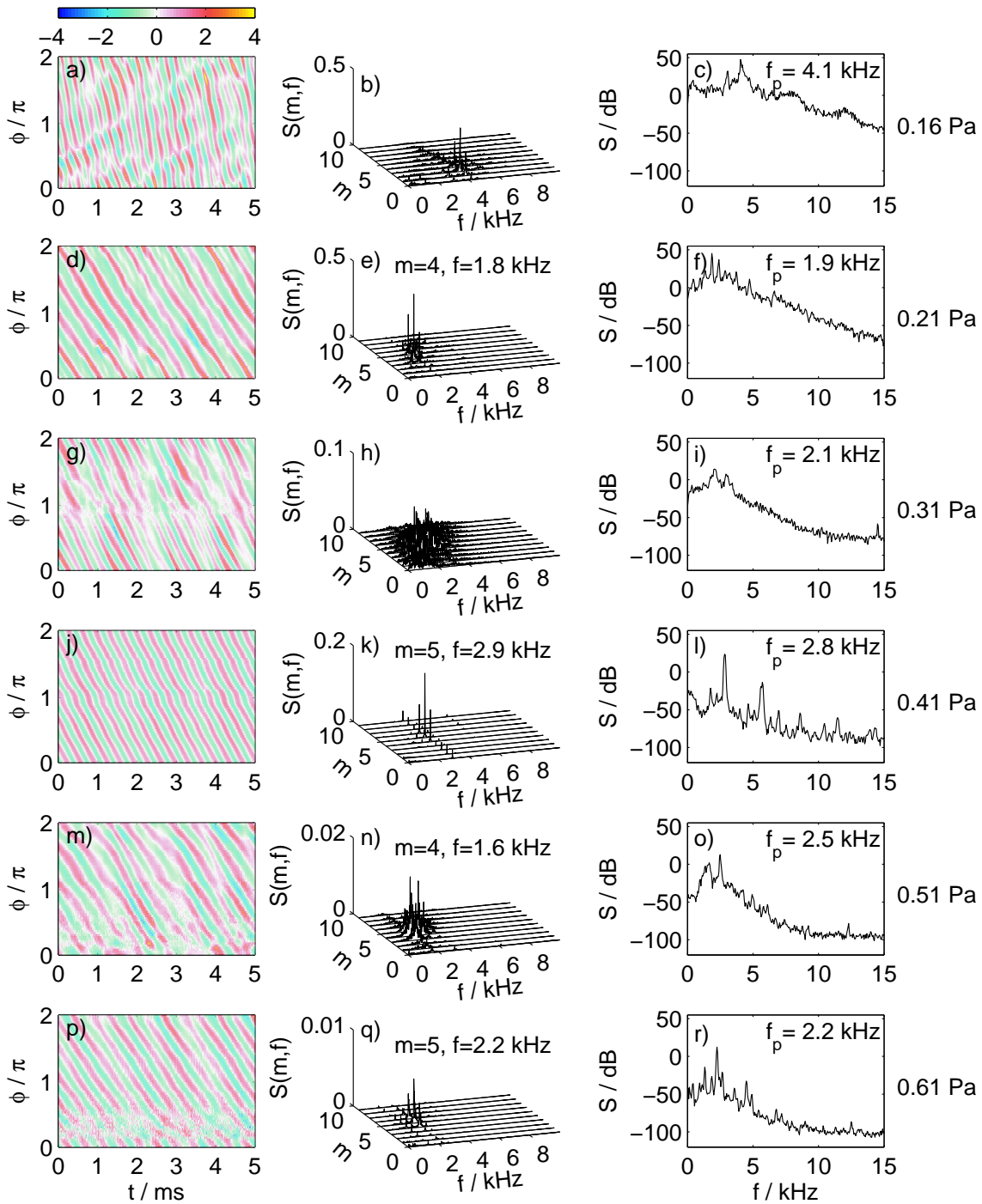


Figure 6.15: Dependency of the dynamics on neutral gas pressure: The first column shows color coded space-time diagrams measured with the probe array. The second column shows frequency-mode-number spectra in linear scaling. The third row shows a logarithmical power spectrum obtained from a time series of one probe of the probe array. Note the different scaling of the frequency-mode-number spectrum indicating the change of the fluctuation amplitude. Discharge parameters: $B = 67$ mT, $P_{RF} = 2.8$ kW.

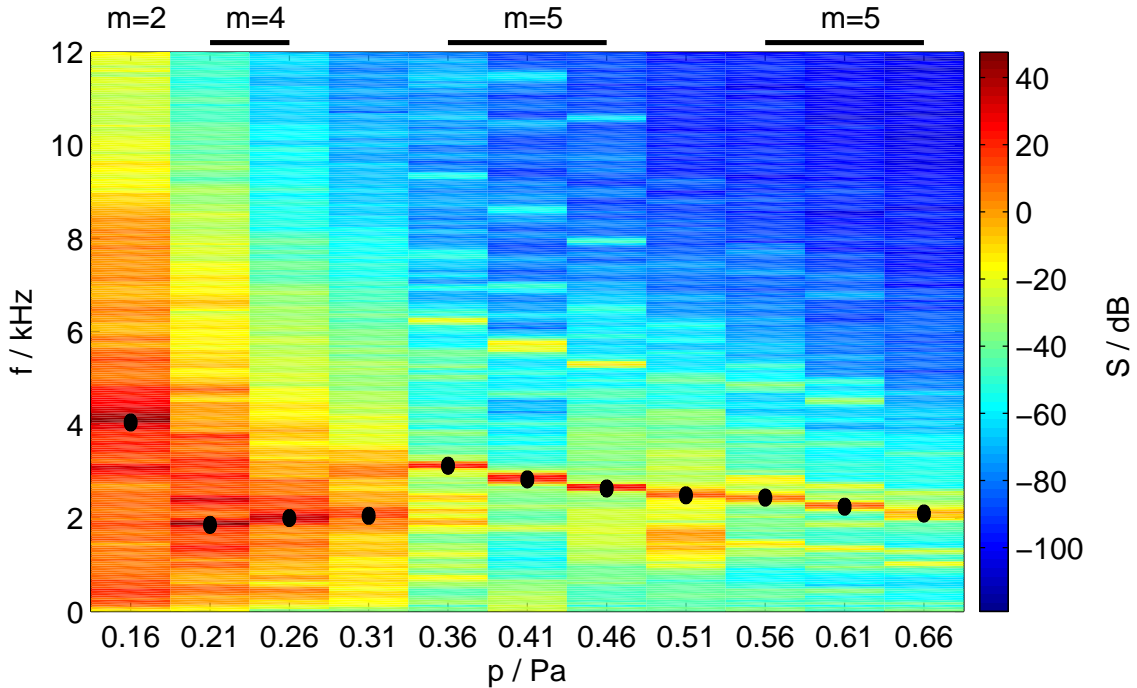


Figure 6.16: *Dependency on neutral gas pressure: Color-coded power spectra for different pressures. The bars atop the diagram indicate the dominating mode while the black dots indicate the maximum of each spectrum.*

with increasing pressure becomes evident. Also the $m = 4$ mode has the same tendency at higher pressures, whereas for pressures between 0.21 Pa and 0.31 Pa the frequency increases a little. However, the $m = 4$ mode is always embedded into a broadband turbulent background such that nonlinear interaction with other modes might dominate the dynamical processes.

In figure 6.17, radial profiles of the mean ion saturation current are shown together with the respective radial fluctuation profiles. Both, the ion saturation current as well as its fluctuations, are normalized to the peak value of the ion saturation profile for 0.61 Pa. Figure 6.17a) demonstrates that the ion saturation current, and thereby the plasma density and/or the electron temperature, increases with increasing neutral gas pressure. At $p \geq 0.41$ Pa the central peak value (at $r = 0$) remains constant and only small deviations in the gradient regions are found. The maximum gradient increases by a factor of 1.4 between $p = 0.16$ Pa and $p = 0.61$ Pa.

Figure 6.17b) shows that the fluctuation level changes rather dramatically. For the lowest pressure of 0.16 Pa, the standard deviation of the fluctuations is about 7.5 % of the peak value and 11 % of the local value of the ion saturation current. As reasoned above, at $p = 0.16$ Pa the fluctuation behavior is different from the other cases. The shape of the fluctuation profile is similar but the fluctuation level is significantly higher and the fluctuations do not vanish in the plasma center. The fluctuation maximum occurs at $r = 20$ mm for $p = 0.16$ Pa and slightly shifts outwards to $r = 25 - 30$ mm for higher pressures. For $p = 0.61$ Pa, the fluctuation level is only 0.5 % in comparison to 11 % for $p = 0.16$ Pa. The mean fluctuation level thus changes by a factor of more than 20 within

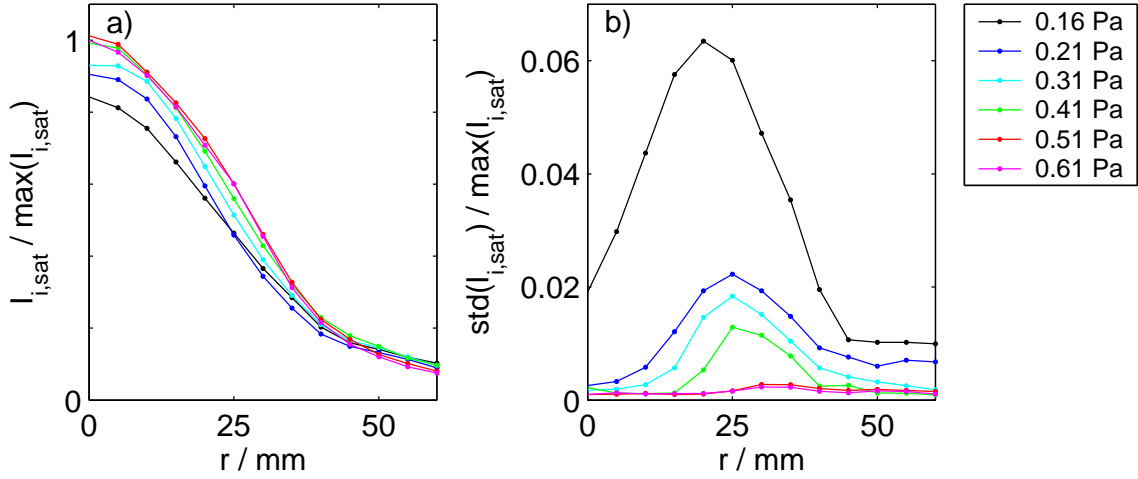


Figure 6.17: *Dependency on neutral gas pressure: Radial profiles of ion saturation current and fluctuations of ion saturation current. Ion saturation and its fluctuations are normalized to the peak value for 0.61 Pa.*

the pressure variation considered. For the pressure range $p = 0.21 - 0.61$ Pa, it decreases by a factor of 7.

6.8 Discussion

The experiments reveal that in the helicon discharge mode of the VINETA device an instability with frequencies well below the ion cyclotron frequency occurs within certain parameter regimes. The experimental findings can be summarized as follows:

- Fluctuations with frequencies in the range $0.7 - 9$ kHz (i.e. well below the ion cyclotron frequency $f_{ci} \gtrsim 15$ kHz) and poloidal mode numbers $m = 1 - 8$ have been observed. Modes with mode numbers $m = 4 - 6$ are found more often than modes with lower m . A variety of dynamical behavior occurs, ranging from single saturated modes to interacting modes and weakly developed turbulence.
- The fluctuations are localized in the density gradient regions of the plasma and nearly vanish in the plasma center.
- \tilde{n}/n and $\tilde{\phi}/T_{[eV]}$ are of similar magnitude. Maximum fluctuation levels are $\tilde{n}/n \approx \tilde{\phi}/T_{[eV]} \approx 30\%$.
- For saturated coherent modes, a phase shift $\angle(\tilde{n}, \tilde{\phi}) \approx 10^\circ - 35^\circ$ between density and potential fluctuations has been measured in the region of highest gradients. The density fluctuations are always ahead of the potential fluctuations.
- Both, single-mode waves as well as large scale turbulent structures, propagate in the direction of the electron diamagnetic velocity.
- The axial wavelength is finite and values close to $1 - 2 \times$ (device length) are observed.

- The plasma is quiescent below $B \approx 50$ mT (weakly dependent on other discharge parameters). The mode frequency increases with increasing magnetic field. Above onset of the fluctuations, the fluctuation level remains relatively constant.
- The mode frequency decreases with increasing neutral gas pressure. The fluctuation levels are highest for lowest possible neutral gas pressures. The plasma fluctuations are small for neutral gas pressures above 0.6 Pa.
- The poloidal mode structures show a spiral shape but rotate rigidly.

Identification of the instability

A low-frequency instability is observed in the helicon plasma of the VINETA device. The Kelvin-Helmholtz instability, the flute instability, and the drift instability have a number of features in common (see chapter 2) and must be taken into careful consideration. In particular, plasma density and plasma potential gradient regions coincide, and thus all these instabilities could occur. Due to similar electron diamagnetic drift and $E \times B$ drift velocity, the frequency ranges are also similar. The clearest distinction between the drift instability and the two other instabilities is the parallel electron dynamics which results in a finite parallel wavelength for drift waves. In contrast, for both the Kelvin-Helmholtz instability and the flute instability, the parallel wavelengths are infinite. It was previously shown that the parallel wavelength of the observed instability is close to once or twice the machine length. Also, the phase shift 10° - 35° between density and potential fluctuations is consistent with drift waves. For the Kelvin-Helmholtz and flute instabilities it must be $> 45^\circ$. Finally, the fluctuation levels of normalized plasma density and plasma potential are similar whereas for both, Kelvin-Helmholtz and flute instability, higher potential fluctuations are expected [60]. In conclusion, the experiments show that the observations are consistent with the drift instability, but not with the Kelvin-Helmholtz and the flute instability.

Variation of the fluctuation dynamics with external parameters

In contrast to other experiments [46,54], no clear-cut transition scenario from single modes towards turbulence was observed. If the ambient magnetic field is increased, the dynamical states just alternate and the most turbulent state was found at medium magnetic field, whereas at the highest accessible magnetic field, the dynamics is quite coherent. For a variation of the neutral gas pressure, a similar behavior is observed. Also here, weakly turbulent states just alternate with relatively coherent modes.

A higher magnetic field tends to result in modes with higher mode numbers m . In particular, the mode frequency increases with increasing magnetic field. At first glance, this seems to be contradictory since the drift wave frequency scales as $\omega^* \propto 1/B$. It was found, however, that in the VINETA device ω^* is nearly independent of B whereas the $E \times B$ rotation frequency ω_E decreases with increasing magnetic field. Thus, the observed increase of frequency with increasing B can be explained by the decreasing Doppler shift.

The mode frequency decreases with increasing neutral gas pressure. The diamagnetic electron drift frequency ω^* turned out to be nearly independent of the neutral gas pressure

as well, whereas the peak value of ω_E increases with pressure. Constant ω^* combined with increasing ω_E yields a decrease of the mode frequency. Again, the Doppler shift due to the $E \times B$ drift can be made responsible for the frequency variation.

Poloidal mode structure

The poloidal mode structure of saturated drift modes has been reconstructed using a cross correlation technique. Experimental as well as numerical results on the poloidal mode structure of drift waves have rarely been discussed for linear devices. Usually, only radial amplitude profiles are shown and poloidal symmetry is assumed. One exception is reference [119] where GRULKE and coworkers show a symmetric mode structure of an $m = 2$ mode, experimentally obtained with the conditional averaging technique [120]. In the VINETA device, poloidal mode structures always turned out to show a clear bending in the maxima and minima of the mode. The question arises whether this is an artefact due to the time averaging of the correlation technique used. The measured maximum and minimum correlation coefficients are, however, quite close to ± 1 which indicates a high phase coherence between the signals. If, for instance, the frequencies of both simultaneously recorded signals would slightly differ or if in one of the time series the frequency would slightly change in time (corresponding to a non-constant phase velocity), the maximum cross correlation would be well below 0.5. Therefore, it is concluded that the actual mode structures in the experiment are correctly reconstructed, i.e. they are indeed sheared. The question is why mode structures appear to be sheared. A possible, rather straightforward explanation is that the sheared $E \times B$ drift distorts poloidal structures. However, this would also limit the lifetime of the coherent mode structures which must be observable as frequency or sudden phase shifts. Neither have been observed in time series and, as reasoned above, this would also result in values of the cross correlation function well below the obtained ones. In addition, the structure rotates like a rigid body, i.e. with a constant angular velocity, which is also incompatible with velocity shear.

As already mentioned, numerical calculations for drift wave dispersion have been conducted and are presented in the next chapter. These calculations also allow for investigation of the poloidal mode structures for both, density and plasma potential. Thus, besides frequencies and growth rates, features of poloidal mode structures are studied as well.

Large time scale behavior

Constant density is reached in the VINETA device several 10 ms after switching on the RF power. This time is longer than in other helicon devices. For instance, in the HE-L device [111] short pulses of 2–8 ms are sufficient to reach stable conditions. The reason for this discrepancy might be the comparatively large plasma chamber of the VINETA device in which the plasma column extends only to a radius of about 30 mm while the chamber has a radius of 200 mm. Thus, the volume occupied by the plasma itself is quite small so that the dynamics of the neutrals could play a much bigger role than in other devices where the plasma fills nearly the entire vacuum chamber. The neutrals have the lowest thermal velocities of all involved particle species. For neutral temperatures between 300 K and 1000 K, the thermal velocity is 250 – 450 ms^{-1} . At these velocities, the device

length of about 5 m is travelled within 10-20 ms, which is close to the time needed to reach constant discharge conditions.

It was shown that the fluctuation dynamics may change within one plasma pulse to remain constant for several 10 ms to several 100 ms. Simultaneously, the mean plasma density remains constant over most of the pulse length. The reasons for this behavior can only be speculated: Neutrals travel the VINETA device on a time scale of several 10 ms. The plasma production by ionization of neutrals and the gas feed are spatially separated by about 5 m. Thus, neutral flows are a candidate for the change of the plasma dynamics by neutral depletion effects.

Chapter 7

Numerical solution of the drift wave dispersion relation

A local slab model yields mode frequencies several times higher than those observed and is thus inconsistent with the observations. For a better comparison between experiment and model, the drift wave dispersion relation must be solved in cylindrical geometry for experimental parameters. As reasoned in chapter 2, this is not an easy task. The linear 2nd order differential equation in cylindrical coordinates has a complex structure and depends on a number of physical quantities. For the present work, a newly developed code, which is referred to as the Risø code¹ in the following, was used to numerically solve the drift wave dispersion relation in cylindrical geometry. The model is similar to the one developed by ELLIS, MARDEN-MARSHALL and coworkers [9] but there, the collision frequencies were assumed to be radially constant. This is clearly not the case in VINETA, owing to the dominating Coulomb collisions that are proportional to the plasma density. The goal of the Risø code is to allow for arbitrary radial profiles for density, plasma potential, and the collision frequencies ν_{ei} , ν_{en} , and ν_{in} .

The following section 7.1 describes briefly the numerical code with emphasis on input and output parameters. In section 7.2, computational results are benchmarked to previously obtained ones based on the model of ELLIS, MARDEN-MARSHALL and coworkers. In section 7.3, computations for VINETA parameters are presented and compared with experimental findings. The main questions to be answered by the code are:

- What is the main destabilizing mechanism in the VINETA device?
- Are the experimentally observed frequencies in agreement with model predictions?
- What is the explanation for the sheared mode structures found in the experiment?

¹The model as well as the code have been developed by V. NAULIN from the Risø National Laboratory, Roskilde, Denmark.

7.1 The numerical model

In chapter 2, a second order ordinary differential equation for the dispersion of drift waves in a cylindrical plasma was given:

$$\partial_{rr}\phi + \left(\frac{1}{r} - \kappa(r) + RD(r)\right) \partial_r\phi + \left(Q(r) - \frac{m^2}{r^2}\right) \phi = 0 \quad (7.1)$$

where

$$RD(r) := i \frac{1}{\tilde{\omega} + i\nu_{in}} \left(\frac{\omega^* + iP}{\tilde{\omega} - \omega_1 + iP} \right) \nu_{in} r V_p$$

and

$$Q(r) := \frac{1}{\tilde{\omega} + i\nu_{in}} \left[\omega^* + \frac{m}{r} S_p - \tilde{\omega} \frac{\omega^* + iP}{\tilde{\omega} - \omega_1 + iP} \right] .$$

Most of the parameters are a function of radius ($\nu_{\alpha\beta}$, P , κ , V_p , S_p , ω^* and $\tilde{\omega}$). For the numerical solution, the differential equation is reduced to coupled differential equations by introducing

$$y_1 = \phi \quad , \quad y_2 = r y_1' \quad \text{and} \quad K(r) = \kappa(r) - RD(r) \quad (7.2)$$

where the prime ' denotes the partial derivative with respect to r . The system of coupled 1st order ordinary differential equations reads to be

$$\begin{pmatrix} y_1 \\ y_2 \end{pmatrix}' = \frac{1}{r} \begin{pmatrix} 0 & 1 \\ m^2 & 0 \end{pmatrix} \begin{pmatrix} y_1 \\ y_2 \end{pmatrix} + \begin{pmatrix} 0 \\ K(r) y_2 - r Q(r) y_1 \end{pmatrix} \quad (7.3)$$

where $\omega_1, \nu_{\alpha\beta}, \kappa$ and m are real numbers. Splitting (7.3) into real and imaginary parts (denoted by the subscripts R and I , respectively) finally yields

$$\begin{pmatrix} y_{1,R} \\ y_{1,I} \\ y_{2,R} \\ y_{2,I} \end{pmatrix}' = \frac{1}{r} \begin{pmatrix} 0 & 0 & 1 & 0 \\ 0 & 0 & 0 & 1 \\ m^2 & 0 & 0 & 0 \\ 0 & m^2 & 0 & 0 \end{pmatrix} \begin{pmatrix} y_{1,R} \\ y_{1,I} \\ y_{2,R} \\ y_{2,I} \end{pmatrix} \quad (7.4)$$

$$+ \begin{pmatrix} 0 \\ 0 \\ K_R y_{2,R} - K_I y_{2,I} - r Q_R y_{1,R} + r Q_I y_{1,I} \\ K_R y_{2,I} + K_I y_{2,R} - r Q_R y_{1,I} - r Q_I y_{1,R} \end{pmatrix} .$$

Solutions of eigenvalue problem (7.4), satisfying given boundary conditions, exist only for particular complex eigenvalues $\omega = \omega_R + i\omega_I$, that must be found together with the complex eigenfunction $\psi(r) = \psi_R(r) + i\psi_I(r)$. This class of equations is solved numerically by using iterative 'shooting' methods. The RUNGE-KUTTA method is used to solve the ODE system [117,121]. The solution of (7.1) is further complicated by the fact that at $r = 0$ a singularity occurs, owing to the diverging $1/r$ and $1/r^2$ terms. The equation is solved for the radial range $r \geq \epsilon$, where ϵ is a small number close to zero. In the course of the shooting method, an eigenvalue is guessed and the set of ODEs is solved, integrating from $r = \epsilon$ to $r = a$ where a is the 'plasma edge'. The boundary conditions

$$\psi(r = \epsilon) = 0 \quad \text{and} \quad \psi(r = a) = 0 \quad (7.5)$$

are used. If the solution does not satisfy the boundary conditions, the eigenvalue is changed and the equation is integrated again. This procedure is repeated until a complex eigenvalue ω and a function $\psi(r)$ are found, satisfying the differential equations with the boundary conditions to within a predefined error.

The radial positions ϵ and a are parameters of the code. The plasma edge is not sharply defined and therefore, the choice of a has an arbitrary component. In reference [9], $a^2/r_0^2 = 1.76$ was chosen for a Gaussian density profile $n(r) = n_0 \exp(-r^2/r_0^2)$. For this value of a , the density at the plasma boundary is still 17% of the peak density. In the present work, values between $a^2/r_0^2 = 6.5$ and $a^2/r_0^2 = 11$ have been used, such that the density at the plasma edge is below 1% of the peak value.

In principle, arbitrary radial profiles of the mean density n_0 , of the collision frequencies ν_{ei} , ν_{en} , ν_{in} , and of the plasma potential can be used as input parameters. Note that only the sum $\nu_e = \nu_{ei} + \nu_{en}$ enters the equations. Besides the parameter profiles, the parallel electron velocity V and the parallel wavelength λ_z are input parameters of the code. The discussion is restricted to radial density profiles of Gaussian shape and a radially constant plasma potential since this gives best convergence of the numerical results.

For mode numbers in the range $m = 1 - 6$ the ODE system (7.4) was solved and mode frequencies ω_R , growth rates ω_I and radial mode profiles $\psi(r)$ were evaluated. The radial mode structures shown are the modulus of $\psi(r)$. In particular, the assumption of eigenmodes of the form $\phi = \psi(r) \exp(-i\omega t + ik_{\parallel} z + im\theta)$, which was used to obtain the system

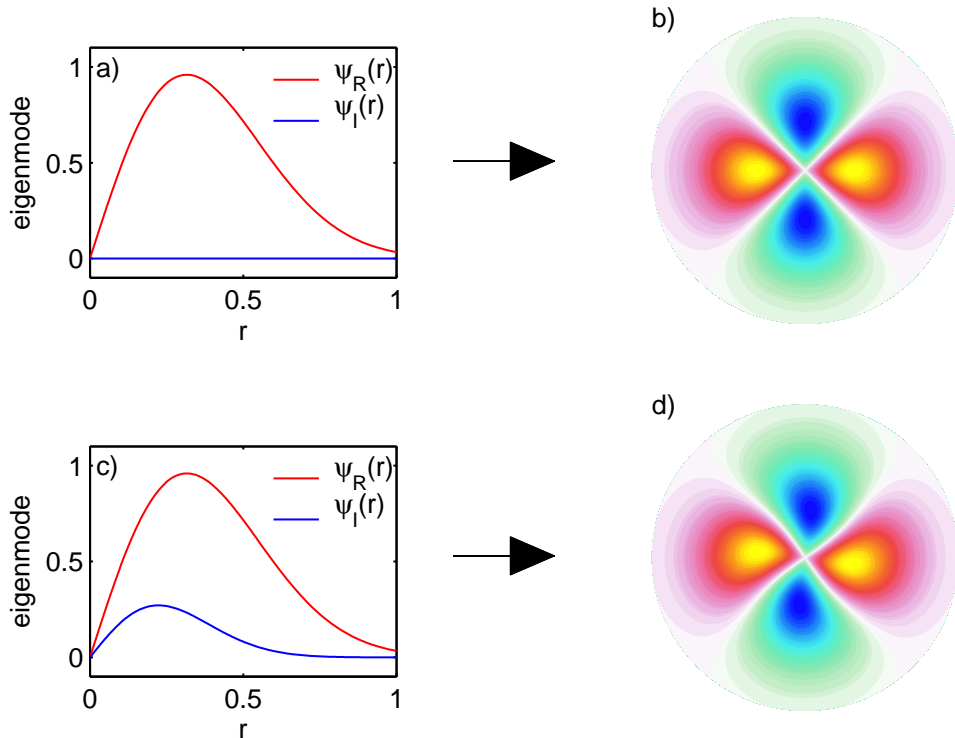


Figure 7.1: Poloidal eigenmodes for sample radial profiles of ψ_R and ψ_I . a) Real and imaginary part of $\psi(r) = 5r \exp(-r^2/0.2)$. b) Resulting poloidal eigenmode. c) real and imaginary part of $\psi(r) = 5r \exp(-r^2/0.2) + i2r \exp(-r^2/0.1)$. d) Resulting poloidal eigenmode.

of differential equations, also allows one to determine the poloidal eigenmodes for a fixed time instant t and a fixed axial position z . With $\alpha = \exp(-i\omega t + ik_{\parallel}z)$ one obtains

$$\phi(r, \theta) = \alpha \psi(r) \exp(im\theta) \quad (7.6)$$

$$= \alpha (\psi_R(r) + i\psi_I(r)) (\cos(m\theta) + i \sin(m\theta)) \quad (7.7)$$

$$\text{Re}(\phi(r, \theta)) \propto \psi_R(r) \cos(m\theta) - \psi_I(r) \sin(m\theta) \quad . \quad (7.8)$$

If the real part ψ_R and the imaginary part ψ_I are non-zero and have different shapes, the resulting poloidal mode structure becomes sheared. This is demonstrated in figure 7.1. In the case of a real eigenfunction ψ , the poloidal eigenmode is not sheared (figure 7.1a,b). Otherwise, the poloidal eigenmode becomes sheared (figure 7.1c,d). In reference [9], ψ was assumed to be real for Gaussian density profiles and complex eigenfunctions ψ were allowed only in the case of non-Gaussian density profiles (but not further discussed). To our best knowledge, no numerical results on poloidal drift mode structures in cylindrical geometry have been published to date.

7.2 Comparison with previous results

To benchmark the new code, a comparison with similar previous studies is meaningful. In reference [9], numerical results of a nonlocal, cylindrical model of the collisional drift instability are reported. This model is similar to one introduced here. Table 7.1 summarizes the code parameters taken from reference [9] as well as the input parameters of the Risø code. For comparison, the collision frequencies were kept radially constant. The density profile is a Gaussian $n(r) \propto \exp(-r^2/(17.6 \text{ mm})^2)$. The collision frequencies were calculated using the formulae compiled in appendix B. We note that from the data given in the paper it is not possible to deduce the exact input parameters, used to obtain figure 4 of reference [9]. For instance, no collision frequencies and not all parameters determining the Gaussian density profile are given. Additionally, a higher value for the plasma edge a is chosen here such that the density at $r = a$ is well below 1% of the peak value. Some deviations are thus expected for the eigenfrequency and growth rates.

parameters from ref. [9]	corresponding input parameters for the Risø code	
$B = 200 \text{ mT}$	$\Omega_{ci} = 4.8 \cdot 10^5 \text{ s}^{-1}$	$\rho_s = 5 \text{ mm}$
$T_e = 2 \text{ eV}$	$v_{th} = 6 \cdot 10^5 \text{ m/s}$	$c_s = 2.5 \cdot 10^3 \text{ m/s}$
$p_0 = 1 \text{ mtorr}$	$\nu_{in}/\Omega_{ci} = 0.01$	$\nu_{en}/\Omega_{ci} = 5.4$
$n = 1 \cdot 10^{16} \text{ m}^{-3}$	$\nu_{ei}/\Omega_{ci} = 0.27$	
$V/v_{th} = 0.2$	$V/c_s = 50$	
no $E \times B$ drift	$\phi_0(r) = 0$	

Table 7.1: Plasma parameters given in reference [9] and corresponding input parameters used for calculation with the Risø code.

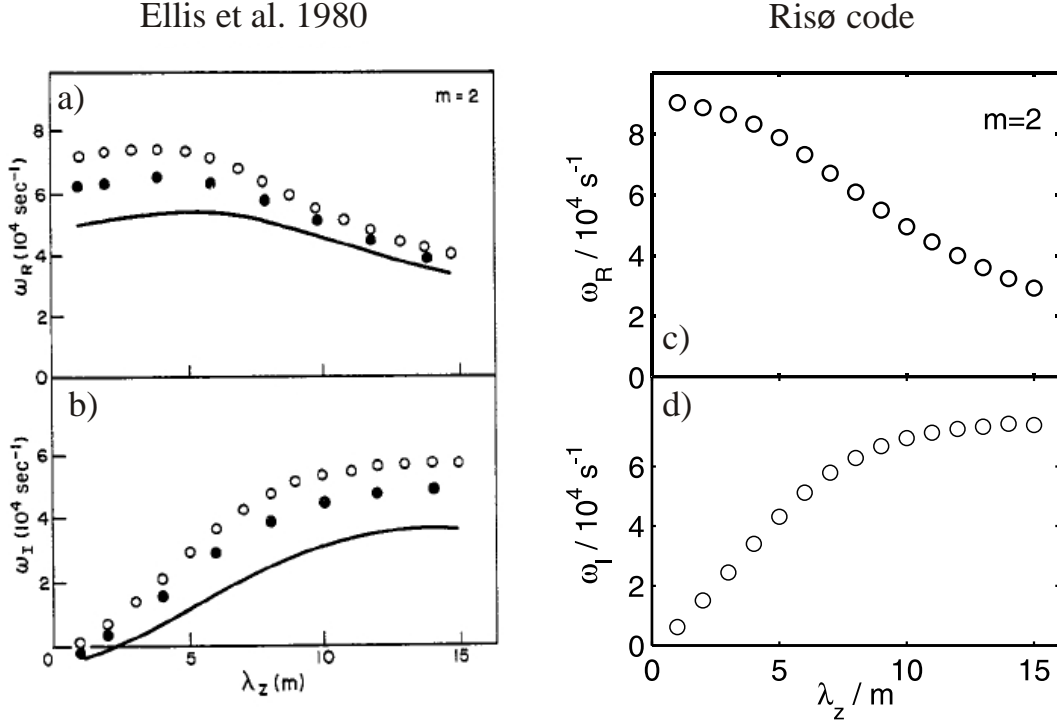


Figure 7.2: a,b) Figure 4 taken from reference [9]. Real and imaginary part of ω versus parallel wavelength for $m = 2$ from three theoretical models (local slab –, Gaussian numeric \circ , full numeric \bullet). c,d) Real and imaginary part of ω versus parallel wavelength for $m = 2$ calculated with the new Risø code for a Gaussian density profile. The input parameters (see table 7.1) are chosen similar to the parameters given in reference [9].

In figure 7.2, the results from reference [9] and the Risø code are compared. It is found that the previous result is qualitatively well reproduced. In both cases the mode frequency ω_R decreases monotonically with increasing parallel wavelength. The Risø code finds slightly higher frequencies for small wavelengths but smaller frequencies for higher wavelengths. In both models, the growth rate increases with increasing wavelength and nearly saturates for wavelength $\lambda_z \gtrsim 10$ m. The Risø code gives slightly higher values than the model of ELLIS et. al. This might well be an effect of deviating input parameters.

The poloidal mode structures for density and potential are calculated from $\psi(r)$ and (2.33). The results for $\lambda_z = 2$ m and $\lambda_z = 15$ m (see figure 7.2) are shown in figure 7.3. For a parallel wavelength of 2 m the mode structures for density and potential look the same and the phase shift is only $\angle(\tilde{n}, \tilde{\phi}) = 1.3^\circ$. Nearly no shear is observed. For higher parallel wavelength $\lambda_z = 15$ m the mode structures look very different: The mode structure is sheared similar to the experimental result (see chapter 6). In addition, a large phase shift between density and potential is found, $\angle(\tilde{n}, \tilde{\phi}) = 32^\circ$.

Figure 7.4 compares the results for two different radial profiles of the electron collision frequency, a flat $\nu_{en}(r)/\Omega_{ci} = 5.4$ profile and a Gaussian profile of the form $\nu_{en}(r)/\Omega_{ci} = 5.4 \exp(-r^2/(17.6 \text{ mm})^2)$. The parallel wavelength is chosen to be $\lambda_z = 4$ m. All other parameters are the same as for figure 7.2. It is found that the mode frequencies are similar

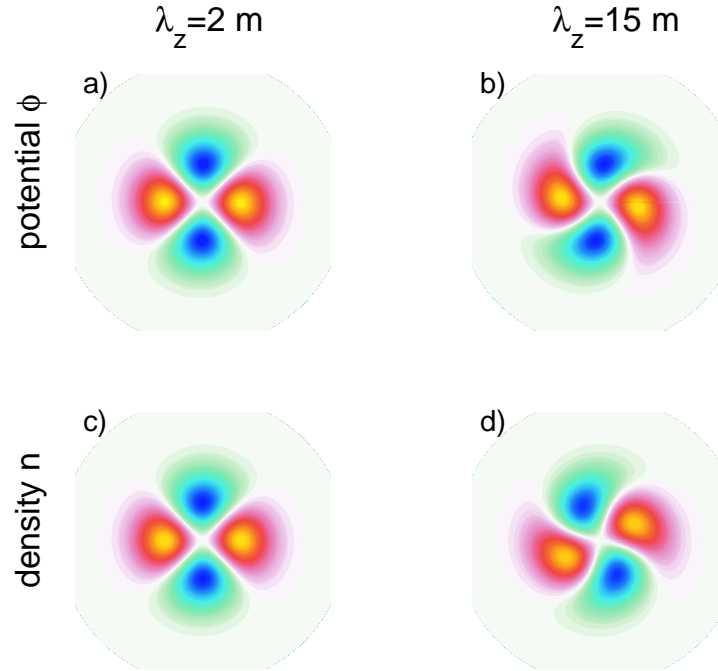


Figure 7.3: Calculated poloidal mode structures for density and potential obtained for the scan of figure 7.2. Left side: $\lambda_z = 2 m$. Right side: $\lambda_z = 15 m$. First row: plasma potential mode structure. Second row: plasma density mode structure.

in both cases, although ω_R with a flat profile is slightly smaller for all mode numbers $m = 1 - 4$. Figure 7.4b) shows, however, that the growth rates differ significantly: the growth rates for the Gaussian collision frequency profile are approximately a factor of three smaller than for the flat profile. This might be due to the different total area of the collision frequency profiles which is a factor of three higher for the flat collision profile than for the Gaussian collision profile with the same peak value. For slightly higher peak values of the Gaussian collision frequency profile, the mode frequencies remain almost constant but the growth rates increase proportional to the peak value. Figure 7.4c,d) shows radial eigenmodes for flat and Gaussian collision profiles with the same peak value. The black curve indicates the density profile. All modes have their maximum in the gradient region of the density profile. Modes with higher mode number m are always localized further away from the plasma center than modes with lower mode number. This is in agreement with previous results [9]. The shape of the collision frequency profile has no visible influence on the localization of the modes. In figures 7.4e,f) poloidal mode structures of the plasma potential are shown for the different collision profiles. For both cases, only a small amount of shear is observed and the structures look very similar.

In summary, it is found that the Risø code reproduces the results of reference [9] quite well. In addition, it is found that poloidal mode structures are sheared for higher values of λ_z . Thus, the assumption of real valued eigenfunctions seems to be too strict even for the case of Gaussian density profiles.

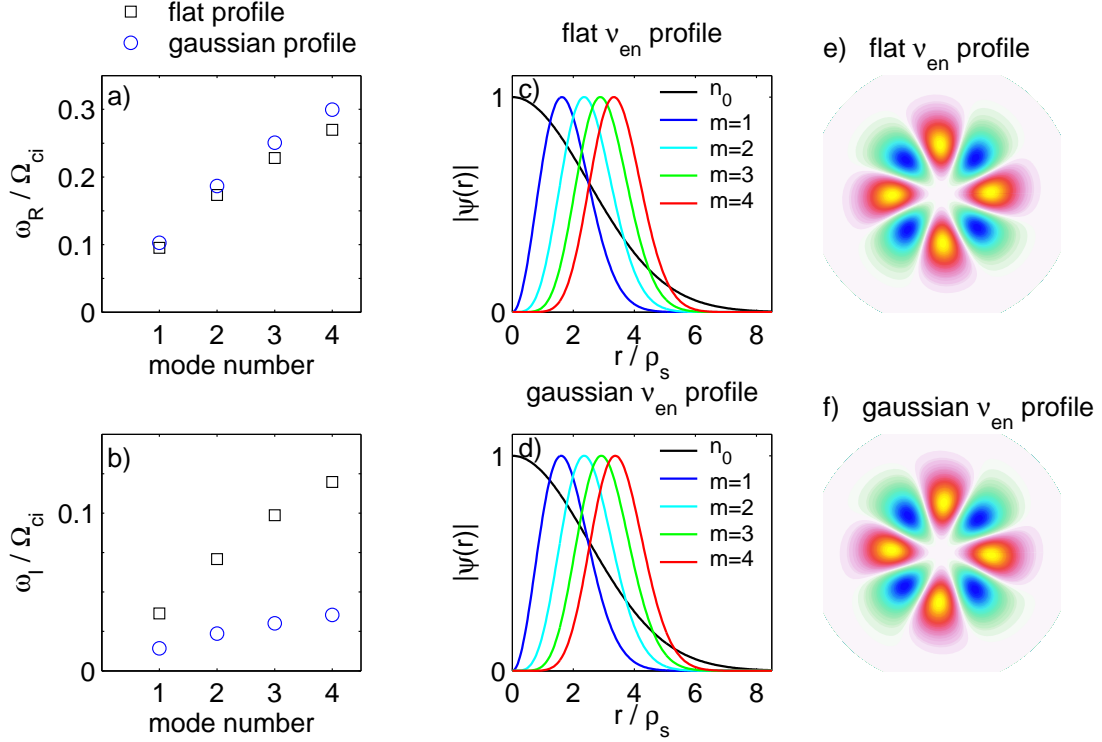


Figure 7.4: Comparison between a flat electron collision profile $\nu_{en}/\Omega_{ci} = 5.4$ and a Gaussian electron collision profile $\nu_{en}/\Omega_{ci} = 5.4 \exp(-r^2/(3\rho_s)^2)$. The parallel wavelength is $\lambda_z = 4$ m. The other parameters are the same as given in table 7.1.

parameter	input parameter of the code
$B = 75$ mT, $T_e = 2$ eV	$\Omega_{ci} = 1.8 \cdot 10^5$ s ⁻¹ $\rho_s = 13$ mm
$\nu_{ei} \approx 1 \cdot 10^8$ s ⁻¹	$\nu_{ei}/\Omega_{ci} \approx 600$
$\nu_{en} \approx 5 \cdot 10^6$ s ⁻¹	$\nu_{en}/\Omega_{ci} \approx 30$
$\nu_{in} \approx 6 \cdot 10^4$ s ⁻¹	$\nu_{in}/\Omega_{ci} \approx 0.3$
$\lambda_z \approx 5$ m (11 m)	$\lambda_z/\rho_s \approx 400$ (850)
	$V/c_s = 1$

Table 7.2: Typical plasma parameters in the VINETA device and derived input parameters used for the code.

7.3 Results for VINETA parameters

A Gaussian density profile $n(r) = n_0 \exp(-r^2/r_0^2)$ is assumed with $r_0 = 3\rho_s$, which is close to the experimental situation². The input parameters of the code have been calculated

²In principle, the density profiles can be arbitrarily defined. However, due to numerical instabilities, the code does not find adequate solutions for density profiles obtained from the experiment.

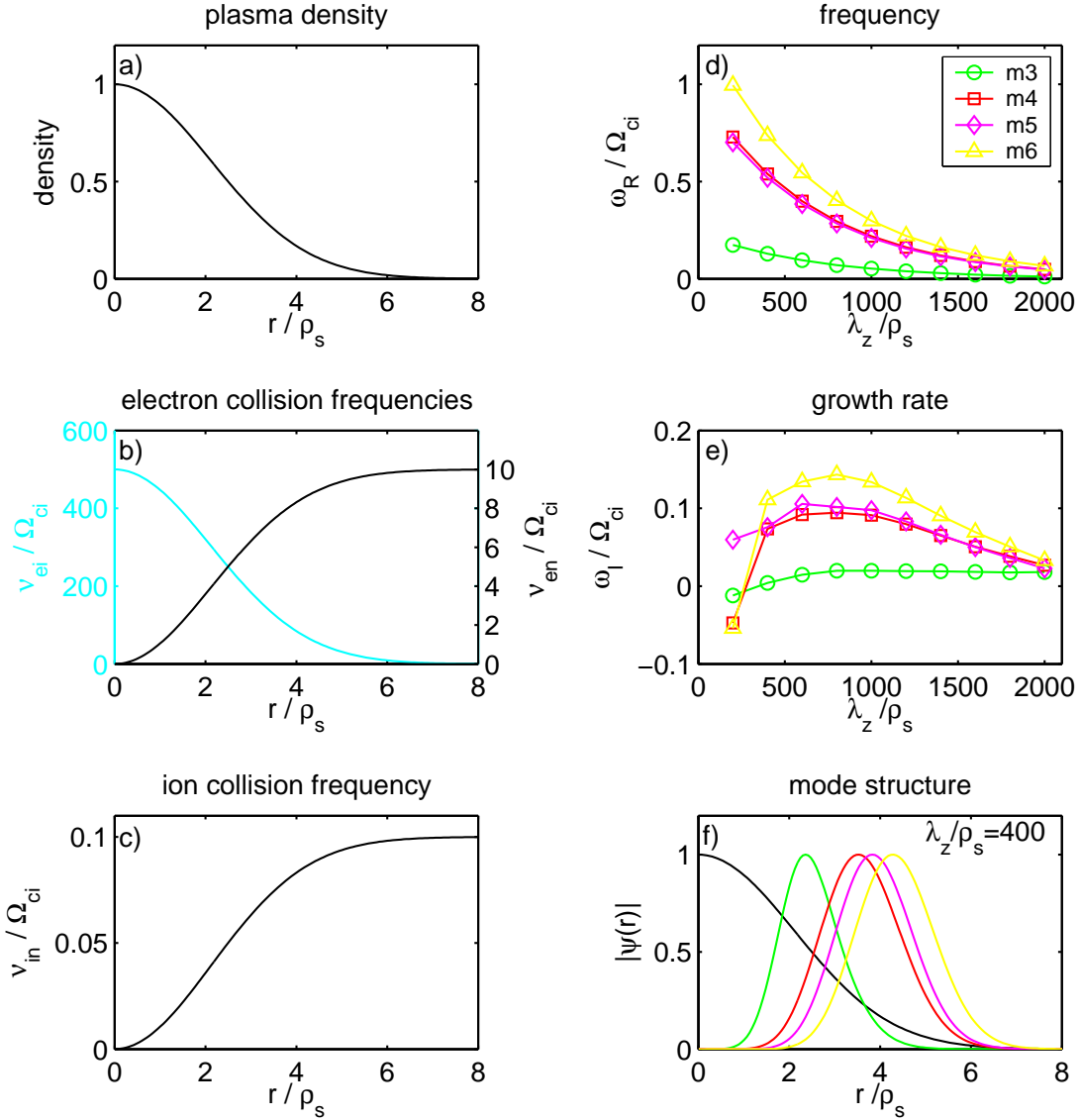


Figure 7.5: Scan of the parallel wavelength. a-c) show the input radial profiles of background density n_0 , electron collision frequencies ν_{ei} , ν_{en} and ion collision frequency ν_{in} , respectively. A flat plasma potential profile (i.e. no $E \times B$ drift) and $V = c_s$ are assumed.) The calculated mode frequencies ω_R are shown in d), the growth rates ω_I in e). Radial mode profiles $|\psi(r)|$ are shown in f). Results for mode numbers $m = 1, 2$ are not shown due to numerical instabilities.

for conditions in the VINETA device (see chapter 5). An overview is given in table 7.2.

Dependency on the parallel wave length

Figure 7.5 shows the result of a scan of the parallel wave length. The input density profile is shown in figure 7.5a). Radially dependent collision frequencies are assumed as shown in figure 7.5b,c). The collision frequency for Coulomb collisions is proportional to the plasma density profile and thus the collision frequency in the plasma center is much higher than

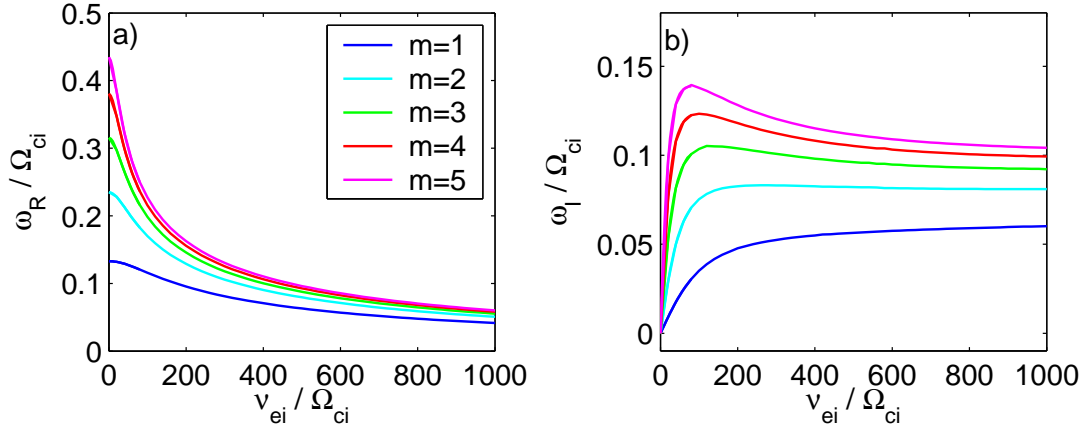


Figure 7.6: Parameter scan for Coulomb collisions ν_{ei} . a) frequency ω_R vs. ν_{ei} , b) growth rate ω_I vs. ν_{ei} . (Gaussian profiles $n(r) \propto \exp(-r^2/(3\rho_s)^2)$ for density and Coulomb collisions ν_{ei} , $\lambda_z/\rho_s = 400$, $V/c_s = 1$, $\nu_{en} = \nu_{in} = 1 \cdot 10^{-5}$).

at the plasma edge. If one considers neutral depletion in the core plasma (see chapter 5), the electron-neutral and ion-neutral collision frequencies are lower in the plasma center than further outside. Here, the extreme case of 100% ionization degree in the plasma center is assumed. The collision frequencies ν_{en} and ν_{in} vanish in the plasma center and increase toward the edge.

The dependency of the mode frequencies and growth rates on the parallel wave length is shown in figure 7.5d,e). Again, it is found that with increasing parallel wavelength the mode frequencies decrease. For mode numbers $m = 4 - 6$ the growth rates increase first but then decrease. For the $m = 3$ mode, this decrease is not observed, instead saturation occurs. In the experimentally observed range $\lambda_z/\rho_s = 400 \dots 850$, the growth rates change only slightly for each mode which might lead to mode competition between modes with different parallel wavelength. At $\lambda_z/\rho_s = 2000$, all growth rates are similar $\omega_I/\Omega_{ci} \approx 0.03$. Figure 7.5f) shows radial eigenmodes for $\lambda_z/\rho_s \approx 400$. As before, higher modes are localized at larger radial positions. However, the spacing between the different modes is seen to be more irregular than previously seen in figure 7.4.

Collisions

Figure 7.6 shows a scan of the Coulomb collision frequency and its effect on mode frequencies and growth rates. Here, the collision frequencies for collisions with neutrals are assumed to be small and radially constant $\nu_{en}/\Omega_{ci} = \nu_{in}/\Omega_{ci} = 1 \cdot 10^{-5}$. Figure 7.6a) shows that the frequency of the drift waves strongly decreases with increasing electron collision frequency ν_{ei} for all mode numbers $m = 1 - 5$. The growth rates are shown in figure 7.6b). For all mode numbers, they increase very steeply in the range $\nu_{ei}/\Omega_{ci} = 0 \dots 100$. For mode number $m = 1$, the growth rate increases monotonically for the whole ν_{ei} -range, while for the higher mode numbers the growth rate decreases gradually after peaking around $\nu_{ei}/\Omega_{ci} \approx 100$. For all frequencies the highest growth rate is found for $m = 5$ and the lowest for $m = 1$. This agrees quite well with the experimental findings in the

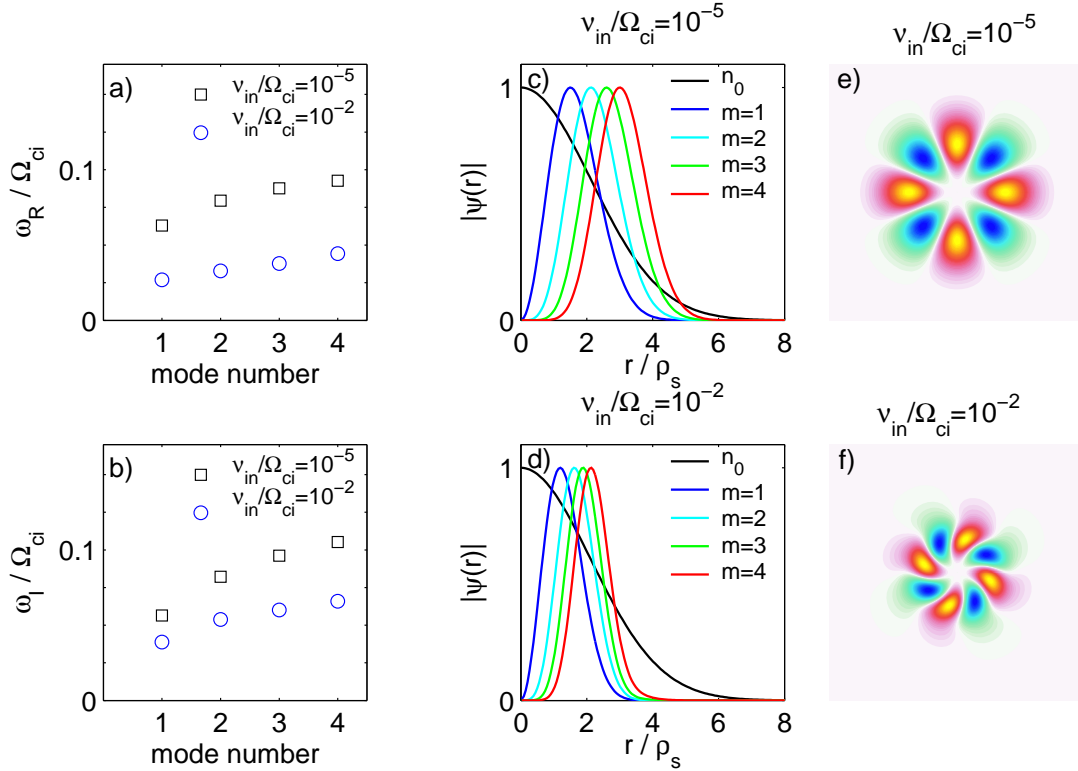


Figure 7.7: Comparison of eigenvalues and mode structures for $\nu_{in}/\Omega_{ci} = 10^{-5}$ and $\nu_{in}/\Omega_{ci} = 10^{-2}$. a) mode frequency ω_R , b) growth rates ω_I , c,d) radial eigenfunctions $|\psi(r)|$ for $m = 1 - 4$, e,f) poloidal mode structures of the plasma potential. (Gaussian profiles $n(r) \propto \exp(-r^2/(3\rho_s)^2)$ and $\nu_{ei}(r)/\Omega_{ci} = 500 \exp(-r^2/(3\rho_s)^2)$. $\lambda_z/\rho_s = 400$, $V/c_s = 1$, $\nu_{en}/\Omega_{ci} = 1 \cdot 10^{-5}$).

VINETA device, where modes with higher mode numbers ($m = 4 - 6$) are usually easier to destabilize than modes with low mode numbers.

Figure 7.7 compares numerical results for different ion collision frequencies ($\nu_{in}/\Omega_{ci} = 10^{-5}$ and $\nu_{in}/\Omega_{ci} = 10^{-2}$). The other input parameters are the same as for figure 7.6, but the peak value of the electron-ion collision frequency profile is chosen to be $\nu_{ei}/\Omega_{ci} = 500$. Figure 7.7a,b) shows that higher ion-neutral collisionality leads to lower mode frequencies as well as to lower growth rates for all mode numbers $m = 1 - 4$. The latter is consistent with the local slab model (chapter 2). Also the phase shift between density and potential is provided by the Risø code: $\angle(\tilde{n}, \tilde{\phi}) = 14^\circ$ is found for $\nu_{in}/\Omega_{ci} = 10^{-5}$ and $\angle(\tilde{n}, \tilde{\phi}) = 16^\circ$ for $\nu_{in}/\Omega_{ci} = 10^{-2}$, i.e., nearly independent of the ion collisionality although the growth rates differ significantly. From figure 7.7c,d) one finds that higher ion collision frequencies lead to a shift of the radial eigenmodes towards the center of the plasma column. This is also seen in the ‘shrinking’ of the poloidal mode structures figure 7.7e,f). Also the shear of the mode structures is increased with the ion collisionality.

Parallel electron velocity

The parallel electron velocity has not been measured, but was estimated in section 5.4 to be close to c_s , which is an order of magnitude lower than the values of other devices

where drift waves have been investigated (see chapter 5).

Figure 7.8 shows a scan of the parallel electron velocity. The mode frequencies are nearly independent of the parallel velocity (a) while the growth rates increase monotonically with increasing parallel electron velocity (b). For the $m = 2$ mode, the growth rate increases by more than a factor of three by increasing V/c_s from 0.4 to 10. The phase shift between density and potential is $\angle(\tilde{n}, \tilde{\phi}) = 5^\circ$ for $V/c_s = 0.4$ and $\angle(\tilde{n}, \tilde{\phi}) = 10^\circ$ for $V/c_s = 10$. The higher growth rate is found together with increased phase shift between density and potential. For low values of the parallel velocity the growth rate of the $m = 2$ mode is smaller than for the higher mode numbers. In contrast, for $V/c_s \gtrsim 4$ the growth rate of the $m = 2$ mode exceeds the growth rates of modes with higher m .

Figure 7.8c,d) shows radial mode profiles for $V/c_s = 0.4$ and $V/c_s = 10$, respectively. It is found that for higher parallel velocities the modes are localized a little further outside than for lower velocities. Poloidal mode structures for the same parallel velocities are

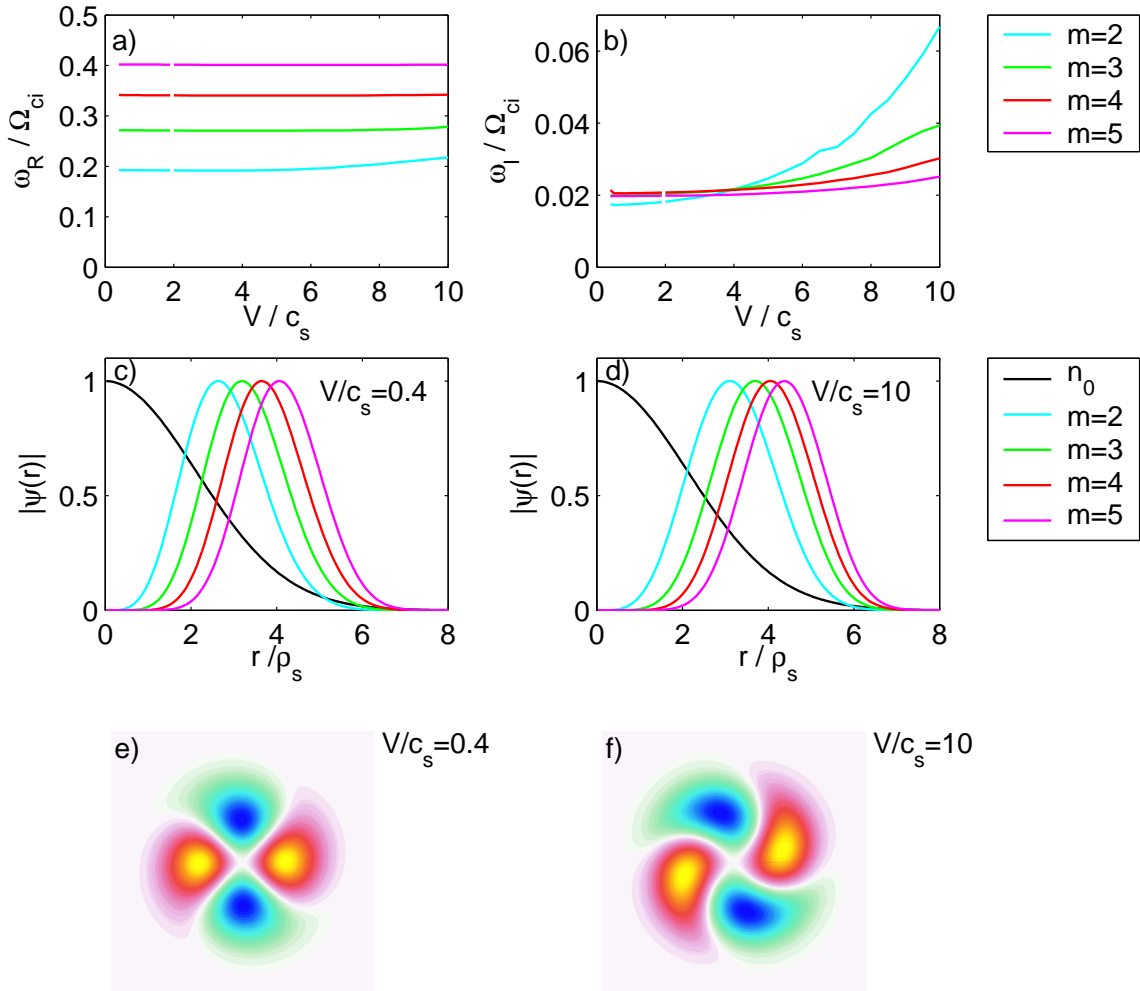


Figure 7.8: Parameter scan for the parallel electron velocity V . a) mode frequencies ω_R , b) growth rates ω_I , c,d) radial eigenmodes $|\psi(r)|$ for $V/c_s = 0.4$ and $V/c_s = 10$, respectively, e,f) poloidal mode structure of the plasma potential ϕ_0 for these velocities. (Gaussian profile $n(r) = \exp(-r^2/(3\rho_s)^2)$, $\nu_{ei}(r)/\Omega_{ci} = 200 \exp(-r^2/(3\rho_s)^2)$, $\nu_{en}/\Omega_{ci} = \nu_{in}\Omega_{ci} = 10^{-5}$, $\lambda_z/\rho_s = 800$)

shown in figure 7.8e,f). In both cases, the mode structures are sheared, but for $V/c_s = 10$ the shear is much more pronounced than for $V/c_s = 0.4$. This underlines the fact that not only one parameter is responsible for a sheared mode structure.

7.4 Discussion

In the last two sections, numerical results obtained with the Risø code were presented. It solves the 2nd order differential equation obtained from linearizing the two-fluid equations in cylindrical geometry. The main results of this chapter are summarized and discussed.

The results of reference [9] are quite well reproduced by the Risø code. A comparison between flat and radially dependent collision frequency profiles reveals that the mode frequencies as well as the mode structures remain nearly the same if the flat collision profile is replaced with a Gaussian profile with the same peak value. The growth rates, however, change significantly and are rather sensitive to the shape of the collision profile, suggesting that they are more determined by the total area of the collision profile than by its peak value. In the DLPD device – for which the previous numerical calculation was conducted – electron neutral collisions are dominant and the assumption of a flat collision profile was justified. In the VINETA device, Coulomb collisions are dominating, which suggests to use profiles proportional to the plasma density. Actually, for VINETA parameters, no reasonable solutions could be obtained with flat collision frequency profiles.

Mode frequencies

For both parameter regimes investigated (see tables 7.1 and 7.2), the mode frequencies decrease for increasing parallel wavelength. Increasing electron collisions lead to monotonically decreasing mode frequencies. Between $\nu_{ei}/\Omega_{ci} \approx 0$ and $\nu_{ei}/\Omega_{ci} = 1000$ the frequencies are reduced by factors between 3 and 9 ($m = 1 - 5$). The growth rates change significantly only for $\nu_{ei}/\Omega_{ci} < 100$. Ion collisions decrease the mode frequencies. The parallel electron velocity V shows nearly no influence on the mode frequencies.

One of the main reasons for numerical calculations was to obtain a better idea about what determines the mode frequencies. For comparison with the experiment, the case of 75 mT of section 6.6 is used. There, an $m = 5$ mode at 3.1 kHz was observed embedded in a rather turbulent background. Figures 7.5, 7.6 and 7.8 show mode frequencies ω_R for $m = 5$ modes for parameters similar to the experimental parameters. Values between $\omega_R/\Omega_{ci} \approx 0.1$ and $\omega_R/\Omega_{ci} \approx 0.5$ are found. The numerically obtained mode frequencies are clearly sensitive to a number of parameters. In particular, the result obtained for the collision frequency scan gives very low values compared to others. In the experiment, the electron diamagnetic drift frequency was found to be about 12 kHz. From the numerical calculations, mode frequencies in the range 2.8 kHz–14.3 kHz are obtained. To get the frequency in the laboratory frame, the $E \times B$ Doppler shift has to be taken into account. The peak value of f_E reduces the frequency by 9.5 kHz. Then, the frequency range in the laboratory frame is -6.6 kHz to 4.8 kHz. The negative sign indicates a propagation in the direction of the $E \times B$ drift, i.e., opposite to the electron diamagnetic drift velocity. If, instead, a radially averaged value is taken for the $E \times B$ frequency, the obtained frequencies

are reduced by about 4.5 kHz. This gives a frequency range in the laboratory system of -1.7 kHz to 9.8 kHz. For both cases, the observed mode frequency of 3.1 kHz lies within the given frequency ranges. A propagation in the $E \times B$ direction seems plausible but has never been observed in the experiment.

The estimation of mode frequencies is further complicated by the sensitivity of numerical solutions on the input parameters as well as by the fact that both drifts – the electron diamagnetic drift and the $E \times B$ drift – are similar and must be subtracted. In particular, the accuracy of the measurement of the $E \times B$ drift is not very good. Since the plasma does not rotate rigidly, it is also not fully clear which role the sheared rotation plays and which value for f_E is appropriate. The numerical results show that the experimentally observed frequencies are generally consistent with drift waves.

Mode destabilization

Different physical mechanisms can destabilize the drift instability. The question, however, is which of these is the dominating destabilization mechanism in the VINETA device.

Electron collisions destabilize drift waves because they impede the parallel dynamics of the electrons. The growth rate is close to zero if electron collisions vanish and, at the same time, the parallel electron velocity is small. The highest increase in the growth rate is found below $\nu_{ei}/\Omega_{ci} = 100$ whereas for larger values the changes are relatively small. If the electron collision frequency would be reduced by a factor of 5-10, the growth rates should remain similar. An increase of the electron temperature from 2 eV to the order of 10 eV would result in a reduction of the collisionality by an order of magnitude. This regime is very attractive because magnetic fluctuations are expected to play a role [4].

Ion collisions decrease the growth rate, i.e., they are a stabilizing effect, as expected from the local slab model. The parallel electron velocity (corresponding to a current through the discharge) is a strongly destabilizing effect, as predicted by the local slab model. In the VINETA device V is of the order of c_s . In the other devices, the parallel velocity is of the order of several $10 c_s$. In particular, in devices like DLPD, MIRABELLE, and KIWI, low mode numbers $m = 1 - 3$ are destabilized whereas higher mode numbers are rarely observed. In VINETA the opposite is true and indeed for higher V the lower mode numbers have the highest growth rates. For small V , the growth rates of different modes are much closer, and the $m = 2$ mode has a lower growth rate than the modes $m = 3 - 5$. This might be an explanation for the fact that in the VINETA device the mode numbers $m = 4 - 6$ are most easily destabilized.

The growth rates also depend on the parallel wavelength of the mode. In VINETA, two values for the parallel wavelength were measured: $\lambda_z \approx 5$ m corresponding to $\lambda_z/\rho_s \approx 400$ and $\lambda_z \approx 11$ m corresponding to $\lambda_z/\rho_s \approx 850$. The growth rate does not change significantly within the experimentally observed λ_z range. Previous drift wave experiments mostly established a relationship between the parallel wavelength and the device length. Axial boundary conditions seem to restrict the parallel wavelength to $\lambda_z/4 = nL$ where L is the machine length and n is a small integer number [9,14]. Since the growth rates between different λ_z are nearly the same, for slightly different parameters different wavelengths are possible to establish. The numerical results indicate that a higher parallel wavelength is connected with a lower mode frequency (a factor of two between $\lambda_z/\rho_s \approx 400$

and $\lambda_z/\rho_s \approx 850$). The experimentally obtained frequencies for the higher wavelength were slightly lower. However, the difference is below 15%.

Poloidal mode structure

The poloidal mode structures of the drift waves observed in the VINETA device are sheared. The numerical studies reveal that sheared poloidal mode structures are not at all unusual if complex eigenfunctions ψ are allowed. A close agreement is found between observed and numerically calculated mode structures.

The results show that the mode structure shear is not caused by a single parameter only. It seems that increased parallel wavelength, parallel electron velocity, and ion collision frequencies lead to sheared mode structures. Higher shear in the mode structure tends to occur for higher growth rates which coincides with increased phase shift between density and potential.

The numerical results strongly suggest that sheared mode structures are a general phenomenon, present at different parameters - even for Gaussian density profiles, without any $E \times B$ rotation and for flat collision profiles.

Chapter 8

Summary and Conclusions

Within the scope of the present thesis, a new experimental device – the VINETA – was designed, constructed and put into operation. It is a large, linear, magnetized plasma experiment which is very flexible and thus allows for a wide range of highly controllable plasma conditions. Care was taken in the design to permit easy accessibility and maintenance of the device. VINETA is primarily intended for studies of different kinds of plasma waves and instabilities. Besides the investigations of the present work, it has already been successfully used for investigations on helicon and whistler waves [78], and on ion acoustic waves [122]. For the investigation of the present work, Langmuir probes were used for the study of the mean plasma parameters as well as for investigation of the drift instability. Several computer controlled positioning systems and a poloidal probe array were implemented and permit spatiotemporal measurements of low-frequency instabilities.

In VINETA, the range of achievable plasma parameters is considerably extended when compared to other linear devices in which drift waves have been investigated before. In the helicon wave sustained discharge mode, the plasma- β exceeds the electron-ion mass ratio. The comparatively high plasma density ($\approx 10^{19} \text{ m}^{-3}$) at low electron temperatures ($\approx 2 \text{ eV}$) results in very high electron Coulomb collision frequencies which clearly dominate the electron neutral collisions. Even though $\beta > m_e/M$, electromagnetic effects are negligible for the drift instability due to the high collisionality.

Background plasma profiles, of crucial importance for the identification of the observed instability, have been studied. Along the magnetic field, gradients of the electron temperature ($\approx 50\%$ decrease for $\Delta z = 1 \text{ m}$) and the plasma potential ($\approx 10\%$ decrease for $\Delta z = 1 \text{ m}$) exist. Despite the axial inhomogeneities the instability develops with an axially constant frequency. This finding is in agreement with previous studies conducted in the KIWI device [123,124] where global monochromatic drift waves establish despite axial inhomogeneities of density and potential profiles.

A low-frequency instability, occurring in the helicon discharge mode of the VINETA device, has been studied in detail. All experimentally observed features of the instability, namely

- localization,
- fluctuation amplitudes,

- phase shift between density and potential fluctuations,
- propagation direction,
- parallel wavelength

are consistent with the theory of resistive drift waves. A direct comparison between theoretically predicted mode frequencies and experimentally observed modes is not straightforward to do, because many (partially unknown) parameters influence the results. The observed frequencies are, however, of the same order as the numerically calculated ones. In conclusion, the observed instability can be identified as a resistive drift instability.

Both the ambient magnetic field and the neutral gas pressure influence the dynamics of the drift instability and are thus suitable control parameters for the drift wave dynamics. Different drift wave dynamical states – from single saturated modes via interaction of several modes towards weakly developed turbulence – can be established. No clear-cut transition scenario is observed, the dynamical states just alternate with variation of ambient magnetic field or neutral gas pressure. The mode frequencies change with varying magnetic field and neutral gas pressure. This is caused by changes of the $E \times B$ rotation of the plasma column, leading to a Doppler shift of the mode frequencies.

A new code, based on a non-local linear cylindrical model for the drift wave dispersion, was used to gain more insight into the dominating destabilization mechanisms, and also into dependencies of mode frequencies and growth rates on different parameters. In contrast to previous models, radial profiles of the collision frequencies are taken into account. Since Coulomb collisions, dominant for the electrons, are proportional to the plasma density, this enhancement is important. The numerical model showed that electron collisions decrease the mode frequencies significantly. This might explain why the local slab model, where the mode frequency is found to be independent of the collision frequencies, yields too high mode frequencies. This underlines the importance of using non-local cylindrical models for an adequate description of drift waves.

Both, experimentally and in the numerical model, sheared poloidal mode structures were found. To the best of our knowledge, this was observed for the first time regarding collisional drift waves in cylindrical geometry. Similar mode structures are found in numerical solutions of linear models for ion temperature gradient modes in both, toroidal geometry [125] and cylindrical geometry [126]. Since the sheared mode structures rotate like a rigid body, sheared poloidal drifts cannot be made responsible for this phenomenon. The numerical results show that the shear of the mode structure is dependent on various parameters and sheared mode structures are found for very different parameter regimes. This strongly suggests that sheared mode structures are a general phenomenon.

In the context of destabilization mechanisms of drift waves, the numerical results show that the high electron collision frequencies provide the strongest destabilizing mechanism in the helicon plasma of VINETA. Contrary, in thermionic discharges such as KIWI, MIRABELLE and DLPD, the parallel electron drift contributes significantly to destabilization [9,110]. The experimental findings show that the parallel electron drift is an order of magnitude lower than in those devices and thus this effect is much less important in VINETA.

Drift waves are destabilized only above a critical magnetic field $B_c \approx 50$ mT. For lower

magnetic fields, the plasma was found to be quiescent. This agrees well with the results reported by LIGHT et al. [42,45] and TYNAN and coworkers [46]. Below the onset of the fluctuations, the density gradients increase significantly with increasing magnetic field. For higher magnetic fields, a saturation is observed. For magnetic fields $\gtrsim 40$ mT, the diamagnetic drift frequency $\omega^* \propto \partial_r n_0 / n_0 B$ remains almost constant. Assuming $T_e = \text{const.}$, the expression $\partial_r n_0 / n_0 B$ (and not $\partial_r n_0$ only) enters the equations describing the drift waves (see equations (2.20)-(2.22)¹). Therefore, the variation of the dynamics with varying magnetic field is presumably not caused by varying background density profiles but by finite Larmor radius effects. The drift scale $\rho_s \propto 1/B$ is of the order of several mm and decreases from 30 mm at $B = 30$ mT to 9 mm at $B = 100$ mT. Thus, ρ_s is not small compared to the density gradient scale length $L_\perp \approx 20$ mm, especially for relatively low magnetic field. This means that the density gradient is relevant for the ions during the gyromotion. Finite Larmor radius effects are known to be stabilizing [9,14,22] and the observed dependency on the magnetic field strongly suggests that the reduction of finite Larmor radius damping could explain the destabilization above a threshold magnetic field.

The neutral gas pressure has a significant influence on the drift wave dynamics as well. For the lowest attainable neutral gas pressures (0.1 Pa) usually the highest fluctuation levels were observed. With increasing neutral gas pressure the fluctuation level drops significantly until at pressures about 0.65 Pa the fluctuations essentially vanish. The maximum gradient of the ion saturation current increases only slightly with increasing neutral gas pressure, which cannot explain the drastic decrease of the growth rate. The strong damping of the drift instability at higher pressures rather suggests that collisions with neutrals play an important role. Ion neutral collisions are known to stabilize the drift instability [10] and could be responsible for the damping that occurs at higher pressures. Electron collisions, on the other hand, are destabilizing but are dominated by the pressure independent Coulomb collisions.

Final remarks

It was generally accepted that plasmas produced by helicon sources are relatively quiescent. As late as 2001, it was reported by LIGHT and coworkers that a low-frequency wave-like instability is observed in a helicon discharge, exhibiting characteristics of both the resistive drift instability and the Kelvin-Helmholtz instability [42,45]. At conferences in 2001, TYNAN and coworkers reported on first observations of resistive drift waves in the CSDX device [46]. Also in the CSDX device, resistive drift waves were found to occur above a critical magnetic field. These findings lead to the conclusion that resistive drift waves generically exist in helicon plasmas within certain parameter regimes. In particular, the magnetic field always plays a major role in the destabilization of drift waves, i.e., the instability is found only above a critical magnetic field. Finite Larmor radius effects are believed to be responsible for this threshold behavior.

The access to different fluctuation dynamics provides many opportunities for further investigations. In particular, if an increase of the electron temperature to ~ 10 eV can be accomplished by an extra microwave heating (which is planned to go into operation in the near future), the very attractive regime of electromagnetic drift waves (drift Alfvén waves)

¹Recall that $\partial_r N$ reads in physical units $\rho_s \partial_r n_0 / n_0 \propto \partial_r n_0 / n_0 B$.

would become accessible. This would allow for a comparison between electrostatic and electromagnetic drift waves within one experimental device. For investigations of other instabilities and waves the occurrence of a low-frequency instability is often undesired. It was also shown here, that parameter regimes exist where the plasma is very quiescent and which might be thus more suitable for such investigations.

Part II

Synchronization of drift waves

Chapter 9

Introduction

In the following chapters, a different aspect of the drift instability is addressed: the control of drift wave dynamics by mode-selective synchronization. Attempts to control the drift wave dynamics have been reported since the late 1960s [48,49]. This has been motivated by the anomalous transport, closely connected to drift waves [8,14]. Changing the drift wave dynamics is expected to change the fluctuation-induced transport. Drift waves can be stabilized by changing the global plasma parameters (see chapter 6). This is, however, sometimes undesired or even impossible. An option to change the plasma dynamics without altering the global plasma parameters is thus desirable.

An overview of common control schemes is given in figure 9.1 [127]. Schematic diagrams of three different closed-loop control schemes are shown in figure 9.1a-c). A common feature of these schemes is that signals obtained from the system itself are fed back and used to control the system. The chaos control schemes in figure 9.1a,b) aim at stabilizing particular unstable periodic orbits that are part of the uncontrolled chaotic dynamics of the system. Stabilization is achieved by tiny adjustments of one or more accessible parameters. The success of this conception was demonstrated on various different plasma waves and instabilities [127]. Using a time-delayed feedback technique (figure 9.1b), drift wave chaos (existing only in a narrow regime of the transition route to turbulence [54]) was successfully controlled [53].

The goal of the classical feedback in figure 9.1c) is to remove the instability. This is done by feeding back a filtered, phase-shifted and amplified signal obtained from the system itself [127]. Attempts to apply relatively simple feedback schemes to drift waves and other plasma instabilities have been reported since the late 1960s [48,49] but often with ambiguous conclusions. The fluctuations of a certain dynamical state could indeed be reduced and the confinement was improved. However, only single modes could be suppressed with one circuit and thus no broadband reduction of the fluctuations was achieved. More recently, multimode feedback stabilization of two different instabilities with a single sensor-suppressor pair was experimentally demonstrated [128]. Feedback techniques have also been tested in the edge turbulence of fusion devices, but a global change of the particle transport has not yet been achieved [129].

For open-loop control (figure 9.1d), the control signal is typically pre-determined and not directly derived from the actual dynamics of the system at the time [127]. The synchronization technique presented here follows such an open-loop scheme.

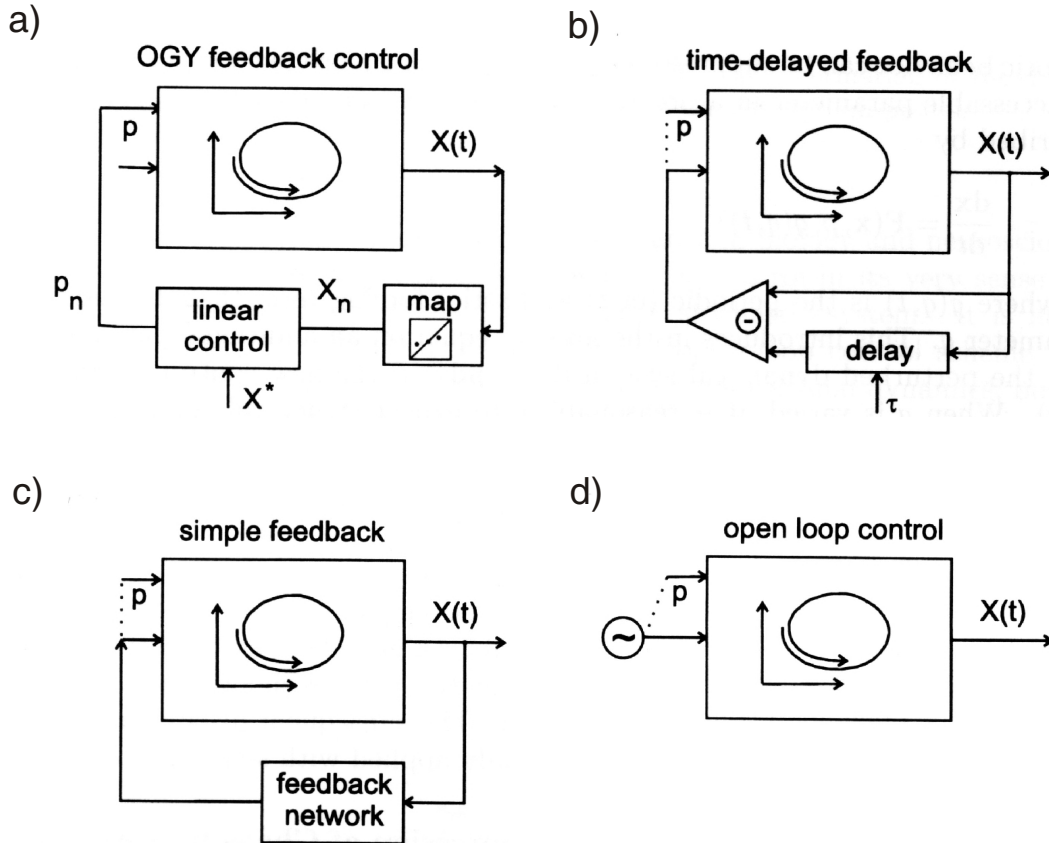


Figure 9.1: *Conceptual overview over different control schemes (from reference [127]).*

Since drift wave dynamics is a spatiotemporal phenomenon, purely temporal or spatial control techniques can barely be expected to be efficient and robust. Nevertheless, the spatial dynamics was almost never taken into account in the attempts to use feedback techniques to control the drift instability. The present work aims at applying a spatiotemporal control scheme. To achieve this, a recently proposed strategy was followed, open-loop control (synchronization) acting in both space and in time [55]. Inherently, application of such a method does not allow for a suppression of all fluctuations, but a certain dynamical state can be selected out of broadband turbulence. Here, it is intended to drive preselected drift modes at the expense of the broadband turbulence. Initial steps conducted in the KIWI device were reported in reference [115] and showed that drift wave dynamics can be influenced – to some extent – with spatiotemporal driver signals. However, the result was not fully satisfying because the broadband turbulence background could not be significantly reduced. Our experiments were conducted in the MIRABELLE device at the LPMI in Nancy (France) and show that synchronization of drift wave dynamics is possible with a modified setup. In the following, the concept of synchronization is briefly introduced.

9.1 What is synchronization?

The synchronization phenomenon was first observed and scientifically described by HUYGENS as early as in the 17th century [130]. Synchronization is widely encountered in various fields of science and engineering, and although it has been known for a long time, it were the developments in radio communication and electronics that lead to more in-depth studies on the subject. In the mid-1920s, VAN DER POL and VAN DER MARK constructed radio tube oscillators which became frequency locked when driven with a sinusoidal signal [131]. VAN DER POL was among the first who studied synchronization effects theoretically [132]. The practical application of these studies was the possibility to stabilize the frequency of a powerful generator with the help of a weak but very precise reference signal. During the last 20 years, also the synchronization of chaotic systems became a field of intense research [52,130]. It has been found that due to an interaction of two or more identical chaotic systems the dynamical states can coincide while the dynamics remain chaotic [130]. Another possibility is ‘chaos-destroying’ synchronization when a periodic external force acting on a chaotic system changes the dynamics of the system from a chaotic to a periodic state [130]. The rather new area of chaos synchronization opens new possibilities for secure transmission of information since synchronization may provide the possibility to recover information transmitted with broadband chaotic carrier signals [133].

Synchronization is a basic nonlinear phenomenon and can be defined as the adjustment of rhythms of self-sustained oscillating objects due to a weak interaction between them [130]. Synchronization means that the frequencies of interacting periodic systems may become the same or lock in a rational ratio. This is also called entrainment. Interacting periodic systems with frequencies ω and ω_0 are usually called synchronized if either their phases ϕ and ϕ_0 are locked

$$|n\phi - m\phi_0| < \text{const}, \quad n, m \in \mathbb{N} \quad (9.1)$$

or if the weaker condition of frequency entrainment

$$\omega : \omega_0 = n : m, \quad n, m \in \mathbb{N} \quad (9.2)$$

is fulfilled [134]. Synchronization phenomena can be classified by different features: [52, 130]:

Mutual synchronization: Two or more oscillating systems equally affect each other and mutually adjust their rhythms. The coupling between the systems is bi-directional.

Synchronization by external forces: The coupling between the systems is uni-directional, i.e., one oscillator drives the other one.

Phase synchronization: Only the phases (or frequencies) are adjusted and the amplitude of the oscillating systems can be completely uncorrelated.

Complete synchronization: Amplitude and phase of the oscillating systems are adjusted and thus correlated.

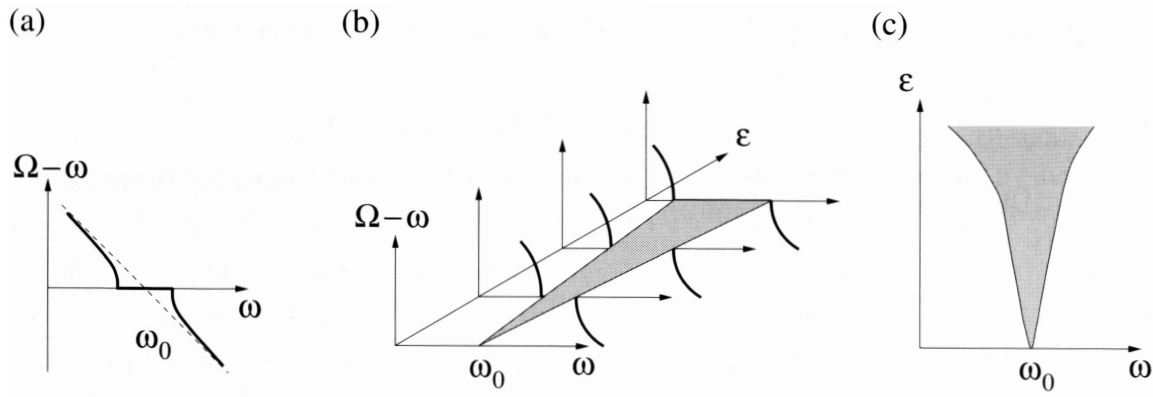


Figure 9.2: a) For a fixed value of the forcing amplitude ϵ the frequency response of the system is shown. b) Same as in a) for different values of ϵ . c) The so-called Arnold tongue describes the domain where the frequency Ω of the driven oscillator is the same as the driver frequency ω . Taken from reference [130]

Synchronization is possible for both, oscillators showing periodic behavior and oscillators of which at least one exhibits chaotic behavior [130]. Two driving methods are possible: The coupling between the oscillators can either be continuously applied or can be switched on at discrete times $t_n = nT$ if the coupling and the time interval T are suitably chosen (sporadic drive) [130]. The coupling depends on two quantities:

1. The coupling strength describes how strong the interaction between the systems is.
2. The frequency mismatch $\omega - \omega_0$ describes the difference between the uncoupled oscillators.

Figure 9.2 shows the influence of an external harmonic force $f(t) = \epsilon \sin(\omega t + \phi)$ on a periodic, self-sustained harmonic oscillator $x(t) = \epsilon_0 \sin(\omega_0 t + \phi_0)$ with a natural frequency ω_0 . In case of driving, its frequency changes and is denoted with Ω . Figure 9.2a) depicts the frequency response if the forcing amplitude ϵ is kept constant. For a sufficiently small detuning, $\omega - \omega_0$, the driver $f(t)$ is able to entrain the oscillator $x(t)$, such that the frequency Ω of the driven oscillator equals the driver frequency ω . If the detuning exceeds a critical value, Ω starts to deviate from the driver frequency ω , although it is still not identical with ω_0 . The driving force is too weak to entrain the oscillator, but it ‘pulls’ the frequency of the system towards its own frequency. For this case of incomplete entrainment, periodic pulling is often observed which means that the dynamics is frequency modulated [130]. Figure 9.2b) shows a family of curves $\Omega - \omega$ vs. ω for different values of the forcing amplitude ϵ . The gray area displays the region where $\Omega = \omega$. This region is plotted also in figure 9.2c) and is known as the synchronization region or Arnold tongue [130].

Chapter 10

Experimental setup for the synchronization of drift waves

10.1 The MIRABELLE device

The synchronization experiments were conducted in the linear, magnetized, low- β , triple plasma device MIRABELLE. A schematic view of the device is given in figure 10.1. It consists of two plasma source chambers and a magnetized cylindrical midsection where the experiments are done. The midsection has a diameter of 26 cm and a length of 1.4 m. In the source chambers, argon plasma is produced by a thermionic hot-cathode discharge in steady state operation. Each source chamber is separated from the midsection by a stainless steel mesh grid with a transparency of more than 60%. Both grids can be biased

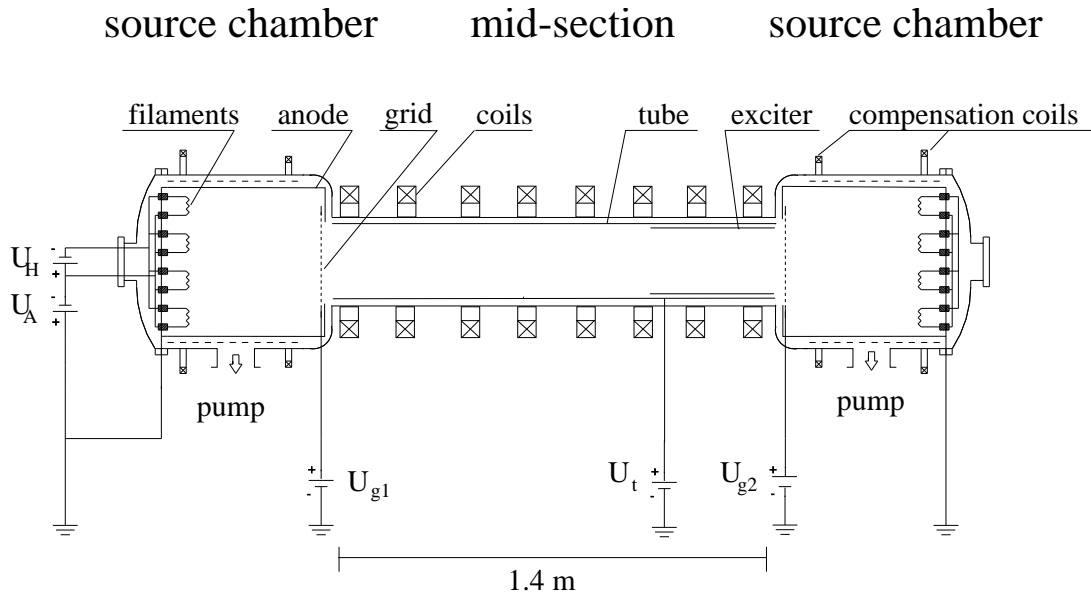


Figure 10.1: Schematics of the MIRABELLE device. $U_{g1,2}$ are the bias voltages of the grids that separate the source chambers from the midsection. U_t is the bias voltage of the tube inside the midsection.

with respect to the vacuum vessel. For the synchronization experiments, only one of the source chambers is operated. The grid between the active chamber and the midsection is positively biased with U_g , while the other grid is connected to ground, acting as a loss surface. In this way, electrons are injected from the active chamber into the midsection and, to a certain degree, an $E \times B$ rotation of the plasma column is established [16]. In the midsection, a magnetic field of up to 110 mT is produced by a set of 25 water-cooled coils. The magnetized plasma column is immersed in a stainless-steel tube (diameter 23 cm) which is positively biased with U_t and predefines the potential at the poloidal boundary. The magnetic field in the source chambers is compensated in order to avoid a magnetic mapping of the filaments into the midsection [109].

Like in VINETA, drift waves propagate poloidally in the magnetized plasma column [116]. In MIRABELLE, the main control parameters for drift wave dynamics are the grid bias U_g and the tube bias U_t . Both superimpose a radial electric field across the plasma column and thereby determine the $E \times B$ rotation of the plasma column and the electron flux from the source chamber into the plasma column of the midsection. The parallel electron drift is, as outlined above, a mechanism leading to a destabilization of drift waves [9]. Increasing either U_g or U_t leads to a transition scenario from a stable plasma state to drift wave turbulence [54,116].

Table 10.1 summarizes typical operation and plasma parameters. Differences between the plasma parameters of the VINETA device and the MIRABELLE device have already been discussed in section 5.4. Further reading is found in references [109,116].

Figure 10.2 shows typical radial plasma density and plasma potential profiles [116]. The density peaks in the plasma center and the radial profile is close to a Gaussian. The plasma potential has a minimum in the plasma center and its shape is close to a parabola. The radial shapes of plasma density and plasma potential imply that both, the diamagnetic and the $E \times B$ drift, are unshered (see section 5.2). In contrast to the VINETA device,

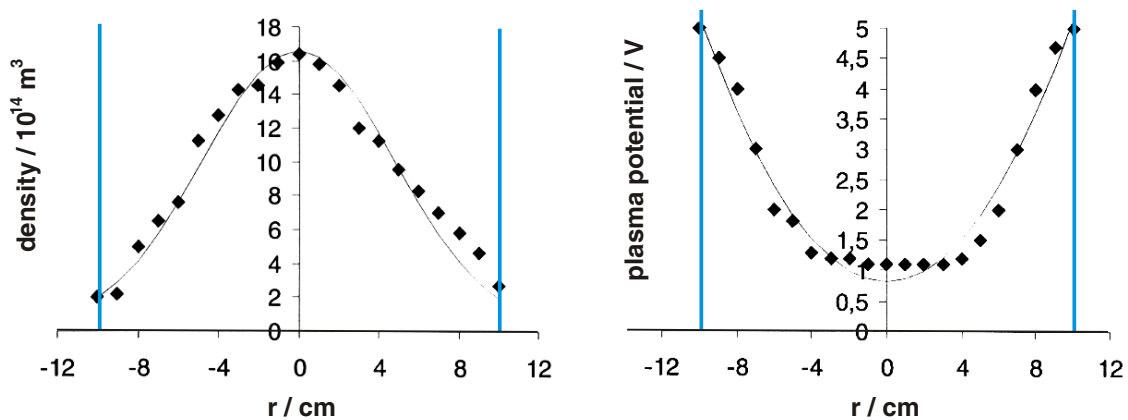


Figure 10.2: Typical radial plasma density and plasma potential profiles for the MIRABELLE device. The measured values are indicated by filled symbols \blacklozenge . The density profile is fitted by a Gaussian. The plasma potential profile is fitted by a parabola. The vertical blue lines indicate the radial position of the octupole exciter which is installed in the edge of the plasma column. From reference [116] (measured without exciter installed).

parameter	typical value/range
base pressure	$3 \cdot 10^{-3}$ Pa
neutral gas pressure (Argon)	$4 \cdot 10^{-2}$ Pa
magnetic field	25-40 mT
tube bias	$0 < U_t < 14$ V
grid bias	$3.6 < U_g < 15$ V
peak electron density	$2 \cdot 10^{15}$ m ⁻³
electron temperature	2 eV
ion temperature	≈ 0.03 eV
electron gyrofrequency	$7 \cdot 10^9$ rad/s
ion gyrofrequency	$1 \cdot 10^5$ rad/s
electron gyro radius	0.08 mm
ion gyro radius	2.8 mm
effective gyro radius	23 mm
Debye length	0.2 mm
thermal electron velocity	$6 \cdot 10^5$ m/s
thermal ion velocity	270 m/s
ion sound velocity	2200 m/s
diamagnetic. electron drift velocity.	1400 m/s
plasma β	10^{-6}
β_μ	10^{-1}

Table 10.1: Typical operation and plasma parameters for the MIRABELLE device. Plasma parameters taken from reference [116].

they point in the same direction and the drift wave frequency is thus increased due to Doppler shift.

10.2 Diagnostics

The drift wave dynamics are observed using cylindrical Langmuir probes. Time series were recorded of either the floating potential or the electron saturation current. Temperature fluctuations are neglected and it is assumed that $\tilde{I}_{e,sat} \propto \tilde{n}$ and $\tilde{\phi}_f \propto \tilde{\phi}_p$ (see section 4.2.1).

The spatiotemporal drift wave dynamics are observed using a circular probe array of cylindrical Langmuir probes (COURONNE) [110], schematically shown in figure 10.3. The probe array installed in the MIRABELLE consists of only 32 probes and is usually operated in the electron saturation regime. The cylindrical probes have a diameter of 0.2 mm, a length of 4 mm and are arranged on a circle with 14 cm diameter which corresponds to a poloidal spatial resolution of 1.4 cm. The probe array was installed at an axial distance of about 40 cm from the source grid.

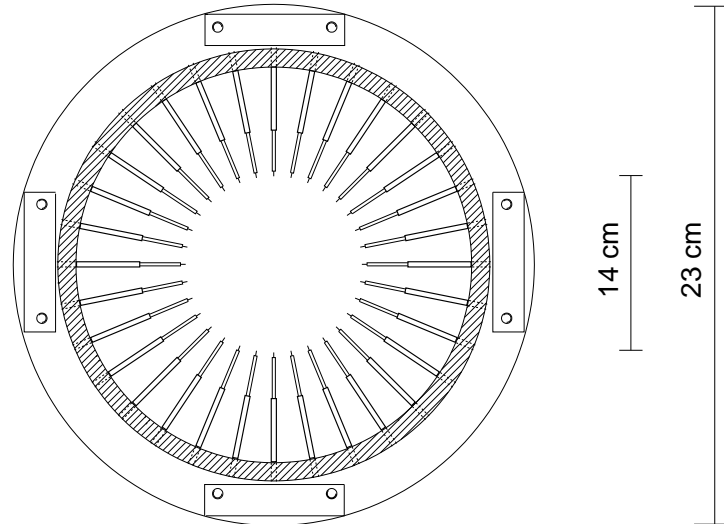


Figure 10.3: The 32 probe array COURONNE which is used in the MIRABELLE device.

10.3 The octupole exciter

For the synchronization experiments, an arrangement of eight stainless-steel electrodes (octupole exciter) is positioned in flush-mounted geometry in the edge region of the plasma column (see figure 10.4). The electrodes have a length of 32 cm and are arranged on a circle with diameter 20 cm, such that they are 15 mm separated from the surrounding tube. The gap between each two neighboring plates is 2 mm. Each of the electrodes is driven by a sinusoidal signal with the same frequency but a fixed, preselected phase angle δ between neighboring electrodes.

The driver signals are generated by a 8 channel PC-based analog output board with 12-bit resolution. The signal of each output channel is amplified and connected to one of the electrodes. In this way an (AC) current can be drawn to each electrode. The maximum applied peak to peak voltage was 20 V while the maximum possible current was limited by the power amplifier to 1 A. The possibility to draw a current to the electrodes is the main difference between the setup presented here and a previously used setup for measurements conducted in the KIWI device [115] where the electrodes were galvanically decoupled from the frequency generator.

In figure 10.5 typical driver signals are shown. The chosen phase shift between the channels leads to a poloidally propagating wave pattern. The frequency determines the propagation velocity, while the sign of the phase shift determines the direction of propagation and controls the poloidal wavelength. A phase shift $\delta = m_d\pi/4$ corresponds to poloidal mode number m_d . For the octupole exciter, NYQUIST's sampling theorem restricts the mode number range to $m_d = 1, 2, 3$. A pattern corresponding to an $m_d = 4$ mode can be established but with ambiguous propagation direction.

In the laboratory frame, the phase velocity of drift waves is determined by the diamagnetic drift velocity and the $E \times B$ drift velocity of the plasma column. The wave pattern applied to the octupole exciter can propagate either in the same direction as the drift waves or in the opposite direction. This is referred to as corotating or counterrotating exciter field,

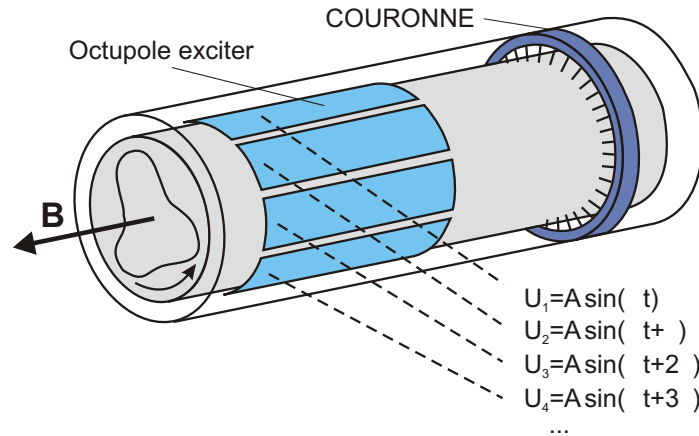


Figure 10.4: Experimental arrangement used for the synchronization of drift waves. Shown are the octupole exciter in the edge region of the plasma and the poloidal probe array COURONNE which was used for the observation of the spatiotemporal dynamics. Sinusoidal signals are applied to the exciter plates #1-#8. Between neighboring electrodes the signals are phase shifted.

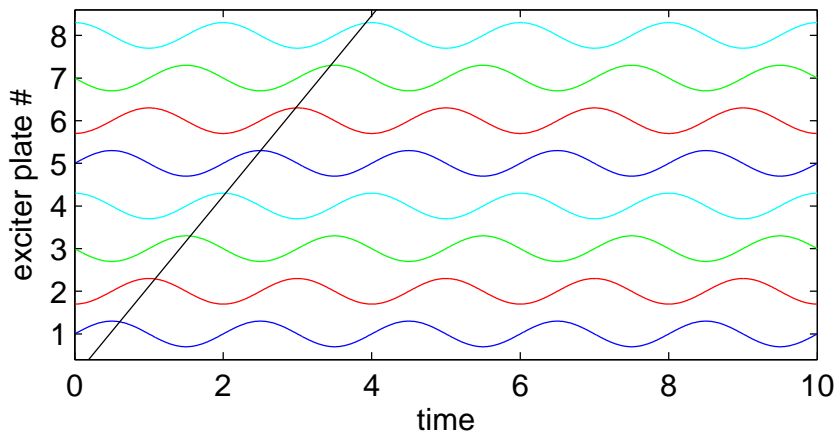


Figure 10.5: Sinusoidal voltage signals applied to the eight exciter electrodes. All signals have the same frequency but a fixed phase shift is applied between each two neighboring plates. The straight line indicates the poloidal propagation of one maximum of the applied exciter field in the plasma column.

respectively. The idea is that the rotating exciter field created with the octupole exciter drives a specific drift mode with phase velocity $v_\phi = 2\pi f_d r_x / m_d$ with r_x being the radial position of the exciter electrodes. Frequency and mode number of the applied signals are chosen such that they are compatible with the drift wave dispersion. The frequency is chosen to be close to an experimentally observed peak in the power spectrum, while the corresponding mode number can be determined from instantaneous measurements with the poloidal probe array.

Chapter 11

Synchronization of drift waves: experimental results

Different drift wave dynamics can be observed in the MIRABELLE device, e.g., single coherent saturated modes, chaotic drift wave states, and weakly developed drift wave turbulence [116]. Synchronization experiments have been conducted for different initial states. Three examples of synchronization of drift waves are presented subsequently in some detail. The spatial information of the driver signal is believed to play an important role in the concept of the spatiotemporal open-loop synchronization. In section 11.1 results obtained using purely temporal driver signals are compared to those obtained by applying spatiotemporal driver signals. Additionally, the influence of both, corotating as well as counterrotating exciter fields, on the initial states is investigated.

11.1 Temporal versus spatiotemporal drive

With the exciter setup it is possible to investigate the influence of purely temporal as well as of spatiotemporal driver signals on the drift wave dynamics. In figure 11.1, the results for different driver signals are compared. A power spectrum and a frequency-mode-number spectrum for a weakly developed turbulent state are shown in the first row of figure 11.1. Here, no signals were applied to the electrodes. The power spectrum $S(f)$ is broadband (figure 11.1a), even though a few pronounced peaks are seen in the low-frequency regime ($f < f_{ci} = 15$ kHz, the ion cyclotron frequency). Such low-frequency peaks embedded into broad-band spectra have previously been observed for drift wave turbulence in plasmas with cylindrical geometry [23,135]. In the frequency-mode-number spectrum $S(f, m)$, shown in figure 11.1b), spectral components are scattered over a broad area in the (f, m) -plane and show no pronounced peaks. The other rows of figure 11.1 show the dynamics for different exciter signals. In all cases, the frequency and the amplitude of the exciter signals are kept constant at 8 kHz and 4 V, respectively. In the second and third row, results are shown for temporal exciter signals applied to the electrodes: Figure 11.1c,d) show the resulting dynamics if the same exciter signal is applied to all eight exciter electrodes, i.e., the phase shift δ is zero. In figure 11.1e,f), the exciter signal is applied only to one single plate of the octupole exciter while the other electrodes are kept floating. This corresponds to a local temporal perturbation. In both cases, the drift

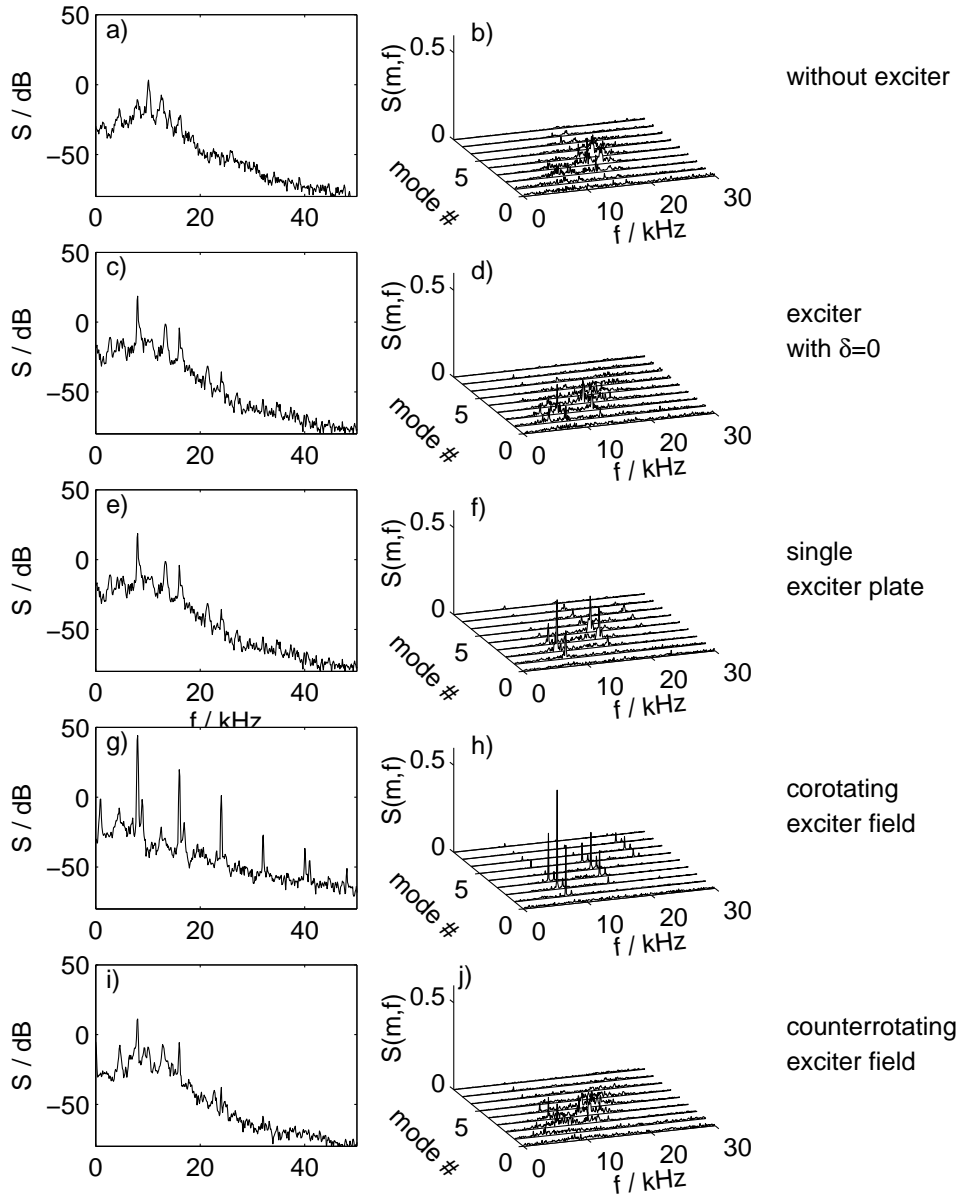


Figure 11.1: Comparison of the influence of temporal and spatiotemporal driver signals: Shown are power spectra and frequency-mode-number spectra for a,b) initial state without exciter signal applied, c,d) exciter field with zero phase shift between the plates, e,f) exciter signal applied to only one of the eight plates, g,h) spatiotemporal $m_d = 2$ corotating exciter field, i,j) spatiotemporal $m_d = 2$ counterrotating exciter field. For all cases, the exciter field is driven with a frequency of 8 kHz and an amplitude of 4 V.

wave dynamics are similar to the state without any driver signal applied. The peak at the driver frequency is slightly more pronounced but the low-frequency background of the spectra remains uninfluenced.

In figure 11.1g,h), a corotating exciter field with a wave pattern corresponding to $m_d = 2$ mode is applied. The drift wave dynamics change completely. Both spectra are now dominated by a sharp peak at the driver frequency, while the broadband background is suppressed to some degree. Note that the relatively strong sidebands in the mode in figure 11.1h) are an artefact due to the limited number of probes of the poloidal array. We may conclude that the drift wave dynamics are synchronized to the exciter field. Figure 11.1i,j) depicts the effect of a counterrotating $m_d = 2$ exciter field. This has only a weak influence on the drift wave dynamics, quite similar to the temporal drive. To summarize, only a corotating exciter field yields a significant modification of the drift wave dynamics.

11.2 Spatiotemporal synchronization

Figure 11.2 shows the synchronization of a weakly developed turbulent drift wave state. This state was established by choosing grid bias $U_g = 5$ V and tube bias $U_t = 12$ V. The unperturbed case is depicted in figure 11.2a-d). The time trace of the floating potential

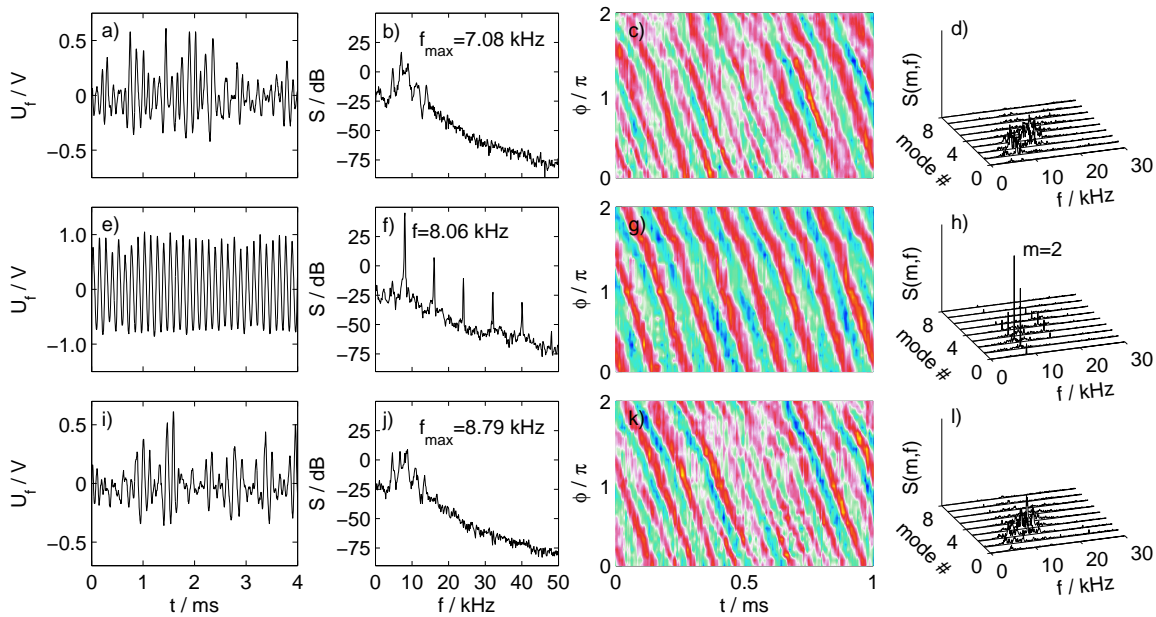


Figure 11.2: Temporal and spatiotemporal drift wave dynamics for a weakly developed turbulent state: The three rows correspond from top to bottom to the unperturbed case without any exciter signal applied, active exciter with a corotating field and active exciter with a counterrotating field, respectively. The four columns show time series of the floating potential fluctuations, frequency power spectra (obtained from a single tip of the probe array), space-time diagrams of the floating potential fluctuations and frequency-mode-number power spectra (linear scale). The driver amplitude is $A = 1.0$ V. Published in reference [136].

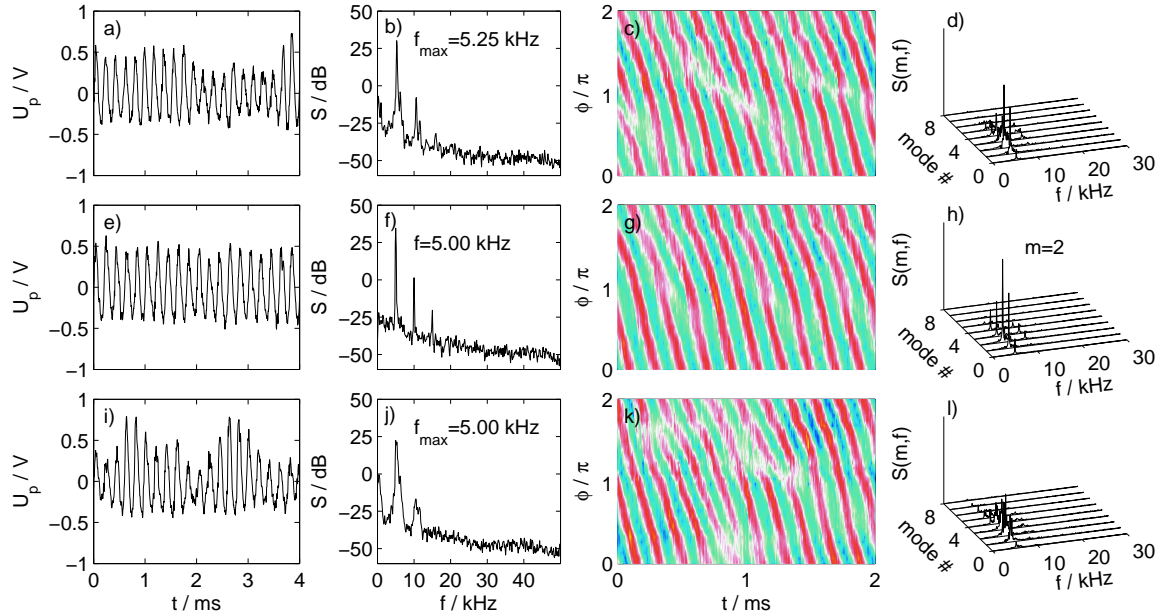


Figure 11.3: Temporal and spatiotemporal drift wave dynamics for another dynamical drift wave state. The organization of the figure is the same as in figure 11.2. Driver amplitude: 1.0 V. Published in reference [137].

fluctuations (figure 11.2a) exhibits irregular features and the corresponding frequency power spectrum $S(f)$ (figure 11.2b) is broadband with a few more pronounced small peaks. The spatiotemporal data (figure 11.2c), obtained with the probe array, is dominated by irregular features and no clear-cut mode structure is observed [16,54]. This is corroborated by the frequency-mode-number spectrum (figure 11.2d) where no pronounced peaks are found but the spectral power is scattered over a broad area in the (f, m) -plane. For synchronization of drift wave turbulence, a driver frequency f_d is chosen to be close to pronounced spectral features in the low-frequency regime. An exciter signal with mode number $m_d = 2$, driver frequency $f_d = 8.0$ kHz, and driver amplitude $A = 1.0$ V is chosen. When a corotating exciter field is applied, the drift wave turbulence is successfully synchronized as shown in figure 11.2e-h). The floating potential fluctuations (figure 11.2e) are now fairly regular and have a relatively large amplitude, of the order of twice the largest events in the turbulent state (figure 11.2a). Note the different scale here. The frequency power spectrum (figure 11.2f) is sharply peaked at 8.06 kHz and its higher harmonics, meaning that the preselected mode is enhanced at the expense of broadband low-frequency spectral components. Regular dynamics dominate also the spatiotemporal data (figure 11.2g). A wave structure with mode number $m = 2$ is found, which is also seen in the sharply peaked frequency-mode-number spectrum $S(f, m)$.

To verify that the control effect is really of spatiotemporal nature, the sign of the phase shift δ and thus the rotation direction of the exciter field is reversed. Except for the sign of δ , all other parameters are kept the same. Figure 11.2i-l) shows the result. A counterrotating exciter field has almost no influence on the drift wave turbulence (see above). The features of the fluctuations are barely distinguished from the unperturbed case (figure 11.2a-d). This means that the interaction between the counter-rotating exciter

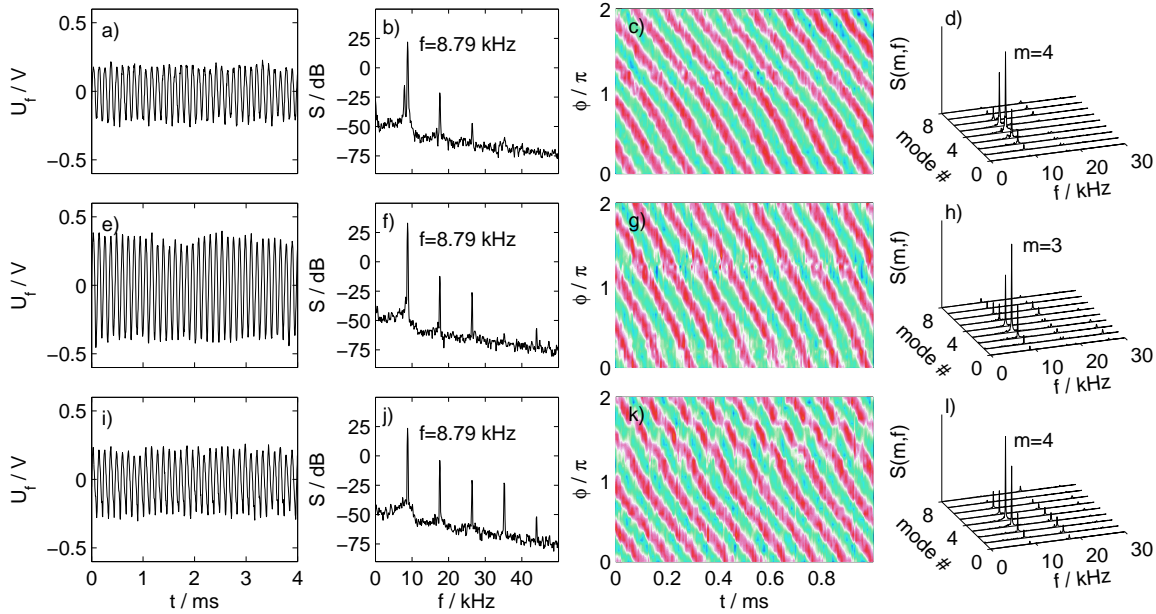


Figure 11.4: Temporal and spatiotemporal drift wave dynamics for a saturated $m = 4$ mode which is synchronized to a mode with a different mode number $m_d = 3$. The picture is organized in the same way as figure 11.2. Driver amplitude: 7.0 V. Published in reference [137].

field and the drift wave turbulence is weak.

Figure 11.3 compiles the influence of the octupole exciter on a more coherent drift wave state ($U_g = 15$ V, $U_t = 0$ V). Without any driver signal applied, the probe signal fluctuations (figure 11.3a) show regular sequences alternating with irregular ones. The amplitudes of the fluctuations are irregular and change by a factor of two. The frequency power spectrum (figure 11.3b) has a broadened peak at 5.25 kHz. The spatiotemporal pattern in figure 11.3c) shows an $m = 2$ mode, which is occasionally broken by phase defects [54]. In summary, figure 11.3a-d) shows a state at the transition from a single coherent $m = 2$ mode to weakly developed turbulence [54]. The mode structure dominates the dynamics but regular sequences are alternating with irregular ones, both in space and time.

In the second row (figure 11.3e-h), this drift wave state is synchronized with a corotating exciter signal of frequency 5.0 kHz, amplitude 1.0 V and phase shift $\delta = \pi/2$, corresponding to an $m_d = 2$ mode structure. As a result, the potential fluctuations become significantly more regular (figure 11.3e) with a sharply peaked frequency power spectrum (figure 11.3f). Also the higher harmonics become more pronounced. The drift wave dynamics is synchronized to the preselected mode as in the weak turbulence case above. This is confirmed by the spatiotemporal pattern (figure 11.3g). The $m = 2$ mode clearly rules the dynamics and no phase defects are observed. The result for the counterrotating case is shown in figure 11.3i-l) and is again similar to the undriven case, leading to the conclusion that the right orientation and speed of the synchronization signal are essential.

Figure 11.4 presents another case: a saturated drift mode is driven with an exciter field with a frequency equal to the observed frequency but with a different mode number m_d ($U_g = 9.9$ V, $U_t = 0$ V). In figure 11.4a-d) the initial state is shown, a single saturated $m = 4$ mode with frequency 8.8 kHz. The spatiotemporal pattern shows a regular drift

mode (figure 11.3c) and sharp peaks are seen in the frequency-mode-number spectrum (figure 11.3d). In the second row is the octupole exciter driven at a frequency of 8.85 kHz, with amplitude 7.0 V, and phase shift $\delta = 3/4\pi$, corresponding to $m_d = 3$. Application of a corotating exciter field (at relatively high drive amplitude) enforces a saturated drift wave with the same frequency, but with different mode number $m = 3$ (figure 11.3e-h). Due to the strong drive the fluctuation amplitude grows by a factor of two. If the exciter is driven with a counterrotating field, again the drift wave dynamics remains almost uninfluenced (figure 11.3i-l).

11.3 Final remarks

It was demonstrated that mode-selective synchronization is possible for different drift wave dynamical states. Weakly developed turbulence can be tamed, i.e., can be suppressed by driving one single mode with the octupole exciter. Modes which are not fully coherent can be driven into coherent ones and it is even possible to transform one mode into another with the same frequency but a different mode number. The frequencies of the drift waves are fully entrained by the driver signals, while the amplitudes are still slightly changing in time. Thus, at least phase synchronization was achieved. Synchronization is possible for different mode numbers $m_d = 1 - 3$, if the frequency is chosen appropriately. However, $m_d = 2$ usually requires the lowest driver amplitude.

Counterrotating driver patterns as well as purely temporal driver signals are found to have almost no influence on the drift wave dynamics. This strongly supports the idea of *spatiotemporal* synchronization [138]. Only for a spatial resonance with standing driver pattern in the wave frame, drift modes can be amplified at the expense of the broadband background turbulence.

From the experiments, it remains unclear how the octupole exciter couples to the drift wave dynamics. This point will be discussed in chapter 13 in connection with numerical results given in chapter 12.

Chapter 12

Synchronization of drift waves: simulation results

Numerical simulations of the synchronization of drift wave turbulence were conducted in cooperation with NAULIN from Risø National Laboratory, Denmark. The main motivation is to identify the basic physical mechanism how the external synchronization signal is coupled to the drift wave dynamics.

12.1 The theoretical model

For the numerical simulations the HASEGAWA-WAKATANI drift wave model [65] is used (see equations (2.34) and (2.35)). The radial background density profile $n_0(r)$ is kept fixed and no local approximation for the density gradient is employed. The exciter is modelled by an oscillatory parallel current profile. The driver term $S = \nabla_{\parallel} J_{ext}$ is assumed to be of the functional form

$$S = \nabla_{\parallel} J_{ext} = A \sin(\pi r/r_0) \sin(2\pi m_d \theta - \omega_d t) \quad , \quad (12.1)$$

where r_0 is the radius of the plasma, θ is the poloidal coordinate, m_d and ω_d are the driver mode number and the driver frequency, respectively. The poloidal structure of S is depicted in figure 12.1. We underline that a rotating electric field distribution instead of a current profile was found not to be able to lead to synchronization.

The three-dimensional model is reduced to two spatial dimensions by introducing an effective parallel wavenumber $\nabla_{\parallel}^2 \approx -k_{\parallel}^2$ (see also section 2.4). The equations of the 2D model including the additional driver term S are

$$\frac{\partial}{\partial t} \nabla_{\perp}^2 \phi + \vec{V}_E \cdot \nabla \nabla_{\perp}^2 \phi = \tilde{\sigma} (\phi - n) - S + \mu_w \nabla_{\perp}^4 \phi \quad (12.2)$$

$$\frac{\partial}{\partial t} n + \vec{V}_E \cdot \nabla (n_0 + n) = \tilde{\sigma} (\phi - n) - S + \mu_n \nabla_{\perp}^2 n \quad (12.3)$$

where $\tilde{\sigma} = k_{\parallel}^2 \sigma$. In small layers around $r = 0$ and $r = r_0$ the viscosities were enhanced by a factor 200. These layers act as sources and sinks and sustain the background density gradient. Equations (12.2) and (12.3) are solved using the ARAKAWA scheme [139] to

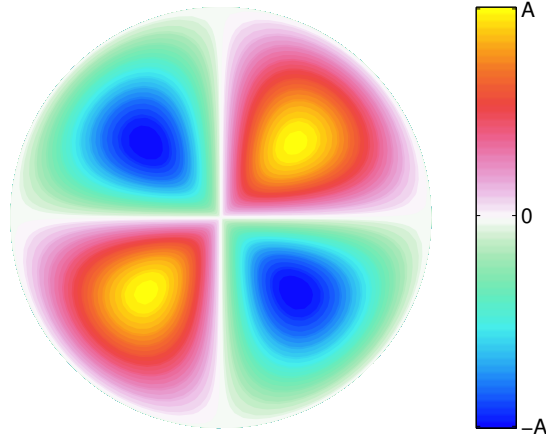


Figure 12.1: *Poloidal structure of the driver term S in the numerical simulation.*

discretize nonlinearities and the density background term, and second order centered finite differences for the remaining terms. For time stepping a third-order stiffly stable splitting method is used [140]. Simulations are performed in poloidal coordinates on a disk, with 64×128 grid points in the radial and poloidal direction, respectively.

The simulations aim at a qualitative reproduction of the synchronization effect. A quantitative agreement between experiment and numerical simulation cannot be expected from the model applied. In principle, simulations may give insight into further interesting points, especially in the change of the fluctuation-induced transport. This is not the case in the 2D model used here since the model is not self-consistent due to the artificially fixed radial density profiles.

12.2 Simulation results

The density profile used is of the form $n_0 = 2.5 \cos(r/r_0)$, with $r_0 = 10$ and the viscosities $\mu_{n,w}$ are of the order of 10^{-3} and $\tilde{\sigma} = 0.1$. These parameters were chosen to establish a saturated turbulent state similar to the experimentally observed one (see figure 11.2). Time series of the density and potential fluctuations are analyzed using the same data analysis tools as for the experimental data.

The simulation results for a turbulent state is shown in figure 12.2. By comparing figures 11.2 and 12.2 it becomes evident that the experimental findings discussed above are qualitatively reproduced by the simulation. In figure 12.2a-d) unperturbed drift wave turbulence is found in the simulation which has similar characteristics as in experiment: broad peaks are observed in the low-frequency regime and the spectral power drops towards higher frequencies. A synchronized $m = 2$ state is achieved at relatively small driver amplitude ($A = 0.75$) if a corotating current profile with $m_d = 2$ is applied (figure 12.2e-h). The fluctuations are fairly regular and the amplitudes are much higher than for the undriven case. The power spectrum is sharply peaked at the driver frequency and higher harmonics. A counterrotating current profile of the same amplitude has almost no effect on the drift wave dynamics (figure 12.2i-m).

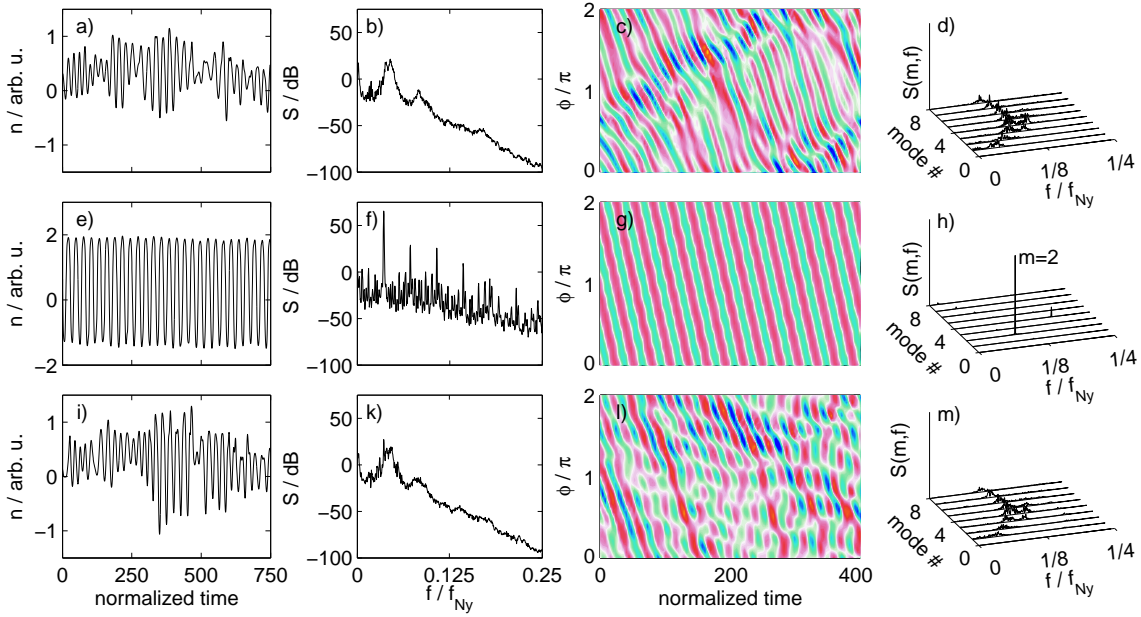


Figure 12.2: Simulation results for drift wave turbulence without driver term (top row), corotating driver (middle row) and counterrotating driver (bottom row). The figure is organized in the same way as figures 11.2–11.4. (Published in reference [136].)

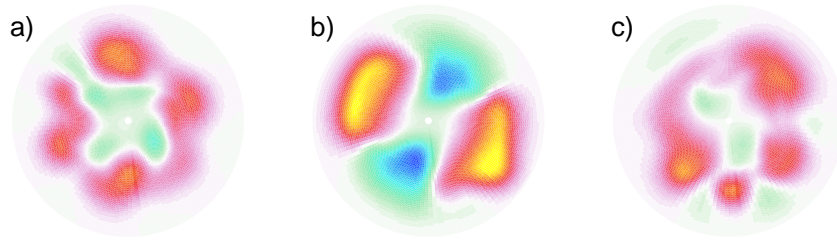


Figure 12.3: Snapshot of the drift wave mode structures in the poloidal plane obtained from the numerical simulation. Color coded plots of the density fluctuations. a) without driver term (corresponding to figure 12.2a-d). b) corotating driver (corresponding to figure 12.2e-h). c) counterrotating driver (corresponding to figure 12.2i-l). Published in reference [136].

The numerical model allows for inspection of the drift mode structure in the entire poloidal plane, as shown in figure 12.3. In the undriven case (figure 12.3a), irregular structures prevail. If a corotating driver term with $m_d = 2$ is included (figure 12.3b), a clear $m = 2$ mode structure is obtained, corroborating that synchronization is achieved. For a counterrotating driver term, irregular structures similar to those in the undriven case are observed (figure 12.3c).

We conclude that the experiment is qualitatively reproduced by simulation. The two model equations (12.2) and (12.3) are coupled mode-selectively via $\nabla_{\parallel} J_{ext}$ of a rotating current profile. In the drift wave frame, the poloidal symmetry is broken by the structured current profile leading to a mode-selection. As a result, the preselected mode is amplified at the expense of the broadband low-frequency spectral components.

Chapter 13

Summary and Conclusions

Mode-selective control of drift wave turbulence by spatiotemporal synchronization was demonstrated in experiment and numerical simulation. In the experiment, synchronization of drift modes was achieved by using phase-shifted sinusoidal driver signals applied to an octupole exciter which creates a poloidally propagating drive pattern. If the spatiotemporal drive pattern is resonant in the moving frame of a preselected drift mode, it is phase-locked and amplified at the expense of the broadband underground of coupled modes. These experimental findings are qualitatively well reproduced in simulations based on a HASEGAWA-WAKATANI model modified to match the experimental conditions. Also in the numerical simulation, synchronization of a weakly developed turbulent state to a single (preselected) mode is observed.

In a co-activity, BLOCK conducted experiments in the KIWI device (resembling the MIRABELLE) with the same experimental arrangement. It was found that a coherent drift mode can be phase synchronized within a certain frequency range [123]. The phase shift of the drift wave density fluctuations and the exciter potential signal is then zero [141]. Consequently, at each time instant, the drift wave maximum (positive density/potential fluctuations) is at the same poloidal position as the positive potential of the exciter signal. For exciter frequencies close to the synchronization boundaries, periodic pulling with spatiotemporal features is observed [141,142]. Synchronization of a single drift mode leads to reduction of the fluctuation-induced transport by about 30% [142]. For incomplete synchronization, the fluctuation-induced transport remains nearly the same but its features differ significantly from the undriven case. The findings of BLOCK are fully consistent with the results presented here.

A combination of active and passive probe tips was used by THOMSEN to investigate the coupling between an externally applied propagating wave pattern and the turbulent plasma dynamics in the scrape-off layer of a fusion device [143]. Enhanced coupling was found for copropagating wave patterns compared to counterpropagating patterns. In case of copropagation, the driven wave was not only localized to the injection area but could also be observed parallel to the ambient magnetic field at a distance of 12 m. The coupling to the fully developed broadband plasma turbulence was found to be limited to a narrow frequency regime centered around the driver frequency.

In the laboratory experiments KIWI and MIRABELLE, the driver amplitudes required for synchronization never exceeded 10 V, sometimes 1 V were sufficient. These amplitudes

are of the order of the local potential fluctuations and do not mean violent variations of the background plasma.

The synchronization method always drives one drift mode and already single modes lead to radial net-transport [141]. Thus, it can not be expected that the fluctuation-induced transport is suppressed entirely. The results of BLOCK et al. suggest that the synchronization significantly alters the fluctuation-induced transport. Both, suppression as well as enhancement, are possible depending on the drift wave dynamics as well as on the driven mode [144]. The question of transport control by synchronization is not the subject of the present work.

A basic question is how the exciter interacts with the plasma. Two explanations are possible: the coupling between exciter and plasma can either happen via the imposed electric field or via the current drawn to the exciter electrodes. In reference [141], the interaction between exciter signal and the drift mode was explained in terms of the vacuum electric field generated by the exciter at the position where the maximum drift wave fluctuations are localized. Externally applied electric potentials are usually shielded on spatial scales given by the sheath perpendicular to the magnetic field which is in the sub-mm range here. The electric field of the exciter is shielded already far away from the position of the maximum drift wave fluctuations and is thus unlikely to be responsible for the coupling between exciter and the drift wave dynamics. Two points support the idea that the electric current plays the leading role in the coupling mechanism:

1. In previous experiments by LATTEN [115] a slightly different experimental arrangement was used. The electrodes were galvanically decoupled from the frequency generator in order to avoid a net current through the plasma. A weak influence on the drift wave dynamics was observed but even at driver potentials $\geq \pm 30$ V no complete phase synchronization could be achieved.
2. In the numerical simulation, the dynamics could not be influenced when the exciter signal was modelled as a localized potential perturbation. Only with current drive, synchronization was observed [136].

The results presented here stress the importance of the role of the spatial dynamics in the control of drift wave dynamics. Relatively weak driver signals couple efficiently to the drift wave dynamics without changing the global equilibrium significantly. It is concluded that spatiotemporal methods are much more promising candidates for an efficient and robust control of the drift wave dynamics than purely temporal (as well as purely spatial) control methods. A further improvement of the control of drift waves could be obtained by using a combination of the presented spatiotemporal synchronization method and feedback techniques (see chapter 9). It remains an open question, to what extent the application of synchronization methods is possible in fusion devices. There, the spatial scale of the (fully developed) turbulence is smaller and the poloidal cross-section is much larger compared to low-temperature laboratory plasmas. Thus, an application of an adequate exciter arrangement would be more challenging. However, the results of reference [143] also indicate that for a significant and systematic influence on the turbulence – and thereby the anomalous transport – in the edge region of fusion devices, spatiotemporal methods are more promising than temporal methods.

Appendix A

Derivation of the drift wave dispersion relation

The aim of this appendix is to show the derivation of the drift wave dispersion relation in cartesian and cylindrical geometry in some more detail than in chapter 2. The same notation and abbreviations are used as in that chapter (see tables 2.3 and 2.4). The basic equations are first normalized and linearized. The drift wave dispersion relations for both, cartesian and cylindrical coordinate system, are derived assuming harmonic perturbations of a form adequate to the geometry.

A.1 Preparative remarks

From the definitions

$$\rho_s = \sqrt{\frac{k_B T_e M}{e^2 B^2}} \quad , \quad c_s = \sqrt{\frac{k_B T_e}{M}} \quad \text{and} \quad \Omega_{ci} = \frac{eB}{M}$$

one obtains the relations

$$\rho_s c_s = \frac{k_B T_e}{eB} \quad \text{and} \quad \frac{\rho_s}{c_s} = \frac{1}{\Omega_{ci}}$$

which are used in the normalization procedure.

Normalization of the $\mathbf{E} \times \mathbf{B}$ Drift

Following the normalization rules given in table 2.2, the normalized $\mathbf{E} \times \mathbf{B}$ drift is obtained:

$$\begin{aligned} \mathbf{V}_E &= \frac{\mathbf{E} \times \mathbf{B}}{B^2} = -\frac{1}{B^2} \nabla \phi \times \mathbf{B} \\ c_s \hat{\mathbf{V}}_E &= -\frac{1}{\rho_s} \frac{k_B T_e}{e} \frac{1}{B} \hat{\nabla} \hat{\phi} \times \mathbf{e}_{\parallel} \\ \hat{\mathbf{V}}_E &= -\hat{\nabla} \hat{\phi} \times \mathbf{e}_{\parallel} \end{aligned}$$

Splitting the total plasma potential ϕ_t into the time-averaged part ϕ_0 and the fluctuating part $\tilde{\phi}$ and assuming $\phi_0 = \phi_0(x)$ one obtains in cartesian coordinates:

$$\begin{aligned} \mathbf{V}_E &= -\nabla\phi_t \times \mathbf{e}_{\parallel} = -(\partial_x\phi_t, \partial_y\phi_t, \partial_z\phi_t) \times (0, 0, 1) \\ &= -(\partial_y\phi, -\partial_x(\phi_0 + \phi), 0) = (-\partial_y\phi, \partial_x(\phi_0 + \phi), 0) \quad . \end{aligned}$$

With $\phi_t = \phi_0 + \tilde{\phi}$ and the assumption $\phi_0 = \phi_0(r)$, one obtains in cylindrical coordinates:

$$\begin{aligned} \mathbf{V}_E &= -\nabla\phi \times \mathbf{e}_{\parallel} = -(\partial_r\phi, 1/r\partial_{\theta}\phi, \partial_z\phi) \times (0, 0, 1) \\ &= -(1/r\partial_{\theta}\phi, -\partial_r(\phi_0 + \phi), 0) = (-1/r\partial_{\theta}\phi, \partial_r(\phi_0 + \phi), 0) \quad . \end{aligned}$$

Convective derivative

From $d_t = \partial_t + \mathbf{v}_E \cdot \nabla_{\perp}$ and the formula for \mathbf{v}_E derived above one finds for cartesian coordinates

$$d_t = \partial_t + v_x\partial_x + v_y\partial_y = \partial_t - \partial_y\phi\partial_x + \partial_x(\phi_0 + \phi)\partial_y$$

and for cylindrical coordinates

$$d_t = \partial_t + v_r\partial_r + v_{\theta}\frac{1}{r}\partial_{\theta} = \partial_t - \frac{1}{r}\partial_{\theta}\phi\partial_r + \frac{1}{r}d_r(\phi_0 + \phi)\partial_{\theta} \quad .$$

A.2 Normalization

The first step towards the drift wave dispersion relations given in chapter 2 is to normalize equations (2.2), (2.4) and (2.8). The result of the normalization procedure are equations (2.20–2.22).

Electron momentum equation

From equation (2.4)

$$nm_e d_t \mathbf{v} = -\nabla p - ne(\mathbf{E} + \mathbf{v} \times \mathbf{B}) + n\nu_{ei}m_e(\mathbf{u} - \mathbf{v}) - n\nu_{en}m_e \mathbf{v}$$

only the parallel part is considered. With the assumptions given in section 2.2 and with $V \neq V(x, y, z)$ one obtains

$$\begin{aligned} nm_e d_t V &= -k_B T_e \nabla_{\parallel} n + ne \nabla_{\parallel} \phi - \nu_{ei} n m_e V - \nu_{en} n m_e V \\ d_t V &= -\frac{k_B T_e}{m_e n} \nabla_{\parallel} n + \frac{e}{m_e} \nabla_{\parallel} \phi - (\nu_{ei} + \nu_{en}) V \quad . \end{aligned}$$

Normalization yields

$$\begin{aligned} \Omega_{ci} c_s \hat{d}_t \hat{V} &= -\frac{k_B T_e}{nm_e \rho_s} \hat{\nabla}_{\parallel} n + \frac{k_B T_e e}{em_e \rho_s} \hat{\nabla}_{\parallel} \hat{\phi} - c_s \Omega_{ci} (\hat{\nu}_{ei} + \hat{\nu}_{en}) \hat{V} \\ \hat{d}_t \hat{V} &= -\frac{k_B T_e}{m_e \rho_s \Omega_{ci} c_s} \hat{\nabla}_{\parallel} N + \frac{k_B T_e}{m_e \rho_s \Omega_{ci} c_s} \hat{\nabla}_{\parallel} \hat{\phi} - (\hat{\nu}_{ei} + \hat{\nu}_{en}) \hat{V} \\ &= -\frac{M}{m_e} \hat{\nabla}_{\parallel} N + \frac{M}{m_e} \hat{\nabla}_{\parallel} \hat{\phi} - (\hat{\nu}_{ei} + \hat{\nu}_{en}) \hat{V} \quad . \end{aligned}$$

This yields equation (2.20):

$$\hat{d}_t \hat{V} = \frac{M}{m_e} \hat{\nabla}_{\parallel} (\hat{\phi} - N) - (\hat{\nu}_{ei} + \hat{\nu}_{en}) \hat{V} \quad . \quad (\text{A.1})$$

Electron continuity equation

From the electron continuity equation (2.2)

$$\partial_t n + \nabla \cdot (n\mathbf{v}) = 0$$

one obtains

$$\begin{aligned} \partial_t n &= -\nabla \cdot (n\mathbf{v}) = -n(\nabla \cdot \mathbf{v}) - \mathbf{v} \cdot \nabla n \\ &= -n(\nabla_{\perp} \cdot \mathbf{v}_{\perp} + \nabla_{\parallel} V) - \mathbf{v}_{\perp} \cdot \nabla_{\perp} n - V \nabla_{\parallel} n \\ \frac{1}{n} \partial_t n &= \left[-\frac{1}{n} V \nabla_{\parallel} n - \nabla_{\parallel} V \right] - \nabla_{\perp} \cdot \mathbf{v}_{\perp} - \frac{1}{n} \mathbf{v}_{\perp} \cdot \nabla_{\perp} n \quad . \end{aligned}$$

For the perpendicular electron velocity only the $\mathbf{E} \times \mathbf{B}$ drift and the diamagnetic drift are considered. Thus $\nabla_{\perp} \cdot \mathbf{v}_{\perp} = 0$. For the electron diamagnetic drift the $1/n \mathbf{v}_{D,e} \cdot \nabla_{\perp} n$ term vanishes and the $1/n \mathbf{v}_E \cdot \nabla_{\perp} n$ term is absorbed by the convective derivative. Thus, one obtains

$$\frac{1}{n} d_t n = -\frac{1}{n} V \nabla_{\parallel} n - \nabla_{\parallel} V \quad .$$

Normalization

$$\Omega_{ci} \frac{1}{n} \hat{d}_t n = \frac{c_s}{\rho_s} \left[-\frac{1}{n} \hat{V} \hat{\nabla}_{\parallel} n - \hat{\nabla}_{\parallel} \hat{V} \right]$$

and simplification yields equation (2.21):

$$\hat{d}_t N = -\hat{V} \hat{\nabla}_{\parallel} N - \hat{\nabla}_{\parallel} \hat{V} \quad . \quad (\text{A.2})$$

Quasineutrality

From equation (2.8)

$$\nabla_{\perp} \cdot \mathbf{J}_{\perp} = -\nabla_{\parallel} \cdot \mathbf{J}_{\parallel} \quad (\text{A.3})$$

follows

$$\begin{aligned} e \nabla_{\perp} \cdot (n\mathbf{u}_{\perp} - n\mathbf{v}_{\perp}) &= e \nabla_{\parallel} \cdot (nV) \\ en \nabla_{\perp} \cdot (\mathbf{u}_{\perp} - \mathbf{v}_{\perp}) + e(\mathbf{u}_{\perp} - \mathbf{v}_{\perp}) \cdot \nabla_{\parallel} n &= en \nabla_{\parallel} \cdot V + V \cdot \nabla_{\parallel} n \quad . \end{aligned}$$

The perpendicular velocities are given in equations (2.13) and (2.17). The $\mathbf{E} \times \mathbf{B}$ drift is identical for ions and electrons and therefore vanishes in the difference. The diamagnetic drift terms vanish because they are divergence free. The polarization drift of the electrons can be neglected because of the mass ratio $M \gg m_e$. The only remaining terms are, consequently, the ion polarization drift and the ion Pedersen drift due to the collisions:

$$\mathbf{u}_{\perp} - \mathbf{v}_{\perp} = \frac{M}{eB^2} (d_t \mathbf{E}_{\perp} - \nu_{in} \nabla_{\perp} \phi) = \frac{M}{eB^2} (-d_t \nabla_{\perp} \phi - \nu_{in} \nabla_{\perp} \phi) \quad .$$

Thus, one yields

$$\frac{M}{B^2} (\nabla_{\perp} n \cdot (-d_t \nabla_{\perp} \phi - \nu_{in} \nabla_{\perp} \phi) - n d_t \nabla_{\perp}^2 \phi - \nu_{in} n \nabla_{\perp}^2 \phi) = e n \nabla_{\parallel} \cdot V + V \cdot \nabla_{\parallel} n \quad .$$

Normalization of the left hand side yields

$$\begin{aligned} & \frac{M}{B^2} \left[\frac{1}{\rho_s} \hat{\nabla}_{\perp} n \cdot \left(-\Omega_{ci} \hat{d}_t \frac{k_B T_e}{e \rho_s} \hat{\nabla}_{\perp} \hat{\phi} - \Omega_{ci} \hat{\nu}_{in} \frac{k_B T_e}{e \rho_s} \hat{\nabla}_{\perp} \hat{\phi} \right) \right] \\ & + \frac{M}{B^2} \left[-n \frac{1}{\rho_s^2} \frac{k_B T_e}{e} \Omega_{ci} \hat{d}_t \hat{\nabla}_{\perp}^2 \hat{\phi} - \Omega_{ci} \hat{\nu}_{in} n \frac{k_B T_e}{e \rho_s^2} \hat{\nabla}_{\perp}^2 \hat{\phi} \right] \\ & = \frac{M}{B^2} \Omega_{ci} \frac{k_B T_e}{e \rho_s^2} \left(\hat{\nabla} n \cdot \left(-\hat{d}_t \hat{\nabla}_{\perp} \hat{\phi} - \hat{\nu}_{in} \hat{\nabla}_{\perp} \hat{\phi} \right) - n \hat{d}_t \hat{\nabla}_{\perp}^2 \hat{\phi} - \hat{\nu}_{in} n \hat{\nabla}_{\perp}^2 \hat{\phi} \right) \\ & = \frac{e^2 B}{M} \left(\hat{\nabla} n \cdot \left(-\hat{d}_t \hat{\nabla}_{\perp} \hat{\phi} - \hat{\nu}_{in} \hat{\nabla}_{\perp} \hat{\phi} \right) - n \hat{d}_t \hat{\nabla}_{\perp}^2 \hat{\phi} - \hat{\nu}_{in} n \hat{\nabla}_{\perp}^2 \hat{\phi} \right) \end{aligned}$$

and normalization of the right hand side yields

$$\frac{e c_s}{\rho_s} \left(n \hat{\nabla}_{\parallel} \cdot \hat{V} + \hat{V} \cdot \hat{\nabla}_{\parallel} n \right) = e \Omega_{ci} \hat{\nabla}_{\parallel} \left(n \cdot \hat{V} + \hat{V} \cdot \hat{\nabla}_{\parallel} n \right) = \frac{e^2 B}{M} \left(n \hat{\nabla}_{\parallel} \cdot \hat{V} - \hat{V} \cdot \hat{\nabla}_{\parallel} n \right) \quad .$$

Leaving out the common factor $e^2 B/M$ and introducing $\hat{\Omega} = \nabla^2 \phi$ one finds

$$\begin{aligned} \hat{\nabla}_{\perp} n \cdot \left(-\hat{\nu}_{in} \hat{\nabla}_{\perp} \hat{\phi} - \hat{d}_t \hat{\nabla}_{\perp} \hat{\phi} \right) - n \hat{d}_t \hat{\nabla}_{\perp}^2 \hat{\phi} - \hat{\nu}_{in} n \hat{\nabla}_{\perp}^2 \hat{\phi} &= n \hat{\nabla}_{\parallel} \hat{V} + \hat{V} \hat{\nabla}_{\parallel} n \\ \hat{\nabla}_{\perp} N \cdot \left(-\hat{\nu}_{in} \hat{\nabla}_{\perp} \hat{\phi} - \hat{d}_t \hat{\nabla}_{\perp} \hat{\phi} \right) - \hat{d}_t \hat{\Omega} - \hat{\nu}_{in} \hat{\Omega} &= \hat{\nabla}_{\parallel} \hat{V} + \hat{V} \hat{\nabla}_{\parallel} N \end{aligned}$$

which yields equation 2.22:

$$\hat{d}_t \hat{\Omega} = \hat{\nabla} N \cdot \left(-\hat{\nu}_{in} \hat{\nabla}_{\perp} \hat{\phi} - \hat{d}_t \hat{\nabla}_{\perp} \hat{\phi} \right) - \hat{\nu}_{in} \hat{\Omega} - \hat{\nabla}_{\parallel} \hat{V} - \hat{V} \hat{\nabla}_{\parallel} N \quad . \quad (\text{A.4})$$

A.3 Cartesian coordinates (Local slab model)

The goal of this section is the derivation of the dispersion relation for collisional drift waves in cartesian geometry – (equation 2.25) – from equations (2.20–2.22). The abbreviations (see table 2.3) and assumptions made in chapter 2 for the local slab model are used.

Electron momentum equation

From equation (2.20)

$$d_t V = \frac{M}{m_e} \nabla_{\parallel} (\phi - N) - \nu_e V$$

by omitting all zero order terms and all second order terms one obtains

$$\begin{aligned} \partial_t V - \partial_y \phi \partial_x (V_0 + V) + \partial_x (\phi_0 + \phi) \partial_y (V_0 + V) &= \frac{M}{m_e} \nabla_{\parallel} (\phi - n) - \nu_e (V_0 + V) \\ \partial_t V &= \frac{M}{m_e} \nabla_{\parallel} (\phi - n) - \nu_e (V_0 + V) \quad . \end{aligned}$$

By neglecting the time dependence of V an equation for V is found:

$$V = \frac{M}{m_e \nu_e} \nabla_{\parallel} (\phi - n) - V_0 \quad .$$

Replacing all the derivatives and assuming harmonic perturbations of the form of equation (2.24) yields

$$V = \frac{M}{m_e \nu_e} i k_{\parallel} (\phi - n) - V_0 \quad .$$

From this an equation for $\nabla_{\parallel} V$ is obtained:

$$\nabla_{\parallel} V = -\frac{M}{m_e \nu_e} k_{\parallel}^2 (\phi - n) = -\tau_e (\phi - n) \quad .$$

Electron continuity equation

From equation (2.21)

$$d_t N = -V \nabla_{\parallel} N - \nabla_{\parallel} V$$

one obtains the linearized form

$$\begin{aligned} \partial_t n - (\partial_y \phi) \partial_x \ln n_0 + \partial_x \phi (\partial_y \ln n_0 + \partial_y n) &= -V_0 \nabla_{\parallel} n - \nabla_{\parallel} V \\ \partial_t n - (\partial_y \phi) \partial_x \ln n_0 &= -V_0 \nabla_{\parallel} n - \nabla_{\parallel} V \quad . \end{aligned}$$

Replacing all the derivatives and assuming harmonic perturbations of the form of equation (2.24) yields

$$-i\omega n - i k_y \phi \partial_x \ln n_0 = -i k_{\parallel} V_0 n + \tau_e (\phi - n)$$

and thus

$$-i\omega n = -i\omega^* \phi - i w_1 n + \tau_e (\phi - n) \quad .$$

Quasineutrality

From equation (2.22)

$$d_t \Omega = \nabla N \cdot (-d_t \nabla \phi - \nu_{in} \nabla \phi) - \nu_{in} \Omega - \nabla_{\parallel} V - V \nabla_{\parallel} N$$

one obtains the linearized left hand side:

$$\begin{aligned} d_t \Omega &= \partial_t (\Omega_0 + \Omega) - (\partial_y \phi) \partial_x (\Omega_0 + \Omega) + \partial_x (\phi_0 + \phi) \partial_y (\Omega_0 + \Omega) \\ &= \partial_t \Omega = -\partial \nabla_{\perp}^2 \phi = (-i\omega) (i k_y)^2 \phi = i\omega k_y^2 \phi \end{aligned}$$

where harmonic fluctuations are assumed, equation (2.24). For the last three terms of the right hand side one obtains

$$\begin{aligned} -\nu_{in} \Omega &= \nabla_{\parallel} V - V \nabla_{\parallel} N \\ &= -\nu_{in} \nabla_{\perp}^2 (\phi_0 + \phi) - \nabla_{\parallel} (V_0 + V) - (V_0 + V) (\nabla_{\parallel} \ln n_0 + \nabla_{\parallel} n) \\ &= -\nu_{in} \nabla_{\perp}^2 \phi + \tau_e (\phi - n) - V_0 \nabla_{\parallel} n \\ &= -\nu_{in} (i k_y)^2 \phi + \tau_e (\phi - n) - V_0 i k_{\parallel} n \\ &= \nu_{in} k_y^2 \phi + \tau_e (\phi - n) - i w_1 n \quad . \end{aligned}$$

The $\nabla N \cdot (\dots)$ terms vanish since all non-zero terms are zero order or second order terms. Combining all terms of the equation again yields

$$i\omega k_y^2 \phi = \nu_{in} k_y^2 \phi + \tau_e (\phi - n) - iw_1 n \quad . \quad (\text{A.5})$$

Derivation of the dispersion relation

With $b = k_y^2$ equations (A.3) and (A.5) can be written as

$$\begin{aligned} (\tau_e + iw_1) n &= (-i\omega b + \nu_{in} b + \tau_e) \phi \\ (-i\omega + iw_1 + \tau_e) n &= (-i\omega^* + \tau_e) \phi \end{aligned}$$

which allows elimination of n and ϕ :

$$\begin{aligned} (-i\omega b + \nu_{in} b + \tau_e)(-i\omega + iw_1 + \tau_e) &= (\tau_e + iw_1)(-i\omega^* + \tau_e) \\ -\omega^2 b + b\omega w_1 - i\tau_e \omega b - ib\nu_{in}\omega + ib\nu_{in}w_1 + \tau_e b\nu_{in} - i\omega\tau_e + iw_1\tau_e + \tau_e^2 &= -i\omega^*\tau_e + w_1\omega^* + \tau_e^2 + iw_1\tau_e \\ 0 = b\omega^2 + (-bw_1 + i\tau_e b + ib\nu_{in} + i\tau_e)\omega + (-ib\nu_{in}w_1 - \tau_e b\nu_{in} - i\omega^*\tau_e + w_1\omega^*) & \\ 0 = b\omega^2 + (i\tau_e(1+b) + ib\nu_{in} - bw_1)\omega - \tau_e(b\nu_{in} + i\omega^*) + w_1(\omega^* - ib\nu_{in}) & \quad . \quad (\text{A.6}) \end{aligned}$$

This is equation (2.25). Also, the phase relation between n and ϕ can be obtained

$$n = \frac{-i\omega b + \nu_{in} b + \tau_e}{\tau_e + iw_1} \phi = \frac{-i\omega^* + \tau_e}{-i\omega + iw_1 + \tau_e} \phi \quad . \quad (\text{A.7})$$

A.4 Cylindrical coordinates

The goal of this section is to derive the differential equation (2.30) from the normalized equations (2.20–2.22). The abbreviations (see table 2.4) and assumptions made in chapter 2 for the cylindrical model are used.

Linearization

The first step towards equation (2.30) is the linearization of equations (2.20–2.22).

Electron momentum equation

From equation (2.20)

$$d_t V = \frac{M}{m_e} \nabla_{\parallel} (\phi - N) - (\nu_{ei} + \nu_{en}) V$$

using $\nu_e = \nu_{ei} + \nu_{en}$, $\nabla_{\parallel} \phi_0 = 0$ and $\nabla_{\parallel} n_0 = 0$ one obtains

$$\begin{aligned} \partial_t (V_0 + V) - \frac{1}{r} (\partial_{\theta} \phi) \partial_r (V_0 + V) + \frac{1}{r} (\partial_r (\phi_0 + \phi)) \partial_{\theta} (V_0 + V) & \\ = \frac{M}{m_e} (\nabla_{\parallel} \phi_0 + \nabla_{\parallel} \phi - \nabla_{\parallel} \ln n_0 - \nabla_{\parallel} n) - \nu_e (V_0 + V) & \quad . \end{aligned}$$

This yields

$$\partial_t V + V_p \partial_{\theta} V = \frac{M}{m_e} \nabla_{\parallel} (\phi - n) - \nu_e (V_0 + V) \quad . \quad (\text{A.8})$$

Electron continuity equation

From equation (2.21)

$$d_t N = -V \nabla_{\parallel} N - \nabla_{\parallel} V$$

one obtains by linearization

$$\begin{aligned} \partial_t N - \frac{1}{r} \partial_{\theta} \phi \partial_r N + \partial_r (\phi_0 + \phi) \frac{1}{r} \partial_{\theta} N &= -(V_0 + V) (\nabla_{\parallel} \ln n_0 + \nabla_{\parallel} n) - \nabla_{\parallel} (V_0 + V) \\ \partial_t n - \frac{1}{r} \partial_{\theta} \phi \partial_r \ln n_0 + \partial_r \phi_0 \frac{1}{r} \partial_{\theta} n &= -(V_0 \nabla_{\parallel} \ln n_0 + V_0 \partial_z n + V \nabla_{\parallel} \ln n_0 + V \partial_z n) - \partial_z V \\ \partial_t n + \frac{1}{r} \kappa \partial_{\theta} \phi + V_p \partial_{\theta} n &= -V_0 \nabla_{\parallel} n - \nabla_{\parallel} V \quad . \end{aligned}$$

This yields

$$\partial_t n + V_p \partial_{\theta} n = -\frac{1}{r} \kappa \partial_{\theta} \phi - V_0 \nabla_{\parallel} n - \nabla_{\parallel} V \quad . \quad (\text{A.9})$$

Quasineutrality

From equation (2.22)

$$d_t \Omega = \nabla N \cdot (-\nu_{in} \nabla_{\perp} \phi - d_t \nabla_{\perp} \phi) - \nu_{in} \Omega - \nabla_{\parallel} V - V \nabla_{\parallel} N \quad (\text{A.10})$$

one obtains the linearized form of the left hand side

$$\begin{aligned} \partial_t (\Omega_0 + \Omega) - \frac{1}{r} \partial_{\theta} \phi \partial_r (\Omega_0 + \Omega) + \frac{1}{r} d_r (\phi_0 + \phi) \partial_{\theta} (\Omega_0 + \Omega) \\ = \partial_t \Omega - \frac{1}{r} \partial_{\theta} \phi \partial_r \Omega_0 + \frac{1}{r} d_r \phi_0 \partial_{\theta} \Omega = \partial_t \Omega - \frac{1}{r} \partial_{\theta} \phi S_p + V_p \partial_{\theta} \Omega \quad . \end{aligned}$$

The linearized form of the last three terms of the right hand side is

$$\begin{aligned} -\nu_{in} \Omega - \nabla_{\parallel} V - V \cdot \nabla_{\parallel} N &= -\nu_{in} (\Omega_0 + \Omega) - \nabla_{\parallel} (V_0 + V) - (V_0 + V) (\nabla_{\parallel} \ln n_0 + \nabla_{\parallel} n) \\ &= -\nu_{in} \Omega - \nabla_{\parallel} V - V_0 \nabla_{\parallel} n \quad . \end{aligned}$$

Keeping in mind that both n_0 and ϕ_0 depend only on r and that only first order terms are kept, the first of the $\nabla N \cdot$ terms reads

$$\begin{aligned} -\nu_{in} \nabla N \cdot \nabla_{\perp} \phi &= -\nu_{in} [(\partial_r \ln n_0) (\partial_r \phi) + (\partial_r n) (\partial_r \phi_0)] \\ &= -\nu_{in} [-\kappa (\partial_r \phi) + (\partial_r n) r V_p] \\ &= \nu_{in} \kappa \partial_r \phi - \nu_{in} r V_p \partial_r n \quad . \end{aligned}$$

In an analogue way for the last term one obtains

$$\begin{aligned} -\nabla N \cdot d_t \nabla_{\perp} \phi &= -\partial_r \ln n_0 d_t \partial_r \phi - \partial_r n d_t \partial_r \phi_0 \\ &= \kappa \left(\partial_t \partial_r \phi - \frac{1}{r} \partial_{\theta} \phi \partial_{rr} \phi + \frac{1}{r} \partial_r (\phi_0 + \phi) \partial_{\theta} \partial_r \phi \right) \\ &\quad - \partial_r n \left(\partial_t \partial_r \phi_0 - \frac{1}{r} \partial_{\theta} \phi \partial_r \partial_r \phi_0 + \frac{1}{r} \partial_r (\phi_0 + \phi) \partial_{\theta} \partial_r \phi_0 \right) \\ &= \kappa (\partial_t \partial_r \phi + V_p \partial_{\theta} \partial_r \phi) \quad . \end{aligned}$$

Combining all terms yields

$$\begin{aligned} \partial_t \Omega + V_p \partial_\theta \Omega &= -\nu_{in} \Omega - \nabla_{\parallel} V - V_0 \nabla_{\parallel} n \\ &+ \kappa (\partial_t + V_p \partial_\theta + \nu_{in}) \partial_r \phi - \nu_{in} r V_p \partial_r n + \frac{1}{r} \partial_\theta \phi S_p \quad . \end{aligned} \quad (\text{A.11})$$

From the linearized equations to the differential equation

Assuming harmonic fluctuations of the form of equation (2.29) the derivatives ∂_t , $\nabla_{\parallel} = \partial_z$ and ∂_θ are subsequently replaced by $-i\omega$, ik_{\parallel} and im , respectively. The resulting equations are combined to obtain the differential equation (2.30).

Electron momentum equation

From equation (A.8)

$$\partial_t V + V_p \partial_\theta V = \frac{M}{m_e} \nabla_{\parallel} (\phi - n) - \nu_e (V_0 + V)$$

one finds by neglecting the time dependence in the electron parallel velocity

$$\begin{aligned} V_p \partial_\theta V &= \frac{M}{m_e} \nabla_{\parallel} (\phi - n) - \nu_e (V_0 + V) \\ \left(1 + \frac{V_p im}{\nu_e}\right) V &= \frac{M}{m_e \nu_e} \nabla_{\parallel} (\phi - n) - V_0 \\ V &= \frac{ik_{\parallel}}{\nu_e + im V_p} \frac{M}{m_e} (\phi - n) - \alpha(r) V_0 \quad . \end{aligned}$$

For $\nabla_{\parallel} V$ one obtains

$$\nabla_{\parallel} V = -\frac{k_{\parallel}^2}{\nu_e + im V_p} \frac{M}{m_e} (\phi - n) = -P(\phi - n) \quad .$$

Electron continuity equation

From equation (A.9)

$$\partial_t n + V_p \partial_\theta n = -\frac{1}{r} \kappa \partial_\theta \phi - V_0 \nabla_{\parallel} n - \nabla_{\parallel} V$$

one obtains

$$\begin{aligned} -i\omega n + V_p imn &= -\frac{1}{r} \kappa(r) im\phi - V_0 ik_{\parallel} n + P(\phi - n) \\ -i\tilde{\omega} n &= -i\omega^* \phi - iw_1 n + P(\phi - n) \\ (-i\tilde{\omega} + iw_1 + P)n &= (-i\omega^* + P)\phi \\ n &= \frac{\omega^* + iP}{\tilde{\omega} - w_1 + iP} \phi \quad . \end{aligned}$$

This is an equation which connects n and ϕ and from which the phase shift between density and potential fluctuations can be found. For the further analysis it is also useful to get an expression for $P(\phi - n)$:

$$P(\phi - n) = -i\tilde{\omega}n + i\omega^*\phi + iw_1n \quad .$$

Quasineutrality

The resubstitution of Ω to ϕ is given by the following expression

$$\Omega = \nabla^2\phi = \frac{1}{r}\partial_r(r\partial_r\phi) + \frac{1}{r^2}\partial_{\theta\theta}\phi = \left(\partial_{rr} + \frac{1}{r}\partial_r - \frac{m^2}{r^2}\right)\phi \quad .$$

From equation (A.11)

$$\begin{aligned} \partial_t\Omega + V_p\partial_\theta\Omega &= -\nu_{in}\Omega - \nabla_{\parallel}V - V_0\nabla_{\parallel}n \\ &\quad + \kappa(\partial_t + V_p\partial_\theta + \nu_{in})\partial_r\phi - \nu_{in}rV_p\partial_r n + \frac{1}{r}\partial_\theta\phi S_p \end{aligned}$$

one obtains

$$\begin{aligned} -i\omega\Omega + imV_p\Omega &= -\nu_{in}\Omega + P(\phi - n) - V_0ik_{\parallel}n \\ &\quad + \kappa(-i\omega + imV_p + \nu_{in})\partial_r\phi - \nu_{in}rV_p\partial_r n + \frac{1}{r}im\phi S_p \\ -i\tilde{\omega}\Omega &= -\nu_{in}\Omega + P(\phi - n) - iw_1n \\ &\quad + \kappa(-i\tilde{\omega} + \nu_{in})\partial_r\phi - \nu_{in}rV_p\partial_r n + \frac{1}{r}im\phi S_p \quad . \end{aligned}$$

This yields

$$\begin{aligned} (-i\tilde{\omega} + \nu_{in})\Omega - P(\phi - n) + iw_1n - \kappa(-i\tilde{\omega} + \nu_{in})\partial_r\phi + \nu_{in}rV_p\partial_r n - \frac{1}{r}im\phi S_p &= 0 \\ (-i\tilde{\omega} + \nu_{in})\left(\partial_{rr} + \frac{1}{r}\partial_r - \frac{m^2}{r^2}\right)\phi - P(\phi - n) + iw_1n \\ - \kappa(-i\tilde{\omega} + \nu_{in})\partial_r\phi + \nu_{in}rV_p\partial_r n - \frac{1}{r}im\phi S_p &= 0 \\ (-i\tilde{\omega} + \nu_{in})\left(\partial_{rr} + \frac{1}{r}\partial_r - \frac{m^2}{r^2} - \kappa\partial_r\right)\phi - P(\phi - n) + iw_1n \\ + \nu_{in}rV_p\partial_r n - \frac{1}{r}im\phi S_p &= 0 \quad . \end{aligned}$$

Using the abbreviations

$$A = \frac{1}{\tilde{\omega} + i\nu_{in}}, \quad \text{and} \quad B = \frac{\omega^* + iP}{\tilde{\omega} - w_1 + iP}$$

and replacing $P(\phi - n)$ and n leads to

$$\begin{aligned} (-i\tilde{\omega} + \nu_{in})\left(\partial_{rr} + \frac{1}{r}\partial_r - \frac{m^2}{r^2} - \kappa\partial_r\right)\phi + i\tilde{\omega}n - i\omega^*\phi - iw_1n + iw_1n \\ + \nu_{in}rV_p\partial_r n - \frac{1}{r}im\phi S_p &= 0 \end{aligned}$$

$$\begin{aligned}
(-i\tilde{\omega} + \nu_{in}) \left(\partial_{rr} + \frac{1}{r} \partial_r - \frac{m^2}{r^2} - \kappa \partial_r \right) \phi + i\tilde{\omega} B \phi - i\omega^* \phi + B \nu_{in} r V_p \partial_r \phi - \frac{1}{r} i m \phi S_p &= 0 \\
(\tilde{\omega} + i\nu_{in}) \left(\partial_{rr} + \frac{1}{r} \partial_r - \frac{m^2}{r^2} - \kappa \partial_r \right) \phi - \tilde{\omega} B \phi + \omega^* \phi + i B \nu_{in} r V_p \partial_r \phi + \frac{1}{r} m \phi S_p &= 0 \\
\partial_{rr} + \left(\frac{1}{r} \partial_r - \kappa \partial_r \right) \phi - \frac{m^2}{r^2} \phi - \tilde{\omega} A B \phi + A \omega^* \phi + i A B \nu_{in} r V_p \partial_r \phi + A \frac{1}{r} m \phi S_p &= 0 \\
\partial_{rr} + \left(\frac{1}{r} - \kappa + i A B \nu_{in} r V_p \right) \partial_r \phi + \left(A \omega^* + A \frac{1}{r} m S_p - \tilde{\omega} A B - \frac{m^2}{r^2} \right) \phi &= 0 \quad .
\end{aligned}$$

Finally, using the two definitions for RD and Q given in chapter 2

$$RD(r) := i \frac{1}{\tilde{\omega} + i\nu_{in}} \left(\frac{\omega^* + iP}{\tilde{\omega} - w_1 + iP} \right) \nu_{in} r V_p = i A B \nu_{in} r V_p$$

and

$$Q(r) := \frac{1}{\tilde{\omega} + i\nu_{in}} \left[\omega^* + \frac{m}{r} S_p - \tilde{\omega} \frac{\omega^* + iP}{\tilde{\omega} - w_1 + iP} \right] = A \left[\omega^* + \frac{m}{r} S_p - \tilde{\omega} B \right]$$

one finally obtains the second order differential equation (2.30)

$$\partial_{rr} \phi + \left(\frac{1}{r} - \kappa(r) + RD(r) \right) \partial_r \phi + \left(Q(r) - \frac{m^2}{r^2} \right) \phi = 0 \quad .$$

This equation is numerically solved in chapter 7.

Appendix B

Collisions

In a plasma, collisions between the different kinds of particles play an important role since they can change the momentum and energy of the interacting particles or even change the particles themselves, for instance, in the case of ionization of an atom. As seen in chapter 2, collision frequencies also determine the dynamics of drift waves and, therefore, for numerical calculations numbers for collision frequencies are needed. Unfortunately, collision frequencies are difficult to determine accurately. In this chapter the main collision processes in argon plasmas are briefly summarized and formulas used in this work for the estimation of collision frequencies of the most important collision processes are given. An overview on collisions can be found in reference [145].

Energy and momentum are conserved during collision processes. Principally, one distinguishes between elastic and inelastic collisions. For elastic collisions the sum of the kinetic energy of the particles is conserved. In inelastic collisions a fraction of the kinetic energy is changed into internal energy of the involved atom or ion and also the number of particles can change. Examples for inelastic processes are ionization and excitation of neutrals. Usually, inelastic collisions are rare compared to elastic collisions.

In weakly ionized gases the charged particles collide more frequently with neutral atoms than with each other, while for higher ionization degrees, Coulomb collisions between charged particles dominate. In a helicon discharge, both Coulomb collisions as well as collisions between charged particles and neutrals, play a role. For this reason, both kinds of collisions are discussed in this section.

The collision frequency between the species α and β is defined by

$$\nu_{\alpha\beta} = n_{\beta} \langle \sigma_{\alpha\beta} v_{\alpha} \rangle \quad (\text{B.1})$$

where $\sigma_{\alpha\beta}$ is the cross section for collisions between the species α and β , n is the density and v is the velocity. Usually, $\nu_{\alpha\beta}$ is different from $\nu_{\beta\alpha}$. For a Maxwellian distribution, this reads to be

$$\nu_{\alpha\beta} = n_{\beta} \frac{4}{\pi} \left(\frac{m_{\alpha}}{2k_{\text{B}}T_{\alpha}} \right)^{3/2} \int_0^{\infty} \sigma_{\alpha\beta}(v) v_{\alpha}^3 \exp\left(\frac{-m_{\alpha}v_{\alpha}^2}{2k_{\text{B}}T_{\alpha}}\right) dv_{\alpha} \quad . \quad (\text{B.2})$$

The rate constant is defined by

$$K_{\alpha\beta} = \langle \sigma_{\alpha\beta} v_{\alpha} \rangle \quad . \quad (\text{B.3})$$

B.1 Coulomb-Collisions

Charged particles ‘feel’ each other’s electric field from a certain distance. That means that their momentum changes even if they do not actually collide. Most of these collisions occur at a small angle but the cumulation of these many small-angle collisions leads to large momentum changes. For Coulomb collisions an analytic expression for the cross section can be found. Thus, the collision frequency can also be given by a formula:

$$\nu_{ei} = \left(\frac{1}{4\pi\epsilon_0} \right)^2 \frac{4\sqrt{2\pi} Z^2 e^4 n_i}{3\sqrt{m_e} (k_B T_e)^{3/2}} \ln \Lambda \quad (\text{B.4})$$

where

$$\ln \Lambda = \ln \left[\left(\frac{1}{4\pi\epsilon_0} \right)^{-3/2} \frac{3 (k_B T_e)^{3/2}}{2\sqrt{\pi} e^3 \sqrt{n_e}} \right], \quad (\text{B.5})$$

Z is the charge number, T_e is the electron temperature in units of K and n_e is the plasma density in m^{-3} [146]. From this a handy formula for ν_{ei} can be derived:

$$\nu_{ei} = 2.91 \cdot 10^{-12} \frac{n}{T_{[\text{eV}]^{3/2}}^2} \ln \Lambda$$

where the electron temperature $T_{[\text{eV}]}$ is expressed in eV and the plasma density n in m^{-3} .

The electron-electron collision frequency is $\nu_{ee} = \nu_{ei}/\sqrt{2}$. The ion-ion collision frequency depends on ion mass and ion temperature [146]:

$$\nu_{ii} = \left(\frac{1}{4\pi\epsilon_0} \right)^2 \frac{4\sqrt{\pi} Z^4 e^4 n_i}{3\sqrt{M} (k_B T_i)^{3/2}} \ln \Lambda \quad (\text{B.6})$$

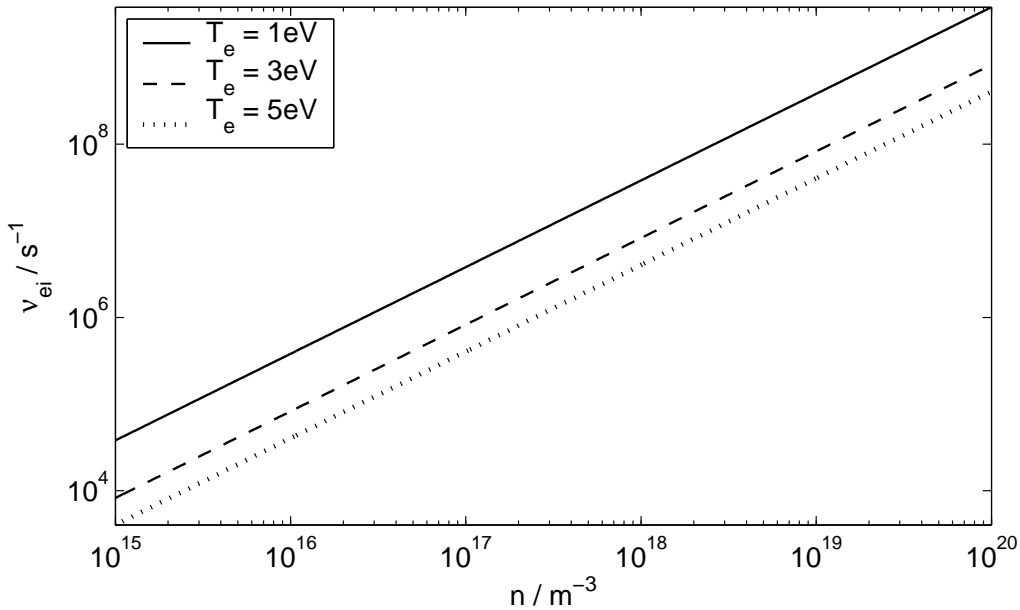


Figure B.1: Electron-ion collision frequency in dependency of the plasma density.

B.2 Electron-neutral collisions

Neutrals do not have an external electric field. So charged particles ‘feel’ their presence only when they come within the range of an atomic radius. For elastic collisions one can think of electron-atom collisions as collisions between billiard balls. For higher electron energies inelastic collisions become more important.

Elastic collisions

Since electrons are much lighter than atoms, there is a considerable change of the electron momentum when it collides with a neutral. The neutral on the other hand is nearly unaffected. The cross section for such collisions depends on the type of gas as well as on the energy of the electron. At high energies, the cross section decreases because the electron passes the atom so fast that there is not enough time for the electric field of the outermost electrons of the atom to change the momentum of the passing electron. The momentum transfer cross section for elastic electron-atom collisions in argon is plotted in Figure B.2. It is found that, especially for low energies, the cross section depends on the electron energy. Using formula B.1, the collision frequency can be calculated numerically. The result of the calculation for three neutral gas pressures is shown in

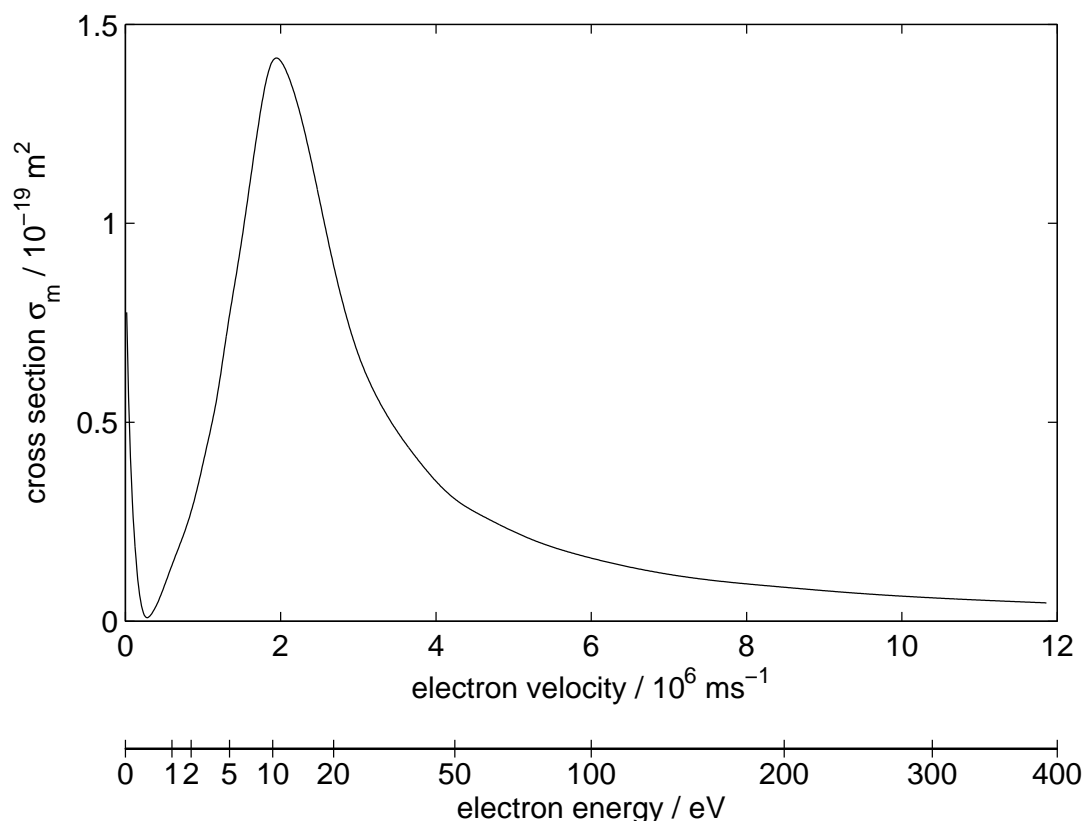


Figure B.2: Momentum transfer cross section for elastic electron neutral collisions in argon [147]. The electron energy E and the electron velocity v are connected by $E = mv^2/2e$ where E is in units of eV.

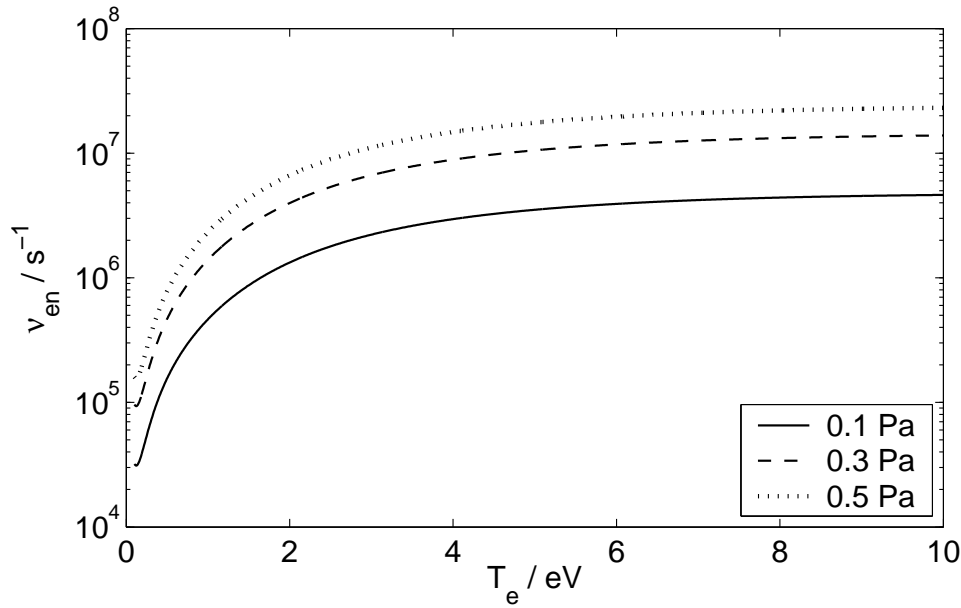


Figure B.3: *Electron-neutral collision frequency.*

figure B.3. It is found that for temperatures above approximately 2 eV the collision frequency is relatively constant. Below 2 eV, changes in the collision frequency of more than two orders of magnitude are found. The collision frequency for elastic electron-neutral collisions increases with the neutral gas pressure.

Inelastic collisions between electrons and neutrals

The most important inelastic processes between electrons and neutral gas atoms are ionization and excitation. For argon, the ionization threshold is 15.76 eV and the excitation threshold is 11.55 eV. A comparison between the three most important collision rates is shown in figure B.4. It is found that the collision rate for elastic collisions dominates by far for low temperature plasmas. Insofar, only the collision frequency for elastic collisions is taken into account in this work.

B.3 Ion-neutral collisions

Besides elastic collisions, for collisions between ions and neutrals, the ion-atom charge transfer reaction $A + A^+ \rightarrow A^+ + A$ is also an important process. A comparison of cross sections for both processes is shown in figure B.5. It can be seen that cross sections for both processes are of the same order of magnitude and increase towards low energies where not much data exists. In reference [146] a formula for the cross-section for resonant charge exchange between an argon ion and an argon atom (both in the ground state) is given:

$$\sigma_{ct}[\text{m}^2] = 4.8 \cdot 10^{-19} \text{ m}^2 \left(1 + 0.14 \ln \left(\frac{1 \text{ eV}}{E[\text{eV}]} \right) \right)^2 \quad (\text{B.7})$$

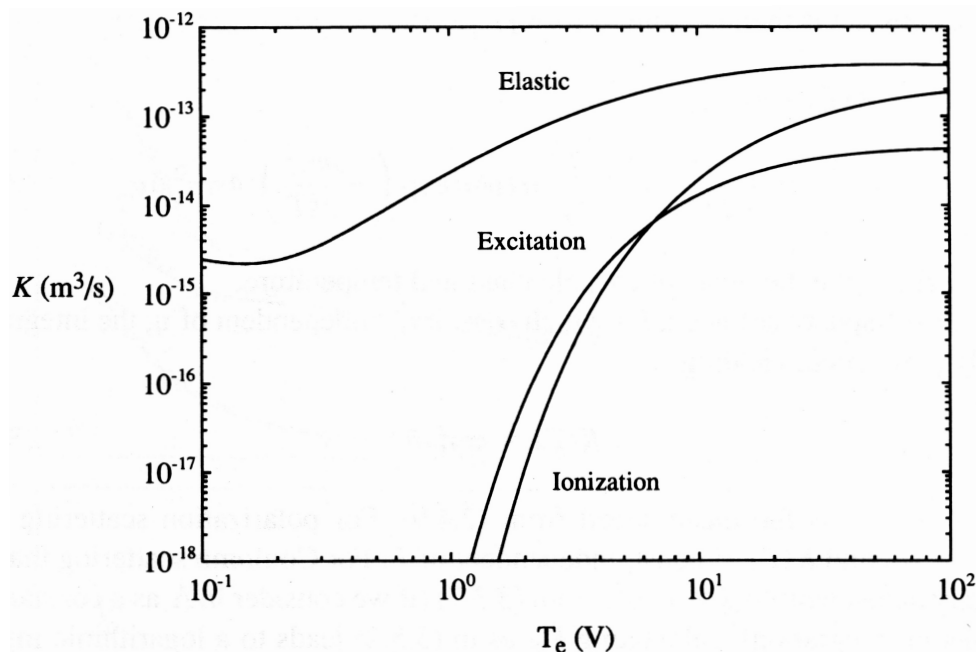


Figure B.4: Comparison between collision rates for elastic electron-neutral collisions, ionizing collisions and exciting collisions. From Reference [145].

where E is the kinetic energy of the ion with respect to the atom. For room temperature $E = 0.025$ eV this yields $\sigma_{in} = 1.1 \cdot 10^{-18}$ m² and for $E = 0.3$ eV a value $\sigma_{in} = 6.5 \cdot 10^{-19}$ m² is obtained. This is also in good agreement with the value of the total ion-atom cross-section at low temperatures of $\sigma_{in} \approx 10^{-18}$ m² which is given in reference [145]. Ionization due to ion-atom collisions is significant only for energies higher than 100 eV and can therefore be neglected when discussing laboratory plasmas [145].

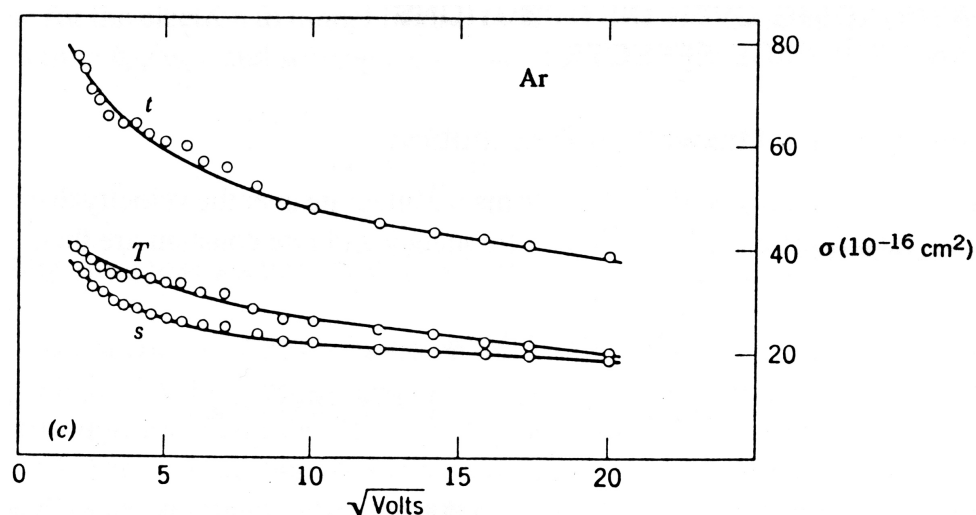


Figure B.5: Comparison between collision rates for elastic ion-neutral collisions (s) and charge transfer collisions (T). t denotes the sum of both mechanisms. From reference [145].

Appendix C

List of Symbols

<i>A</i>	Vector potential	
<i>B</i>	magnetic field	
<i>B</i>	z-component of the magnetic field	
<i>e</i>	elementary charge	
<i>b</i>	$b = k_y^2$ (normalized units)	table 2.3
β	ratio of plasma pressure to magnetic-field pressure	
β_μ	$\beta/(m_e/M)$	
c_s	ion sound velocity	table 2.2
δ	phase shift between exciter plates	chapter 10
<i>f</i>	frequency	
$f_{D,e}$	electron diamagnetic drift frequency	
f_E	E×B frequency	
<i>I</i>	current	
$I_{e, \text{isat}}$	electron saturation current	chapter 4
$I_{i, \text{isat}}$	ion saturation current	chapter 4
<i>i</i>	$\sqrt{-1}$	
<i>j, J</i>	current density	chapters 2 and 4
<i>K</i>	$\kappa - RD$	
<i>k</i>	wave vector	
k_{\parallel}, k_{\perp}	parallel / perpendicular part of <i>k</i>	
κ	inverse density gradient scale length	table 2.4
k_B	Boltzmann constant	table 2.4
L_{\perp}	density gradient length scale	
λ_D	Debye length	table 4.2
λ_z	parallel wavelength	
<i>M</i>	ion mass	
<i>m</i>	poloidal mode number	
m_d	poloidal driver mode number	chapter 10
m_e	electron mass	
μ_0	vacuum permeability	
<i>N</i>	$\ln n$	
<i>n</i>	total plasma density $n = n_0 + \tilde{n}$, also used instead of \tilde{n}	
n_0	mean plasma density	

\tilde{n}	fluctuating part of the plasma density	
n_g	neutral gas density	
ν_{ei}	electron ion collision frequency	
ν_{en}	electron neutral collision frequency	
ν_e	electron collision frequency $\nu_{ei} + \nu_{en}$	table 2.2
ν_{in}	ion neutral collision frequency	
P	abbr. used in num. model	table 2.4
p	plasma pressure	
p_g	neutral gas pressure	
ϕ	plasma potential $\phi = \phi_0 + \tilde{\phi}$, also used instead of $\tilde{\phi}$	
φ	phase angle	chapter 4
ϕ_0	mean plasma potential	
$\tilde{\phi}$	fluctuating part of the plasma potential	
ϕ_f	floating potential	section 4.2
ϕ_p	plasma potential	section 4.2
Q	abbr. used in num. model	equation (2.31)
ψ	parallel component of \mathbf{A}	
ψ	eigenfunctions	chapter 7
$r_{c,e}, r_{c,i}$	electron / ion gyro radius	table 4.2
R	normalized cross correlation function	chapter 3
RD	rotational drag term	equation (2.32)
ρ_s	drift scale	table 2.2
S	spectral power density	chapter 3
S_p	curvature of flow profile	table 2.4
σ	standard deviation	
T_α	temperature of species α in K	
$T_{[eV]}$	electron temperature in eV	
t	time	
τ	time lag or normalized collision frequency	table 2.3
τ_e	$Mk_{\parallel}^2/m_e\nu_e$	table 2.3
U	\mathbf{u}_{\parallel} , parallel ion velocity	chapter 2
U	probe bias with respect to ground	chapter 4
U_g	grid bias	chapter 10
U_t	tube bias	chapter 10
\mathbf{u}	ion velocity	
V	\mathbf{v}_{\parallel} parallel electron velocity	chapter 2
V	probe bias with respect to the plasma potential	chapter 4
V_p	normalized $E \times B$ drift	table 2.4
\mathbf{v}	electron velocity	
$\mathbf{v}_{D,\alpha}$	diamagnetic drift velocity for species α	equation 2.15
\mathbf{v}_E	$E \times B$ drift velocity	equation 2.14
$v_{p,\alpha}$	polarization drift velocity for species α	equation 2.16
$v_{th,e}, v_{th,i}$	electron / ion thermal velocity	table 4.2
Ω	vorticity	chapter 2
Ω_{ci}	ion cyclotron frequency	
ω	angular frequency	
ω_R, ω_I	real / imaginary part of the drift wave frequency	

$\omega_{c,e}$	electron cyclotron frequency	table 4.2
$\omega_{p,e}, \omega_{p,i}$	electron / ion plasma frequency	table 4.2
ω^*	frequency corresponding to $V_{D,e}$	tables 2.3, 2.4
ω_1	electron parallel drift frequency	table 2.4
$\tilde{\omega}$	$\omega - mV_p$	table 2.4
(r, θ, z)	cylindrical coordinates ($\mathbf{e}_z \parallel \mathbf{B}$)	
(x, y, z)	cartesian coordinates ($\mathbf{e}_z \parallel \mathbf{B}$)	

Bibliography

- [1] F. F. Chen. *Introduction to Plasma Physics and Controlled Fusion*. Plenum Press, New York, 2nd edition, 1984.
- [2] F. F. Cap. *Handbook on Plasma Instabilities*, volume 1. Academic, New York, 1976.
- [3] A. B. Mikhailovskii. *Theory of plasma instabilities: Instabilities of an Inhomogeneous Plasma*, volume 2. Consultants Bureau, Berlin, 1974.
- [4] A. B. Mikhailovskii. *Electromagnetic instabilities in an inhomogeneous plasma*. Plasma Physics Series. Institute of Physics Publishing, 1992.
- [5] F. Wagner and U. Stroth. Transport in toroidal devices - the experimentalist's view. *Plasma Phys. Controlled Fusion*, 35:1321–1371, 1993.
- [6] B. A. Carreras. Progress in anomalous transport research in toroidal magnetic confinement devices. *IEEE Trans. Plasma Sci.*, 25(6):1281–1321, 1997.
- [7] P. C. Liewer. Measurements of microturbulence in tokamaks and comparison with theories of turbulence and anomalous transport. *Nucl. Fusion*, 25(5):543–621, 1985.
- [8] W. Horton. Drift waves and transport. *Reviews of Modern Physics*, 71(3):735–778, 1999.
- [9] R. F. Ellis, E. Marden-Marshall, and R. Majeski. Collisional drift instability of a weakly ionized argon plasma. *Plasma Physics*, 22:113–132, 1980.
- [10] E. Marden-Marshall. *Drift Waves in a nonuniformly rotating plasma column*. PhD thesis, Dartmouth College Hanover, 1980.
- [11] N. D'Angelo and N. Rynn. Diffusion of a cold cesium plasma across a magnetic field. *Phys. Fluids*, 4:275–276, 1961.
- [12] N. D'Angelo. Low-frequency oscillations in cesium thermionic converters. *Phys. Fluids*, 4:1054–1055, 1961.
- [13] N. D'Angelo and N. Rynn. Diffusion and recombination of a highly ionized cold plasma in a magnetic field. *Phys. Fluids*, 4:1303–1306, 1961.
- [14] H. W. Hendel, T. K. Chu, and P. A. Politzer. Collisional drift waves—identification, stabilization, and enhanced plasma transport. *Phys. Fluids*, 11:2426–2439, 1968.
- [15] E. Marden Marshall, R. F. Ellis, and J. E. Walsh. Collisional drift instability in a variable radial electric field. *Plasma Phys. Controlled Fusion*, 28(9B):1461–1482, 1986.
- [16] T. Klinger, A. Latten, A. Piel, and G. Bonhomme. Chaos and turbulence studies in low- β plasmas. *Plasma Phys. Controlled Fusion*, 39:B145–B156, 1997.

- [17] O. Grulke and T. Klinger. Large-scale fluctuation structures in plasma turbulence. *New Journal of Physics*, 4:67.1–67.23, 2002.
- [18] S. S. Moiseev and R. Z. Sagdeev. On the Bohm diffusion coefficient. *Sov. Phys. - JETP*, 17:515–517, 1963.
- [19] J. D. Jukes. Micro-instabilities in magnetically confined, inhomogeneous plasma. *Phys. Fluids*, 7:1468–1474, 1964.
- [20] F. F. Chen. Normal modes for electrostatic ion waves in an inhomogeneous plasma. *Phys. Fluids*, 7:949–955, 1964.
- [21] F. F. Chen. Effect of sheaths on drift instabilities in thermionic plasmas. *Phys. Fluids*, 8:752–754, 1965.
- [22] F. F. Chen. Resistive overstabilities and anomalous “diffusion”. *Phys. Fluids*, 8:912–919, 1965.
- [23] F. F. Chen. Spectrum of low- β plasma turbulence. *Phys. Rev. Lett.*, 15(9):381–383, 1965.
- [24] F. F. Chen. “Universal” overstability of a resistive, inhomogeneous plasma. *Phys. Fluids*, 8:1323–1333, 1965.
- [25] H. Lashinsky. Universal instability in a fully ionized inhomogeneous plasma. *Phys. Rev. Lett.*, 12:121–123, 1964.
- [26] R. F. Ellis and R. W. Motley. Collisional drift instability driven by an axial current. *Phys. Rev. Lett.*, pages 1496–1499, 1971.
- [27] F. F. Chen. Nonlocal drift modes in cylindrical geometry. *Phys. Fluids*, 10:1647–1651, 1967.
- [28] T. K. Chu, B. Coppi, H. W. Hendel, and F. W. Perkins. Drift instabilities in a uniform rotating plasma cylinder. *Phys. Fluids*, 12(1):203–208, 1969.
- [29] R. F. Ellis and E. Marden-Marshall. Comparison of local and nonlocal theories of the collisional drift instability. *Phys. Fluids*, 22(11):2137–2139, 1979.
- [30] P. A. Politzer. Drift instability in collisionless alkali metal plasmas. *Phys. Fluids*, 14(11):2410–2425, 1971.
- [31] Y. Nishida and K. Ishii. Observation of the coupled mode of a collisional drift wave and an Alfvén wave. *Phys. Rev. Lett.*, 33(6):352–355, 1974.
- [32] J. T. Tang, Jr. and Y. Nishida N. C. Luhmann, and K. Ishii. Destabilization of hydromagnetic drift-Alfvén waves in a finite- β , collisional plasma. *Phys. Rev. Lett.*, 34(2):70–73, 1975.
- [33] J. T. Tang and Jr. N. C. Luhmann. Destabilization of hydromagnetic drift-Alfvén waves in a finite pressure collisional plasma. *Phys. Fluids*, 19(12):1935–1946, 1976.
- [34] R. W. Boswell. Very efficient plasma generation by whistler waves near the lower hybrid frequency. *Plasma Phys. Controlled Fusion*, 26(10):1147–1162, 1984.
- [35] K. P. Shamrai and V. B. Taranov. Volume and surface rf power absorption in a helicon plasma source. *Plasma Sources Sci. Technol.*, 5:474–491, 1996.

- [36] D. D. Blackwell, T. G. Madziwa, D. Arnush, and F. F. Chen. Evidence for trivelpiece-gould modes in a helicon discharge. *Phys. Rev. Lett.*, 88(14):145002, 2002.
- [37] A. W. Molvik, A. R. Ellingboe, and T. D. Rognlien. Hot-electron production and wave structure in a helicon plasma source. *Phys. Rev. Lett.*, 79(2):233–236, 1997.
- [38] F. F. Chen and D. D. Blackwell. Upper Limit to Landau Damping in Helicon Discharges. *Phys. Rev. Lett.*, 82(14):2677–2680, 1999.
- [39] S. Cho. The role of the lower hybrid resonance in helicon plasmas. *Phys. Plasmas*, 7(1):417–423, 2000.
- [40] M. M. Balkey, R. Boivin, J. L. Kline, and E. E. Scime. Ion heating and density production in helicon sources near the lower hybrid frequency. *Plasma Sources Sci. Technol.*, 10:284–294, 2001.
- [41] F. F. Chen. Helicon plasma sources. In O. A. Popov, editor, *High Density Plasma Sources*. Noyes Publications, New Jersey, 1995.
- [42] M. Light, F. F. Chen, and P. L. Colestock. Low frequency electrostatic instability in a helicon plasma. *Phys. Plasmas*, 8(10):4675–4689, 2001.
- [43] A. W. Degeling, T. E. Sheridan, and R. W. Boswell. Model for relaxation oscillations in a helicon discharge. *Phys. Plasmas*, 6(5):1641–1648, 1999.
- [44] A. W. Degeling, T. E. Sheridan, and R. W. Boswell. Intense on-axis plasma production and associated relaxation oscillations in a large volume helicon source. *Phys. Plasmas*, 6(9):3664–3673, 1999.
- [45] M. Light, F. F. Chen, and P. L. Colestock. Quiescent and unstable regimes of a helicon plasma. *Plasma Sources Sci. Technol.*, 11:273–278, 2002.
- [46] G. R. Tynan and coworkers. Bull. Am. Phys. Soc. 46(8), BM1.13, LP1.134-136.
- [47] T. K. Chu and H. W. Hendel (Ed.). *Feedback and Dynamic Control of plasmas*. American Institute of Physics, New York, 1970.
- [48] K. I. Thomassen. Feedback stabilization in plasmas. *Nucl. Fusion*, 11:175–186, 1971.
- [49] V. V. Arsenin and V. A. Chuyanov. Suppression of plasma instabilities by the feedback method. *Sov. Phys. Usp.*, 20(9):736–762, Sept. 1977.
- [50] H. W. Hendel, T. K. Chu, F. W. Perkins, and T. C. Simonen. Remote feedback stabilization of collisional drift instability by modulated microwave energy source. *Phys. Rev. Lett.*, 24(3):90–92, 1970.
- [51] P. W. Terry. Suppression of turbulence and transport by sheared flow. *Rev. Mod. Phys.*, 72(1):109–165, 2000.
- [52] H. G. Schuster (Ed.). *Handbook of Chaos Control*. VCH-Wiley, Weinheim, 1999.
- [53] E. Gravier, X. Caron, and G. Bonhomme. Control of the chaotic regimes of nonlinear drift-waves in a magnetized laboratory plasma. *Phys. Plasmas*, 6(5):1670–1673, 1999.
- [54] T. Klinger, A. Latten, A. Piel, T. Pierre, G. Bonhomme, and T. Dudock de Wit. The route to drift wave chaos and turbulence in a bounded low- β plasma experiment. *Phys. Rev. Lett.*, 79(20):3913–3916, 1997.

- [55] T. Shinbrot. Progress in the control of chaos. *Adv. Phys.*, 44(2):73–111, 1995.
- [56] U. Kauschke, G. Oelerich-Hill, and A. Piel. Experimental investigation of coherent drift waves at low magnetic fields. *Phys. Fluids B*, 2(1):38–43, 1990.
- [57] B. Scott. *Low Frequency Fluid Drift Turbulence*, habilitation thesis, Heinrich-Heine-Universität Düsseldorf, 2000. IPP report 5/92, Max-Planck-Institut für Plasmaphysik.
- [58] F. Jenko and B. D. Scott. Numerical computation of collisionless drift wave turbulence. *Phys. Plasmas*, 6(6):2418–2424, 1999.
- [59] W. Baumjohann and R. A. Treumann. *Basic Space Plasma Physics*. Imperial College Press, London, 1996.
- [60] D. L. Jassby. Transverse velocity shear instabilities within a magnetically confined plasma. *Phys. Fluids*, 15(9):1590–1604, 1972.
- [61] A. Hasegawa and K. Mima. Stationary spectrum of strong turbulence in magnetized nonuniform plasma. *Phys. Rev. Lett.*, 39(4):205–208, 1977.
- [62] A. Hasegawa and K. Mima. Pseudo-three-dimensional turbulence in magnetized nonuniform plasma. *Phys. Fluids*, 21(1):87–92, 1978.
- [63] P. W. Terry and W. Horton. Drift wave turbulence in a low-order k space. *Phys. Fluids*, 26(1):106–112, 1983.
- [64] B. Scott. Three-dimensional computation of drift alfvén turbulence. *Plasma Phys. Controlled Fusion*, 39:1635–1668, 1997.
- [65] A. Hasegawa and M. Wakatani. Plasma edge turbulence. *Phys. Rev. Lett.*, 50(9):682–686, 1983.
- [66] E. Guyon, J.-P. Hulin, and L. Petit. *Hydrodynamik*. Vieweg, Braunschweig, 1997.
- [67] T. E. Faber. *Fluid Dynamics For Physicists*. Cambridge University Press, Cambridge, 1995.
- [68] A. R. Choudhuri. *The Physics of Fluids and Plasmas – An Introduction for Astrophysicists*. Cambridge University Press, Cambridge, 1998.
- [69] G. I. Kent, N. C. Jen, and F. F. Chen. Transverse Kelvin-Helmholtz instability in a rotating plasma. *Phys. Fluids*, 12(10):2140–2151, 1969.
- [70] F. W. Perkins and D. L. Jassby. Velocity shear and low-frequency plasma instabilities. *Phys. Fluids*, 14(1):102–115, 1971.
- [71] P. H. Rutherford R. J. Goldston. *Introduction to Plasma Physics*. Institute of Physics Publishing, 1995.
- [72] M. B. Priestley. *Spectral Analysis and Time Series*. Academic Press, San Diego, 7th edition, 1992.
- [73] J. L. Pécseli. *Fluctuations in Physical Systems*. Cambridge University Press, 2000.
- [74] R. W. Boswell and F. F. Chen. Helicons – the early years. *IEEE Trans. Plasma Sci.*, 25(6):1229–1244, 1997.

- [75] F. F. Chen. Experiments on helicon plasma sources. *J. Vac. Sci. Technol.*, A10:1389–1401, 1992.
- [76] M. Light and F. F. Chen. Helicon wave excitation with helical antennas. *Phys. Plasmas*, 2(4):1084–1093, 1996.
- [77] G. Chevalier and F. F. Chen. Experimental modeling of inductive discharges. *J. Vac. Sci. Technol.*, A11:1165–1171, 1993.
- [78] C. M. Franck. *Experiments on Whistler Wave Dispersion in Bounded Magnetised Plasmas*. PhD thesis, Ernst–Moritz–Arndt Universität Greifswald, 2003.
- [79] P. Aigrain. Les "hélicons" dans les semiconducteurs. In *Proc. Conf. Semicond. Phys.*, pages 224–227, Prague, Czechoslovakia, 1960.
- [80] C. R. Legédy. Macroscopic theory of helicons. *Phys. Rev.*, 135(6A):1713–1724, 1965.
- [81] J. A. Lehane and P. C. Thonemann. An experimental study of helicon wave propagation in a gaseous plasma. *Proc. Phys. Soc.*, 85:301–316, 1965.
- [82] F. F. Chen, J. D. Evans, and G. R. Tynan. Design and performance of distributed helicon sources. *Plasma Sources Sci. Technol.*, 10:236–249, 2001.
- [83] F. F. Chen. Helicon plasma sources. In O. A. Popov, editor, *High Density Plasma Sources*, pages 1–75. Noyes Publications, Park Ridge, NJ, USA, 1995.
- [84] F. F. Chen and R. W. Boswell. Helicons – the past decade. *IEEE Trans. Plasma Sci.*, 25(6):1245–1257, 1997.
- [85] A. W. Degeling, C. O. Jung, R. B. Boswell, and A.R. Ellingboe. Plasma production from helicon waves. *Phys. Plasmas*, 3(7):2788–2796, 1996.
- [86] Th. Enk and M. Krämer. Radio frequency power deposition in a high density helicon discharge with helical antenna coupling. *Phys. Plasmas*, 7(10):4308–4319, 2000.
- [87] I. V. Kamenski and G. G. Borg. An evaluation of different antenna designs for helicon wave excitation in a cylindrical plasma. *Phys. Plasmas*, 3(12):4396–4409, 1996.
- [88] C. Franck, O. Grulke, and T. Klinger. Mode transitions in helicon discharges. *Phys. Plasmas*, 10(1):323–325, 2003.
- [89] A. Stark. private communication.
- [90] N. Hershkowitz. How Langmuir Probes Work. In O. Auciello and D. L. Flamm, editors, *Plasma Diagnostics - Discharge Parameters and Chemistry*, pages 113–183. Academic Press, Boston, MA, 1989.
- [91] F. F. Chen. Electric probes. In H. Huddlestone, editor, *Plasma Diagnostic Techniques*, pages 113–200. Academic Press, New York, 1965.
- [92] C. Franck, O. Grulke, and T. Klinger. Magnetic fluctuation probe design and capacitive pickup rejection. *Rev. Sci. Instrum.*, 73(11):3768–3771, 2002.
- [93] I. Duran et. al. Measurements of magnetic field fluctuations using an array of Hall detectors on the TEXTOR tokamak. *Rev. Sci. Instrum.*, 73(10):3482–3489, 2002.

- [94] H. M. Mott-Smith and I. Langmuir. The theory of collectors in gaseous discharges. *Phys. Rev.*, 28:727, 1926.
- [95] I. D. Sudit and F. F. Chen. Rf compensated probes for high-density discharges. *Plasma Sources Sci. Technol.*, 3:162–168, 1994.
- [96] F. F. Chen. Langmuir probe analysis for high density plasmas. *Phys. Plasmas*, 8(2):3029–3041, 2002.
- [97] V. I. Demidov, S. V. Ratynskaia, and K. Rybdal. Electric probes in plasmas: The link between theory and experiment. *Rev. Sci. Instrum.*, 73(10):3409–3439, 2002.
- [98] K. U. Riemann. The Bohm criterion and sheath formation. *J. Phys. D: Appl. Phys.*, 24:493–518, 1991.
- [99] P. C. Stangeby. A problem in the interpretation of tokamak langmuir probes when a fast electron component is present. *Plasma Phys. Controlled Fusion*, 37:1031–1037, 1995.
- [100] T. E. Sheridan. How big is a small Langmuir probe? *Phys. Plasmas*, 7(7):3084–3088, 2000.
- [101] F. F. Chen. Langmuir probe analysis for high density plasmas. *Phys. Plasmas*, 8(6):3029–3041, 2001.
- [102] K. Hansen, T. Klinger, and A. Piel. Computer controlled probe diagnostic system and applications in a magnetized laboratory plasma. *Rev. Sci. Instrum.*, 65(8):2615–2622, 1994.
- [103] V. I. Demidov, S. V. Ratynskaia, R. J. Armstrong, and K. Rybdal. Probe measurements of electron density distributions in a strongly magnetized low-pressure helium plasma. *Phys. Plasmas*, 6(1):350–358, 1999.
- [104] R. R. Arslanbekov, N. A. Khromov, and A. A. Kudryavtsev. Probe measurements of electron energy distribution function at intermediate and high pressures and in a magnetic field. *Plasma Sources Sci. Technol.*, 3:528–538, 1994.
- [105] R. Balbin et. al. Measurement of density and temperature fluctuations using a fast-swept langmuir probe. *Rev. Sci. Instrum.*, 63(10):4605–4607, 1992.
- [106] T. Klinger A. Latten and A. Piel. A probe array for the investigation of spatio-temporal structures in drift wave turbulence. *Rev. Sci. Instrum.*, 66(5):3254–3262, 1995.
- [107] B. Clarenbach, B. Lorenz, M. Krämer, and N. Sadeghi. Time-dependent gas density and temperature measurements in pulsed helicon discharges in argon. *Plasma Sources Sci. Technol.*, 12:345–357, 2003.
- [108] D. G. Miljak and F. F. Chen. Density limit in helicon discharges. *Plasma Sources Sci. Technol.*, 7:537–549, 1998.
- [109] T. Pierre, G. Leclert, and F. Braun. Magnetized double-plasma device for wave studies. *Rev. Sci. Instrum.*, 58(1):6–11, 1 1987.
- [110] A. Latten, T. Klinger, A. Piel, and Th. Pierre. A probe array for the investigation of spatio-temporal structures in drift wave turbulence. *Rev. Sci. Instrum.*, 66(5):3254–3262, 1995.

- [111] M. Krämer, B. Lorenz, and B. Clarenbach. Helicon sources with $m=1$ and $m=2$ helical antenna coupling. *Plasma Sources Sci. Technol.*, 11:A120–A130, 2002.
- [112] F. F. Chen, I. D. Sudit, and M. Light. Downstream physics of the helicon discharge. *Plasma Sources Sci. Technol.*, 5:173–180, 1996.
- [113] I. D. Sudit and F. F. Chen. Discharge equilibrium of a helicon plasma. *Plasma Sources Sci. Technol.*, 5:43–53, 1996.
- [114] R. F. Ellis and R. W. Motley. Current-driven collisional drift instability. *Phys. Fluids*, 17:582–594, 1974.
- [115] A. Latten. *Multisondendiagnostik von Driftwellenturbulenz und anomalem Transport*. PhD thesis, Christian–Albrechts–Universität Kiel, 1997.
- [116] E. Gravier. *Etude expérimentale des régimes dynamiques des ondes de dérive dans un plasma magnétisé de laboratoire. Control du chaos spatio-temporel*. PhD thesis, Université Henri Poincaré Nancy, France, 1999.
- [117] W. H. Press, S. A. Teukolsky, W. T. Vetterling, and B. P. Flannery. *Numerical Recipes in C: The art of scientific computing*. Cambridge University Press, Cambridge, 2nd edition, 1992.
- [118] A. Madon and T. Klinger. Spatiotemporal bifurcations in plasma drift-waves. *Physica D*, 91:301–316, 1996.
- [119] O. Grulke, T. Klinger, and A. Piel. Experimental study of the dynamics of conditionally averaged structures in weakly developed electrostatic turbulence. *Phys. Plasmas*, 6(3):788–796, 1999.
- [120] H. Johnsen, H. L. Pécseli, and J. Trulsen. Conditional eddies in plasma turbulence. *Phys. Fluids*, 30(7):2239–2254, 1987.
- [121] GNU Scientific library, <http://www.gnu.org/software/gsl/>.
- [122] A. Stark. Experimentelle Untersuchungen von Magnetoschallwellen in der linearen Plasmaanlage VINETA. Master’s thesis, Ernst–Moritz–Arndt Universität Greifswald, 2002.
- [123] D. Block, A. Piel, Ch. Schröder, and T. Klinger. Synchronization of drift waves. *Phys. Rev. E*, 63:056401, 2001.
- [124] Ch. Schröder. Experimentelle Untersuchungen des globalen dynamischen Plasma-gleichgewichts im Plasmaexperiment KIWI. Master’s thesis, Christian–Albrechts–Universität Kiel, 1999.
- [125] M. Maccio, J. Vaclavik, and L. Villard. Effect of $E \times B$ flows on global linear ion temperature gradient modes. *Phys. Plasmas*, 8(3):895–906, 2001.
- [126] V. Kornilov. private communication.
- [127] T. Klinger. Control of chaos in plasmas. In H. G. Schuster, editor, *Handbook of Chaos Control*, pages 513–562, Weinheim, 1999. VCH-Wiley.
- [128] A. K. Sen. Remote feedback stabilization of tokamak instabilities. *Phys. Plasmas*, 1(5):1479–1488, 1994.

- [129] B. Richards et al. Modification of tokamak edge turbulence using feedback. *Phys. Plasmas*, 1(5):1606–1611, 1994.
- [130] A. Pikovski, M. Rosenblum, and J. Kurths. *Synchronization - A universal concept in nonlinear sciences*. Cambridge Nonlinear Science Series 12. Cambridge University Press, 2001.
- [131] B. van der Pol and J. van der Mark. Frequency demultiplication. *Nature*, 120(3919):363–364, 1927.
- [132] B. van der Pol. Forced oscillations in a circuit with non-linear resistance. *The London, Edinburgh, and Dublin Philosophical Magazine*, 7. Series, Vol. 3(13):65–80, 1927.
- [133] M. Lakshmanan and K. Murali. *Chaos in nonlinear oscillators: Controlling and Synchronization*. World Scientific Publishing Co. Pte. Ltd., Singapore, 1996.
- [134] U. Parlitz and L. Kocarev. Synchronization of chaotic systems. In H. G. Schuster, editor, *Handbook of Chaos Control*, pages 271–303, Weinheim, 1999. VCH-Wiley.
- [135] H. L. Pécseli, T. Mikkelsen, and S.E. Larsen. Drift wave turbulence in low- β plasmas. *Plasma Phys.*, 25(11):1173–1197, 1983.
- [136] Ch. Schröder, T. Klinger, D. Block, A. Piel, G. Bonhomme, and V. Naulin. Mode selective control of drift wave turbulence. *Phys. Rev. Lett.*, 86(25):5711–5714, 2001.
- [137] Ch. Schröder, T. Klinger, G. Bonhomme, D. Block, and A. Piel. Taming drift wave turbulence. *Contrib. Plasma Phys.*, 41(5):461–466, 2001.
- [138] A. S. Pikovski, M. G. Rosenblum, M. A. Zaks, and J. Kurths. Phase synchronization of regular and chaotic oscillators. In H. G. Schuster, editor, *Handbook of Chaos Control*, pages 305–328, Weinheim, 1999. VCH-Wiley.
- [139] A. Arakawa. Computational design for long-term numerical integration of the equations of fluid motion: Two-dimensional incompressible flow. *J. Comput. Phys.*, 1:119–143, 1966.
- [140] G. E. Kariadakis, M. Israeli, and S. A. Orzag. High-order splitting methods for the incompressible Navier Stokes equations. *J. Comput. Phys.*, 97:414, 1991.
- [141] D. Block. *Synchronization of drift waves and its effect on fluctuation induced transport*. PhD thesis, Christian-Albrechts-Universität Kiel, 2001.
- [142] D. Block and A. Piel. Fluctuation induced transport of driven drift waves: I. monochromatic waves. *Plasma Phys. Controlled Fusion*, 45:413–425, 2003.
- [143] H. Thomsen. *A Dynamics Investigation into Edge Plasma Turbulence*. PhD thesis, Ernst-Moritz-Arndt Universität Greifswald, 2002.
- [144] D. Block and A. Piel. Fluctuation induced transport of driven drift waves: II. weak turbulence. *Plasma Phys. Controlled Fusion*, 45:427–437, 2003.
- [145] M. A. Lieberman and A. J. Lichtenberg. *Principles of Plasma Discharges and Material Processing*. John Wiley & Sons, New York, 1994.
- [146] A. Anders. *A Formulary for Plasma Physics*. Akademie-Verlag, Berlin, 1990.

-
- [147] M. Hayashi. Recommended values of transport cross sections for elastic collision and total collision cross section for electrons in atomic and molecular gases. Institute of Plasma Physics, Nagoya University, Report IPPJ-AM-19, copies may be ordered from the National Technical Information Service, Springfield, VA22161, 1981.

Danksagung

An erster Stelle möchte ich mich bei Prof. Dr. Thomas Klinger für die interessante Themenstellung und das große Vertrauen, das er mir entgegenbrachte, bedanken. Dies ermöglichte mir, die vorliegende Arbeit über weite Teile eigenverantwortlich wissenschaftlich zu gestalten. Seine große Begeisterungsfähigkeit für die Plasmaphysik war stets hilfreich. Schon während der Promotion ermutigte er mich zur Teilnahme an verschiedenen internationalen Konferenzen und ermöglichte mir zwei mehrwöchige Kurzprojekte in Laboren in Nancy und Morgantown durchzuführen. Hierfür sei ihm besonders gedankt.

Dr. Olaf Grulke sei herzlich gedankt für die vielen nützliche Hinweise bei der Entstehung dieser Doktorarbeit, die mich in den letzten Monaten selbst aus dem fernen Amerika erreichten, nicht zu vergessen das intensive Korrekturlesen. Vor allem aber waren die zahlreichen anregenden Diskussionen mit ihm eine große Bereicherung für mich.

Mein herzlicher Dank geht an Dr. Volker Naulin für die Entwicklung von numerischen Modellen und Codes, die diese Arbeit wesentlich bereicherten und viele Erkenntnisse erst ermöglichten. Seine Geduld, immer wieder neu auftauchende Fragen zu beantworten war unerschöpflich.

Je voudrais remercier le professeur Gerard Bonhomme pour la fructueuse collaboration pendant ces dernières années et pour l'ambiance amicale au sein de la LMPI de Nancy.

I am also very grateful for the time I could spend with the group of Prof. Mark Koepke in Morgantown, USA. Working with his group was an outstanding experience and I really enjoyed the friendly atmosphere in his group.

Mein Dank gilt auch der gesamten VINETA-Arbeitsgruppe für das angenehme Arbeitsklima und die Unterstützung bei Problemen jeder Art (Schleppen schwerer Geräte, Kuchenbacken ohne eigenen Ofen, Ärger mit Computern, Fahrradflicken ...) sowie für die alljährliche Fliederbeersuppe, gemeinsame Gruppenausflüge in die nähere Umgebung und andere spannende außerphysikalische Unternehmungen.

Ein besonderer Dank und ein großes Lob geht an die Mitarbeiter der Werkstätten des Instituts für Physik der EMAU Greifswald sowie des Max-Planck-Instituts für Plasmaphysik. Ohne ihre präzise und gute Arbeit wäre die Durchführung der Experimente bereits am Aufbau gescheitert.

Tatkräftig standen uns in der Aufbauphase die studentischen Hilfskräfte Stefan Ullrich, Moritz von Buttlar, Jens Grundmann und Stefan Hadrath zur Seite. Stefan Zegenhagen hat mit diversen Meßprogrammen und einem Programm zur Kennlinienauswertung die Arbeit der gesamten VINETA-Gruppe wesentlich unterstützt. Ihnen allen sei an dieser Stelle recht herzlich gedankt.

Für das Korrekturlesen danke ich (in alphabetischer Reihenfolge) Holmer Denks, Ramin Madani, Dr. Henning Thomsen, Noelle Walsh und Stefan Zegenhagen.

Last but not least möchte ich mich ganz herzlich bei meiner Familie und Holmer Denks für all die Unterstützung in den letzten Jahren bedanken.

Abstract of the dissertation with the topic:

„Experimental investigations on drift waves in linear magnetized plasmas.“

presented by Christiane Schröder

Two main aspects concerning drift wave dynamics in linear, magnetized plasma devices are addressed in the work: In part I of the thesis, drift waves are studied in a helicon plasma. The plasma parameter regime is characterized by comparably high collision frequencies and comparably high plasma- β exceeding the electron-ion mass ratio. Single Langmuir probes and a poloidal probe array are used for spatiotemporal studies of drift waves as well as for characterization of background plasma parameters. The main goals are the identification of a low-frequency instability and its major destabilization mechanisms. All experimentally observed features of the instability were found to be consistent with drift waves. A new code, based on a non-local cylindrical linear model for the drift wave dispersion, was used to gain more insight into the dominating destabilization mechanisms, and also into dependencies of mode frequencies and growth rates on different parameters. In the experiment and in the numerical model, poloidal mode structures were found to be sheared. Part II of the thesis reports about mode-selective spatiotemporal synchronization of drift wave dynamics in a low- β plasma. Active control of the fluctuations is achieved by driving a preselected drift mode to the expense of other modes and broadband turbulence. It is demonstrated that only if a resonance between the driver signal and the drift waves in both space and time is reached, the driver has a strong influence on the drift wave dynamics. The synchronization effect is qualitatively well reproduced in a numerical simulation based on a Hasegawa-Wakatani model.